# Stellar populations of QSO host galaxies

**Dissertation**
zur Erlangung des Doktorgrades
des Fachbereichs Physik
der Universität Hamburg

vorgelegt von
**Knud Jahnke**
aus Hamburg

Hamburg, 27. Juni 2002

| | |
|---|---|
| **Gutachter der Dissertation:** | Prof. D. Reimers<br>PD Dr. L. Wisotzki |
| **Gutachter der Disputation:** | Prof. D. Reimers<br>Prof. H. J. Wendker |
| **Datum der Disputation:** | 30.07.2002 |
| **Vorsitzender des Prüfungsausschusses:** | Dr. F.-J. Zickgraf |
| **Vorsitzender des Promotionsausschusses:** | Prof. G. Huber |
| **Dekan des Fachbereichs Physik:** | Prof. F.-W. Büßer |

# Abstract

We present two new methods to extract spectral information on the host galaxies of quasars enabling us to study their colours, stellar composition, and interstellar gas content. The first method uses images in several optical and near-infrared bands for which host galaxy fluxes are extracted via multi-component modelling of nucleus and host. The second directly extracts the host galaxy component from *on-nuclear* quasar spectra via modelling of the different spatial light distributions of the nuclear and host galaxy component. This is made possible for the first time.

A comparison of the two methods for objects with both broad-band colours as well as spectra available, shows that both methods deliver reliable results as soon as minimal signal-to-noise requirements, and maximal nucleus-to-host ratio are fulfilled.

These methods are applied to date the stellar components of three samples of intermediately luminous low-redshift quasars. The first sample is a complete sample of 19 quasars with $z < 0.2$, observed in seven optical and near-infrared bands with ESO telescopes. For the two other samples deep on-nuclear spectra were obtained, with the ESO 3.6m telescope and the VLT.

We find both disk and elliptical host galaxies. While the disks show largely normal morphologies, colours and stellar population compared to inactive intermediate type disks, the ellipticals are morphologically normal, but show unusually blue colours. Rotating gas disks are found for the majority of our ellipticals. Their stellar populations are much younger than expected from their inactive counterpart, in general compatible with continuous star formation or ages of $\sim$2 Gyrs.

We propose and discuss an explanation within the framework of hierarchical galaxy formation and evolution. Our elliptical quasar hosts would be the result of recent ($< 0.5$ Gyrs) merger events of luminous spiral galaxies. In the merger the spheroidal morphology is created, but the stellar populations present are largely those of the precursor galaxies. The results support a direct connection between the evolution of elliptical galaxies, AGN activity and the evolution of central black holes in galaxies.

# Zusammenfassung

In dieser Arbeit präsentieren wir zwei neue Methoden zur Extraktion von spektralen Information von Quasar Hostgalaxien, um deren Farben und die Zusammensetzung ihrer Sternpopulationen und des interstellaren Gases zu untersuchen. Die erste Methode benutzt Bilder in einer Anzahl Bänder im optischer und nah-infraroten Spektralbereich, für die Hostgalaxieflüsse mit Hilfe von Multi-Komponenten Modellierung von Kern und Hostgalaxie extrahiert werden. Die zweite extrahiert direkt die Hostgalaxiekomponente eines *on-nucleus* Spektrums mittels Modellierung der unterschiedlichen räumlichen Lichtverteilung des Kern- und Hostgalaxieanteils. Dies wird damit zum ersten Mal möglich gemacht.

Ein Vergleich der Anwendung beiden Methoden auf Objekte für die sowohl Breitband-Farben als auch und Spektren vorlagen zeigt, daß beide Methoden zuverlässige Resultate liefern, sobald ein minimales Signal-zu-Rauschen Verhältnis und ein maximales Kern-zu-Hostgalaxie Verhältnis vorliegen.

Die beiden Methoden werden auf die Daten von drei Stichproben von Quasaren mittlerer Leuchtkraft und niedriger Rotverschiebung angewandt. Die erste ist eine vollständige Stichprobe von 19 Quasaren mit $z < 0.2$, für die Bilder in sieben optischen und nah-infraroten Bänder mit ESO Teleskopen aufgenommen wurden. Für die beiden anderen wurden tiefe on-nucleus Spektren mit dem ESO 3.6m und dem VLT aufgenommen.

Wir finden sowohl Scheiben- als auch elliptische Hostgalaxien. Die Scheiben zeigen im Vergleich zu inaktiven Scheibengalaxien weitgehend normale Morphologie, Farben und stellare Populationen. Im Unterschied dazu zeigen die Ellipsen zwar eine normale Morphologie, aber deutlich blauere Farben als erwartet. Dazu finden wir rotierende Gasscheiben in diesen Ellipsen. Ihre stellaren Populationen sind deutlich jünger als von ihren inaktiven Gegenstücken aus erwartet, generell kompatible mit kontinuierlicher Sternentstehung oder einem Alter von 2 Milliarden Jahren.

Für diese Ergebnisse schlagen wir eine Erklärung im Rahmen hierarchischer Galaxienentstehung und -entwicklung vor. Unsere elliptischen Galaxien wären danach das Ergebnis eines Merger zweier leuchkräftiger Spiralgalaxien vor weniger als ca. 500 Mill. Jahren. In dem Merger-Prozess wird die elliptische Morphologie erzeugt, die stellaren Populationen sind hingegen weitgehend die der Vorgängergalaxien. Unsere Resultate unterstützen eine direkte Kopplung der Entwicklung elliptischer Galaxien, AGN Aktivität und der Entwicklung der zentralen schwarzen Löcher in Galaxienzentren.

I’m scanning all my radars
well she said she’s from a quasar
fortythousand million light-years away

She’s just a cosmic girl
from another galaxy
my heart’s in zero gravity

*Jamiroquai*, Cosmic girl,
Travelling without moving, 1999

# Contents

# 1 Introduction

At the point when a natural scientist notices that his field of research appears in pop music, then he is probably an astrophysicist. The night sky, with the constellation of stars, and the romantic moon has always had its place in poetry and music lyrics, but the mentioning of a quasar must be new. Quasar research as a part of pop culture?

When the author of the lines on the previous page talks about his *cosmic girl* coming "from a quasar", he means – of course! – the quasar's host galaxy. He might not be wrong. More and more evidence is found that the host galaxies of AGN might be common galaxies in many respects. Made of stars, many with planets, and statistics predicts some of those might be inhabitable. Even though the nuclei of quasars are the most luminous sources of light – apart from short-timescale gamma ray bursts –, life in the host galaxy of a luminous quasar wouldn't be much different from our own.

Living at 10 kpc distance from the nucleus in the host of one of the more luminous quasars in this study (e.g. HE 1029–1401, $M_V = -24.9$), the nighly sky would not change dramatically. In the optical the nucleus would appear as the brightest source just after the moon, at about $V = -10$. It would be visible during the day and cast an extra shadow at night, but that would be about it.

But the question remains, how similar are quasar host galaxies to inactive galaxies like our own? No final answer is available yet, due to the inherent difficulty of studying galaxies with extremely luminous nuclei, outshining the host. Is an active phase part of all galaxies' life cycle? Most galaxies seem to have a central black hole, so can all galaxies potentially harbour an AGN? What are the prerequisites apart from the existence of the black hole? How are black hole mass and galaxy properties coupled? And how the formation of central black hole and galaxy? Are tidal events and merger required? What kind of star formation and merging history do host galaxies have? What is the current stellar composition of them, how does it compare to inactive galaxies and what does this teach us about the QSO[1] phenomenon?

While in the past mainly morphological information, luminosity distributions and radio properties were used to investigate QSO host galaxies, in this work we[2] want to determine the spectral properties of the hosts. Spectral information is extracted in two complementing ways, *multicolour imaging* on one side and direct *on-nuclear spectroscopy* on the other. We developed algorithms for the difficult task to separate nuclear and galaxy component not only in images, but for spectra, which has not been possible up to now. These techniques open up a multitude of new diagnostic possibilities, a part of which are explored with the application of these techniques to data taken of two samples of low redshift QSOs.

In this chapter we want to give a brief introduction into the field of QSO host galaxies, the current knowledge and the connections to galaxy formation. In chapter 2 we analyse a complete sample of low redshift hostgalaxies via *multicolour imaging*, in chapter 3 the newly developed

---

[1] In the whole of this work quasar and QSO will be used as synonyms, both naming type 1 AGN in general, including the more luminous of Seyfert galaxies, independent of radio emission properties.

[2] If the word "we" is used throughout this work, the author means "I" without wanting to exclude the other members of the Hamburg/Potsdam host galaxy group and others, who were involved in discussion on methodology, provided data, etc., and without whose contribution this work would not be what it is. Nevertheless the work is an original work of the author, who hopes to have given credit to the work of others at all points applicable.

technique for the extraction of host galaxy spectra from *on-nuclear* QSO spectra is described. In chapters 4 and 5 two samples of low redshift host galaxies are modelled with this technique and the resulting spectra analysed. In chapter 6 the results from the analysis of the three samples are finally discussed.

Throughout this study we adopt a cosmological model with $H_0 = 50$ km s$^{-1}$ Mpc$^{-1}$, $q_0 = 0.5$ and $\Lambda = 0$.

## 1.1 Current knowledge on QSO host galaxies

Almost 30 years have passed since the pionieering study by Kristian (1973), suggesting QSOs were the active nuclei in galaxies, similary to the already known Seyfert galaxies. It took five years to find spectroscopic evidence for stellar light in the extended gas emission around QSOs (Morton et al. 1978; Green et al. 1978) and another four to find unequivocal proof (Boroson et al. 1982).

By now it is generally accepted that the QSO phenomenon is part of the family of active galactic nuclei (AGN), related to massive black holes in the centre of galaxies. *All* studies of QSOs searching for host galaxies found the nuclei embedded in luminous galaxies. Potentially "naked" QSOs, reported by a singular study (Bahcall et al. 1995), were shown to be due to suboptimal analysis (McLeod & Rieke 1995a). The question today is not any more *if* galaxies are involved, but *which subset of the present day galaxy population* is capable of hosting quasar-level nuclear activity.

### 1.1.1 Unified models

Several members of the AGN family are described to be intrinsically identical objects only viewed along different lines of sight (Antonucci 1993). According to this unified theory Seyfert 2 galaxies are viewed through a torus of intervening optically thick material. The same object at a smaller inclination would appear as a Seyfert 1 galaxy, if the line of sight missed the torus. Data on QSO host galaxy inclination angles, and measurements in polarized light back this theory. Currently it is being searched for buried nuclei in high luminosity QSOs, suggested to be e.g. present in ultra luminous infrared galaxies (ULIRGs), but in their case the burial would not only be due to geometric effects but to a complete covering of the nucleus by dust.

For radio-loud object similar unifications apply. Radio galaxies would be like radio-lout QSOs, but with a buried nucleus, and there are very similar host galaxy properties found for the two groups, supporting this idea (Dunlop et al. 2001). Similar projection effects appear in the unification of BL Lac objects, and steep- and flat-spectrum radio QSOs, with different orientations of a radio jet relative to the observer.

### 1.1.2 Host morphology

QSO host galaxies are found in a wide variety of morphologies, from late type disks to massive ellipticals, and are generally drawn from the bright end of the galaxy luminosity function (Hutchings et al. 1984; Dunlop et al. 1993; Hamilton et al. 2000; Wisotzki et al. 2001). Ground based and HST optical and near-infrared imaging found a dependence of host morphology on nuclear luminosity, more luminous QSOs are more likely to be found in elliptical galaxies, lower luminosity QSOs more likely in disks, and Seyfert galaxies almost exclusively in disks. Contrary to previous believes it is by now established that this is independent of radio emission properties. Very luminous radio-loud and -quiet QSOs are exclusively found in giant elliptical host galaxies (Dunlop et al. 2001).

Some QSO host galaxies are found in the state of merging, some with visible tidal distortions, or in the presence of companion galaxies. But others appeare completely symmetric, without visible companions, and showing no signs of distortions at all (Schade et al. 2000). Due to the difficulty of selecting appropriate comparison samples of inactive galaxies, it is not clear at the moment if the amount of asymmetries and tidal features found for host galaxies is larger than for the inactive population. For very luminous QSOs there are indications that this is indeed the case (Dunlop et al. 2001), but only for hosts with a significant disk component. A study on lower luminosity hosts found an enhanced fraction of barred spirals compared to inactive galaxies (Hutchings & Neff 1992).

From the current knowledge it is not ruled out that the amount of asymmetry, companions and distortions present in host galaxies changes significantly with luminosity. A vastly enhanced interaction rate compared to inactive galaxies is currently not observed, illustrated by the existence of morphologically absolutely normal host galaxies.

### 1.1.3 Fuelling mechanisms: merger or starburst?

Also accepted by now is the source of energy: Matter falling onto the central massive black hole, creating a accretion disk in which dissipative processes convert the potential energy of the infalling mass into radiation. The variety of morphologies makes it difficult to establish a clear source for the accreted material. Two competing ideas are currently debated: It is possible that stellar wind of massive stars in a circumnuclear starburst might provide some of the material. Connected with this idea, some researchers even assign a significant fraction, or in earlier papers all, of the nuclear radiation to circumnuclear supernovae (Terlevich et al. 1992, 1995; Aretxaga et al. 1997). The by now widely preferred alternative is encounters of the QSO host with other galaxies, inducing tidal distortions that funnel gas from the ISM inwards, accreting onto the nucleus. These encounters can have a range of sizes, from small dwarf galaxies swallowed by a larger galaxy to major merger of two similarly sized galaxies (Lake et al. 1998; Kauffmann & Haehnelt 2000). It is likely that circumnuclear starbursts are created in major merger events from the infalling gas. From this it is not finally ruled out that stellar winds contribute at least some material, only about $1\,M_{\odot}$ per year is necessary to sustain QSO activity.

### 1.1.4 Black hole mass, nuclear and host luminosities

The scenario of smaller and larger merger as the source for infalling material – directly or indirectly via induced starburst – is supported by the theory of hierarchical clustering in the creation and evolution of galaxies (e.g. Kauffmann & Haehnelt 2000), in contrast to QSO activity and nuclear black hole creation in the initial phase of collapse of gas to form a galaxy (e.g. Haehnelt & Rees 1993). With the merging scenario several properties of QSO host galaxies can be explained: As for inactive galaxies it was found that a relation exists between black hole mass and the spheroid mass of the host galaxy – meaning the whole of an elliptical or the bulge of a disk galaxy respectively (Kormendy & Richstone 1995; Magorrian et al. 1998; Merrit & Ferrarese

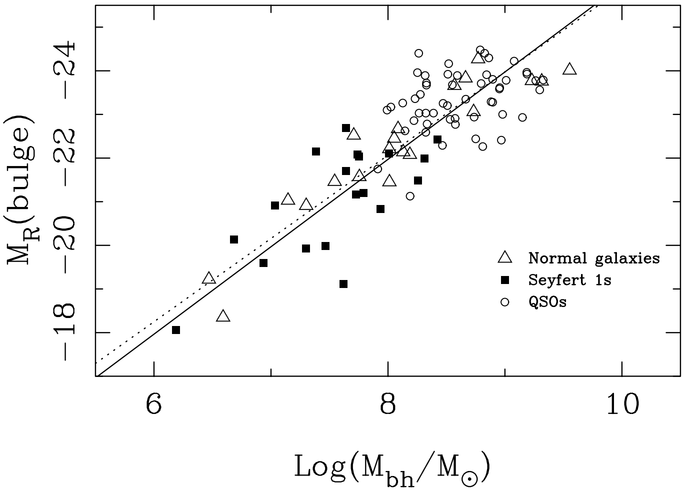

**Figure 1.1.** Bulge luminosity vs. black hole mass for inactive galaxies (triangles), Seyfert 1 galaxies (filled squares) and QSOs (circles). Figure reproduced from McLure & Dunlop (2002).

2001; McLure & Dunlop 2001, 2002). In Figure 1.1 this relation is shows as bulge luminosity vs. black hole mass.

If the nuclear luminosity is limited by Eddington accretion – the amount of infalling material is limited by the outward radiation force of the nucleus – and thus directly related to black hole mass, it is also correlated with the bulge mass of the host. Hierarchical clustering with its joint evolution models of central black holes and galaxies can thus explain the correlated increase of spheroid fraction and nuclear luminosity.

It can also explain the prior finding of a lower limit in host galaxy luminosity for a given nuclear luminosity (McLeod & Rieke 1995b; McLeod et al. 1999, see Fig. 1.2). It was found that QSOs with a nuclear luminosity $M_B = -23$ do not exist in galaxies less luminous than $L^*$. This relation is currently disputed in a study of high luminosity QSOs (Percival et al. 2001), but doubts have been expressed on the reliability of the numerical deconvolution procedure used to extract the host galaxies from the QSO images.

As unclear as the trigger mechanism for the nuclear activity is the *distribution* of the lu-

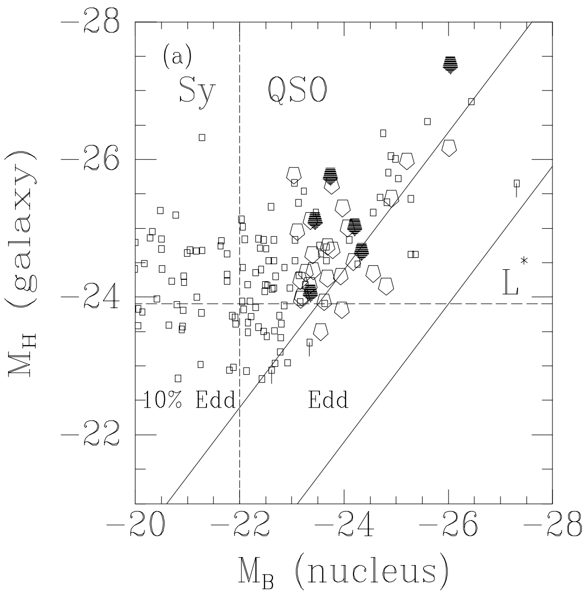

**Figure 1.2.** QSO nuclear vs. host luminosities: It is found that nuclei of a given nuclear luminosity can only exist in host galaxies with a minimal luminosity. Figure reproduced from McLeod et al. (1999), where $H_0 = 80$ km s$^{-1}$ Mpc$^{-1}$, $q_0 = 0$ is assumed.

minosity of QSO hosts, particularly at higher redshifts. In an attempt to determine the local luminosity function of QSOs (Wisotzki, Kuhlbrodt, & Jahnke 2001), it was found that except for the faint end the shape of the $H$ band luminosity function is consistent with early type field galaxies, while in a study by Hamilton et al. (2000) the authors claim that at a galaxy absolute magnitude $M_V = -24.3$ virtually all elliptical galaxies are QSO host galaxies, a result disputed by Wisotzki et al.

### 1.1.5 QSO host galaxies at higher redshifts and radio emission

Thus while using "luminous" when characterising host galaxies at low redshifts might be right, the picture gets more confusing at high redshifts. Only a few studies investigated QSO hosts at $z \geq 1$, using ground bases telescopes with tip-tilt correction or adaptive optics, and the HST. One emphasis was to find potential differences in the properties of the hosts of radio-loud and -quiet QSOs, and to study the evolution of host galaxies.

Several studies conclude that QSO host galaxies are significantly more luminous at $z = 2$ than in the local universe, which is explained with massive star formation of $> 100 M_\odot$ per year in the process of formation of the very young galaxies (Aretxaga et al. 1998b,a). These studies find hosts being 3–4 mag more luminous than a passively evolved $L^*$ galaxy placed at $z = 2$. Though the adaptive optics analysis techniques used by Aretxaga et al. might lead to an erroneous overestimation of the estimated host flux, a second adaptive optics study of $z = 2$ QSO hosts, soon to be published (Kuhlbrodt, Örndahl, Wisotzki & Jahnke, in prep.) using a methodically completely different and potentially more solid approach, comes to similar luminosities in $H$ band imaging.

Lowenthal et al. (1995) and Kukula et al. (2001) find differences between radio-quiet and radio-loud QSOs. In an HST NICMOS study the latter find luminosities for hosts of radio-loud and radio-quiet QSOs compatible with passive evolution from $z = 1$ to the present (see Fig. 1.3). For $z = 2$ they conclude different properties for radio-loud and -quiet QSOs: the hosts of radio-

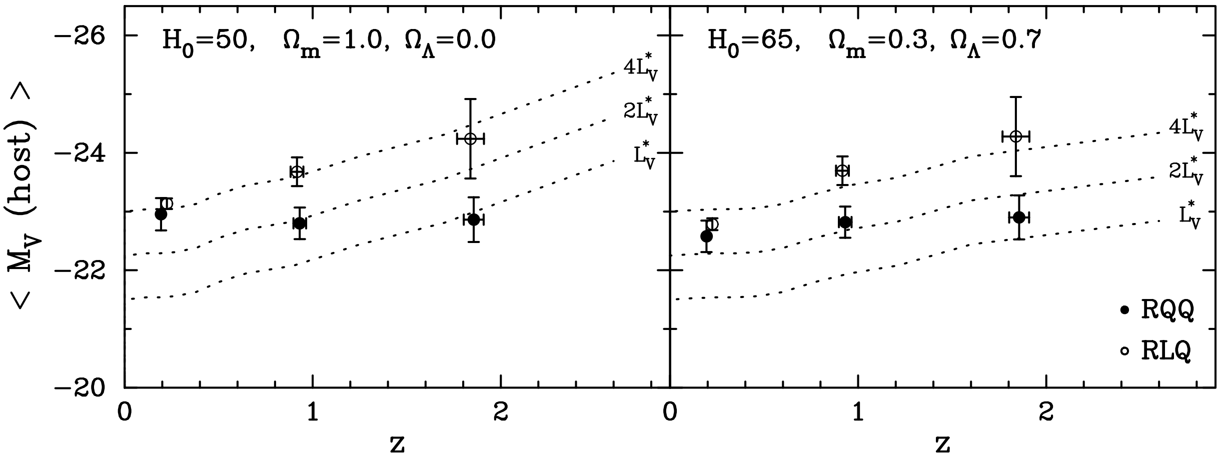

**Figure 1.3.** What is the formation history of QSO host galaxies? Evolution of radio-loud and radio-quiet host galaxies from $z = 2$ to the present. Open symbols represent radio-loud hosts, filled symbols radio-quiet. For the latter passive evolution would be ruled out independent of cosmology. Figure reproduced from Kukula et al. (2001).

loud QSOs would have assembled beyond $z = 2$, being compatible with passive evolution, the radio-quiet hosts would be less massive by a factor of 2–4 then compared to $z = 0.2$. This difference between radio-loud and -quiet QSOs was also suggested by Hutchings (1995).

A similar difference in the luminosities of radio-loud and -quiet QSOs is found already for intermediate redshifts (Örndahl & Rönnback 2001). According to their results the former would become on average more luminous between $z = 0.45$ and $z = 0.7$, while the latter would not.

The acumulated results are inconclusive. The high-redshift studies have strong implications on galaxy formation scenarios, because they link the star formation in galaxies with the formation of galaxies via merging. The samples of QSOs observed in high redshift studies are too small to draw final conclusion.

For low redshifts a number of attempts have been made to link the amount of radio emission to host galaxy properties (e.g. Malkan 1984; Hutchings et al. 1989; Taylor et al. 1996; Dunlop et al. 2001), but also no definite answers are available. So far it is only clear that radio loudness is mainly found for elliptical hosts, while most disks are radio quiet, though not silent. However not exclusive. The majority of ellipticals is radio quiet, while a few disks show radio loudness (e.g. Rönnback et al. 1996). The amount of radio emission does apparently neither scale with black hole mass (Figure 1.4) nor fuelling rate nor clustering properties (Dunlop et al. 2001). The physics of the radio emission remains unknown.

### 1.1.6 Spectral information as a key?

Determining the timescales involved in the QSO activity, the formation of the stellar content and dynamical morphology of the host galaxy and the growth of the black hole is a key to determine the physical processes involved in galaxy and QSO formation. Dating the stellar populations of host galaxies is one part of this. Up to high redshifts we propose that this will be possible in the future via multi-band imaging, using upcoming instruments like ADONIS, the adaptive optics instrument at the VLT, which is combining HST-like resolution with 8m light gathering power. Sampling the host galaxies' SED at several points will yield information about the underlying

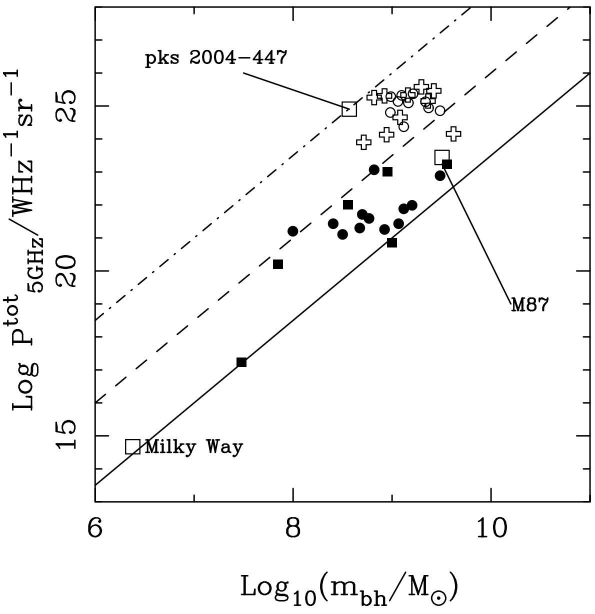

**Figure 1.4.** Total radio luminosity vs. black hole mass for radio-loud QSOs (open circles), radio-quiet QSOs (filled circles), radio galaxies (crosses) and inactive galaxies (squares) reproduced from Dunlop et al. (2001). The solid line suggests a lower limit to the amount of radio emission as a function of black hole mass. Also a scatter in radio luminosity over several orders of magnitude for similar black hole masses is seen. The reasons for this are unknown.

stellar populations, and the star formation rate. For low redshifts we propose to use *on-nucleus* spectroscopy to extract host galaxy spectra. If it were possible to use these methods to directly date the stellar populations, this would be a very promising way to study the history of the galaxies, and their future.

While for $z = 2$ this will have to wait for intrumentation to be developed, at low redshift dating the host galaxies is already possible, which we want to prove in this study. Several open questions are adressed:

- What is the material accreted onto the black hole? Stellar winds or ISM or both?
- What is the exact mechanism that triggers the accretion process?
- Is the AGN phase a part of every galaxies' evolution within a hierarchical clustering scenario? Can major merger *not* produce an AGN?
- How do QSO host galaxies evolve from the earliest QSOs to $z = 0$?
- What are the physical processes involved in creating the AGN zoo and the morphological properties involved beside orientation effects?
- Which processes regulate the radio emission? How do amount of emission and morphology of the emission relate to other properties of the QSO and the host galaxy?
- How large is the escape fraction of UV radiation emitted by the QSO nucleus, ionising the IGM? Is the QSO UV radiation responsible for reionisation of the universe?

# 2 Multicolour imaging

## 2.1 Introduction

In this chapter we develop the use of broad band imaging to extract spectral information on QSO host galaxies. We first give an overview over the currently available techniques to extract the host galaxy from a QSO image with strong nuclear contribution and over the current use of colour information in host galaxy studies. In section 2.2 we introduce a study with observations in seven optical and near-infrared (NIR) bands of a complete sample of low-$z$ QSOs. We describe the process of extracting the host galaxy (section 2.3) and the photometry of the host (section 2.4) and present the extracted morphologies, luminosities and colours of the sample (section 2.5). In section 2.6 we compare the obtained colours to the general population of inactive galaxies and finally determine ages of the stellar populations in the hosts (section 2.7). The results are discussed in chapter 6 together with the spectroscopic results from the following chapters.

### 2.1.1 QSO imaging analysis: disecting the monster

Most research on QSO host galaxies in the optical and NIR wavelength range used imaging to study distributions of morphology, luminosities, clustering properties. Spectroscopic studies are scarce because of the inherent difficulties posed by a luminous nucleus in the centre of a galaxy (more on spectroscopic studies and a solution to this problem is presented in chapter 3). This fundamental problem also exists in imaging studies, because standard techniques for the analysis of galaxies like aperture photometry or the study of morphologies can only be performed after the amount of light from the nucleus, and preferably its spatial distribution, can be estimated.

Because of this, host galaxy studies have for a long time been searching for an optimal way to remove the nuclear contribution of the QSO light from the data. Several techniques have been developed over the years, for different applications. Generally one- and two-dimensional techniques have to be distinguished, all involve the use of the point-spread-function (PSF). The PSF is the two-dimensional surface brightness distribution of the image of a point source as observed by the detector, thus, being a point source in optical and NIR imaging, also of the nucleus of the QSO. The PSF can vary with position in the field-of-view (FOV), and with time, and is not known a priori. The best way to estimate the PSF is usually the analysis of other point sources in the field of view, i.e. foreground stars.

One-dimensional methods are based on the creation of azimuthally averaged radial surface brightness profiles of the QSO image, being only one-dimensional functions, and a comparison to either analytical or empirical profiles of the PSF. A simple comparison can, for low-$z$ objects, show if the host galaxy is resolved in an image or not, if the PSF profile appears significantly more compact than the QSO profile (left plot in Fig 2.1). For high redshift QSOs, very compact objects at low redshifts or for low S/N, the uncertainty in the PSF become too large even for this. Generally only qualititative statements are possible in this way.

The next step in complexity is the attempt to subtract a scaled version of the PSF profile from the QSO profile to remove the nuclear contribution. The amount of optical and NIR nuclear flux however is unknown, and can not be determined from other observables like radio- or X-ray flux. But assumptions can be made about geometrical properties of the surface brightness of the

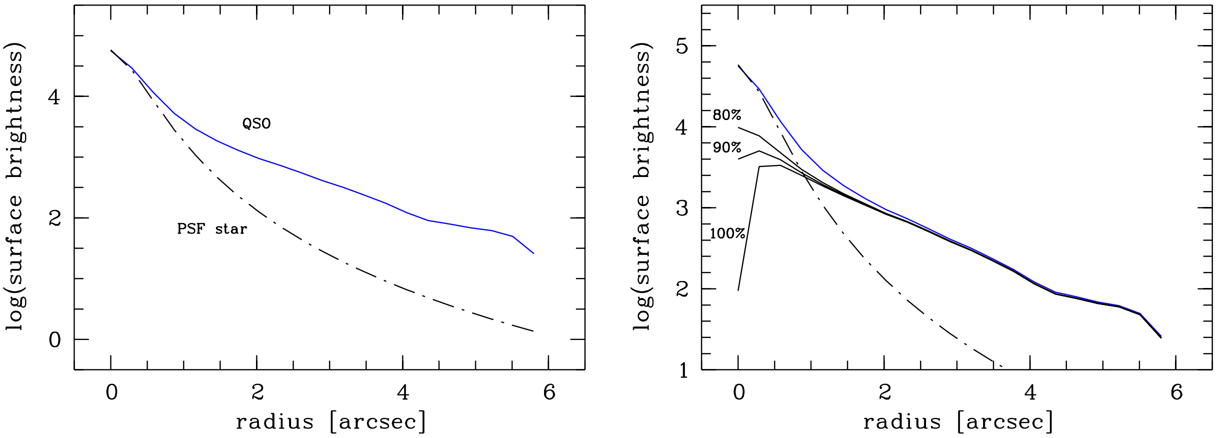

**Figure 2.1.** Use of one-dimensional radial profiles for extraction of the host. Left: A simple comparison of QSO profile (blue solid line) and PSF profile (dot-dashed line) can, if at all, show if the host is resolved. Right: Subtracting scaled versions of the PSF profile from the data profile need a criterium for amount to subtract. The solid black lines are the profile after subtraction of the PSF scaled to 80, 90 and 100% of the central flux.

nucleus–host compound object:

- the first one is already the distribution of the nuclear light in the shape of the PSF;
- a boundary condition has to be met: the individual central fluxes of nucleus and host have to be positive;
- the host galaxy can be assumed to generally have a radial profile intrinsically monotonously increasing towards the center;
- assumptions can be made about the morphological shape of the host, disk or elliptical galaxy, with appropriate radial profile shapes.

These conditions combined allow to search for PSF scaling factors that leave no negative central flux in the QSO profile after subtraction of the scaled PSF profile, or result in a monotonous increase, as shown in the right plot in Fig 2.1. In addition both the PSF scaling as well as the geometry parameters of a galaxy model can be fitted to the data. Both criteria as well as model fitting criteria have been widely used to determine host galaxy luminosities (e.g. Dunlop et al. 1993; McLeod & Rieke 1994a; Rönnback et al. 1996; Aretxaga et al. 1998b; McLeod et al. 1999), also by us (Jahnke 1998). They can deliver solid results, especially for local QSOs and Sy 1 galaxies, but are prone to systematic errors. The reason for this is that in the process of azimuthal averaging, information about the two-dimensional structure of QSO image and PSF shape is lost. Both can and will show non-circular geometries, also non-elliptical shapes can be expected, through tracking errors or diffraction spikes, being very prominent e.g. for the HST. While azimuthal averaging can be perfomed along elliptical isophotes, after averaging, a radius point in the QSO profile will not represent the same area as in the PSF profile, because of the mix of isophotes of host and nucleus in the QSO image. Also the effect of the PSF on the host galaxy light distribution, usually modelled with a convolution of the host model with the PSF model, has to be taken into account in two spatial dimensions to not induce additional errors.

Thus the logical next step is to use both spatial dimensions all through the separation. If the two-dimensional PSF has been estimated, again the possibilities from above apply: scaling or modelling, and in addition, the numerical deconvolution of the image (e.g. Magain et al. 1998; Percival et al. 2001). The latter has the drawback of easily creating numerical artefacts, which is very unwanted if the resulting host galaxy images are subject to analysis also with respect to mophology, distortions and potential companions. The technique has potential, but is technically very demanding, thus few implementations exist. Its reliability for difficult cases, e.g. for higher redshift QSOs, still has to be demonstrated.

Some groups have therefore used two dimensional subtraction of the PSF or multi-component modelling. The latter seems to deliver the most objective results and involves the simultaneous fitting of the flux of the nucleus, the shape parameters of one or two host components (disk and/or spheroid) and potentially a constant background (Taylor et al. 1996; McLure et al. 1999). Recently our group also has developed a modelling package (described in Kuhlbrodt, Wisotzki, & Jahnke 2001, a full report is in preparation and an introduction is given in section 2.3). It allows to first determine the PSF shape parameters and then simultaneously fit the PSF and one or two galaxy components. As an output it delivers the absolute scaling of the nuclear model, and flux, ellipticity, position angle and scale length of the galaxy components. The resulting host galaxy models, or the host galaxy image after subtraction of the nuclear model, are then used for further analysis.

### 2.1.2 (Not much) colour in host galaxy studies

In many of past imaging studies the emphasis was set on the morphology and luminosity distribution of host galaxies, their correlation with e.g. radio emission as noted in chapter 1. Only few studies obtained data in more than one band per object; thus for most of the 200-300 or so host galaxies studied so far no colour information is available. A few authors, however, aimed at deriving host galaxy colours, and we want to shortly summarise their motivation for doing so and their results obtained:

- First attempts to observe a relatively large sample of low-$z$ QSOs in the $B$ and $R$ band by Hutchings (1987) had little diagnostic value, because of the very simple host flux extraction method used. For their results substantial errors are to be expected.

- The same group studied five *IRAS* selected infra-red bright QSOs one year later (Hutchings & Hickson 1988) and find very blue host galaxies. They suspect star formation as the cause but their colours don't allow a more detailed analysis.

- Several years later (Hutchings 1995) combined ground based and HST images in the $V$ and $R$ band for six objects with $z < 0.3$, and use the colour information to find blue colours in tidal features.

- Host galaxy images, now in the $R$ and $K$ band yielding an optical-to-NIR colour were interpreted by Dunlop et al. (2001), compiled from two earlier studies (Taylor et al. 1996; McLure et al. 2000). They compared three samples of relatively luminous radio galaxies, and radio loud and quiet QSOs, to test unified theories on the three groups of objects. They find red colours suggestive of old stellar populations, compatible with the elliptical morphology.

- Rönnback et al. (1996) and Örndahl & Rönnback (2001), obtained $V$, $R$ and mostly also $I$ band images for a sample of intermediate redshift QSOs ($0.3 < z < 0.65$). Their objects are slightly less luminous than the ones investigated by Dunlop et al. and several objects with clear elliptical morphology show very blue colours, more appropriate for late type spirals at the redshift in question. They use one-dimensional PSF subtraction which leaves room for errors but it was attempted to perform a similar subtraction for the differents images of an object. Thus the blue colours are likely to be real.

- One further study, maybe the first in real "multicolour" (*BIHK*), was concerned with the ULIRG-QSO connection, imaging 14 QSOs with strong far infrared excess (Surace et al. 2001). They found host galaxies very luminous in the $H$ band, and they conclude from the analysis that some but not all QSOs may evolve from ULIRGs.

- Schade et al. (2000) observe 76 low redshift QSOs ($z < 0.15$) of intermediate total luminosity with the HST in the F814W band and in the $B$ and $R$ band from the ground. They find host galaxies with all properties very similar to the general galaxy population, only with a morphological distribution skewed towards earlier type.

- More colours were obtained for less luminous AGN. Kotilainen & Ward (1994) imaged 32 Sy 1 galaxies in the optical *BVRI* and near-infrared *JHK* bands. Aim was the description of the amount of starlight from a potential circumnuclear starburst, and the stellar content of the host. For the disk shaped hosts they find perfectly normal colours as for inactive galaxies.

One important argument exists *against* obtaining multiband data of QSO hosts: observing time. A few years ago even 2m-class telescope time was expensive, and for projects with the HST or VLT, obtaining even a single band for a larger sized sample still is. To ask for twice or seven times the observation time had to be very well justified, and was more likely to fail in a proposal.

But as we noted in the introduction, some very important properties can not be assessed unless spectral information is available. The few examples showed: information about the stellar composition of host galaxies and direct evidence for unusual star formation activity or unusual stellar content will only be accessible with colour information. The observing time is well invested!

We initiated and carried out the study described in this chapter in order to systematically characterise the local QSO host galaxy population in terms of their stellar content. Previous hints to normal or particularly blue objects are of limited diagnostic value when single objects are involved or samples were selected to display certain properties. Contrary to this we compiled a complete sample of low redshift QSOs for multicolour imaging. This sample will be the local reference base for the stellar content in comparison with higher luminosity and higher redshift samples.

## 2.2 The multicolour sample

### 2.2.1 Sample and observations

We compiled a sample of 19 objects with $z < 0.2$, drawn from the Hamburg/ESO survey (HES) (Reimers et al. 1996; Wisotzki et al. 1996, 2000). The sample is statistically complete from a sky area of 611 deg$^2$, a low-$z$ subsample of a sample defined by Köhler et al. (1997) to study the luminosity function of QSOs. The distribution in redshift and absolute magnitude is shown in Fig. 2.2. The sample represents optically moderately luminous QSOs when compared to the total population at all redshifts, the radio properties of the sample are currently under investigation. For most of the objects in the sample they are not yet known, but as a subset of the QSO population most will be radio-quiet. Table 2.1 lists the objects, redshifts, apparent and absolute $V$ magnitude and radio properties, if known.

In order to sample the SED from the optical to the NIR, we imaged the 19 objects of the sample in the optical Johnson $B$, Bessel $V$ and $R$, Gunn $i$, and NIR $J$, $H$, and $K_s$ bandpasses (from now called *BVRIJHK* for simplicity). As an illustration, Fig. 2.3 shows spectra of a young and an old stellar populations and the resulting transmission for the seven filters; note the very different distribution of fluxes for the two ages. The three NIR bands are primarily meant to sample the SED of old populations in the host galaxy spectra, while the optical bands are sensitive to the emission of young stars. A redundancy in the NIR is used in order to stabilise fits of template spectra later on. As an added bonus for future applications, this even sampling of the SED allows us to make comparisons of sample properties to samples at higher redshift without the need for $K$-corrections.

For the majority of the observations ESO telescopes were used, the NTT and SOFI for the NIR bands, the 1.54m Danish telescope for the optical except most of the $B$ images. These were acquired with the ESO 3.6m and EFOSC1/EFOSC2, and the 2.5m Nordic Optical Telescope (NOT) on La Palma. Table 2.2 gives a summary of the telescopes used and observational parameters like integration times and pixel scales.

The images in the $V$, $R$, $I$ and NIR bandpasses are similarly deep for most objects. This is different for the $B$ band images taken with EFOSC1/2: They originate from the HES spectroscopic follow-up campaign to identify QSO candidates, being acquisition frames for slit positioning. With their integration time of only 30 s they are much less deep than the remaining data, and were exchanged with deeper images from other campaigns available in four cases.

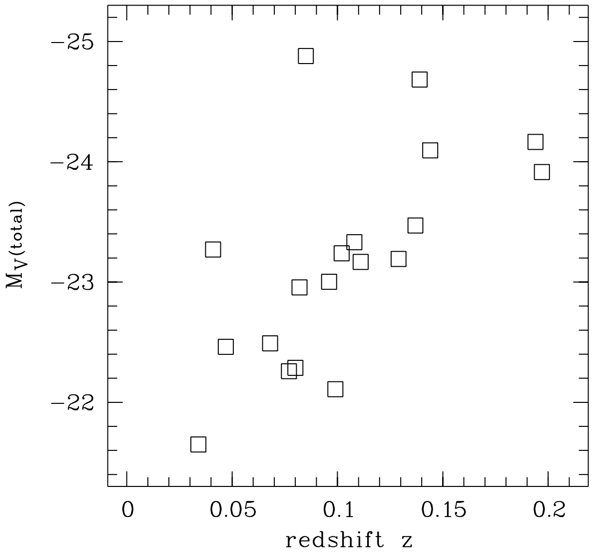

**Figure 2.2.** Sample properties. Total absolute $V$ band magnitude of the QSOs as a function of redshift.

**Table 2.1.** Objects in the multicolour sample. Listed are redshift $z$, total apparent $V$ magnitude and total $K$-corrected $V$ band magnitude of the objects, and known information on radio loud- or quietness.

| Object | Alternative name | $z$ | $V$ | $M_V$ | Radio |
|---|---|---|---|---|---|
| HE 0952–1552 | | 0.108 | 15.8 | –23.3 | |
| HE 1019–1414 | R 04.01 | 0.077 | 16.1 | –22.3 | |
| HE 1020–1022 | PKS 1020–103 | 0.197 | 16.6 | –23.9 | loud |
| HE 1029–1401 | | 0.085 | 13.7 | –24.9 | quiet |
| HE 1043–1346 | | 0.068 | 15.7 | –22.5 | |
| HE 1110–1910 | | 0.111 | 16.0 | –23.2 | |
| HE 1201–2409 | | 0.137 | 16.3 | –23.5 | |
| HE 1228–1637 | | 0.102 | 15.8 | –23.2 | |
| HE 1237–2252 | | 0.096 | 15.9 | –23.0 | |
| HE 1239–2426 | | 0.082 | 15.6 | –23.0 | |
| HE 1254–0934 | | 0.139 | 14.9 | –24.7 | |
| HE 1300–1325 | R 12.01 | 0.047 | 14.9 | –22.5 | |
| HE 1310–1051 | PG 1310–1051 | 0.034 | 14.9 | –21.7 | |
| HE 1315–1028 | | 0.099 | 16.8 | –22.1 | |
| HE 1335–0847 | | 0.080 | 16.3 | –22.3 | |
| HE 1338–1423 | R 14.01 | 0.041 | 13.7 | –23.3 | |
| HE 1405–1545 | | 0.194 | 16.2 | –24.2 | |
| HE 1416–1256 | PG 1416–129 | 0.129 | 16.4 | –23.2 | |
| HE 1434–1600 | | 0.144 | 15.7 | –24.1 | |

### 2.2.2 Data reduction

Data reduction in the $V$, $R$, and $I$ was done using “superflats”, i.e. flatfield frames created from the object frames themselves. The fields are sufficiently empty and contained enough sky background for this task, yielding higher quality flatfields than the sky flats taken. Bias frames were obtained every night at the telescope. Otherwise a standard reduction procedure was followed. For the ALFOSC and EFOSC $B$ band images twilight and dome flats were used, respectively.

The NTT/SOFI NIR data suffered from a detector peculiarity, a time and illumination depen-

**Table 2.2.** Telescope and observation properties. Listed are band, telescope and instrument used, number of objects, integration time, and pixel scale.

| Band | Instrument | Objects | $t_{\mathrm{int}}$ [s] | Scale |
|---|---|---|---|---|
| $B$ | ESO 3.6m/EFOSC2 | 12 | 30 | $0\farcs61$/pix |
| $B$ | ESO 3.6m/EFOSC1 | 3 | 30 | $0\farcs34$/pix |
| $B$ | ESO 1.54m/DFOSC | 2 | 380/730 | $0\farcs39$/pix |
| $B$ | NOT/ALFOSC | 2 | 1000/1200 | $0\farcs19$/pix |
| $V$,$R$,$I$ | ESO 1.54m/DFOSC | 19 | 300–1200 | $0\farcs39$/pix |
| $J$,$H$,$K_s$ | ESO NTT/Sofi | 19 | 160–900 | $0\farcs29$/pix |

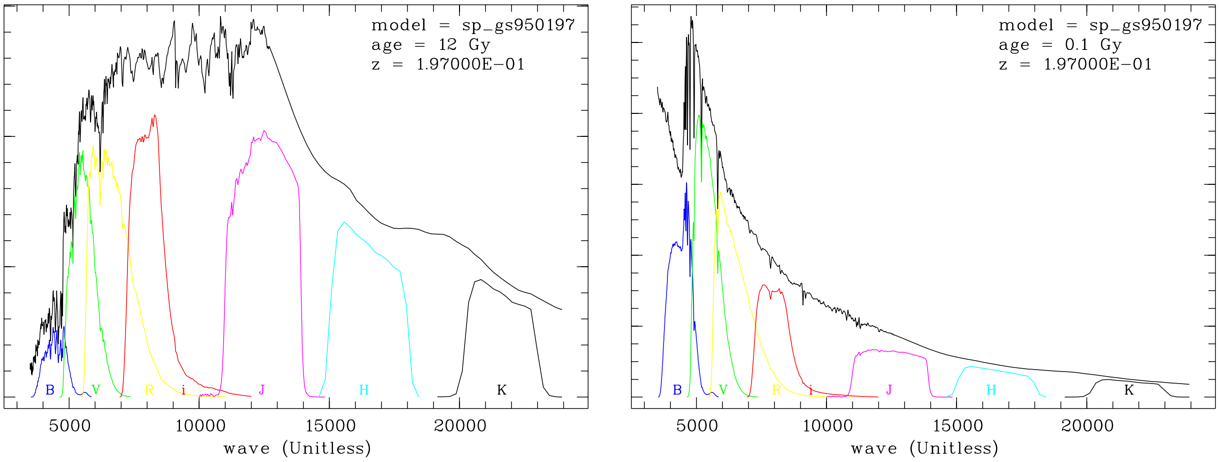

**Figure 2.3.** The bands used in this study. The seven curves trace the integrated flux when the filter curve is multiplied with the SED. The areas underneath the curves are the resulting broad band fluxes for an example of an old (12 Gyr, left) and very young (0.1 Gyr, right) population of stars.

dent bias pattern. This seems to be common for the array model used, the same problem arises for the VLT ISAAC array. Normally spatially variable bias in NIR arrays is – under standard conditions – automatically removed when subtracting a sky frame from the data frame, thus the bias is spatially variable but constant otherwise. The Sofi chip/controller unit used[1] on the other hand produced a bias pattern that depended on the time since last reset and illumination level, thus the amount of sky background. At the time of reduction the effect was not finally investigated by ESO, only later a reduction routine was suggested in the manuals.

We therefore developed a reduction procedure to compute a combined background/bias frame. For each data frame we constructed an individual background/bias, by variance weighed averaging of a sequence of frames (usually three), with the data frame in question in the middle of the sequence. Before averaging we masked all objects in the (dithered) frames. This step was critical, because this had to be done *before* flatfielding, because the frames contained the bias. Thus objects had to be detected in frames without properly defined background, which was solved by creating preliminary, roughly background and bias corrected images by image-pair subtraction.

The constructed background/bias frame was then subtracted from the data frame, removing the background and most of the bias pattern. Residual structures were cleaned in each read-out quadrant by median filtering of rows, because the bias residual increased toward the centre of the chip along columns.

For each object and band (except EFOSC1/2 *B* band data, and the optical bands of HE 1434–1600) more than one image per band was observed and the individual frames dithered between integrations. Variance weighed stacking plus exclusion of outlier pixel values for these dithered frames allowed to remove artefacts created by cosmics, dead columns, hot pixels and other localised errors. The variance weighed stacked images were then further processed by multi-component modelling.

---

[1] chip ID: HASCI01 Assembly 9-73R-5

## 2.3 QSO multi-component modelling

As mentioned in the introduction, for analysis of the host galaxy, nuclear and host component of the QSO image have to be separated. For this task we created a package for two-dimensional multi-component modelling of the QSO by fitting a parametrised host model plus a nuclear contribution. The software and algorithms were developed and tested by B. Kuhlbrodt (Kuhlbrodt et al. 2001), we will give an extended description in Kuhlbrodt, Wisotzki & Jahnke (2002, in prep.).

The modelling steps are:

- analytical modelling of the local PSF for all stars in the FOV
- fitting the variations of the PSF parameters over the FOV and estimating from this the PSF at the position of the QSO
- masking background objects, asymmetries, companions and cosmics around the QSO to be excluded from the modelling fit
- modelling of nucleus, represented by the PSF, and host galaxy, represented by one or two analytical functions, convolved with the PSF in each band
- fixing of the host's morphological parameter from the fits in the seven bands and redoing the fits for all bands with identical values, only the fluxes of nucleus and host remain as free parameters

### 2.3.1 Local PSF estimate and variation fit

First the shape of the (varying) PSF is determined at all positions in the FOV where PSF stars are available. This is done by fitting an analytical model to all stellar images in the object frame. Doing so for each individual frame gives an estimate of the local PSF at the time of observation, incorporating the current state of atmosphere and instrument.

As the PSF model we use an elliptical Moffat function. It is necessary to allow for non-circular symmetry in order to model the different optical distortions present in detectors with complex optical layout. Especially focal reducer instruments like EFOSC, DFOSC or ALFOSC used in this study show strong variations in their PSF over the field (Fig. 2.4). The PSF is varying in ellipticity and position angle in a rather complex pattern.

For the elliptical Moffat the functional form after Stetson (1987) was chosen in order to fit the two-dimensional variation of the ellipticity parameters. In this particular representation ellipticity, position angle and radial scale are replaced by non-periodic parameters. This avoids numerical problems for fitting the position angle of the PSF ellipse. The variation of the individual PSF parameters over the FOV are then fitted with zero to third order polynomials, with a manual selection of the order after inspection of the results.

### 2.3.2 Modelling nucleus and host galaxy

The variation fit yields the best estimate for the shape of the PSF at the position of the QSO in the FOV, thus also for the shape of the QSO nucleus. In the following second step the amount

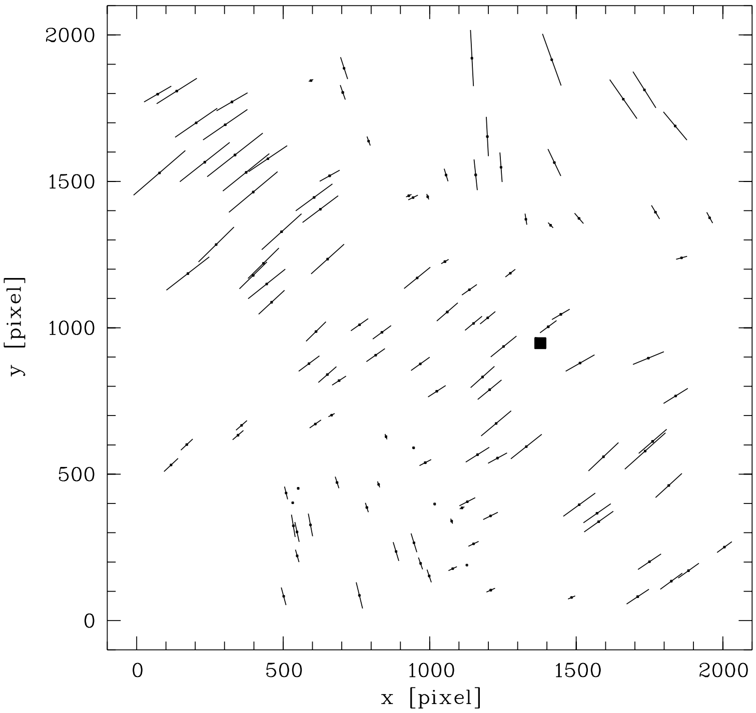

**Figure 2.4.** Variation of the PSF shape over a typical field of a DFOSC frame from the ESO 1.54m Danish telescope. Each point marks the X-Y-position of a star. The isophotes of the star are fitted with ellipses, the direction of each line gives the position angle $\varphi$ of the ellipse, the length is a measure of the ellipticity $e$. The square marks the position of the QSO in the field. The pixel scale is $0\farcs39$ thus the FOV is $13' \times 13'$.

of flux contained in the nucleus is fitted simultaneously with the shape and flux of the host galaxy component. The latter is represented by an analytic elliptical galaxy model consisting of either a de Vaucouleurs spheroidal (de Vaucouleurs 1948; de Vaucouleurs & Capaccioli 1979), an exponential disk (Freeman 1970), or a combination of both.

The galaxy models are convolved numerically with the PSF to mimic the effect of the atmosphere. The convolution is done by computing the model on an adaptive subsampling grid to reach the desired numerical precision of the convolution in regions of strong gradients.

The values for nuclear and host flux and the host's geometrical parameters, scale length, ellipticity, position angle are varied in a downhill simplex $\chi^2$ minimisation procedure after Press et al. (1995) until a given precision is reached. As a result we receive models of nucleus and host component(s) and a residual after subtraction of both, showing the deviation from the model assumptions (illustrated in Fig. 2.6 for a spiral host galaxy).

We restrict the data pixels used in modelling to a region of interest defined as an elliptical anullus centred on the nucleus. This is chosen to be large enough to contain all visible flux of the object. Geometrical or physical companion objects as well as strong asymmetric components like tidal tails, are masked out. Masking excludes these areas from the fit, and is required to satisfy the model assumptions, i.e. a smooth galaxy component. E.g. tidal arms are not part of the model and will bias the resulting best fit model in an unpredictable and uncorrectable way.

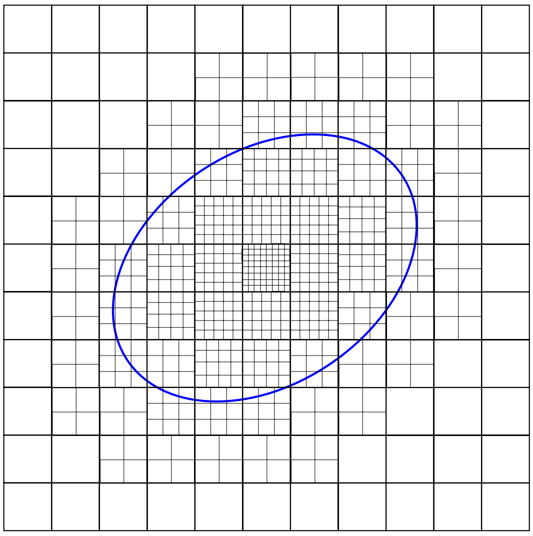

**Figure 2.5.** Adaptive subpixel grid for computation and convolution of the host model. The number of subpixel points is chosen depending on the gradient of the model. The blue ellipse is marking the geometry of the host. In the outer parts no subpixels are used, the number increasing towards the center.

### 2.3.3 Homogeneous treatment for all bands

In order to guarantee for a consistent procedure in all bands of the multicolour sample, we used identical modelling areas and identical masks for all observations of a given object. Only unique artfacts like cosmics and dead pixels were added in the masks of the individual bands. The sky background was adjusted to be zero in an anulus around the object in each frame, determined from the analysis of curves of growth. Thus background variations in the frame are accounted for.

One effect that has not been investigated before is the strongly rising sky brightness from $B$ to $K$ band. This yields a different relative weight or S/N of low count (host outskirts) and high count (centre) areas of the QSO, when using formal variances (Fig. 2.7). This will have an influence on modelling, because even for the theoretical case of an identical physical surface brightness distribution in e.g. $B$ and $K$, the outskirts of the host will have a larger weight in the modelling in $B$ than in $K$, vice versa for the nucleus.

Simulation with other weighing schemes than formal variances resulted in no generally valid receipt for weights and thus formal variances were used. However, this aspect has to be borne

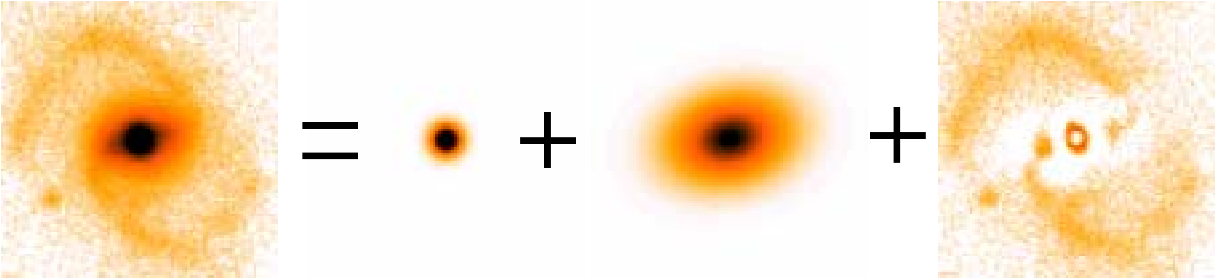

**Figure 2.6.** Example for the 2d multi-component modelling: The input QSO image (left) is decomposed into a nuclear model (second from left) and host model (second from right). Left over after subtraction of both components is the residual (right) showing the deviation from the model assumptions. In this case the fit region did not include the arms of the spiral.

in mind when comparing optical and NIR data of an object, particularily from low S/N images.

In order to minimise the influence of this effect on the modelling process in the different bands, we decided to use two consecutive QSO modelling iterations. In a first iteration we left all model parameter free, and derived global values valid for all bands, for scale length $r_{1/2}$, ellipticity $e$ and position angle $\varphi$. In step two these parameters were fixed for the modelling, with only the fluxes of nucleus and host component(s) as free parameters, thus forcing identical host geometry. We discuss the validity and implications of this approach in section 2.5.1.

## 2.4 Photometry

The multi-component modelling procedure yields models for host galaxy as well as the nucleus. Judging from the results of disk and spheroidal model fits, the residual images after model subtraction, and radial profiles allows to decide on the general type of the host, if it is disk dominated or primarily a spheroid. The model then gives the general morphological parameters of the host.

For photometry of the host we then do not integrate the host model, but use the model of the nucleus to subtract the nuclear light contribution from the composite QSO image, resulting in a host galaxy frame containing all asymetries, spiral arms, etc. This method has an advantage over simply integrating the galaxy model as has been done in the past (e.g. McLeod & Rieke

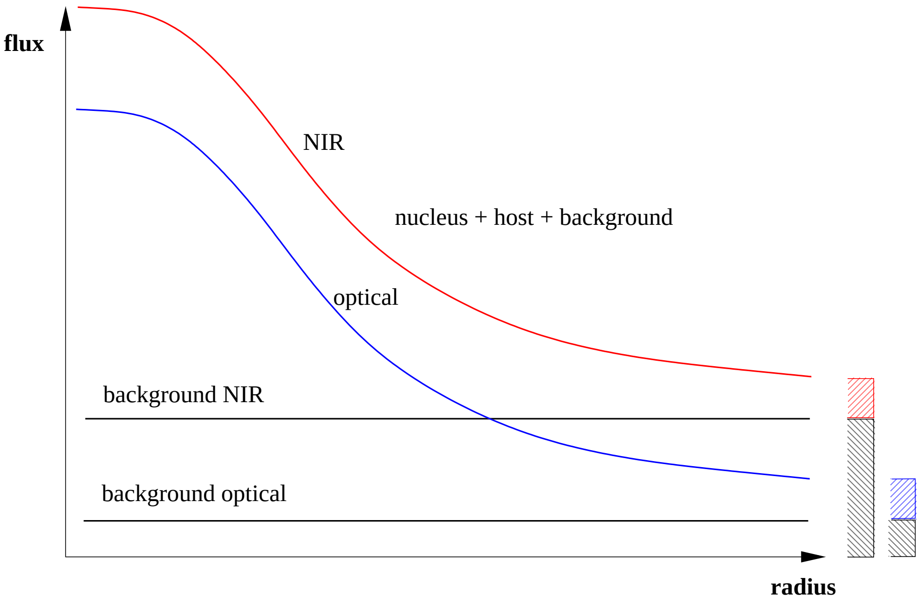

**Figure 2.7.** Different S/N ratios for the host galaxy in optical and NIR bands: Shown are the schematic relation between background (black lines) and object flux (radial profile in red and blue). In the NIR the sky background is much larger than in optical bands (not drawn to scale). While in the center region the S/N of the host galaxy might be dominated by nuclear flux in both cases, it is different in the outer parts. Here the S/N of the host is much smaller in the NIR case (red curve) than in the optical case (blue curve). Thus the weight of the outer parts of the host have less weight in multi-component modelling in the NIR, compared to the optical.

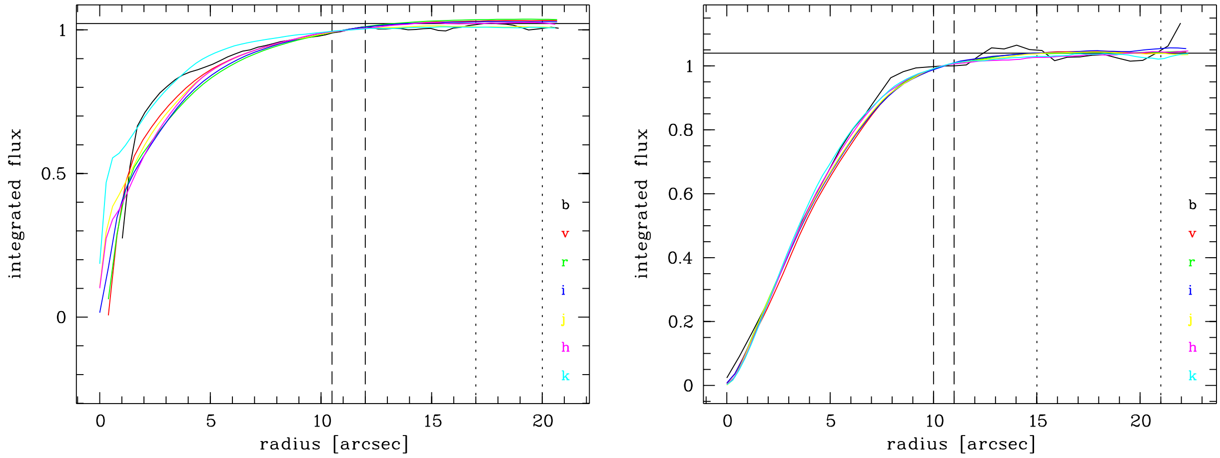

**Figure 2.8.** Simultaneous photometry in all bands: Shown are, for two objects, the curves of growth for all bands. They are normalised to the flux in the region between the dashed vertical lines ($r_{\rm eq}$). From the bands with the highest S/N, in both case all bands except *B*, the flux between the dotted vertical lines ($r_{\rm conv}$) is averaged and taken as 100%. The integrated flux for each band at $r_{\rm eq}$ is then scaled accordingly and used as the total flux for this band. This reduces the influence of background noise at large radii, without integrating to different isophote levels. for different bands.

1994a,b; Schade et al. 2000). Asymmetries in the host like arms or distortions due to tidal events can be accounted for in this way. Also modelling errors for the galaxy e.g. in scale length might have a negligible effect on the nuclear flux, but they can be magnified when the model is simply integrated. Particularly in cases where the type of the galaxy cannot be firmly established this might be a problem. Fits with a spheroidal model will yield, when integrated, 0.5–1.5 mag systematically higher fluxes than the best fitting exponential disk model (McLeod & Rieke 1994a,b).

Photometry of the host image is done via aperture photometry. The aperture used is an ellipse with the geometry of the modelled host, and thus fixed for each object. The size of the aperture was chosen to minimise errors from to background noise. Since the observations in the different bands have, in general, different depths, curves of growth of the host flux will begin to be dominated by background noise at different radii for different bands. If we assigned each image an individual integration aperture depending on S/N, we would be integrating up to different isophotes. Instead we determined two radii (Fig. 2.8): One radius, $r_{\rm eq}$, typically containing 90–98% of the total flux, was chosen so that the curves of growth in all bands would not deviate much from each other for larger radii, and the curves of growth were normalised at this radius. A second radius, $r_{\rm conv}$, was chosen at which the curve of growth of the band(s) with the highest S/N would converge. The flux in this band inside $r_{\rm conv}$ was taken as 100% of the host's flux, and the fraction of flux inside $r_{\rm eq}$ determined. The fraction of flux contained inside $r_{\rm eq}$ for this band, 90–98%, was then assumed to be valid for all bands and the total flux computed from the value inside $r_{\rm eq}$. This again assumes identical profile shapes and scale lengths in all bands (see sec. 2.5.1) but has the advantage of a homogenous treatment independent of S/N.

Photometric calibration was performed using photometric standards obtained during the observing runs. The *B* band data taken with EFOSC/EFOSC2 was calibrated using the original band photometry from Köhler et al. (1997), used with updated galactic dust extinction values.

**Table 2.3.** Adopted $K$-corrections for nucleus and host, in general valid only for $z < 0.2$. The nuclear $K$-corrections are derived from the averaged QSO SED by Elvis et al. (1994). For the host values are taken from Fukugita et al. (1995) in the optical and Mannucci et al. (2001) in the NIR.

| Band $X$ | $K(X)$ [mag/z] | | |
|---|---|---|---|
| | nucleus | spheroid | disk (Sb) |
| $B$ | | 5.0 | 3.25 |
| $V$ | –0.99 | 2.25 | 1.0 |
| $R$ | | 1.0 | 0.75 |
| $I$ | | 0.75 | 0.5 |
| $J$ | | 0.25 | 0.15 |
| $H$ | –1.25 | –0.25 | –0.25 |
| $K$ | | –2.4 | –2.4 |

We used the values from Schlegel et al. (1998), and applied a correction in all bands. We also applied airmass corrections in the $B$ and $V$ band using average La Silla extinction coefficients.

Conversion to absolute magnitudes required $K$-correction terms, which we applied separately to QSO nucleus and host. For the computation of optical and NIR nucleus-to-host ratios in Table 2.4 we also needed $K$-corrections for the nucleus. We use the average QSO SED as published by Elvis et al. (1994), computed the $V$ and $H$ band flux as function of redshift using the appropriate filter curve and converted to magnitudes. It showed that for $z < 0.5$ a linear relation $K(V) = -0.99 \cdot z$ is a very good description, for the $H$ band $K(H) = -1.25 \cdot z$ is adequate for $z < 0.2$.

For the host we used the $K$-correction terms published by Fukugita et al. (1995) in the optical and Mannucci et al. (2001) in the NIR. We adopted separate values for predominantly spheroidal and disk hosts, for the latter we assumed intermediate type Sb disks. In $H$ and $K$ the differences between E and Sb galaxies are negligible. We approximate the $K$-correction as a linear function of $z$, which yields errors less than 0.05 mag in all bands for $z < 0.2$. The adopted values are compiled in Table 2.3.

## 2.5 Modelling results and analysis

We clearly resolve all objects in all bands. In Figure 2.9 we show for all images a grey scale plot of the host galaxy after subtraction of the nuclear model as well as the radial profiles of the different components involved in the modelling in the $J$ band (profiles for all bands can be found in Appendix A).

In the *VRIJHK* bands the modelling was successful and straightforward for all objects. The EFOSC $B$ band data were more troublesome and could in general only be modelled with presetting the host's scale length $r_{1/2}$ from the other bands. In the 2d multi-component modelling $r_{1/2}$ is generally not a well constrained parameter (Abraham et al. 1992; Taylor et al. 1996) and is strongly correlated with central surface brightness of the host. This is due a finite width of the PSF, blurring the very peaked host galaxy profile, and allowing a range of combinations of $r_{1/2}$ and central surface brightness with similar resulting profiles. The total flux $F_{\mathrm{host}}$ however is much better defined. With $r_{1/2}$ given in $B$, all but seven of the 19 objects could be modelled. In these seven cases the host galaxy can be seen, but the residuals are too large to reliably extract fluxes or morphological parameters.

In some cases, most of them in the $B$ band, the fixed $r_{1/2}$ fit ended with a host model systematically under- or overestimating the data, visible in the analysis of radial profiles of data and model (Fig. 2.10). In these cases the fit was influenced by imperfections in the PSF definitions. The PSF variations in focal reducer instruments are complex and not all variations could be modelled. Thus a residual PSF mismatch was present in most cases, enhanced by low S/N in the $B$ band. This occured in 15 of our 133 images. We corrected this by rescaling the resulting host models to fit the QSO at radii where the influence of the nucleus was negligible and reran the modelling with the host model fixed to receive the best fitting model of the nucleus for this constellation. In Figure 2.10 we show as examples the radial profiles of HE 1434–1600 ($R$ band) and of HE 1029–1401 ($J$ band). In the first case (top left) the host was overestimated in the fit with fixes scale length. We downscaled the host *model* by about 15% (top right) and received as a result of the new fit a nucleus subtracted host image of 10% less flux. In the second case the host was underestimated (bottom left). We upscaled the spheroid model by 40% and received a nucleus subtracted image with about 20% more flux (bottom right).

For seven objects the extracted morphology in the $B$ band was distorted to a degree that our galaxy model ceased to be valid and no reliable flux information about the host could be extracted. Their radial profiles are included in Appendix A but these frames were left out from further analysis.

### 2.5.1 Variable scale lengths

For modelling the nucleus and host surface brightness distribution we assumed that the hosts' scale lengths $r_{1/2}$ are constant for all bands. Studies of inactive galaxies found significantly varying scale lengths for intermediate and late type spirals (e.g. de Grijs 1998; Möllenhoff & Heidt 2001). The dominant contribution to a change comes from active star formation, producing a population of young, blue stars with a $M/L$ ratio much smaller than for the dynamically dominant old population. In a simple picture the star formation occurs rather evenly spread in the spiral arms of later type spirals, a distribution much different from the old population. Thus compared to NIR bands tracing the e.g. exponential disk distribution of old stars, the $B$ and $V$ band will add the radially more or less constant contribution of the young population. In comparison a spiral will at larger radii show more flux in the optical than in the NIR, thus $r_{1/2}$ will decrease with wavelength.

De Grijs (1998) studied a multicolour sample to describe morphological properties of normal galaxies from ellipticals to late type spirals. For early type galaxies up to Sa he finds no change in $r_{1/2}$ from $B$ to $K$. This changes for later types. For Sb the ratio $r_{1/2}(B)/r_{1/2}(K) = 1.3$, for Sc 1.6, but always with a large spread.

We observe a significant trend only for HE 1043–1346 and possibly HE 1335–0847. In the latter case the modelling was inconclusive to a degree that neither a pure exponential disk nor a spheroidal model fitted all bands (Fig. A.15). While a spheroidal agrees very well with the profile in $V$, the fit is worse for radii $> 6''$ in the NIR. However between $3''$ and $6''$ an exponential disk would fit quite well, but would underestimate the data for larger radii for all but the $K$ band.

For HE 1043–1346 the case is much clearer, as we see resolved spiral arms typical for an Sc spiral (a grey scale plot is shown in Fig. 2.9). The colours of the arms are significantly bluer than

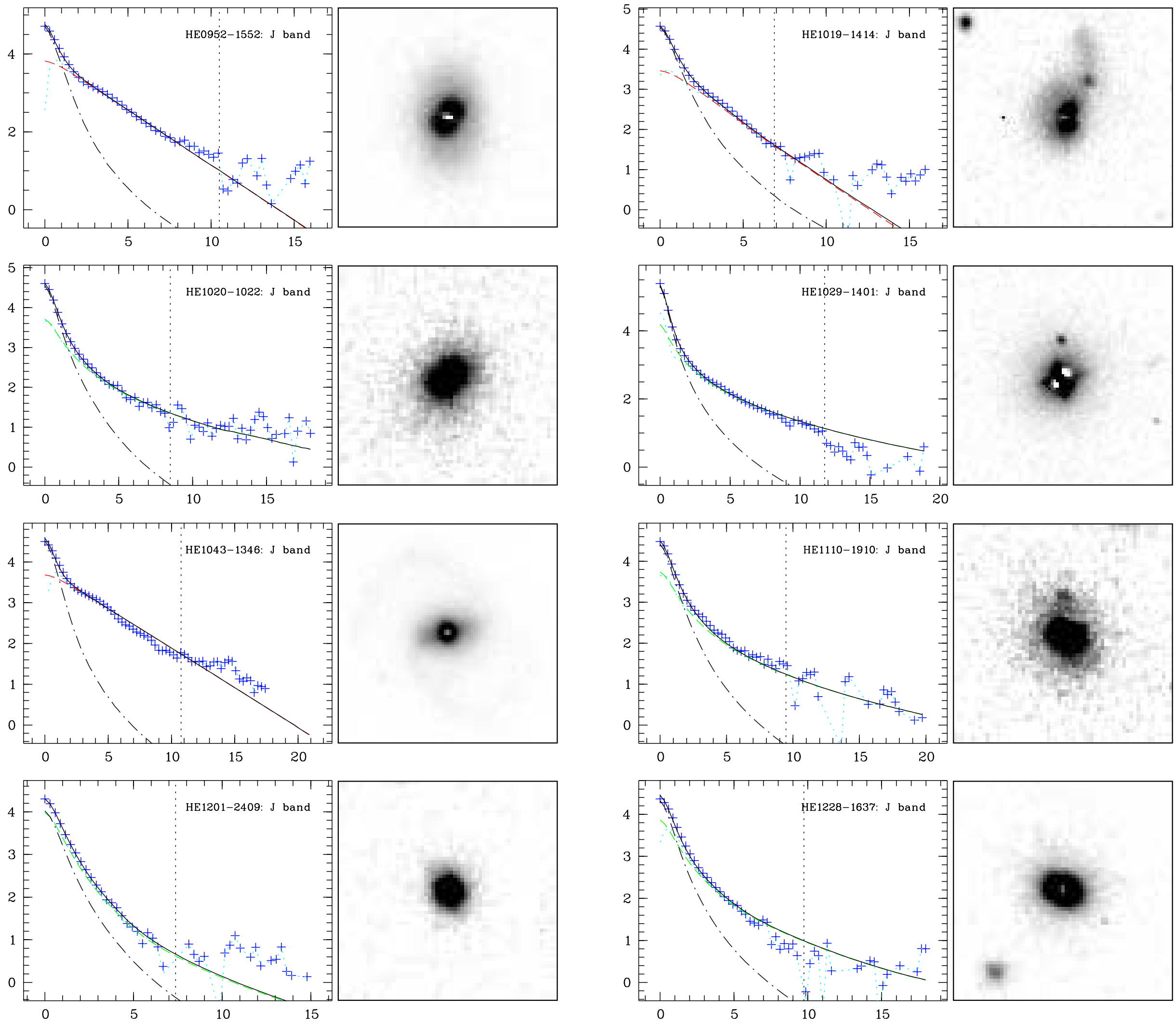

**Figure 2.9.** The objects in the multicolour sample: The diagrams show radial surface brightness profiles of the objects in the *J* band, flux is logarithmic in arbitrary units, radius is in arcseconds. The symbols mark the data points, the different lines are: nuclear model (dot-dashed black), host model (long dashed, green spheroidal, red disk), combined nuclear plus host model (solid black), remaining host after subtraction of the nuclear model (dotted light blue). The vertical line marks the radius of the ellipse inside which was fitted. A full set of profiles for all bands can be found in Appendix A. The grey scale images show the host galaxy after subtraction of the nucleus in the NIR *J* band (for HE 1043–1346, HE 1254-0934, and HE 1310–1051 the *R* band). Images are centered on the nucleus. The side lengths of the images differ: 21.75″ for HE 1310–1051 and HE 1338–1423, 17.5″ for HE 1043–1346, 11.6″ for HE 1019–1414, HE 1029–1401, HE 1237–2252, HE 1239–2426 and HE 1300–1325, and 8.7″ for the remaining objects.

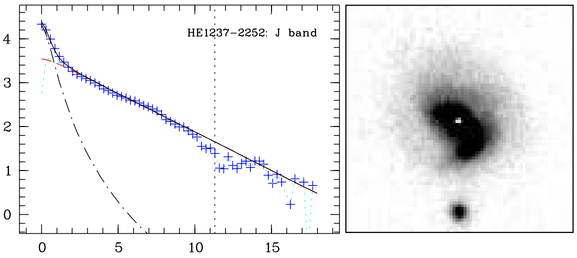
HE1237−2252: J band
0
1
2
3
4
0
5
10
15

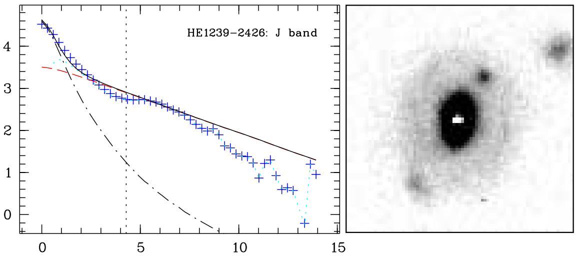
HE1239−2426: J band
0
1
2
3
4
0
5
10
15

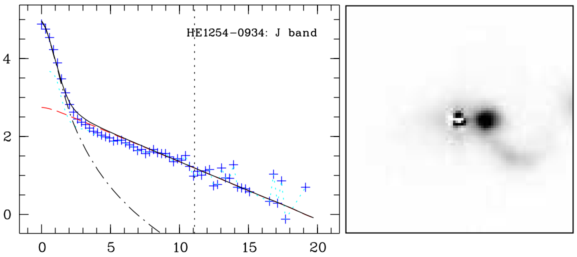
HE1254−0934: J band
0
2
4
0
5
10
15
20

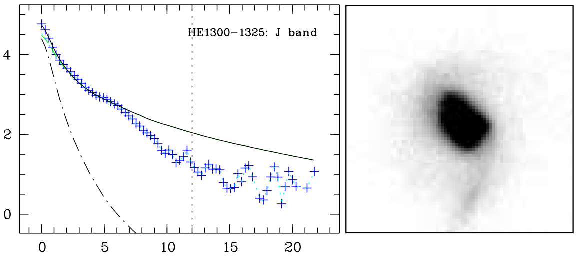
HE1300−1325: J band
0
2
4
0
5
10
15
20

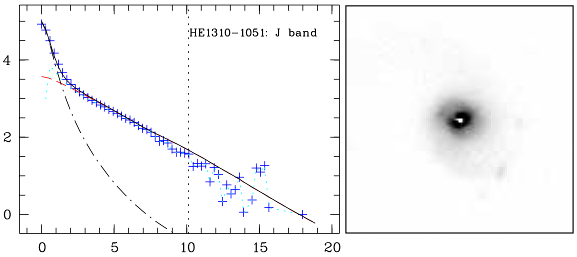
HE1310−1051: J band
0
2
4
0
5
10
15
20

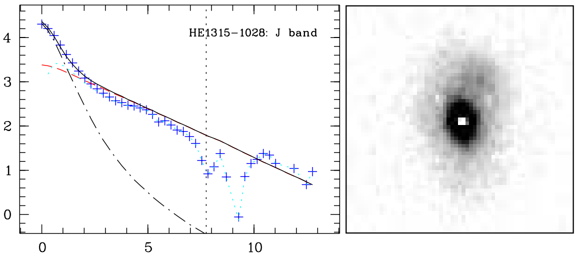
HE1315−1028: J band
0
1
2
3
4
0
5
10

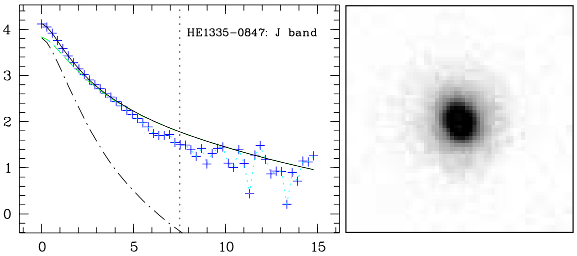
HE1335−0847: J band
0
1
2
3
4
0
5
10
15

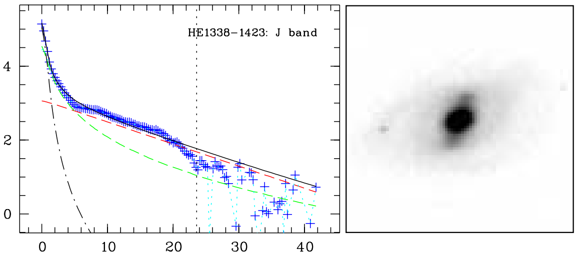
HE1338−1423: J band
0
2
4
0
10
20
30
40

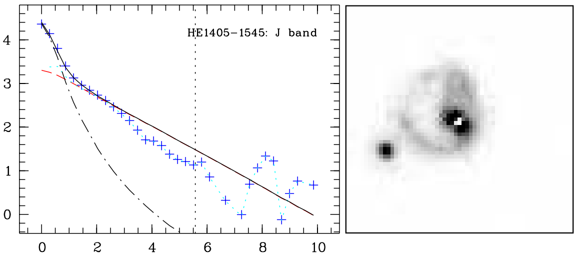
HE1405−1545: J band
0
1
2
3
4
0
2
4
6
8
10

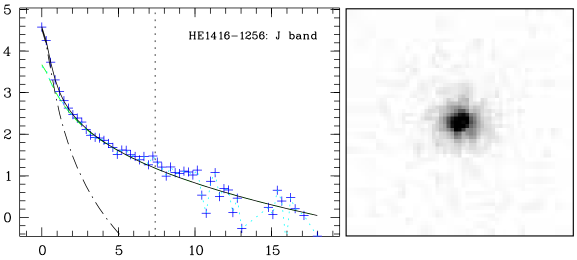
HE1416−1256: J band
0
1
2
3
4
5
0
5
10
15

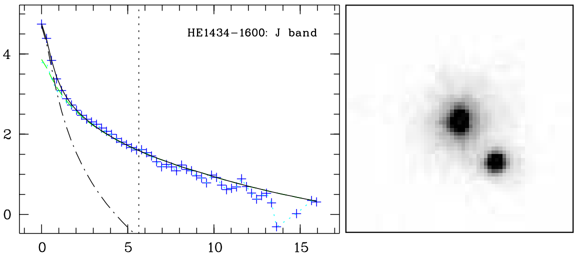
HE1434−1600: J band
0
2
4
0
5
10
15

for the center, while prominent in $B$ and $V$, they are hardly detectable in $H$ and $K$ (see Fig. A.5 in the appendix). This produces exactly the effect described above. When constrained to $r < 8''$ (27 kpc) as we did in the modelling, changes in the profile are visible, but small. The subtraction of the nuclear component is biased only by a small amount. When on the other hand the spiral arms were included, $r_{1/2}$ would change.

Also the photometry as described in section 2.4 is sensitive to varying scale lengths, because this corresponds to a changing shape of the curve of growth of the host. The NIR bands with smaller $r_{1/2}$ reach a given fraction of their total light at smaller radii than in blue bands. To avoid a bias in photometry for the two objects, we moved the radius $r_{\mathrm{eq}}$ to larger radii than in the other cases. For HE 1043–1346 in addition we extracted the optical and NIR band separately to account for different shape. In total we estimate the remaining systematic error between $B$ and $K$ band to be less than 5% in flux.

Because of the sign of the potential change, $r_{1/2}$ *decreasing* with wavelength, the fixed scale-

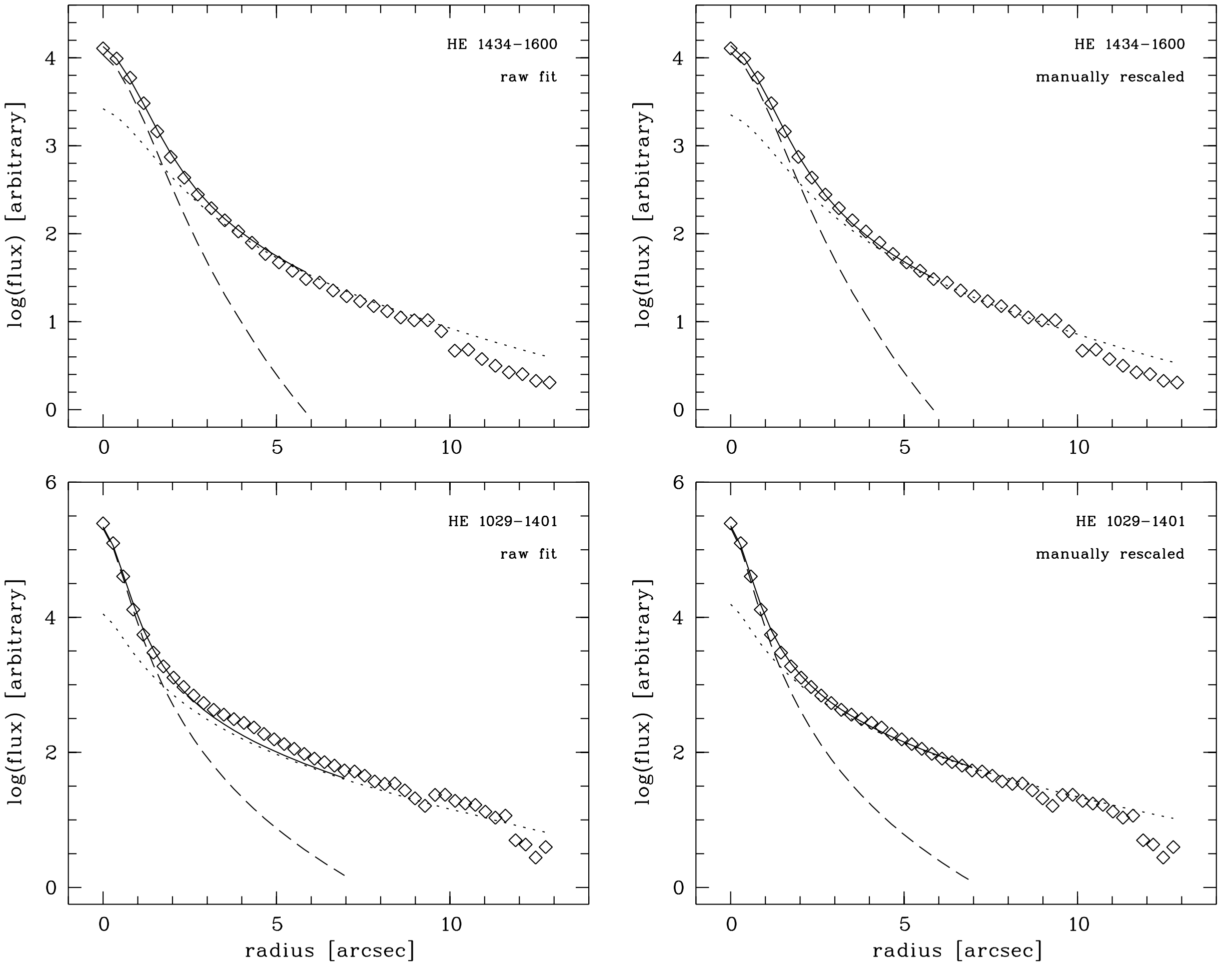

**Figure 2.10.** Misestimates for the host model from fits with fixed scale length. Shown are radial profiles for the components of two objects: Lozenges are the data points, the dashed line is the nuclear model, the dotted line the host model, and the solid line the sum of both models. Top row: HE 1434–1600, bottom row: HE 1029–1401. Left hand side: raw fit results, right hand side: profiles after manual rescaling.

**Table 2.4.** Multi-component modelling results. Shown are the general morphological type of the host, (E)lliptical or (D)isk and in one case a (B)ulge, half light radius $r_{1/2}$ in kpc, ellipticity $e$, resulting inclination angles for the disks $i$, position angle from north, and nucleus-to-host ratio N/H in restframe $V$ and $H$ band. Comments on morphology are given for the individual objects in the text.

| Object | Type | $r_{1/2}$ [kpc] | $e$ | $i$ [°] | $\varphi$ [°] | N/H(V) | N/H(H) |
|---|---|---|---|---|---|---|---|
| HE 0952–1552 | D | 6.8 | 0.33 | 48.0 | 175.9 | 1.17 | 0.59 |
| HE 1019–1414 | D | 5.0 | 0.26 | 42.3 | 147.1 | 1.54 | 1.36 |
| HE 1020–1022 | E | 10.4 | 0.28 |  | 132.6 | 1.53 | 1.28 |
| HE 1029–1401 | E | 4.2 | 0.0 |  | - | 3.86 | 2.53 |
| HE 1043–1346 | D | 6.7 | 0.32 | 47.2 | 102.7 | 0.25 | 0.42 |
| HE 1110–1910 | E | 5.6 | 0.24 |  | 14.2 | 1.39 | 1.33 |
| HE 1201–2409 | E | 1.5 | 0.29 |  | 8.4 | 0.50 | 0.66 |
| HE 1228–1637 | E | 3.5 | 0.15 |  | 62.6 | 1.41 | 1.57 |
| HE 1237–2252 | D | 9.9 | 0.16 | 32.9 | 39.4 | 0.34 | 0.28 |
| HE 1239–2426 | D | 9.2 | 0.22 | 38.7 | 162.7 | 0.48 | 0.85 |
| HE 1254–0934 | D | 16.0 | 0.28 | 43.9 | 95.5 | 6.18 | 4.77 |
| HE 1300–1325 | E | 4.9 | 0.39 |  | 34.0 | 0.36 | 0.19 |
| HE 1310–1051 | D | 3.5 | 0.11 | 27.1 | 88.7 | 1.54 | 1.21 |
| HE 1315–1028 | D | 8.1 | 0.47 | 58.0 | 1.3 | 1.03 | 0.93 |
| HE 1335–0847 | E | 5.0 | 0.19 |  | 22.0 | 0.57 | 0.43 |
| HE 1338–1423 | D | 13.7 | 0.43 | 55.2 | 105.0 | 0.93 | 0.31 |
|  | B | 4.6 | 0.33 |  | 145.3 | 0.93 | 0.31 |
| HE 1405–1545 | D | 8.8 | 0.35 | 49.5 | 165.0 | 1.28 | 1.11 |
| HE 1416–1256 | E | 6.4 | 0.0 |  | – | 1.26 | 1.12 |
| HE 1434–1600 | E | 7.2 | 0.15 |  | 3.5 | 1.44 | 1.04 |

length in modelling would *bluen* the resulting colours, the bias in photometry would make the host's colours systematically *redder*. Since we exclude an effect for modelling except for the objects mentioned, the colours discussed in section 2.5.3 are not biased towards bluer values from these effects.

### 2.5.2 Morphology

Of the 19 objects nine were classified as disk dominated, nine as spheroid dominated and one object as a disk plus bulge. A summary of the morphological parameters is given in Table 2.4. Scale lengths ranged from 3.5 to 16.0 kpc, average 8.8 kpc, for the disks and from 1.5 to 10.4 kpc, average 5.4 kpc for the elliptical hosts. Ellipticities average to 0.19 for the ellipticals and 0.29 for the disks. Since we use only a single component for the host galaxy, we lack information about the relation between bulge and disk luminosities. Thus we do not know about the disks' thicknesses, and can not give inclinations as defined by Hubble (1926). We thus compute tentative inclinations $i$ assuming the disks to be thin, $i = \arccos(b/a) = \arccos(1-e)$. With this definition the average inclination for the disks in the sample is 44.8°. The distribution is plotted in Fig. 2.11.

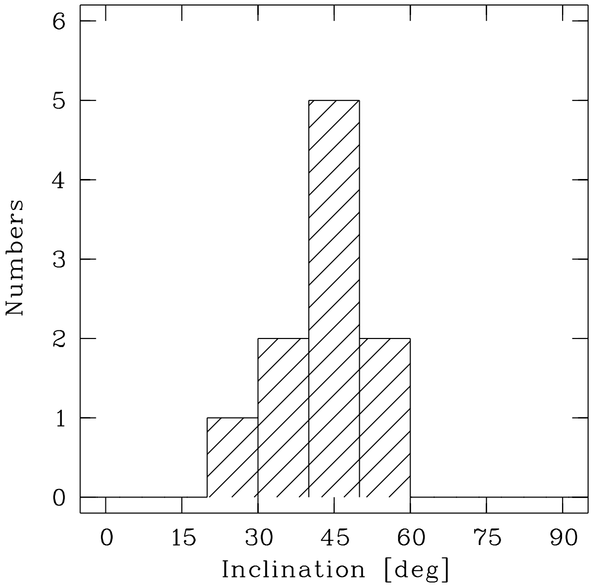

**Figure 2.11.** Inclinations of the ten disks in the sample. Apparent is the lack of high inclinations $i > 60°$ conforming to the unified AGN scheme.

The residual PSF mismatch and the presence of individual features (knots, weak unmasked foreground stars, etc.) has an influence on ellipticities, potentially biasing against values close to zero. A feature like a PSF mismatch or a foreground object will generally show a non-circular geometry. When fitted – by force – with elliptical isophotes, the feature will therefore display a non-zero ellipticity. When the $\chi^2$ minimisation attempts to model the feature geometry by adjusting host model parameters accordingly, the ellipticities of the host are shifted. The resulting host does not need to show any apparent fault, nor does a slight mismatch have a significant influence on the flux of the nuclear model, but ellipticities will be biased away from zero.

We see this to be the case for two objects. HE 1029–1401 and HE 1416–1256 were both assigned ellipticities between 0.15 and 0.2 in the free parameter fit, even though their appearance on the chip is very circular. For the fixed parameter fit we therefore forced $e = 0$. Both objects are clear elliptical galaxies and we do not not find similar cases for the disks in our sample.

Thus the absence of face-on disks with $i < 25°$ ($e < 0.1$) in the sample is real (Fig. 2.11). Also missing are high inclinations $i > 60°$ ($e > 0.5$). Similar results were found in several other host galaxy studies. Taylor et al. (1996) find only one of eleven disks with $e < 0.1$ and a highest ellipticity $e = 0.51$. McLeod & Rieke (1995b) investigate a large Sy 1 sample, and also finding a strong bias against edge-on galaxies, with only four of 42 Sy 1 showing $e > 0.5$. All samples including our own peak around $e = 0.3 - 0.4$, which suggests an intrinsic ellipticity for the disks. The distribution would rise towards $e = 0$ if only an inclination angle were the source. Missing edge-on hosts comply with the unified models of AGN (Antonucci 1993). If for a significant range of viewing angles the line of sight the QSO nucleus is obscured by a circumnuclear dust torus, and thus would not appear as a QSO. This correlation is only the case under the assumption that dust torus and disk are aligned, which is not necessarily the case. A detailed discussion on this matter can be found in McLeod & Rieke (1995b).

Our distribution of axial ratios for the ellipticals is very similar to numbers found by Tremblay & Merritt (1996). The authors perform statistical test on axial ratios on a large sample of elliptical galaxies, finding two distinct populations of ellipticals dependent on luminosity. They

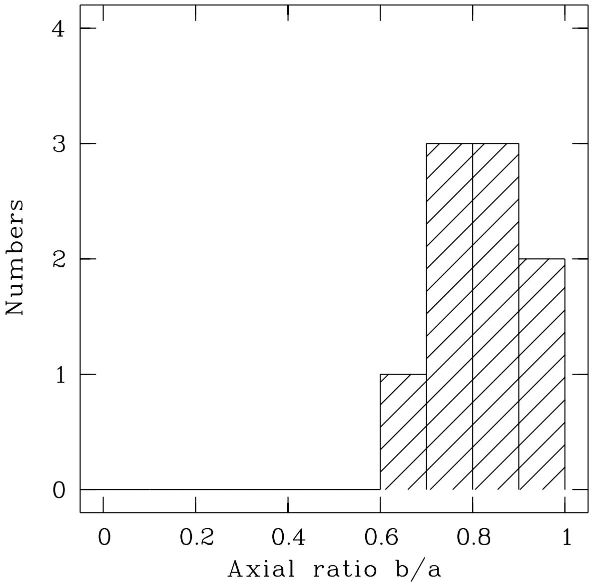

**Figure 2.12.** Axial ratios of the nine ellipticals in the sample. No host exists more elliptic than E4. Average and distribution are very similar to the general population of bright inactive ellipticals.

separate faint and bright ellipticals at $M_B \sim -20.5$, which classifies all of our elliptical hosts as the latter. The axial ratio ($q = b/a = 1 - e$) averages around 0.75 for their faint sample and 0.85 for the bright counterpart. Our ellipticals have $q = 0.82 \pm 0.04$ when assuming $e = 0.3$ for HE 1300–1325 (see "comments on individual objects" below), with a spread of 0.11. Tremblay & Merritt find a spread of 0.08. Thus we find very similar values to the axial ratio distribution of bright inactive ellipticals (Fig. 2.12).

We want to give some comments on the morphologies of the 19 objects. Spectral information about association of companions was obtained by M. Raue (priv. comm.):

**HE 0952–1552**: Isolated disk galaxy with $r_{1/2} = 6.8$ kpc and $i = 48°$. An isophote twist in the NIR suggests spiral arms, but no arms are resolved. Otherwise very symmetric.

**HE 1019–1414**: Disk with $r_{1/2} = 5.0$ kpc and $i = 42°$. No visible spiral arms. An asymmetry to the north is leading into a prominent tidal arm that was excluded from photometry, extending $10''$ or 20 kpc to the north. A knot in this arm is a companion galaxy about 2 mag fainter in $V$ than the host.

**HE 1020–1022**: This is the most distant object in the sample, at $z = 0.197$ and with $r_{1/2} = 10.4$ kpc also the largest elliptical, and in the NIR also the most luminous. It appears very symmetric, with no signs of distortions. A luminous galaxy exists 90 kpc projected distance away to the north-west.

**HE 1029–1401**: One of the brightest QSOs in the sky, and showing the most luminous nucleus in the sample. The host is nearly circular, very luminous elliptical that can be traced out to $> 35$ kpc from the nucleus, $r_{1/2} = 4.2$ kpc. A weak "blob" 16 kpc to the north and a galaxy 50 kpc to the north are confirmed physical companions. This object suffers from a very poor quality of the available PSF stars and a very bright nucleus, both increasing the uncertainty of the modelling.

**HE 1043–1346**: This objects shows rather open spiral arms, typical of an Sb or Sc spiral, plus a bar-like structure surrounding the nucleus. For nucleus removal only the inner 12 kpc were fitted, corresponding to the bar. It follows clearly an exponential disk law with $r_{1/2} = 6.7$ kpc and ellipticity $e = 0.32$. The spiral arms further out are less elongated, corresponding to an inclination angle of $i = 34°$ or $e = 0.17$. This spiral is isolated with no galaxies or other companions visible.

**HE 1110–1910**: This host is a rather symmetric elliptical galaxy, with $r_{1/2} = 5.6$ kpc and $e = 0.24$. A galaxy to the north-west is a confirmed companion. It is bluer than the host in $V - K$ by about 0.5 mag.

**HE 1201–2409**: Symmetric and most compact elliptical in the sample with $r_{1/2} = 1.5$ kpc, in $B$ the host is barely resolved. No further structure or interaction is visible. Around the object a group of galaxies is visible, at 80, 86, 134, 166 and 205 kpc projected distance. No redshifts exist for these galaxies, thus the physical association is not confirmed.

**HE 1228–1637**: Elliptical host with $r_{1/2} = 3.5$ kpc and a slight E–W asymmetry. It lies in the vicinity of of a group of galaxies with 37, 75, 175 and 235 kpc projected distance, but no tidal connection is visible. The closest galaxy to the east is a confirmed companion at the same redshift. No information is available on the association of the remaining galaxies.

**HE 1237–2252**: Large disk with $r_{1/2} = 9.9$ kpc and $i = 33°$. An armlike asymmetry to south is visible in all bands and appears to be of tidal origin.

**HE 1239–2426**: This is a more complex object with a central bulge or a bar and very tightly wound arms, almost a ring. At least one bright knots in the ring is visible from $B$ to $K$. A two-component host fit was not successful, thus we stayed with a one component disk model that fits the inner parts better than a spheroidal model. The parameters thus only describe the inner part with $r_{1/2} = 9.2$ kpc and $e = 0.22$. The ringlike outer structure has the same orientation as the inner part, and slightly lower ellipticity of $e = 0.17$, corresponding to $i = 34°$. A confirmed associated companion is located at only 26 kpc to the north-west.

**HE 1254–0934**: Complex interacting system of the QSO and at least one, possibly two other galaxies. The host shows an exponential disk profile, with $r_{1/2} = 16.0$ kpc and ellipticity $e = 28$. The first companion is of similar luminosity as the host, 14 kpc away to the west. A tidal arm extends in an arc to the south and west towards the second companion at 60 kpc distance, 1.3 mag fainter than the host in $V$. About 460 kpc projected distance to the east exists a small group of five bright galaxies. Both companions an the tidal arm were masked in the modelling.

**HE 1300–1325**: Interacting galaxy classified as an elliptical with $r_{1/2} = 4.9$ kpc and $e = 0.39$. The morphology is complex and assymetric to the center, thus $e$ might be slightly overestimated and more likely have the value 0.3. The host is interacting with a luminous galaxy 43 kpc to the east. Both galaxies are tidally disturbed, the host is displaying two tidal arms and a tidal bridge exists between the two galaxies.

**HE 1310–1051**: Clear disk with two asymmetric spiral or tidal arms, $r_{1/2} = 3.5$ kpc, $i = 27°$. There is no luminous companion visible as a source for tidal interaction, the closest extended objects are a galaxy 0.5 mag fainter than the host in $V$, 45 kpc to the north, and a second, 110 kpc east, 2 mag fainter, but their redshifts are not known.

**HE 1315–1028**: Disk with $r_{1/2} = 8.1$ kpc, $i = 58°$, but the latter seems slightly overestimated judging from the produced model. The host is assymetric in the north-west. An also assymetric companion exists 82 kpc in the same direction, 0.6 mag fainter than the host in $V$.

**HE 1335–0847**: A decision between disk and spheroidal was difficult in this case. In the range between $3''$ and $6''$ an exponential disk would also be a good fit, so we could have a disk with additional flux at larger radii from star formation. This excess decreases somewhat from $V$ to the NIR. The results were inconclusive and in total we opted for the spheroid model. The host is very symmetric, with $r_{1/2} = 5.0$ kpc, $e = 0.19$. No companions or galaxies in the vicinity are visible.

**HE 1338–1423**: Prominent spiral with bulge or bar. The disk was modelled with $r_{1/2} = 13.7$ kpc, $i = 55°$, the bulge/bar with a spheroid with $r_{1/2} = 4.6$ kpc, $e = 0.33$, but other geometries for the bulge/bar are possible.

**HE 1405–1545**: Highly disturbed disk with tidal arms to the north and south. There is a luminous knot 24 kpc south-east of the nucleus, touched by the southern arm, that could be an interacting companion. The morphological parameters are $r_{1/2} = 8.8$ kpc, $i = 49.5°$. The modelling of this object was very difficult. It excluded the complete north-eastern half of the frame and left significant residuals.

**HE 1416–1256**: Very symmetric circular elliptical (sic!) with $r_{1/2} = 6.4$ kpc. The closest galaxies are at 150, 180, and 240 kpc distance.

**HE 1434–1600**: Symmetric elliptical with low ellipticity. A companion 2 mag fainter in $V$ is located 14 kpc to the south-west.

### 2.5.3 Colours

The derived apparent and absolute magnitudes of the host galaxies of our objects in the seven bands $B$, $V$, $R$, $I$, $J$, $H$, and $K$ are collected in Table 2.5. From these we derived the rest-frame colours in Table 2.6 including the $K$-correction terms from Table 2.3. Since the $B$ band images on average have much lower S/N than the rest of the bands, and data is not avalable for all objects, we include $V - K$ as a long wavelength baseline colour. In Table 2.7 mean and median colours are listed for the sample as a whole and for subsamples of ellipticals and disks.

The errors of the colours are dominated by the uncertainties of the modelling process. Simulations performed in Kuhlbrodt, Wisotzki & Jahnke (2002, in prep., see also Kuhlbrodt et al. 2001) suggest that modelling errors for our objects are of the order of 0.05 mag in host galaxy magnitude, possibly 0.1 mag for the very compact elliptical HE 1201–2409.

In Table 2.7 no significant difference can be seen between disks and ellipticals for colours of neighbouring bands. For the long baseline $V - K$ however 0.25 mag (for the median 0.35 mag) difference exist, the ellipticals being *bluer* than the disks. This is not created by statistical outliers, as Figure 2.13 illustrates: The distribution of ellipticals (open symbols) has systematically bluer colour than the disks (filled symbols). Some of the difference might be caused by emission lines, which could contribute 0.15 mag to the $V - K$ colours. This would make the colours of disks and ellipticals similar, but not make ellipticals as red as their inactive counterparts. This effect is discussed in detail in chapter 6.

**Table 2.5.** Apparent and absolute magnitudes for the host galaxies. Conversion to absolute magnitudes uses the *K*-corrections from Table 2.3. In *B* no value is given if the modeling process failed to deliver satisfactory results.

| Object | $B$ | $V$ | $R$ | $I$ | $J$ | $H$ | $K$ | $M_B$ | $M_V$ | $M_R$ | $M_I$ | $M_J$ | $M_H$ | $M_K$ |
|---|---|---|---|---|---|---|---|---|---|---|---|---|---|---|
| HE 0952–1552 | 17.6 | 16.7 | 16.1 | 15.6 | 14.5 | 13.9 | 13.4 | –21.9 | –22.5 | –23.1 | –23.6 | –24.6 | –25.2 | –25.5 |
| HE 1019–1414 | 18.0 | 17.2 | 16.5 | 16.1 | 15.2 | 14.5 | 14.1 | –20.6 | –21.3 | –21.9 | –22.4 | –23.2 | –23.9 | –24.1 |
| HE 1020–1022 | 19.2 | 18.0 | 17.2 | 16.5 | 15.6 | 14.9 | 14.3 | –22.2 | –22.9 | –23.5 | –24.1 | –24.9 | –25.5 | –25.8 |
| HE 1029–1401 | * | 15.6 | 15.2 | 14.7 | 14.1 | 13.5 | 12.3 | * | –23.2 | –23.4 | –23.9 | –24.5 | –25.1 | –25.8 |
| HE 1043–1346 | 16.6 | 15.9 | 15.4 | 14.9 | 14.0 | 13.3 | 13.0 | –21.7 | –22.3 | –22.8 | –23.3 | –24.1 | –24.8 | –24.9 |
| HE 1110–1910 | 17.9 | 17.2 | 16.5 | 16.0 | 15.4 | 14.7 | 14.1 | –21.8 | –22.2 | –22.8 | –23.2 | –23.8 | –24.5 | –24.8 |
| HE 1201–2409 | 17.9 | 16.9 | 16.3 | 16.0 | 15.5 | 14.8 | 14.0 | –22.5 | –23.0 | –23.5 | –23.8 | –24.2 | –24.8 | –25.3 |
| HE 1228–1637 | 17.7 | 16.9 | 16.3 | 16.0 | 15.1 | 14.5 | 14.1 | –21.8 | –22.3 | –22.8 | –23.1 | –24.0 | –24.5 | –24.6 |
| HE 1237–2252 | 17.1 | 16.3 | 15.7 | 15.2 | 14.3 | 13.7 | 13.3 | –22.1 | –22.7 | –23.2 | –23.7 | –24.6 | –25.2 | –25.4 |
| HE 1239–2426 | 16.7 | 16.1 | 15.5 | 15.1 | 14.0 | 13.5 | 13.1 | –22.1 | –22.5 | –23.0 | –23.5 | –24.5 | –25.0 | –25.2 |
| HE 1254–0934 | * | 17.3 | 16.9 | 16.0 | 15.3 | 14.8 | 13.9 | * | –22.5 | –22.9 | –23.7 | –24.4 | –24.9 | –25.5 |
| HE 1300–1325 | * | 15.3 | 14.7 | 14.2 | 13.3 | 12.7 | 12.4 | * | –22.1 | –22.6 | –23.1 | –24.0 | –24.6 | –24.8 |
| HE 1310–1051 | 16.5 | 16.0 | 15.5 | 15.0 | 14.1 | 13.6 | 13.3 | –20.2 | –20.6 | –21.1 | –21.6 | –22.4 | –23.0 | –23.2 |
| HE 1315–1028 | * | 17.7 | 17.0 | 16.4 | 15.4 | 14.9 | 14.5 | * | –21.3 | –22.0 | –22.6 | –23.5 | –24.1 | –24.2 |
| HE 1335–0847 | 17.5 | 16.8 | 16.3 | 15.9 | 15.1 | 14.5 | 14.3 | –21.3 | –21.8 | –22.2 | –22.6 | –23.4 | –23.9 | –23.9 |
| HE 1338–1423 | 15.1 | 14.5 | 14.0 | 13.4 | 12.5 | 11.8 | 11.4 | –22.0 | –22.6 | –23.0 | –23.6 | –24.5 | –25.2 | –25.4 |
| HE 1405–1545 | * | 17.4 | 16.9 | 16.3 | 15.6 | 15.0 | 14.4 | * | –23.3 | –23.7 | –24.2 | –24.9 | –25.4 | –25.6 |
| HE 1416–1256 | * | 17.5 | 17.0 | 16.3 | 15.9 | 15.2 | 14.7 | * | –22.3 | –22.6 | –23.3 | –23.7 | –24.3 | –24.5 |
| HE 1434–1600 | * | 17.0 | 16.4 | 15.8 | 15.1 | 14.4 | 13.7 | * | –23.1 | –23.5 | –24.1 | –24.8 | –25.3 | –25.7 |

**Table 2.6.** Host galaxy rest-frame colours after application of the $K$-corrections from Table 2.3. For $B-V$ no value is given if the modeling process failed to deliver satisfactory results.

| Object | $B-V$ | $V-R$ | $R-I$ | $I-J$ | $J-H$ | $H-K$ | $V-K$ |
|---|---|---|---|---|---|---|---|
| HE 0952–1552 | 0.57 | 0.64 | 0.47 | 1.04 | 0.60 | 0.22 | 2.96 |
| HE 1019–1414 | 0.62 | 0.68 | 0.42 | 0.86 | 0.64 | 0.24 | 2.84 |
| HE 1020–1022 | 0.68 | 0.58 | 0.65 | 0.78 | 0.61 | 0.22 | 2.84 |
| HE 1029–1401 | * | 0.27 | 0.48 | 0.63 | 0.55 | 0.71 | 2.64 |
| HE 1043–1346 | 0.57 | 0.54 | 0.48 | 0.86 | 0.63 | 0.19 | 2.70 |
| HE 1110–1910 | 0.41 | 0.62 | 0.39 | 0.59 | 0.66 | 0.34 | 2.61 |
| HE 1201–2409 | 0.57 | 0.47 | 0.26 | 0.44 | 0.65 | 0.48 | 2.29 |
| HE 1228–1637 | 0.48 | 0.49 | 0.35 | 0.84 | 0.49 | 0.19 | 2.35 |
| HE 1237–2252 | 0.61 | 0.51 | 0.47 | 0.95 | 0.56 | 0.17 | 2.66 |
| HE 1239–2426 | 0.48 | 0.50 | 0.47 | 0.98 | 0.53 | 0.21 | 2.70 |
| HE 1254–0934 | * | 0.38 | 0.78 | 0.68 | 0.49 | 0.60 | 2.92 |
| HE 1300–1325 | * | 0.47 | 0.49 | 0.92 | 0.63 | 0.20 | 2.70 |
| HE 1310–1051 | 0.47 | 0.48 | 0.46 | 0.86 | 0.53 | 0.20 | 2.53 |
| HE 1315–1028 | * | 0.67 | 0.54 | 0.96 | 0.53 | 0.12 | 2.83 |
| HE 1335–0847 | 0.47 | 0.42 | 0.43 | 0.74 | 0.52 | 0.05 | 2.14 |
| HE 1338–1423 | 0.56 | 0.43 | 0.65 | 0.88 | 0.65 | 0.28 | 2.89 |
| HE 1405–1545 | * | 0.43 | 0.52 | 0.63 | 0.55 | 0.17 | 2.31 |
| HE 1416–1256 | * | 0.33 | 0.64 | 0.41 | 0.58 | 0.19 | 2.16 |
| HE 1434–1600 | * | 0.34 | 0.64 | 0.65 | 0.58 | 0.38 | 2.59 |

**Table 2.7.** Colours of the sample as a whole and for subsamples of hosts identified as disks or as ellipticals. Listed are mean with error of mean, and median values in *italics*.

| | $B-V$ | $V-R$ | $R-I$ | $I-J$ | $J-H$ | $H-K$ | $V-K$ |
|---|---|---|---|---|---|---|---|
| Whole sample | 0.54 | 0.49 | 0.50 | 0.77 | 0.58 | 0.27 | 2.61 |
| | (0.02) | (0.03) | (0.03) | (0.04) | (0.01) | (0.04) | (0.06) |
| | *0.56* | *0.47* | *0.47* | *0.78* | *0.56* | *0.20* | *2.64* |
| Ellipticals | 0.52 | 0.44 | 0.48 | 0.67 | 0.59 | 0.31 | 2.48 |
| | (0.05) | (0.04) | (0.05) | (0.06) | (0.02) | (0.07) | (0.08) |
| | *0.47* | *0.42* | *0.43* | *0.63* | *0.58* | *0.20* | *2.35* |
| Disks | 0.55 | 0.53 | 0.53 | 0.87 | 0.57 | 0.24 | 2.73 |
| | (0.02) | (0.03) | (0.04) | (0.04) | (0.02) | (0.04) | (0.06) |
| | *0.56* | *0.50* | *0.47* | *0.86* | *0.55* | *0.20* | *2.70* |

## 2.6 Comparison to inactive galaxies

While the comparison of ellipticals and disks in the sample is already illustrative, we are rather interested to relate our results to the general population of galaxies to draw conclusions about possible parent populations or find systematic peculiarities. Thus we want to compare our sample against numbers representative for *inactive* galaxies.

Empirical colours of inactive galaxies on one side and colour predictions for from population synthesis models on the other do not yet completely agree – the models are still being refined. While optical colours are quite consistent by now, values for optical to NIR colours still show a substantial spread between empirical studies and between different models.

Optical colours in the past have been studied more extensively than the NIR bandpasses, because of the longer accessability of optical spectra. However, not many homogenous studies exist that studied the whole optical to infrared wavelength range with the same techniques.

### 2.6.1 Empirical colours of inactive galaxies

Optical-optical colours of inactive galaxies are well established. Based on systematic spectrophotometric catalogues (e.g. Kennicut 1992; Kinney et al. 1996) broad band colours of galaxies can be computed, and average values predicted. In the UV and optical e.g. Fukugita et al. (1995) list average colours of inactive galaxies for 48 standard photometric bands. For ellipticals their numbers agree down to about 0.05 mag with the effective colours derived by Mannucci et al. (2001), who compiled colours for galaxies with $M_V < -21$ from a large number of publications (but not from Fukugita et al.). Since *effective* colours are computed from fluxes inside an aperture with constant *radius* for all bands, a comparison to total colours is only possible for ellipticals, showing small radial colour gradients.

In a statistically extensive study of more than 1000 galaxies from catalogue data, Fioc & Rocca-Volmerange (1999) compute total and effective NIR–NIR and optical–NIR colours, using type-dependent curves of growth for converting aperture photometry data. The authors also

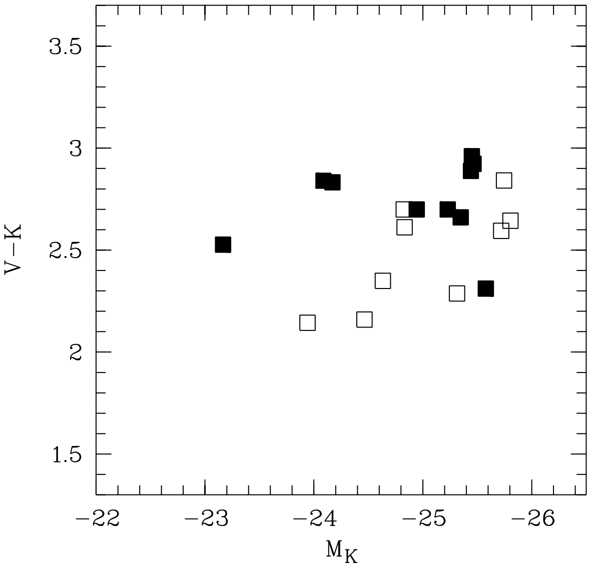

**Figure 2.13.** $V - K$ colours against $K$ band absolute magnitude $M_K$ of the individual hosts in the multicolour sample. Open symbols mark ellipticals, filled symbols disks.

**Table 2.8.** Disk and ellipticals in the sample and comparison with inactive galaxies. For the disks intermediate type Sb is used. Sources: optical colours from Fukugita, Shimasaku, & Ichikawa (1995), optical–NIR and NIR colours computed from Fioc & Rocca-Volmerange (1999) as described in the text. $I-J$ was calculated from the other colours. For $V-K$ the spread is given in parentheses.

|  | $B-V$ | $V-R$ | $R-I$ | $I-J$ | $J-H$ | $H-K$ | $V-K$ |
|---|---|---|---|---|---|---|---|
| Ellipticals |  |  |  |  |  |  |  |
| Inactive | 0.96 | 0.61 | 0.70 | 0.77 | 0.71 | 0.20 | 2.99 (0.12) |
| QSO host sample | 0.52 | 0.44 | 0.48 | 0.67 | 0.59 | 0.31 | 2.48 (0.25) |
| $\Delta$ | 0.44 | 0.17 | 0.22 | 0.10 | 0.12 | –0.11 | 0.50 |
| Disks (Sb) |  |  |  |  |  |  |  |
| Inactive | 0.68 | 0.54 | 0.63 | 0.67 | 0.78 | 0.25 | 2.87 (0.36) |
| QSO host sample | 0.55 | 0.53 | 0.53 | 0.87 | 0.57 | 0.24 | 2.73 (0.20) |
| $\Delta$ | 0.13 | 0.01 | 0.10 | –0.20 | 0.21 | 0.01 | 0.14 |

investigate the effect of inclination on $B-H$ and the colour-magnitude relation differentiated by Hubble type. The values for NIR–NIR colours are almost independent of type. They find $J-H=0.71$ and $H-K=0.20$ for ellipticals, rising to 0.78 and 0.25 for Sb spirals, which is again consistent with the values by Mannucci et al. Fioc & Rocca-Volmerange find an effective $B-H=3.86$ for ellipticals, which is about 0.2 mag bluer than computed by Mannucci et al. (2001).

We can not resolve the discrepancy in $B-H$ at this point. We will take the colours listed by Fioc & Rocca-Volmerange (1999) as a basis because a) their total colours are closer to the methods used in our study, b) because their sample is larger and the treatment seems very consistent, and c) because their colours in tendency are bluer, which is the same direction of bias as all of our other potential systematic errors. We thus get conservative estimates for the amount of blueness in our sample.

We use their $B-H$ colour relation dependent on inclination and magnitude to calibrate the comparison optical-to-NIR colours for inactive galaxies. Our disk subsample has on average an axial ratio $\overline{R}=\overline{a/b}=1.4$ which yields $B-H=3.34$. If we included the colour-magnitude dependence, the value decreases only slightly to $B-H=3.30$, because the average brightness of their Sb and our disk subsample are very close to each other (0.25 mag difference). For ellipses total colours at the average brightness of the elliptical subsample are $B-H=3.75$, corrected for magnitude.

In Table 2.8 we list the collected colours as taken from Fukugita et al. (1995) for the optical colours, for the optical–NIR and NIR colours are computed from Fioc & Rocca-Volmerange, using $B-H$ as described above. For the disks we use intermediate type (Sb) colours.

### 2.6.2 Model predictions

Synthesised galaxy SEDs composed from libraries of stellar spectra can predict colours, as a function of age and metallicity. Different methods are used in evolutionary population synthesis and discrepancies arise particularly in the NIR. Maraston (1998) compares models by Bruzual & Charlot (1993, 1996) with own models and shows the influence of AGB stars and the abundance of carbon stars on luminosities in the NIR. This explains some of the 0.5 mag differences between the two models in $V-K$ colours and why Maraston's models fit some empirical data better: A strong "AGB bump" for single stellar populations of about 1 Gyr reddens $V-K$ colours by several tenths of a magnitude. Different initial mass functions and stellar libraries cause further differences between models. For models older than 4 Gyrs the predicted colours converge again, with differences less than 0.2 mag between the models. For SSPs older than 8 Gyrs the numbers are also consistent with colours derived for evolved ellipticals by Fioc & Rocca-Volmerange (1999).

### 2.6.3 Very blue host galaxies

In Table 2.8 we compare colours for inactive galaxies with the mean colours of our subsamples (from Table 2.7). We find very blue colours in comparison, particularly for the elliptical hosts. They are bluer in every single colour listed, apart from $H-K$. The long wavelength baseline colour $V-K$ is bluer by 0.5 mag, $B-V$ by slightly less. We perform a Student t-test that the $V-K$ colours of our ellipticals and of their inactive counterparts have the same mean. This hypothesis is rejected at a significance level of 0.001. Also tested was if their colours are identical to late type inactive galaxies, Sc or later, showing strong star-formation. This is not rejectable with the t-test! This fact is even compatible with the $H-K$ colours, which are redder for spirals than for ellipticals (0.20 for E, 0.25 for Sb and still 0.21 for Sc and Sd). Our disks are also in total slightly bluer than their average inactive counterpart, but not significantly.

Now, are these colours real? We stressed several times already that all known systematic effects in our analysis procedure would rather *redden* colours, thus these blueness estimates are conservative. One more artefact that could be created in the modelling procedure is transfer of a constant fraction of nuclear light into the host, as a difference to a *varying* portion from band to band due to a varying scale length of the host as we have discussed in section 2.5.1. Host galaxies with spheroidal morphology are in general more compact than exponential disks, owing to their $r^{1/4}$ surface brightness distribution. They are closer in their appearance to the PSF shape of the nucleus than disks and make modelling of the nuclear contribution generally more sensitive to the properties of the host. A numerical modelling algorithm could transfer flux between nucleus and spheroidal host and thus influence the host's colour.

While for optical colours the nucleus is much bluer than any host, for optical–NIR colours such a transfer would have the opposite effect. The strongest deviation from inactive colours appears for the longest wavelength baseline, $V-K$ – disregarding the low signal-to-noise results of the $B$ band for this comparison. We compare this to the average nuclear $(V-K)_{\rm nuc}$ colours, either taken from our sample – though possibly biased in the same context – or estimated from the average QSO SED published by Elvis et al. (1994). From the latter we estimate $(V-K)_{\rm nuc} = 3.4$ thus similar or even *redder* colours than for inactive galaxies and particularly redder than our host galaxy sample! Thus a constant fraction of nuclear flux transfered to the host would not make $V-K$ bluer, it would redden our data.

But even this we do not see in our modelling. Simulations in Kuhlbrodt, Wisotzki, & Jahnke (2001) show flux transfer to be negligible even for the more compact hosts in our sample and suggest that the colours derived are no artifacts. Also when plotting "angular" scale length, the compactness of the host as appearing in the image, not the geometrical scale, and $V-K$ colour, no trend can be seen (Fig. 2.14). We take this also as an indication that no systematic

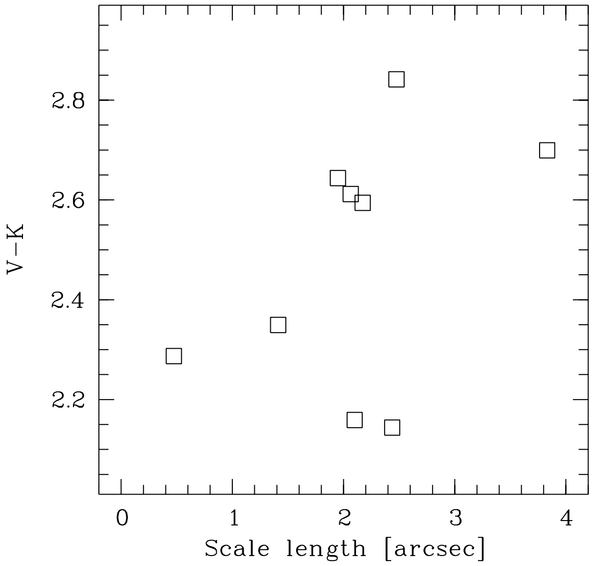

**Figure 2.14.** $V-K$ colours for the ellipticals in the sample vs. scale length in arcsec as a measure of compactness in the image. No trend, as an indication for systematic flux transfer depending on compactness, can be seen.

flux transfer from nucleus to host occurs even for the more compact objects.

On the inactive galaxy side, our reference values for Sb spirals already include the correction for inclination, which, at 1 mag/$\log(a/b)$, can be a strong source for bias: Due to missing high inclinations and edge-on spirals as hosts of QSOs visible for us, the field galaxy population will always be reddened in comparison. Average inclination and thus dust reddening in QSO hosts is on average lower, appearing e.g. as about 0.15 mag bluer colours when comparing to the galaxy sample used by Fioc & Rocca-Volmerange (1999). In ellipticals however, this kind of dust extinction is not expected, thus colour and viewing angle should not be related.

After assessing all of these potential error-sources, we believe the blue colours of the sample, approximately normal for the disks, very blue for the ellipticals, to be real.

### 2.6.4 Colour-magnitude relation for host galaxies

One interesting point is the shown in Fig. 2.15, where we plot three optical–NIR colours vs. absolute $H$ band magnitude as in Fig. 2.13, but also the linear regression fit to the data (solid line) using $M_H$ as an independent variable (this is not strictly true because $M_H$ also has an error bar, but in order to change the regression strongly, the error would need to be a) large, i.e. several tenths of a magnitude, and b) systematic). This relation is the colour-magnitude relation (CMR) for this sample and it is compared to the CMR of inactive galaxies (dashed line), that we took from Fioc & Rocca-Volmerange. We simply averaged their slopes for E and Sb galaxies, no large difference if also S0 and Sa were used, and shifted the relation to a zero-point according to the mean E and Sb $B-H$ colour, as given in Table 2.8. For the CMR in $V-H$ and $V-K$ we applied an offset of 0.8 mag ($B-V$ average for E and Sb) and 0.52 mag ($(B-V)-(H-K)$) accordingly. While the correlations are not strong, the similarity between the CMR for host and inactive galaxies is appealing, even the spread around the CMR is within 15% to the spread found by Fioc & Rocca-Volmerange. A larger brightness baseline would enhance an existing correlation, but the CMR seems to be real, similar to the inactive CMR, only shifted by 0.3 mag.

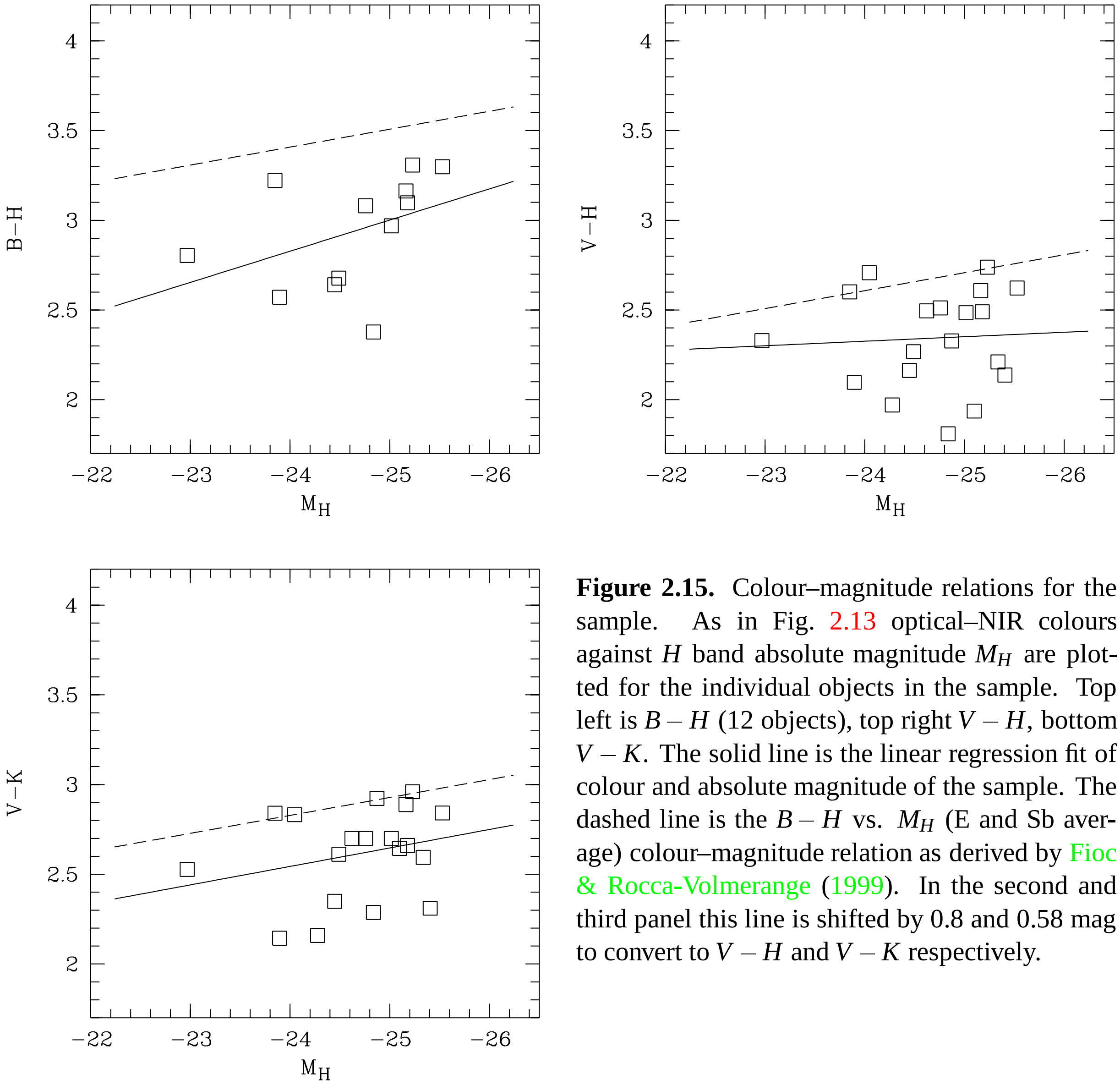

**Figure 2.15.** Colour–magnitude relations for the sample. As in Fig. 2.13 optical–NIR colours against $H$ band absolute magnitude $M_H$ are plotted for the individual objects in the sample. Top left is $B - H$ (12 objects), top right $V - H$, bottom $V - K$. The solid line is the linear regression fit of colour and absolute magnitude of the sample. The dashed line is the $B - H$ vs. $M_H$ (E and Sb average) colour–magnitude relation as derived by Fioc & Rocca-Volmerange (1999). In the second and third panel this line is shifted by 0.8 and 0.58 mag to convert to $V - H$ and $V - K$ respectively.

## 2.7 Fitting stellar populations

Another way of analysing our derived host galaxy luminosities and colours is by comparing them to synthetic model SEDs. We have commented already on individual colours resulting from evolution synthesis models (ESM) of single stellar populations (SSP), and their general agreement with empirical data.

In order to use all colour information at the same time – we *do* have a multicolour sample available – we decided to fit SEDs of ESM to the calibrated fluxes of the hosts at the different wavelengths. With seven bands representing seven data points in the SED of an object our prime goal was a) to reproduce and cross-check the blue colours found, b) to try to estimate an approximate age of the dominant populations in the hosts. We might find clues for an unexpected amount of young, blue stars, thus starburst activity. For this task we used model SSPs of single metallicity, because the age-metallicity degeneracy in model colours cannot be resolved with multicolour data, absorption line measurements are necessary for this task. The simplifying assumption is made that the populations are created instantly at age zero with an initial mass function and then evolve passively (“instantanous burst models”).

As described in 2.6.2, the different existing stellar population models have not yet converged. We chose to use models from the GISSEL96 library (Bruzual & Charlot 1993, 1996), also available via Leitherer et al. (1996). For details on the models see the GISSEL96 documentation in Bruzual & Charlot (1996). We used models based on the Scalo (1986) initial mass function, with solar metallicities for reasons of comparability with Maraston (1998), and because we do not have indications for different metallicities. We selected a coarse grid of model ages, 0.1, 0.7, 2, 6 and 14 Gyr, and in addition constructed a rough continuous star formation (CSF) model with a constant star formation rate, by superpositioning models between ages of 0.01 and 14 Gyr.

For these model spectra we computed broad band fluxes for the seven $BVRIJHK_s$ filters used, and converted our host galaxies’ magnitudes to flux densities using a Kurucz Vega SED as given by Bruzual & Charlot (1996). We then fitted the models to the data via $\chi^2$ minimisation, in two steps: 1) fitting only one SSP, age as free parameter (in the following one-component, “1C”), 2) fitting two SSPs, with the first age fixed (0.1 Gyr), and the age of the second component and the two masses as free parameters (two-component, “2C”).

### 2.7.1 Variances and confidence intervals

In the fitting process we need a weighing scheme for the contributions of the different bands. Also, only knowing the age of the best fitting SSP is of limited diagnostic value without an estimate of a range of ages also compatible with the data set.

To assign statistically “true” variances is not possible, because of the complexity and nonlinearity of the QSO separation modelling procedure. We gave approximate errors for the photometry, but these are rule-of-thumb values, estimated from simulations of artificial QSOs. More complex or more simple morphologies of the host, varying backgrounds, and particularly the varying PSF can result in variances larger or smaller than these values.

We therefore turn away from variances in the statistical sense and try to find a weighing scheme for the different bands. Fluxes in the different bands are of rather different size, the flux in the $V$ band being larger than in the $H$ band by factors of typically 5-8. On the other side the NIR bands yield a certain redundancy in their diagnostic possibilities, all three characterising the population of old evolved red giants.

Following Press et al. (1995) we will try to estimate the absolute values of the standard deviation $\sigma$ from the $\chi^2$ minimisation itself. This requires that for all bands the weights are identical, $\sigma_i = \sigma$. Be $N$ the number of data points and $M$ the number of fixed parameters. We first assign an arbitrary $\sigma$ and then recompute it after the fitting as

$$\sigma^2 = \sum_{i=1}^{N} y_i - y(x_i)^2/\nu$$

$\nu = N - M$ being the degrees of freedom. Even though an independent goodness-of-fit estimate is not possible, we want to use these $\sigma$ to determine a range of good fitting models by *assuming* that for the best fitting model the $\sigma$ are the true values, and that deviations from the data are only due to observational errors, not to systematic errors.

**Table 2.9.** $\Delta\chi^2$ as a function of confidence level and degrees of freedom from Press et al. (1995, p. 697).

| p | $\nu$ | | | | | | |
|---|---|---|---|---|---|---|---|
| | 1 | 2 | 3 | 4 | 5 | 6 | |
| 68.3% | 1.00 | 2.30 | 3.53 | 4.72 | 5.89 | 7.04 | $1\sigma$ |
| 90% | 2.71 | 4.61 | 6.25 | 7.78 | 9.24 | 10.6 | |
| 95.4% | 4.00 | 6.17 | 8.02 | 9.70 | 11.3 | 12.8 | $2\sigma$ |
| 99% | 6.63 | 9.12 | 11.3 | 13.3 | 15.1 | 16.8 | |
| 99.73% | 9.00 | 11.8 | 14.2 | 16.3 | 18.2 | 20.1 | $3\sigma$ |
| 99.99% | 15.1 | 18.4 | 21.1 | 23.5 | 25.7 | 27.8 | |

This is done by analysis of the $\chi^2$ values of the fits after the recomputation of $\sigma$. The probability distribution of parameters for normally distributed errors yields $\chi^2$-values depending on the degrees of freedom $\nu$: The $\chi^2$ statistic has a mean $\nu$, thus a “moderately” good fit has typically $\chi^2 = \nu$ (Press et al. 1995, p. 661). Parameter values inside $x\sigma$ error boundary will then show a $\Delta\chi^2$ depending on $\nu$ as given in Table 2.9.

In our case, the number of data points $N = 7$ (or $N = 6$ in case the *B* band is missing). The number of fixed parameters depends on the number of models fitted, for the 1C case $M = 2$ (age, mass), or for 2C $M = 3$ (two masses and one age). Thus we work with $\nu = 5$ (or 4) and $\nu = 4$ (or 3), respectively.

This method has the drawback of requiring identical weights for all data points, in spite of systematically different flux values for the seven data points. The observations were designed to yield similar S/N for the host in all bands, except *B*, thus the *relative* errors from the modelling process are similar. This makes the *absolute* errors in the lower flux NIR bands smaller, but we assign the same absolute error with this weighing scheme. As a result the NIR bands will have a systematically lower weight.

This effect is countered by the redundancy of information contained in the three NIR bands. All contain information about the older populations. If a modelling error occurs in one of then, its influence is lowered by the two other bands. The exact magnitude of the two effects is difficult to assess, but will be discussed when analysing the model fits.

### 2.7.2 One component fit

We performed two different 1C fits. The first used only the five SSP of ages 0.1, 0.7, 2, 6 and 14 Gyr, in the second we added the CSF model. In Table 2.10 we show the result: We marked the best fitting model with an “x”, those within $1\sigma$, $2\sigma$, and $3\sigma$ according to the above procedure with 1, 2, and 3. As described above, these error bars should not be taken at face value, but only give a rough impression on the ranges of ages involved.

It is interesting how young the best fitting models are. Only for two objects the best fitting model is older than the 2 Gyr model. One of them, HE 1315–1028, is of disk morphology, the other, HE 1020–1022, is an elliptical. Of the rest, twelve prefer the 2 Gyr model, five even the 0.7 Gyr model, whereof three are ellipticals, two are disks. The data for HE 1254–0934 seem to be not fitting the model well, or rather vice versa, all except the youngest model are possible within $3\sigma$. More details on the individual objects are found in the next section.

**Table 2.10.** Single SSP (1C) fit. “x” marks the best fitting profile, 1, 2, and 3 the profiles that are acceptable within $1\,\sigma$, $3\,\sigma$, and $3\,\sigma$ error accordingly. Also shown again is the galaxy type (E)lliptical or (D)isk from Tab. 2.4 for comparison. The last coloumn displays a “y” if a CSF model, when incorporated into the fit, would be accepted as best fitting model.

| Object | Type | 0.1 Gyr | 0.7 Gyr | 2 Gyr | 6 Gyr | 14 Gyr | CSF |
|---|---|---|---|---|---|---|---|
| HE 0952–1552 | D | | | x | 3 | | y |
| HE 1019–1414 | D | | | x | 3 | | |
| HE 1020–1022 | E | | | 1 | x | 3 | |
| HE 1029–1401 | E | | x | 1 | | | |
| HE 1043–1346 | D | | 3 | x | | | y |
| HE 1110–1910 | E | | 1 | x | 1 | | |
| HE 1201–2409 | E | | x | 2 | | | |
| HE 1228–1637 | E | | x | 1 | | | |
| HE 1237–2252 | D | | 3 | x | | | y |
| HE 1239–2426 | D | | 1 | x | 3 | | y |
| HE 1254–0934 | D | | 2 | x | 1 | 3 | |
| HE 1300–1325 | E | | | x | | | |
| HE 1310–1051 | D | | x | 1 | | | |
| HE 1315–1028 | D | | | 1 | x | 3 | |
| HE 1335–0847 | E | | 1 | x | | | |
| HE 1338–1423 | D | | 2 | x | | | y |
| HE 1405–1545 | D | | x | 1 | | | |
| HE 1416–1256 | E | | 1 | x | 2 | | |
| HE 1434–1600 | E | | | x | 3 | | |

In a second step we therefore include a CSF model in the 1C fit, assuming a constant star formation rate over a period of 14 Gyr. The last coloumn “CSF” in Table 2.10 marks those objects with a “y”, for which the CSF is the best fitting model, when incorporated in the fit. This is the case for half of the ten disks and none of the ellipticals. Included in these five disks are the three with visible prominent spiral arms, HE 1043–1346, HE 1239–2426, and HE 1338–1423. For four of the five remaining disks the CSF model ranges on place number two, all inside $1\,\sigma$. Similarly, for the ellipticals the CSF model is not inside $1\,\sigma$ for only two of nine objects, HE 1029–1401 and HE 1201–2409.

### 2.7.3 Two component fit

For the 2C fit we proceed similarly, first a fit without the CSF model. The age of the first component is set to 0.1 Gyr. The age of the second component is left free, as well as both absolute scale parameters (“masses”) that we translate into a percentage of the total (visible baryonic) mass. Results are compiled in Table 2.11, in a similar way to the 1C fit, with the percentage of the 0.1 Gyr component added in parentheses.

As examples, the resulting best fitting SEDs and their relation to data points are plotted for two objects in Table 2.16, the full set can be found in Table B.1 in the appendix. In red the 1C

**Table 2.11.** Two component SSP (2C) fit, one component fixed to 0.1 Gyr. Nomenclature as in Table 2.10, only added in parentheses is the fraction of the total mass of the 0.1 Gyr component in percent. In the CSF column, we now also list the confidence level and percentage, even if the CSF model was not the best fit.

| Object | Type | 0.7 Gyr | 2 Gyr | 6 Gyr | 14 Gyr | CSF |
|---|---|---|---|---|---|---|
| HE 0952–1552 | D |  | 2 (0.7) | 1 (3.3) | x (2.3) | 1 (0.6) |
| HE 1019–1414 | D |  | x (0.8) | 1 (2.6) | 1 (3.3) | 1 (0.0) |
| HE 1020–1022 | E |  | 1 (0.0) | x (1.0) | 2 (1.5) | 2 (0.0) |
| HE 1029–1401 | E | 1 (0.0) | x (10.7) | 1 (11.3) | 1 (8.7) | 1 (7.5) |
| HE 1043–1346 | D |  | 1 (3.9) | x (5.2) | 2 (3.3) | y (1.7) |
| HE 1110–1910 | E | 2 (0.0) | x (2.6) | 1 (4.8) | 1 (4.5) | 1 (2.3) |
| HE 1201–2409 | E | x (0.0) | 1 (12.3) | 1 (10.7) | 2 (7.5) | 1 (8.7) |
| HE 1228–1637 | E |  | x (5.6) | 1 (6.5) | 2 (4.5) | 1 (3.9) |
| HE 1237–2252 | D |  | 2 (3.3) | x (4.8) | 3 (3.1) | 1 (1.3) |
| HE 1239–2426 | D |  | 3 (6.5) | 1 (5.3) | x (4.1) | 1 (3.3) |
| HE 1254–0934 | D | 2 (0.0) | x (0.7) | 1 (3.6) | 2 (3.1) | 1 (0.0) |
| HE 1300–1325 | E |  | 1 (0.7) | x (3.8) |  | y (1.1) |
| HE 1310–1051 | D |  | 2 (7.0) | x (7.0) | 2 (5.2) | 1 (4.5) |
| HE 1315–1028 | D |  | 2 (0.0) | x (1.1) | 2 (2.3) | 2 (0.0) |
| HE 1335–0847 | E |  | x (7.0) | 2 (8.7) | 3 (6.0) | 2 (5.2) |
| HE 1338–1423 | D |  | 1 (2.4) | x (4.5) | 1 (3.3) | 1 (1.8) |
| HE 1405–1545 | D | 1 (0.2) | x (9.3) | 1 (8.7) | 2 (7.0) | 1 (6.5) |
| HE 1416–1256 | E | 1 (0.2) | x (5.2) | 1 (7.5) | 1 (6.0) | 1 (5.2) |
| HE 1434–1600 | E |  | x (0.7) | 1 (4.5) | 1 (3.9) | 1 (0.9) |

SED is plotted, in green the 2C SED. Crosses mark the flux densities of the broad-band fluxes for the *BVRIJHK* data. For better comparison we computed corresponding broad band values also for the models shown. They are plotted as squares for 1C, and triangles for 2C.

### 2.7.4 SSP fitting results

**HE 0952–1552**: Both models fit rather well and differ only little. The largest difference to the data is in *V*, where the models are significantly bluer. This will make CSF a blue limit for the host, and the 0.1 Gyr component is limited to $< 2.2\%$.

**HE 1019–1414**: The two models are virtually identical, also for the 2C model 2 Gyr is selected as the dominant population and the 0.8% of 0.1 Gyr are negligible in their effect. The models show too much flux in *V* but a bit too little in *B*. CSF with no additional young component is possible within $1\sigma$, but in general 2 Gyr seems to be a good fit.

**HE 1020–1022**: For this spheroid the deviations of the model from data are large. The NIR is systematically overestimated by the models, *I* being off to the other direction. It is difficult to judge if omitting one of the data point would significantly change the fit. If *I* would be omitted, the model would get slightly older, for *J* younger. In total the spectral shape would not change

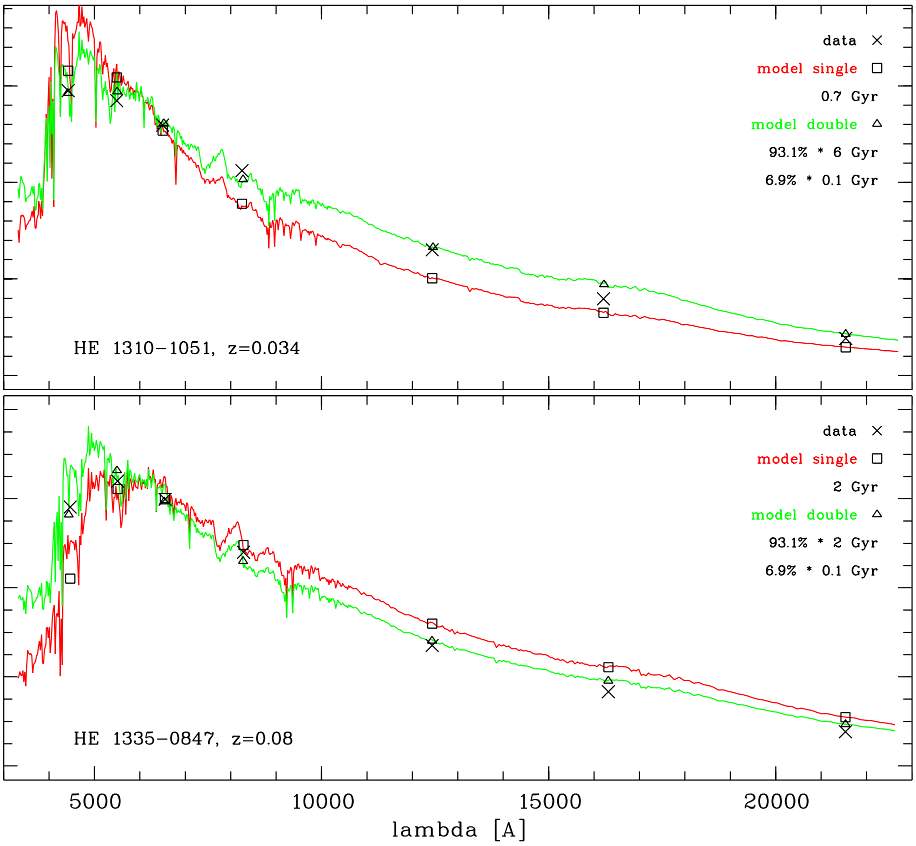

**Figure 2.16.** Two examples for results from SSP fitting. Corresponding plots for all objects are given in Figure B.1 in the appendix. Plotted are flux densities versus λ [Å] in observer frame. Data points of the *BVRIJHK* bands are marked with crosses. The SED of the best fitting 1C SSP is plotted in red, the composite 2C SED from a young, 0.1 Gyr SSP and an older population in green. The broad-band averaged fluxes of the SEDs are marked with symbols: squares for 1C, triangles for 2C. Name of the object and redshift $z$ are given, as well as the ages and relative contributions of the SSPs.

much and the estimate seems good. The additional 0.1 Gyr component decreases the difference to the data in $B$, having lower S/N, but increases it in $V$. The error estimate suggests that in a 2C fit a 2 Gyr component with negligible young component is possible withing $1\sigma$. In total the arguments for this 1% of 0.1 Gyr component are weak.

**HE 1029–1401**: Here judgement is difficult. The $B$ band point is missing and also for the other bands the modelling was difficult due to the poor PSF stars available and the bright nucleus. Both models show very young components, especially for a spheroidal. Without the $B$ band point the reality of the emission from the young component producing the emission between the $B$ and $V$ point can not really be established. On the other hand several arguments support a young population: Two of the three NIR points are already overestimated by the 2C model, which would increase for older populations. $B$ would need to be quite low, if the $V$ value were real, and $V$ would need to be erroneously high. Even then the $I$ value would be strongly overestimated. Thus a relatively blue population is plausible.

**HE 1043–1346**: Excellent fit for CSF plus young component. The modelling of this object in *B* was relatively simple. But as mentioned in section 2.5.1 the scale length is changing with wavelength for this object, which for *B* is visible in the radial profile (Fig. A.5). The effect would slightly overestimate the *B* band host flux and thus the pure CSF model would be plausible, being slightly less blue than the current best fit.

**HE 1110–1910**: Again the fits are difficult to judge. An overestimated because uncertain *B* band would not fundamentally change the fitting results. If however the 0.1 Gyr component is real can not be told from the data. An old evolved population can be ruled out, 2 Gyr seem to be a good fit.

**HE 1201–2409**: For this very compact spheroidal, modelling was very difficult and can potentially show some errors. Here the very young models are much too blue, interestingly due to the low fluxes also in the *J* band. 0.7 Gyr is clearly too young, but a very old population is not possible. Later in section 4.3.2 it will be shown that both spectrum as well as the optical data points are fitted very well by a 2 Gyr population.

**HE 1228–1637**: The 1C model of age 0.7 Gyr is too young, underestimating all NIR points. Nevertheless the 2C model is also quite young, but still overestimating in *V*. An erroneous *B* band flux, being overestimated, could remove some of the 0.1 Gyr contribution in the model, but would not change the overall 2 Gyr population as being dominant. If changing to a CSF model as the underlying population, young component would still contain 3.9% of the stellar mass.

**HE 1237–2252**: Apart from the *B* band value this spectrum is compatible with CSF, but the best 2C fit is very good. In the 2C fit, CSF is good within $1\sigma$, needing only a 1.3% addition of a 0.1 Gyr component. Thus the data suggest a rather young mix of stars, and shows weak evidence for a starburst.

**HE 1239–2426**: Very similar to the previous object, being slightly bluer thus requiring a slightly larger young component. Again a very good 2C fit, CSF possible within $1\sigma$, then requiring an additional 3.3% of the 0.1 Gyr component. In total evidence for starburst and a relatively young spectrum.

**HE 1254–0934**: The modelling uncertainties for this object are large, *B* is missing, and thus the population fits have a limited value. Nevertheless the 2 Gyr model as the best result is consistent with finding young populations for most of the sample.

**HE 1300–1325**: If CSF is assumed to be the dominating population, then the amount of additional 0.1 Gyr population is determined by the *V* band value, as *B* is missing. A *B* band data point could break this degeneracy. In any case a population of 2 Gyr or younger is suggested by the fit.

**HE 1310–1051**: As will be shown later in section 4.3.2 the *B* band point is erroneous for unknown reasons and too high by about 0.5 mag. Thus as suggested by the model overestimating both *V* and *I*, the fitted models are too young. With *B* modified and according to the optical spectra, it is best described with an evolved population plus 1% of a 0.1 Gyr model, thus being rather old.

**HE 1315–1028**: Here again the *B* band data is missing. Both 1C and 2C models are similar, only showing differences in the blue. Both models overestimate the NIR fluxes, pointing to a slightly younger dominating population. This is confirmed from the optical spectrum presented in section 4.3.2, favoring a 4 Gyr old population model, agreeing rather perfectly with both optical spectrum and optical broad band fluxes.

**HE 1335–0847**: The spectrum of this host is modelled very well with 2 Gyr population with a substantial 7% contribution of a young component. The case is very strong against a pure older population, or at least a much smaller percentage of young stars, both being forced not only by a single data point.

**HE 1338–1423**: Even though this bright prominent spiral should be expected to deliver very good data, the models deviate in $R$ and $I$. At the $V$ band point the 2C model is slightly too high. Although the data quality in $B$ is very good, a small overestimate of the $B$ data point would decrease the young contribution and make pure CSF possible. Even now the 2C model with CSF as the dominating part, being good within $1\sigma$, would require only 1.8% of additional 0.1 Gyr stars. Thus this could be a normal spiral with a slightly higher level of star formation.

**HE 1405–1545**: This interacting and disturbed object was difficult to model and large errors are to be expected. The models exclude an old evolved population, which might be the only information to be taken from this object.

**HE 1416–1256**: For this spheroid the difference between the 1C and 2C model could be resolved with the missing $B$ band data point. The data for $I$ is above the models, for the NIR below. If one data point were omitted, the results were as for HE 1020–1022. In total no evidence for a young 0.1 Gyr component, but also evidence against a pure evolved population.

**HE 1434–1600**: Very similar to the previous object. Data in $I$ above the model, in the NIR below, $B$ missing. Also no sign of a significant 0.1 Gyr component, but moderately young spectrum.

In total all of the objects show broad band colours consistent with intermediate stellar populations. The relative young spectra are valid for both types of host, those identified as disks as well as spheroids. Significant contributions of a very young population is required by only two disks. No significant difference can be seen for spheroids vs. disks concerning average age. None of the spheroids shows fluxes that require to be modelled with an old, evolved population, as would be expected for inactive galaxies.

This result is supporting the blue $V-K$ colours found in sec. 2.6.3. Colours as blue as seen for most objects are usually only found in late type inactive galaxies that have a significant component of star formation, thus a significant young population. For the disks in the sample we should expect most of the blue emission to come from continuous star formation normal to spirals, but for the spheroids this is not not expected. The on average slightly bluer $V-H$ colours for spheroids than disks are compatible with the result of the model fitting. Also compatible are the ages of the dominating populations in the spheroids with the found abnormously blue colours compared to inactive galaxies.

In chapter 6 a comparison of these colours and the stellar composition of the objects with the results of the spectra determined for QSO host in the following chapters will be discussed, as well as the other results of this chapter and their astrophysical implications.

# 3 Host galaxy spectroscopy

In the previous chapter we described methods to extract coarse but robust spectral information on QSO host galaxies. Coarse, because broad band imaging samples the SED of a QSO, in our case in seven wavelength intervals between 4000 Å and 23000 Å. The broad band filter integrate over several hundred or thousand Å, in order to collect significant amounts of light.

The method is a very solid one, because by now we understand the uncertainties and caveats of two-dimensional image modelling quite well. Software has been developed and tested, by us and other groups, and the problems of PSF and host modelling have been investigated in depth. Thus the implemented modelling scheme is powerful and has assessable uncertainties.

In spectroscopy the situation is different. Spectroscopic studies of QSO host galaxies are very difficult: The AGN in the centre overpowers the host galaxy's emission much stronger than in broadband imaging, because the narrow slit is integrating much of a compact nucleus and little of an extended galaxy. Up to now it was not possible to access host spectra directly around the nucleus, where the connection between host and nucleus is strongest.

Very few spectroscopic studies were attempted, knowing too well of the problems of the task. In the 30 years of host galaxy research before 2002 only about 20 articles were published on host galaxy spectroscopy – compared to more than 100 on imaging –, and more than half of those appeared before 1985.

The first studies were able to find extended gas emission lines at the same redshift as the nucleus for individual objects (Wampler et al. 1975; Stockton 1976; Richstone & Oke 1977, Wyckoff et al., 1980a), finally confirming the cosmological nature of the QSO redshift. In these early studies no traces of stellar continuum emission were found, leading to suggestions that the nebulosities were only composed of diffuse gas.

At the same time for a small number of objects emission was found that was compatible with a stellar continuum with additional gas emission lines (Morton et al. 1978; Green et al. 1978). Finally signs of stellar absorption lines at the redshift of the nucleus confirmed the presence of stars (Wyckoff et al., 1980b; Boroson & Oke 1982; MacKenty & Stockton 1984). The first larger sample was investigated in a series of papers by Boroson, Oke, & Green (1982), Boroson & Oke (1984) and Boroson, Persson, & Oke (1985), staying the largest study for almost 20 years. They found two characteristic groups of hosts, with either blue continua and strong gas lines, or continua with weak or absent gas emission. They found positive correlations of this classification with the shape of the nuclear Balmer lines, the strength of the nuclear [O III] emission, the strength of Fe features, absorption line strength, radio spectrum shape and radio morphology. As the most likely reason for the optical spectral feature classes they named the geometry of the accretion disk around the nucleus and its orientation with respect to the rest of the host galaxy. Up to the present most of their findings are not disputed because their studies are still the most thorough investigation of the subject. We will return to their study in the discussion in chapter 6.

A few later studies found evidence for star formation possibly induced by tidal events (MacKenty & Stockton 1984; Hutchings & Hickson 1988), coordinated rotation of gas in the host (Hickson & Hutchings 1987; Hutchings & Crampton 1990), and an extention of the gas emission beyond the continuum (Hutchings & Hickson 1988). Ten years later Canalizo & Stockton (2000) performed a deep, spatially resolved study of the host galaxy of 3C 48, which was already investigated before by Wampler et al. (1975), Boroson et al. (1982) and Boroson & Oke (1984). The analysis included modelling the stellar content of 32 regions of the host. They found strong evidence for recent starburst of 5 to 100 Myrs and old evolved stars in other parts, fitting well into the picture of a merger event going on in 3C 48. This result is supported by – or rather vice versa the study was initiated because of – the tidally disturbed structure of the object visible in imaging.

The Keck telescope was used to create high resolution spectra of radio-loud QSOs, so far only to study spatially resolved emission line gas velocities (Sheinis 2001).

At the same time a study attempted to compare the stellar populations of radio-quiet QSOs, radio-loud QSOs and radio galaxies (Hughes et al. 2000; Nolan et al. 2001). The objects investigated were part of an earlier detailed imaging study (Dunlop et al. 1993; Taylor et al. 1996; Dunlop et al. 2001). Model fitting showed evolved stellar populations, with only small contributions to the light from recent star-formation, corresponding to young stars of less then about one percent of the visible mass. The samples however, were manually selected to match in different properties, as luminosity and redshift range, thus are not representative for the general host galaxy population.

In all these studies mentioned, the host spectra were taken *off-nucleus*, at distances of several arcseconds from the centre, to sample regions of the host as far away as possible from the nuclear light scattered by the atmosphere. In Figure 3.1 we show an example of slit positioning from Hughes et al. (2000). In this case the slit is offset from the center by $5''$, corresponding to a mimimum distance of 18.9 kpc distance at the redshift of the example QSO ($z = 0.171$). Thus the slit does not intercept the central regions of the host galaxy.

Even though the distance of the slit to the center of the QSO in the above studies is large, between $2''$ and $5''$, there remain nuclear contributions, scattered into the slit by the seeing. These nuclear residuals were in the abovementioned studies either not corrected or it was attempted to remove them by subtracting a scaled *on-nucleus* spectrum that was assumed to contain only nuclear light. As in the case of one-dimensional spatial host galaxy image separation, the amount of nuclear light to be subtracted is not a priori known. Assuming that the host spectra did not

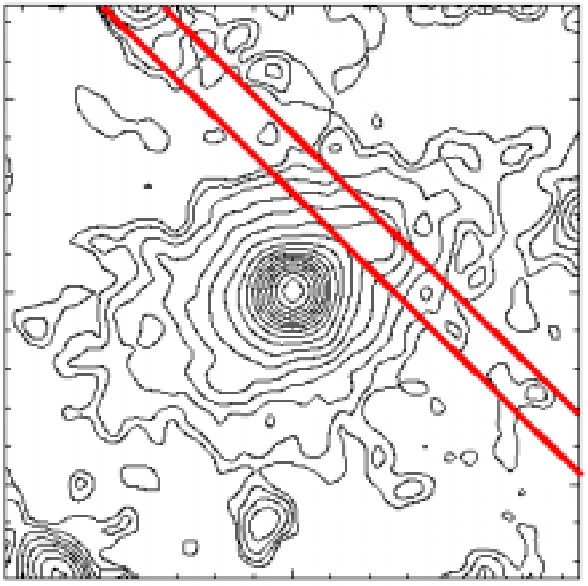

**Figure 3.1.** Slit positioning for off-nuclear spectroscopy. This example shows the object PHL909, reproduced from Hughes et al. (2000). The slit (red lines) is offset about $5''$ from the center, corresponding to 18.9 kpc linear distance. The side length of the frame is $30''$.

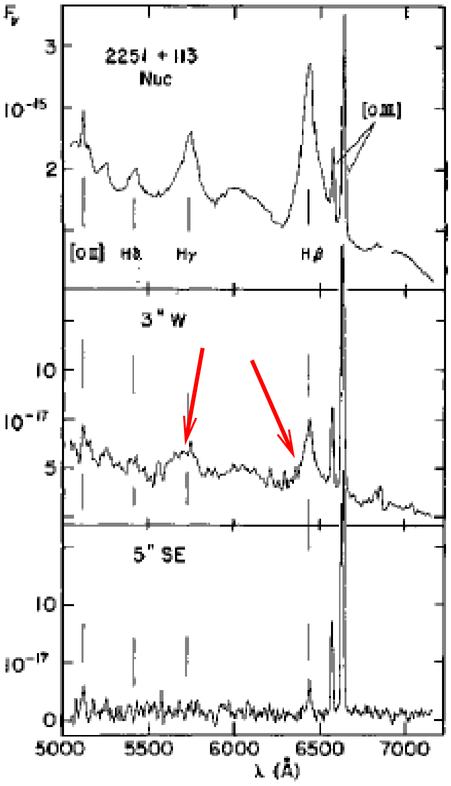

**Figure 3.2.** On-nuclear spectrum (top) and two off-nuclear spectra for an object, reproduced from Hutchings & Crampton (1990). The red arrow mark residual broad H$\alpha$ and H$\gamma$ emission after correction for the nuclear contribution.

contain any broad emission, increasing amounts of nuclear spectrum were subtracted, modified with an ad-hoc function of wavelength, until the broad lines were removed. Typically only H$\alpha$ or H$\beta$ could be taken as a measure. There are no published examples in the literature to demonstrate this process, thus in Figure 3.2 we only show a resulting host spectrum taken from Hutchings & Crampton (1990). The top spectrum shows an nuclear spectrum, the two other spectra are taken 3$''$ and 5$''$ off-nuclear and are the results after a correction for nuclear light. In the centre spectrum broad H$\beta$ and H$\gamma$ emission is visible, marked with the arrows. This is clearly residual nuclear light, even though a scaled nuclear spectrum has already been subtracted from the raw off-nuclear spectrum. This means that also some of the continuum contains residual nuclear flux.

This shows the two major problems of the off-nuclear approach: First, it is difficult to control the creation of artefacts in the resulting spectrum. With only few broad lines available, the scaling has limited precision, allowing for nuclear continuum residuals in the host spectrum. Subtraction is fairly subjective. Also the “nuclear” spectrum contains not only light from the nucleus, but also from the centre of the host. The state of ionisation and the stellar composition of the host can be very different in the centre and at the radius sampled, thus the fraction of host light in the supposed nuclear spectrum can bias the results.

Second, the host can only be sampled at large distances from the centre. A distance of 5$''$ to avoid most of the nuclear contribution translates at $z = 0.1$ to a radius of 12 kpc, far away from the nucleus. Surface brightness is low there and the physical interaction between stars, interstellar gas and the nucleus will be much smaller than close to the centre. Nuclear starburst, for example, would escape observations. Always a tradeoff has to be made between distance to the nucleus and the possible size of subtraction residuals due to the amplitude of the nuclear contribution.

In 1999 we initiated a pilot study for the investigation of QSO hosts with on- and off-nuclear spectroscopy for a complete sample of low redshift QSO hosts – the same sample for which we presented broad band data in the previous chapter. This data is the first for which an attempt was made to extract host galaxy information from *on-nucleus* spectra, thus the very centre of the QSO. The data was observed with the ESO 3.6m telescope and EFOSC (PI L. Wisotzki). With this data the two-dimensional decomposition of spectra described below was first developed.

In collaboration with F. Courbin (Liége) et al. we initiated a second study with improved data quality. This thorough study of QSO hosts aimed at describing the stellar components, gas content and gas and stellar dynamics in the host, not only at the outer limits of the host, but also of the very centre. For this task we were granted telescope time at the ESO VLT to observe high resolution *on-nucleus* spectra between 3600 and 9000 Å with the VLT for a total of 20 luminous QSOs (PI F. Courbin). Half of them having been observed so far.

The extraction of the host spectrum is made possible by two independent and new techniques to separate the host from nuclear light, making use of the so far unused spatial dimension of long-slit spectra. These methods allow to estimate the host SED directly from on-nuclear long slit spectra, without prior assumptions about the resulting host *spectrum*, and allow a spatially resolved investigation directly down to the centre.

The first method is the spatial deconvolution of the two-dimensional (2d) composite spectrum developed by Courbin et al. (2000). The other is the mentioned simultaneous spatial 2d-modelling of nucleus and host spectrum, developed as part of this thesis, and described in the following. Both methods are based on the same principles, using the spatial information contained in 2d spectra, yet the algorithmic approach is different and complementary. Courbin et al. are deconvolving, in the mathematical sense, the spectrum into a point source and an extended source, using a modified version of their algorithms for imaging deconvolution (Magain et al. 1998). Both our groups are working with the same VLT data set, but using their respective separation method and analysis techniques, allowing a detailed comparison of the techniques for identical input data. Details on the Courbin et al. method are also published together with first results of the study in Courbin et al. (2002a) and Courbin et al. (2002b).

In the following we will describe the general principles of our own technique, two-component spatial modelling of 2d spectra, and detailed implementation. In chapters 4 and 5 we present the application of this method to the two data samples. For both samples we present modelling results as well as an analysis of the resulting host galaxies' SEDs.

An astrophysical discussion of the results from the two samples as well as the multicolour sample, and a discussion of the capabilities and limits of the modelling technique are given in chapter 6.

## 3.1 2d decomposition of spectra

It is possible to disentangle host galaxies from the active nucleus. For spectroscopy this is more difficult than for imaging, because of the additional parameter wavelength $\lambda$, and less S/N at each $\lambda$ point than in broadband imaging. Our approach is to incorporate as much information into the separation process as possible. "Information" in this case means knowledge about the QSO, like morphological host galaxy parameters, the shape of the PSF or other information from

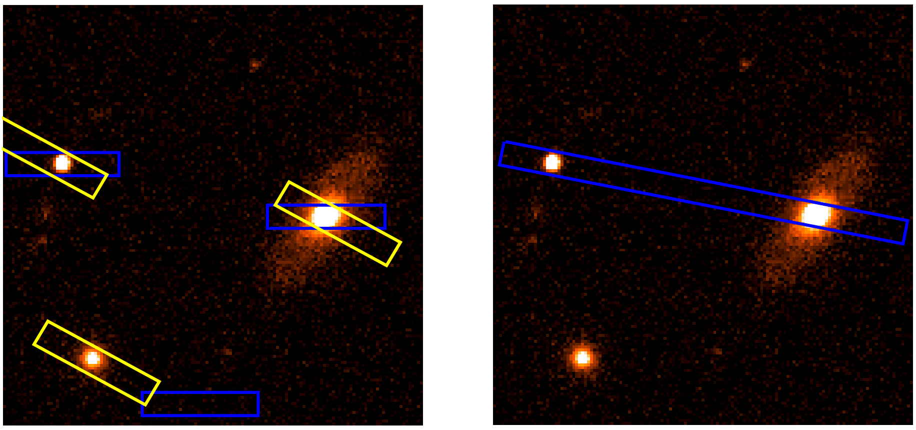

**Figure 3.3.** Schematic comparison of MOS with movable slitlets as used in the FORS1 MOS unit on the left and classical long slit spectroscopy on the right. The slitlets are parallel to each other and can individually be shifted along one axis and the whole setup can be rotated. The long slit on the right can be shifted and rotated in order to observe QSO and PSF star simultaneously, but only objects lying on one line can be observed.

imaging. We combine this with using all *spatial* information available in 2d longslit spectra. Up to now this information was never used for the extraction of host galaxy spectra.

### 3.1.1 Different instruments and data types

Optical and NIR spectral information can be obtained with a multitude of instruments and techniques. Beside classical long slit spectroscopy, currently several types of multi-object spectrographs become available. Units like the multi object spectroscopy unit (MOS) of FORS on the ESO VLT use movable half-masks, that form a number of slitlets of fixed length, but variable width and position in the spatial direction perpendicular to the slitlet (schematical setup in Fig. 3.3). In the case of FORS, this allows to take spectra of up to 19 positions in the FOV. In this process the individual slitlets cannot be rotated individually, only the whole setup. Another possibility is the use of exchangeable masks that are individually manufactured for each observation (e.g. available at the ESO VLT for the FORS2, VIMOS and NIRMOS instruments).

Slitlets and masks can in general spatially sample objects as a long slit can, but without the constraint that all objects have to be aligned, which usually is not the case for more than two objects of interest in a frame.

All of these spectroscopy techniques have in common that spectral information is combined with spatial information. For host galaxy applications the spatial information can be used to disentangle the spectral components of active nucleus and host galaxy. While the approach described below is initially designed for the use with long slit or slitlet spectra, it can be modified to be used with fibre MOS and IFS instruments, using the same principles.

## 3.2 General approach

The spatial component of long slit spectra is usually collapsed after reduction. The reason in applications to point sources for a non-zero slit *length* is photon collection area. While the slit width should be adjusted to match the atmospheric conditions to maximise spectral resolution, there is no such limit to slit length. For point sources as stars, spatial resolution is not achieved in optical or NIR wavelengths anyhow, thus apart from background estimation only a small part of the slit is used. For extended objects like galaxies, on the other hand, the spatial direction can be used to study different areas simultaneously, in our case a slice through the centre of the QSO, sampling along the whole diameter of the galaxy. Thus instead of collapsing the spatial dimension after data reduction, we use the 2d-frames with dispersion and spatial direction during the complete process of separation.

Our general approach to separate active nucleus and host galaxy is very similar to the imaging case described in the previous chapter. For each wavelength element $\lambda$ (a row of the 2d spectrum, if dispersion is running vertically, see Fig. 3.4), the spatial 1d surface brightness distribution of the QSO consist of a superposition of point source like nucleus and extended host. The shape of the point source is defined by the shape of the PSF at the position of the QSO on the chip at the wavelength in question and the time of observation.

In this approach we again build *spatial* models for the light distribution of both the nucleus and the host, after estimating the shape of the PSF and asuming a certain morphological shape for the host, i.e. exponential disk (Freeman 1970) or de Vaucouleurs spheroidal (de Vaucouleurs

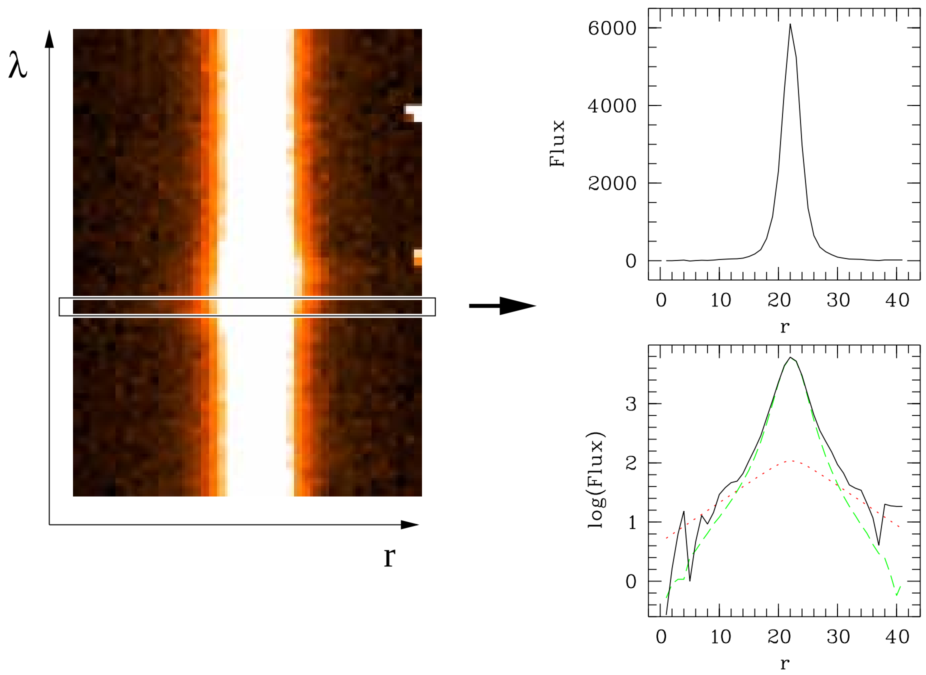

**Figure 3.4.** Schematic view of modelling: 2d-spectrum (left) with spatial direction horizontally, and dispersion direction vertically. For each row the composite spatial surface brightness distribution is modelled (top right). Bottom right shows the logarithm of the total surface brightness distribution from above (solid, black) with best fitting models of nucleus (dashed, green) and host (dotted, red).

1948; de Vaucouleurs & Capaccioli 1979). A fitting procedure determines the best set of parameters for these models. Because of the drastically reduced S/N per wavelength element compared to the imaging case, a simultaneous fit of all parameters (e.g. PSF centre, shape and flux, host centre, scale length and flux) is not possible. Our approach thus exploits knowledge about external information to constrain as many parameters as possible, thus reduce the number of free parameters to successively determines best estimates. As some of these parameters are strongly correlated in adjacent wavelength points, thus vary slowly with $\lambda$, we apply a "smoothing" fit for the variation of a parameter with $\lambda$, between successive fitting steps, to greatly reduce noise in the parameters determined After a parameter has been fitted and smoothed, it is fixed in the following modelling steps until in the final step only the central surface brightnesses of nucleus and host are determined. In this way the fitting routine makes optimal use of the signal, the introduction of additional noise is minimised and the fits can succeed.

The 2d decomposition consists of the following steps, which we will now describe in detail:

- Spatial definition of the PSF with the fit of an analytical funtion to each row of a PSF star. This includes centering, determination of a Moffat shape parameter $\beta$ and width $\alpha$ for all $\lambda$. $\longrightarrow \mathrm{PSF}(x,\lambda)$
- Creation of an analytical look-up-table correction, to account for intrinsic differences in the shapes of PSF model and the "true" PSF, using the residual of the PSF modelling. $\longrightarrow \mathrm{LUT}(x,\lambda)$
- Simultaneous spatial modelling of nucleus, represented by the determined PSF, and the host, represented by a exponential disk or de Vaucouleurs spheroidal.
  - First the center is determined, and its variation with $\lambda$ fitted. $\longrightarrow x_0(\lambda)$
  - Morphological type and width of the host are determined externally from broad band images. $\longrightarrow$ type and $r_{1/2}$
  - In a final step the fluxes of nuclear and host model are fitted with all other parameters fixed.
- If possible, emission lines are modelled separately to avoid numerical flux transfer from nucleus to host model.

## 3.3 PSF definition

The first step of the modelling is estimating the PSF. With current instruments it is not possible to satisfy all three requirements: to know the PSF at the position of the QSO on the chip, at the wavelength in question, and at the time of observation. At least one constraint has to be dropped. Because of different atmospheric conditions at different wavelengths, the wavelength condition is crucial. Also the magnitude of temporal PSF variations is very large, while the variation of the PSF in the FOV is comparably small. Thus the best results will be reached when defining the PSF at the same time and wavelength regime as the QSO observation. This is realised by simultaneously observing a PSF star with the QSO, a requirement that can be realised with longslit, MOS, or in the future potentially integral field spectroscopy.

We describe the PSF as a combination of an analytical function and an empirical correction. The PSF modelling process schematically consists of:

- centering
- global functional form determination
- width determination
- creation of an empirical look-up-table correction

### 3.3.1 Parametric description

The PSF is characterised by using a parametrised functional form, fitted for each $\lambda$. We chose a Moffat profile (Moffat 1969)

$$\mathrm{PSF}(x) = \frac{\beta-1}{\pi\alpha'^2}\left[1+\left(\frac{x-x_0}{\alpha'}\right)^2\right]^{-\beta}.$$

$x_0$ is the centre of the function, the parameter $\beta$ describes the "winginess" of the profile, the relation of flux contained in wings compared to the nucleus. $\alpha'$ is a measure of the width of the Moffat. We use a modified description with $\alpha = \alpha'\sqrt{2^{1/\beta}-1}$

$$\mathrm{PSF}(x) = \frac{\beta-1}{\pi\alpha^2(2^{1/\beta}-1)}\left[1+\left(\frac{x-x_0}{\alpha}\right)^2(2^{1/\beta}-1)\right]^{-\beta}$$

that makes $\mathrm{FWHM} = 2\alpha$.

For $\beta \rightarrow \infty$ the Moffat function reduces to a Gaussian. Atmospheric turbulence theory predicts a shape for the seeing that can be fitted with $\beta = 4.765$ (Saglia et al. 1993; Trujillo et al. 2001), although real data show larger wings (lower $\beta$) due to telescope imperfections. Tests for our image modelling showed a good fit of the shape to the data in most cases. We find a range of $1.8 < \beta < 3.5$ for the spectroscopic data. The Moffat function is more flexible than a simple Gaussian, yet with two parameters describing the shape in a simple enough form to receive good constraints on the parameters.

### 3.3.2 Centroid $x_0$

The centroid of an observed object on the detector chip will vary with wavelength, when the object is not observed in the paralactic angle. Because of the constraints on rotator angle imposed by the orientation of the long slit or slitlet unit this is generally not possible. Thus first of all the centroid is determined for each $\lambda$. For this task a Moffat function is fitted at each wavelength, though any symmetric function showing a maximum in the centre could be used (see below). We use a Moffat function with $\beta$ and width $\alpha$ set to initial values, and allow the centroid $x_0$ and the central flux as free parameters.

Finding the best centroid is done in two iterations. First we use a numerical Levenberg-Marquard least square algorithm (Press et al. 1995, p. 683) with no subsampling of the initial pixels, to get a robust initial estimate for $x_0$. After repeating this for all $\lambda$ we use the fact that $x_0$ is varying only very slowly with wavelength. Thus changes between adjacent rows will be of the order of 1/100th of a pixel in a high resolution 2d spectrum. We use this fact by fitting a polynomial of typical degree 3–7 to the raw $x_0(\lambda)$ to strongly reduce the noise (Fig. 3.5).

The second iteration uses these centroids as input for a downhill simplex algorithm (Press et al. 1995, p. 408) that again determines a centroid value. As for the imaging case in section 2.3.2 we now use a division into a subpixel grid to compute the host model and perform the discrete convolution. This increases the precision in the models and thus the precision in the fit. The number of subpixels is in general only limited by computing power. For the strong gradients in case of a narrow PSF, it is advisable to use at least 50 subpixels. For different numbers of subpixels above 50–100 the numerical differences become negligible.

After this step again a polynomial is fitted for $x_0(\lambda)$, using the Levenberg-Marquard fit result as a zero-line for clipping outliers. This relation is now being used as the best estimate for $x_0(\lambda)$. In the next steps $x_0(\lambda)$ is fixed to this relation and is no longer a free parameter. In this way centering precisions of the order of 1/100 of a pixel are possible.

As mentioned above, for the inital centering it is not important to know the shape parameter $\beta$ and the width $\alpha$ precisely. As the PSF can be assumed to be symmetrical, the centering will yield good results, as soon as the initial estimate for the width will be of the same order as the real, best estimate value, to be determined later (see Fig. 3.6). For $\beta$ an initial value of 2.0–2.5 is usually appropriate. The initial guesses for width and central flux as well as the degree of the smoothing polynomials have to be chosen individually for each spectrum.

It has to be strained that good initial guesses are crucial for a successful fit. Local minima are difficult to escape from in the minimising process, thus starting close to the “real” value is very advantageous.

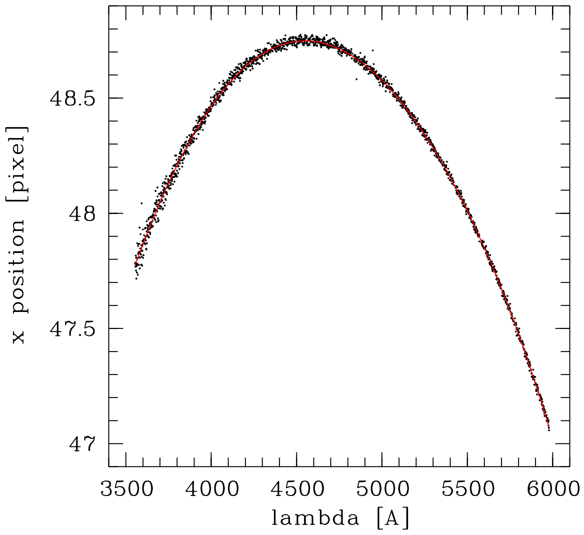

**Figure 3.5.** Example of PSF star centering: Plotted are the individually determined centres for each $\lambda$ (dots). The solid line is a polynomial of degree 7 fitted to the points. This $x_0(\lambda)$ is used as the best estimate for the centre in the following modelling steps.

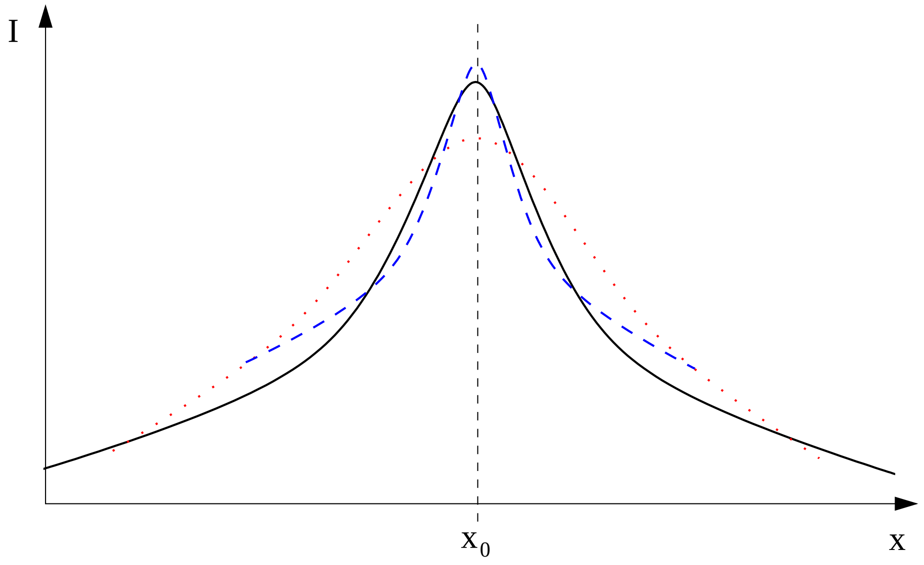

**Figure 3.6.** The functions used to find the least $\chi^2$ for centering do not need to have exactly the same distribution as the data (solid black). Both narrower and wider functions can estimate the centre very precisely, as long as both data and functions are symmetric to the centre. Only the more the shapes deviate from the distribution of the data, the less good the overall fit becomes and the smaller the relative differences between good and bad fits. Thus the influence of pixels which deviate from the symmetry, e.g. unmasked cosmics, increases.

### 3.3.3 Shape parameter $\beta$

The next step after centering is to estimate a global value for the parameter $\beta$ of the Moffat function. Within limits the general shape of the PSF, i.e. the “winginess” of the Moffat function should not change with wavelength. In any case the PSF shape is not perfectly described with a simple two-parameter function, thus residuals are to be expected (they are attempted to be removed with an analytical look-up-table, described later in section 3.4.2). Tests show that $\alpha$ and $\beta$ are directly correlated when fitting a given shape (Fig. 3.8), thus a $\beta$ changing slightly with $\lambda$ can be compensated by a different width $\alpha$, without dramatically worsening the quality of the fit.

With fixed $x_0(\lambda)$ we compute global $\chi^2$-values, i.e. cumulated for all $\lambda$, for different values of $\beta$, with $\alpha$ and central flux as free parameters in a downhill simplex fit. A bracketing algorithm is used to find the global $\beta$ with the lowest resulting $\chi^2$ (Fig. 3.7) and subsequently $\beta$ is held fixed. If we assume that the PSF were constant over the FOV, $\beta$ is then valid for PSF *and* QSO as it describes the functional form of any point source at the time of observation.

However $\beta$ might change for different objects, i.e. time of observation, and also different grisms. We did not find a systematic dependency on central grism wavelength, thus we conclude that the changing ambient atmospheric conditions dominate the value of $\beta$ if certain conditions are met. We discuss these conditions and the influence of the PSF star brightness below in 3.4.1.

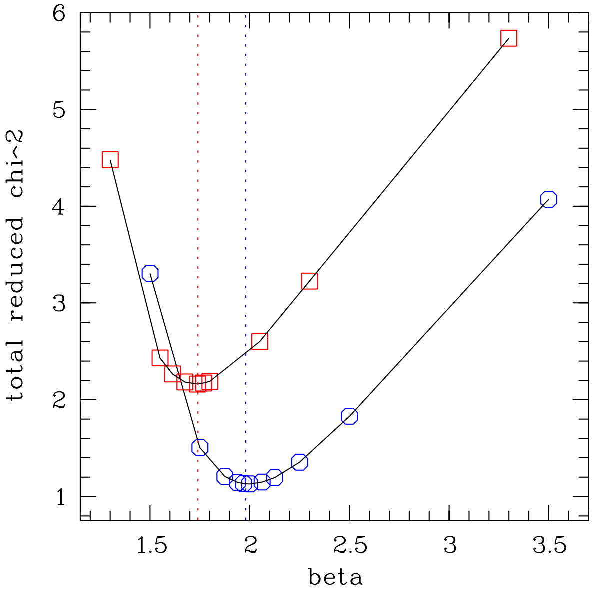

**Figure 3.7.** Bracketing search for the shape parameter $\beta$ for PSF stars. Shown are the $\beta$ values and total reduced $\chi^2$ values for the PSF star spectrum observed for HE 0956–0720 with the 600I (squares) and 600B (circles) grism of VLT FORS1. The vertical lines mark the best fitting values of $\beta$ corresponding to the lowest $\chi^2$.

## 3.3.4 Width $\alpha$

As for the centering, the width $\alpha(\lambda)$ is determined in two steps. Centroids $x_0(\lambda)$ and $\beta$ are now fixed to their best estimates, and only $\alpha$ and central flux remain as free parameters. Using global initial guesses, first a robust Levenberg-Marquard fit without subsampling is used for each $\lambda$, followed by a polynomial smoothing fit. Then this relation is input as an initial guess for a fully subsampled downhill simplex fit, again followed by a polynomial fit over $\lambda$ with clipping of outliers. The width is changing faster with $\lambda$ than the centroids (see Fig. 3.8), over the whole spectroscopic range changes of 30% were observed for some objects. The change seems to be mainly due to a change in shape due to the different atmospheric refraction, depending on wavelength.

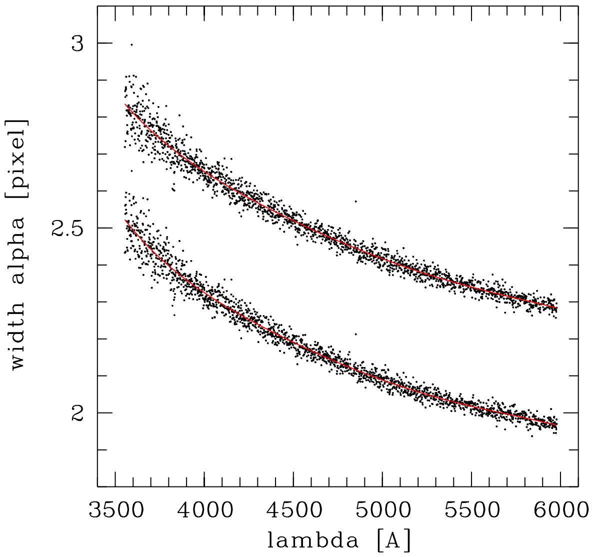

**Figure 3.8.** Example of fitting the width $\alpha$ for a PSF star: Dots are again the individually determined $\alpha$ values for each $\lambda$. The solid line is a polynomial fit. This $\alpha(\lambda)$ is used as the best estimate for the width of the PSF in the QSO modelling steps. As an illustration for the correlation of $\alpha$ and $\beta$ the fits for two values of $\beta$ are given. Top: $\beta = 3.5$, bottom: $\beta = 1.75$. There is a systematic offset of $\Delta\alpha \sim 0.3$, changing slowly with $\lambda$.

## 3.4 PSF variations

Now all parameters $\beta$, $x_0(\lambda)$, and $\alpha(\lambda)$ are determined. With this stepwise approach the effects of noise and numerical artifacts are minimised. However, we initially requested as a third requirement to estimate the PSF at the position of the QSO in the FOV, not at the position of the PSF star. In imaging, we notice variations of the PSF parameter over the FOV, so how strong is the effect in 2d spectroscopy?

First of all the problem is simpler compared to imaging: we only have one, not two spatial coordinates. Thus the variation of ellipticity, position angle and width of the PSF is effectively reduced to a variation of the width. Any change in the other spatial coordinate has only an effect across the width of the slit and thus a (negligible) influence on the spectral coordinate, and none on the spatial.

In the usual case that very few PSF stars are observed simultaneously with the QSO, in many cases only a single one, it is not possible to model PSF shape variations over the field. For crowded fields this is a theoretical posibility. The magnitude of the variation will depend in the instrument and its optical layout. In section 4.1.1 we will comment on focal reducer type instruments, and their general PSF instability.

### 3.4.1 Sensitivity to $\beta$ and S/N effects

Two further sources for errors in the PSF shape are the sensitivity to the exact value of $\beta$ and dependence on the brightness or S/N of the PSF star. Both effects are connected. With decreasing S/N the wings of the PSF will more and more vanish in noise, thus the wings will have less weight in the fit. We already noted the correlation of width $\alpha$ and shape parameter $\beta$ (Fig. 3.8). When determinining the shape of the PSF star for decreasing S/N, $\beta$ will increase and so will $\alpha$, leading to a similar just less wingy shape. So there are two separate effects to be investigated: Variations in shape due to a different $\alpha$–$\beta$ combination, e.g. due to different S/N, and variations in shape for a fixed $\beta$ and different S/N. The first appears when PSF star and QSO nucleus differ strongly in brightness. The second is valid for every PSF star, because a global $\beta$ is determined, but the flux and thus S/N varies with $\lambda$.

An analysis of the residuals after removal of the PSF model shows the magnitude of the effects: If for a given PSF star $\beta$ is varied by $1.75 \leq \beta \leq 3.5$, which represents the complete range of $\beta$ values found for the *whole sample* observed with VLT FORS discussed below in section 5, the differences in the residuals can be significant (Fig. 3.9). For any single object the possible range in $\beta$ can be established much better. For a range of $\Delta\beta < 0.1$ the difference is of the order of one $e^-$/pixel, thus for a “good” bright PSF star small compared to the total PSF star flux.

We also tested the change in $\alpha$ for different S/N and a fixed $\beta$, which simulates different brightness of PSF star and nucleus. In a frame where two PSF stars of different brightness were available, we fixed $\beta$ and determined the width $\alpha$ for both stars. As shown in left diagram of Fig. 3.10 even though the difference in brighness is a factor of three, the widths are virtually identical down to the regime of a few hundred counts (reached around $\lambda = 4200$Å, blue end of the FORS 600B grism). Here differences appear between the two smoothed curves due to noise in the fainter star and an asymmetric scattering of the $\alpha(\lambda)$ values. Since we see no significant difference in shape down to this level, we can expect the shape to be well defined for all $\lambda$ with

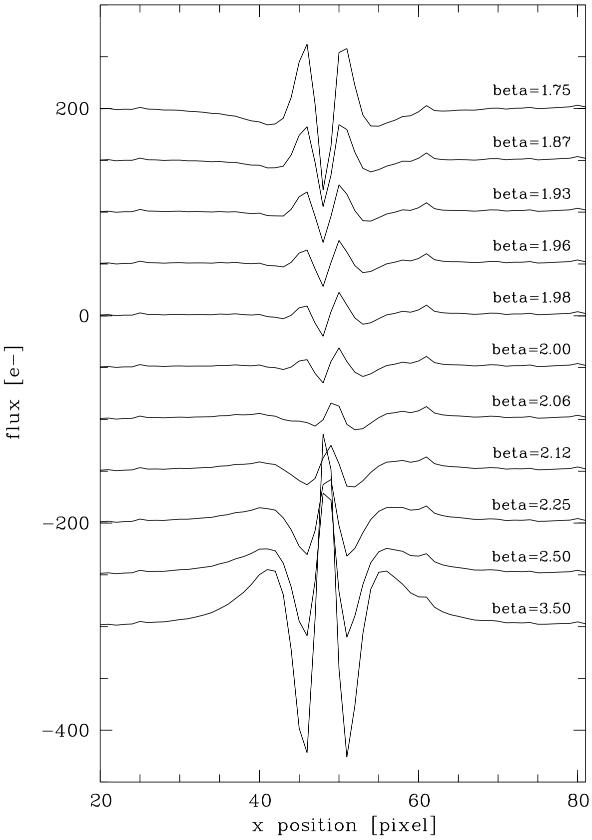

**Figure 3.9.** Dependence of the PSF residual on the shape parameter $\beta$. Plotted is the spatial residual averaged over all wavelengths for the PSF star of HE 0956–0720 (grism 600B) for different values of $\beta$. The curves are offset for better visibility. The magnitude if the residual has to be compared to a central flux of the PSF star of in this case 4600 $e^-$, or 180 times more than the structures in the best fit ($\beta = 1.98$). Size and structure of the residual vary from object to object.

substantial flux. Quantified as a S/N, one should be on the safe side with a S/N in the central pixel of $> 20$.

This agrees well with results for simulated PSF stars of different S/N. We created a noiseless model PSF star with known width, added noise for different amounts of sky background and fitted the width with the technique described above. We used 0.15, 1.0, 7.1 and 71.0 times the sky background noise observed for a typical one of our objects. The width does change systematically, but a very good reconstruction of the width better than 5% can be found for S/N of the central pixel of better than 10–20 (right side of Fig. 3.10).

In the modelling of the "EFOSC" sample in section 4.1.1, further evidence is found that stars below a minimum S/N will create artificially large $\beta$ values, largely independent of ambient conditions.

### 3.4.2 Look-up-table correction

Besides variation of the PSF with S/N and position over the FOV, there is also a systematic mismatch between shape of the PSF star and the describing Moffat function, due to the simplicity of a two-parameter model. The difference between PSF and model is the same for PSF star and QSO, assuming a constant PSF. We attempt to correct some of this mismatch by constructing an empirical look-up-table (LUT) correction, consisting of the modified residual of the PSF modelling process.

The residual smoothed using a moving average along the dispersion direction, in order to

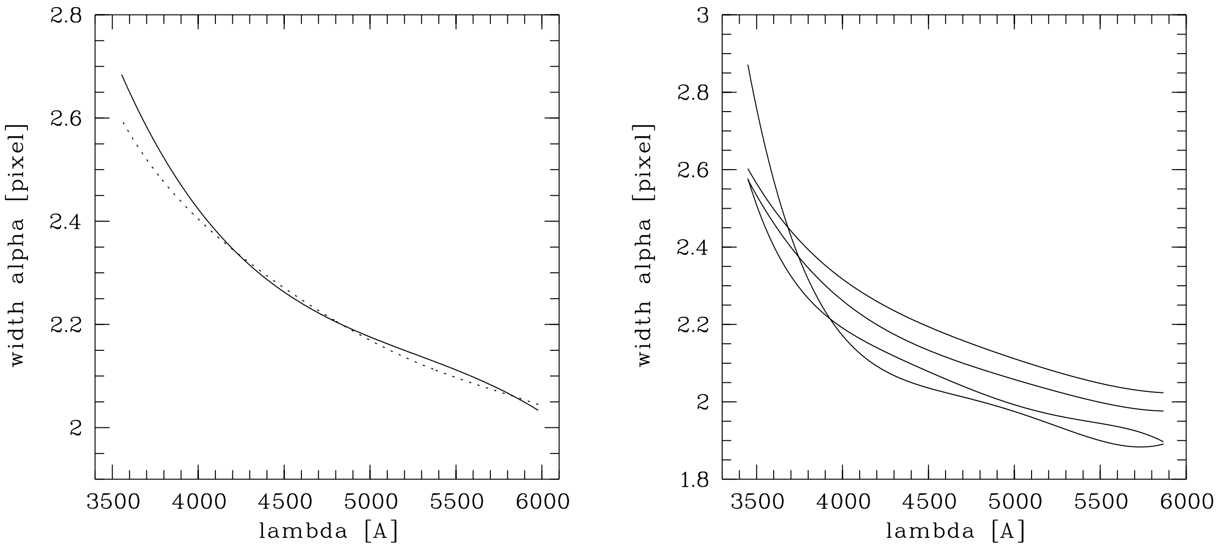

**Figure 3.10.** Dependence of the determined width $\alpha$ on the S/N of the PSF star for given $\beta$. Left: Comparison of two real PSF stars of different flux. The PSF star yielding the solid line is three times brighter than the star for the dashed line. For $\lambda > 4200$ Å the S/N of in the central pixel of the fainter star is $>20$. Right: Simulated PSF stars with different sky background. Curves from top to bottom have increasing background (0.15, 1.0, 7.1 and 71.0 times the sky background actually observed for an example object).

reduce noise. This can be done because we assume the residuals forming the LUT to be strongly correlated in adjacent $\lambda$. In the same process it is normalised with the flux of the PSF star, and rebinned to match centre $x_0$ and $\lambda$ of the QSO.

Tests show that LUTs from different PSF stars vary in their details, but show a generally identical shape. The resulting LUT applies corrections on the order of a few percent, in the best cases less than 1%. Thus the second-order errors in LUT difference are very small. These second order errors, however, scale with the S/N of the PSF star the LUT is taken from. If the QSO is brighter than the star by a certain factor, the second order errors become magnified to an extent that the application of a LUT does not yield better results in the QSO modelling. In this case the LUT can and should be set to zero for the $\lambda$ range in question.

In total we have a smoothed empirical correction function LUT$(x,\lambda)$ to complement the analytical PSF description PSF$(x,\lambda)$.

## 3.5 Modelling QSO and host galaxy

Modelling the QSO follows the same principles used for the PSF star. Parameters are estimated, their variation with $\lambda$ fitted, and this relation fixed in subsequent steps, reducing the number of free parameters in each step as much as possible.

The centering is directly identical to the PSF modelling, using a single Moffat function. In all following steps two components are modelled: a PSF like component representing the nucleus and an extended component for the host. The S/N per wavelength element is generally so low that simultaneously determining parameters for a third component, e.g. gas disk or separate bulge, is not possible (but we will discuss this possibility for the treatment of emission lines in section 3.5.3). For the host we assume a one-dimensional exponential disk or de Vaucouleurs spheroidal profile, as in the imaging case (see section 2.3). These models also have two parameters, central flux $I_0$ and half light radius $r_{1/2}$.

The creation of the spatial models is again done on a subpixel grid. For each point on this grid the value of the PSF from the analytical Moffat function plus the empirical LUT is computed. For the host the model is computed on the grid as the discrete convolution of the analytical host model with the PSF. After computation, the grid points are binned back onto the pixel grid of the data frame. This convolution is the main reason for using a downhill simplex algorithm. As it has to be done numerically, no derivatives are available.

### 3.5.1 Scale length of the host galaxy

In the step after centering the half light radius and the galaxy type (disk/spheroidal) are determined. This can either be done via fitting, with $x_0(\lambda)$ fixed and $I_0$, $r_{1/2}$ and central flux of the nucleus as free parameters. But due to the low S/N this is a source for failure in many cases. The host can be outshined by the nucleus by a factor of 100 or more. In spectroscopy by sampling just along a slice through the QSO which contains most of the nuclear but only a small fraction of the host light, the total nucleus-to-host flux ratio is boosted. We use external information on host galaxy type and $r_{1/2}$ to overcome this problem, by obtaining images for all objects and determining their morphological parameters as described in chapter 2 (the detailed morphological analysis for the sample containing the objects observed with VLT (sec. 5) is in preparation; Wisotzki, Kuhlbrodt & Jahnke, 2002).

The price for a deep 2d image of a QSO host to determine morphological host parameters is very small compared to the price of the spectrum itself. Thus for little extra observation time – for the redshift range accessible to this spectral modelling, $z < 0.5$, one can use 2m-class telescopes, or invest 30–60 s of 8m-class time – the results are greatly enhanced, if not only made possible in many cases.

Thus the functional form and half light radius are set from external sources. As noted in section 2.5.1, the scale lengths of galaxies can be variable with $\lambda$. Because usually no multiband imaging data is available we have to assume it to be constant. $r_{1/2}$ and $I_0$ are strongly correlated parameters. Even though their individual values are not well constrained for low S/N, their product in the form of the total flux can be estimated with a much higher precision (Abraham et al. 1992; Taylor et al. 1996). Thus the quality of the fit and total host flux will not strongly depend on the exact value of $r_{1/2}$.

If $r_{1/2}$ should after all be taken from the spectrum, one way to increase the S/N is to coadd parts or all of the spectral dimension, with care taken about the varying centroid, and all emission lines omitted, and model the resulting 1d frame. In total the S/N of the host is greatly increased. Depending on S/N, even a varying $r_{1/2}$ could be determined by splitting the spectrum into two or more parts. This process can be done iteratively: Modelling is first done with an initial guess. The resulting host spectrum is used to extract a better spatial model to be used in the second iteration etc.

### 3.5.2 Final step: the host spectrum uncovered

In the final step just two parameters are free, the central fluxes of host and nucleus, with all other parameters fixed. The resulting model of the host is not used for further analysis, only the 2d nuclear model image is used as the best estimate for the nuclear component and subtracted from the initial 2d QSO spectrum. The result is a residual host galaxy frame on one hand including all PSF removal imperfections, but on the other hand containing all deviations from symmetry like rotationally shifted lines that are not modelled by the symmetric model, and differences in actual morphology.

This frame can now be subjected to standard 2d spectra calibration and analysis techniques. The 1d spectrum is extracted using the Horne optimal extraction algorithm (Horne 1986).

### 3.5.3 Emission line treatment

Refinements have to be applied in the treatment of emission lines. While the broad emission, narrow emission and continuum of the QSO have an identical spatial shape, this is not the case for the host. The spatial distribution of the interstellar gas, responsible for narrow emission lines visible in the host, does not need to be identical to the distribution of stellar emission. This is particularly obvious in elliptical galaxies, where rotating gas disks can be embedded in the spheroidal distribution of stars.

This has the consequence that at wavelengths with a substantial contribution of gas emission lines, the two-component model of nucleus plus host is a wrong assumption. E.g. in the case of an elliptical galaxy with a gas disk, the gas emission will spatially be more extended and less peaked than the stellar emission. To account for the extra flux at larger radii the numerical algorithm will assign extra flux to the more extended of the two components, i.e. the host. This boosted host model will match the gas emission well in at the radii in question, but will overestimate it in the center. This will be compensated by the nuclear model, that as a result will be underestimated.

Three solutions can be used, for different situations:

- Single sided modelling: In the case of a rotating gas disk, both sides of the line are rotationally shifted away from the nominal position, one side blueward, the other redward. In the case of a narrow line and a rotation curve that does not strongly decrease with radius, e.g. the case for gas disks in elliptical galaxies, only parts or even none of the single sided components overlap in wavelength (marked "G" in Fig. 3.11).

  In the non-overlap wavelength elements (marked "S"in the same figure) it is possible to model just one side of the 2d spectrum. With fixed PSF, $x_0$ and $r_{1/2}$, the nuclear model is determined just for the side free of line and only continuum emission. This nuclear model is then valid also for the other, line emission "contaminated" side of the spectrum. In this way an emission line with non-overlapping sides can be split up into two parts and the single sided nuclear models can be merged with the full models for all other $\lambda$.

- If the two sides of the line do have some overlap, the underestimate for the nucleus might be seen in the resulting spectrum. It could be manifested as a absorption like feature where none is expected, or as a disturbance in the spectrum. In this case the oversubtraction in

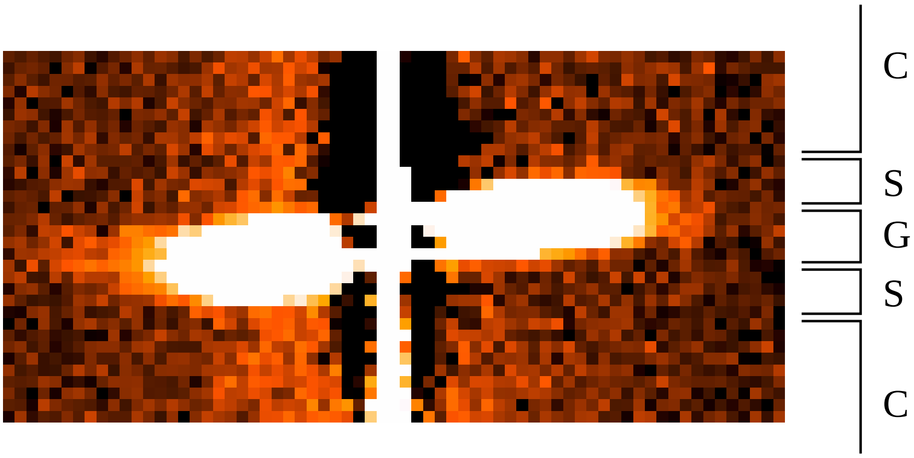

**Figure 3.11.** Emission line in a resulting host spectrum, dispersion vertical, spatial coordinate horizontal. The two sides are rotationally shifted in wavelength due to rotation of the gas disk. Three fundamentally different regions can be identified: Pure continuum emission ("C"), single sided emission line ("S") and double sided gas emission ("G"). For all three regions different modelling conditions apply.

the nucleus model can be estimated and a better nuclear contribution constructed. This however is difficult to judge.

- A third approach, not yet implemented, is the use of a third model component in the emission line. Here the S/N is large and the stellar continuum can be estimated from adjacent spectral intervals (marked "C" in Fig. 3.11). Even with nuclear contamination a good scale length for the gas disk can be obtained from the radial shape, when excluding the central spatial part of the line. The stellar contribution would enter only as a constant component. With a set gas component scale length, again only two free parameters, $I_0$ of nucleus and gas, would be present.

### 3.5.4 Continuum flux transfer

If two spatially different components exist in the object under investigation, and the S/N is sufficiently high, this modelling procedure will find those components. A signal of the host might be found only in the brightest parts of the spectrum, e.g. a narrow gas emission line, while the stellar continuum is outshone by the luminous nucleus. However, if the variation of the PSF is large and the host compact, errors in the PSF will be compensated by the routines with changes in the host model flux. As a result, more or less strong flux transfer can occur from the nucleus to the host or vice versa. This can go as far as negative fluxes for a part or all of the resulting host spectrum. In this case the errors in the PSF determination are larger than the positive signal of the host. When this happens, one can still extract some information from the resulting two component spectra, because the spectrum was still separated into a wider and a more compact component. A solution is to add increasing fractions of the nuclear component, possibly of wavelength dependent size, to compensate for the modelling error, and make the host flux positive again. After such a procedure, it will not be possible to extract detailed host continuum information, but host line ratios, rotation curves etc. can still be extracted to some extent.

### 3.5.5 Quality of fit diagnostics

Similar as for the PSF star modelling, the models used for the galaxy can never describe all of the data. Spiral arms, bulges in disk galaxies or asymmetries are not accounted for. Thus even with a LUT correction for the nuclear component, there can be substantial residuals of data minus best nucleus and host model. This is no particular problem as the modelling is only used to estimate the *nuclear* component. As long as the fit is “good”, the resulting *model* of the host is irrelevant. To asses the “goodness” and quality of a modelling run, six fundamentally different diagnostic principles are available:

- Boundary conditions: Some general boundary conditions from basic physical principles apply, that, when not hardwired into the modelling routine, can be used to check results. The most important are
  - host flux should be zero or positive for all $\lambda$, within the limits of noise,
  - forbidden lines cannot appear in absorption.
- The residuals of the fit can be used to detect misestimates of the host’s scale length. When comparing the residuals it is possible to discriminate between different scale length values. Too compact models show residual flux in the wings.
- The nuclear broad emission lines should not appear as strong mirrored absorption lines in the resulting host flux. Broadened absorption lines can occur in galaxy spectra, but not of a width of several 1000 km/s as the permitted nuclear emission lines.
- Broad band colours existing from imaging studies must be reconstructable within the errors of calibration.
- If more than one PSF star of suitable S/N exists, the results from modelling with both stars can be compared.
- Finally, if several images exist for the same object, taken with different grisms, the fit results in overlapping spectral regions can be compared agains each other.

It has to be kept in mind at all times that every algorithm, also the one described, is limited by S/N. It can not extract information that simply is not there.

# 4 Spectroscopic decomposition: The “EFOSC” sample

The first of two samples modelled with the spatial separation for QSO spectra is a subsample of the objects investigated with broad band imaging (chap. 2). Through the rest of this work we will refer to this sample as the “EFOSC sample” from the instrument used for observations. In terms of S/N, spatial & spectral resolution and quality, the “VLT sample” described in the next chapter is superior to the EFOSC sample. Apart from the astrophysical analysis this sample is used to crosscheck results from broadband imaging, vice versa the broadband results are used to judge the results of the modelling technique.

## 4.1 Sample and data

The EFOSC sample is comprised of eight objects from the multicolour sample investigated in chapter 2. In Table 4.1 the objects are listed together with redshift, apparent visual magnitude, and integration time. Data exists for the majority of the multicolour sample, but in some cases the PSF stars available in the frame were too faint for analysis, in other cases the spectrographic slit was set off-nucleus. Incorporating spatial modelling for off-nuclear spectra with similar techniques is planned for the future, but is not yet available. These objects have been left out, eight remain. Observation were carried out in february 1999 with EFOSC at the ESO 3.6m telescope, using a 2k×2k chip, and the grism#6, B300b. A 2×2 on-chip binning was used to increase S/N, with a resulting pixel scale of $0.314''$ or $\sim$4 Å respectively, the spectral resolution was about 250. The slit size was $2''$.

The total integration times were between 1200 and 4800 s, for some objects split up into up to four exposures. The slit angle was set so that a bright accompanying PSF star could be observed simultaneously with the QSO in the longslit. The PSF star was chosen to be close to the object, bright, but not too bright to reach the non-linear regime of the detector or even saturate. The airmass for all observations was at or below 1.1.

**Table 4.1.** Objects in the EFOSC sample. Listed are redshift $z$, apparent $V$ magnitude, morphological type of the host ((E)lliptical or (D)isk), scale length $r_{1/2}$ used in modelling, and integration time of the spectra. For a note on the two entries of HE 1201–2409 see sec. 4.1.2.

| Object | $z$ | $V$ | Type | $r_{1/2}$ [$''$] | Int. time [s] |
|---|---|---|---|---|---|
| HE 0952–1552 | 0.108 | 15.8 | D | 2.55 | 1800 |
| HE 1029–1401 | 0.085 | 13.7 | E | 1.95 | 4800 |
| HE 1201–2409 | 0.137 | 16.3 | E | 0.47 | 1800 |
| | | | D | 3.1 | |
| HE 1239–2426 | 0.082 | 15.6 | D | 4.4 | 1800 |
| HE 1310–1051 | 0.034 | 14.9 | D | 3.7 | 1800 |
| HE 1315–1028 | 0.098 | 16.8 | D | 3.3 | 1800 |
| HE 1335–0847 | 0.080 | 16.3 | E | 2.45 | 1200 |
| HE 1416–1256 | 0.129 | 16.4 | E | 2.1 | 2700 |

The data were reduced in Hamburg by M. Raue using MIDAS software. Cosmics were masked in variance frames. Flux and wavelength calibration were done using data provided by L. Wisotzki that provided relative flux calibration. A correction for galactic extinction was applied using values from Schlegel et al. (1998).

### 4.1.1 PSF

For modelling the PSF star was used, observed simultaneously with the QSO. EFOSC is a focal reducer type instrument as DFOSC and ALFOSC used for observation of the broad band data and as FORS used for the spectroscopy of the second sample. In section 2.3 we mentioned briefly the problems of focal reducer type instruments and their complex optical layout, with respect to image distortions. The details for the imaging case have been investigated (Kuhlbrodt, Wisotzki, & Jahnke 2001, and Kuhlbrodt, Wisotzki & Jahnke, 2002, in prep.), but the same problem applies to the spectroscopy case.

The multiple optical elements in the light path will produce a shape of the PSF depending on position in the FOV. Width, general shape and orientation can change, depending on focus, telescope orientation, temperature, etc., in a non-symmetric, non-reproducable manner. Generally the difference in shape between two points in the FOV will increase with increasing distance. Therefore it is advisable to observe PSF stars as close as possible to the QSO. However, as noted in section 3.4.1, we require a minimum brightness for the stars, to reduce the uncertainty in PSF shape determination. Thus for most host galaxy studies there is only a small choice of stars to be used. To model the change of spatial shape in spectroscopy over the FOV would only be possible with a MOS unit with a large number ($> 20$) of spatially resolved stars to be observed at the same time with the QSO. Since the distortions show geometrically very complex patterns this remains a theoretical possibility. Generally instruments should be preferred that show a stable shape of the PSF. This can even be of higher priority than light collection power. Too strong variations can not be compensated by higher S/N.

For this sample it was attempted to find a good compromise between brightness of the star and the distance to the QSO. The largest distance between QSO and PSF star was $126''$, corresponding to 2/5 of the FOV, but for most objects the distance was much smaller, on average below $60''$. The brightness of the stars varied strongly. In the diagnostic diagrams for the modelling given in appendix C (third diagram from top) one can see that the maximal central flux of the PSF star used ranges from 500 $e^-$ (HE 1335–0847) to 55000 $e^-$ (HE 1310–1051). The former is on the edge of being usable for PSF definition, showing a S/N in the central pixel of $< 20$ even for the maximum of its spectrum.

The global values determined for $\beta$ were between $1.75 < \beta < 6$, the highest value coming from HE 1335–0847, having the faintest PSF star. A good test for the dependence on flux is to look at successively observed spectra of the same object obtained with the same configuration, apart from the fact that the atmospheric conditions might have changed. One case is HE 1029–1401 for which four integrations of 1200 s each were taken. The star used is quite faint, showing a maximum of 600-1300 $e^-$ in the central pixels in a 1200 s integration. The four $\beta$ values are 3.4, 4.8, 2.78, 2.41 in this order, thus far from being identical. The value determined from the sum of frames is 3.77, possibly inheriting some of the winginess of the $\beta = 4.8$ frame, lying even above the average $\beta$ of the frames.

We conclude that $\beta$ is only describing the ambient conditions, if a certain S/N limit is reached, as already stated in 3.4.1, taking the findings of this sample as further evidence.

### 4.1.2 Modelling

Modelling was done as described in the previous section. We used 80 subpixel per input data pixel in the spatial coordinate, and the LUTs were created by smoothing over a radius of 30 pixels in wavelength.

One peculiarity became apparent. When modelling the QSO center, the raw centres for the individual rows appeared shifted by up to 0.2 pixels in the H$\alpha$ and H$\beta$ emission lines and the atmospheric absorption bands, with opposite direction for absorption and emission (see app. C, bottom diagrams). The reason for this shift is not clear, and about its source can only be speculated. As it does not appear for the VLT sample discussed in the next chapter, it is not an artefact of the modelling but must be real. The cause does not lie in the objects, and must be an effect of the optics system.

We decided to simply locally fit this variation with low order polynomials, and use the shifted centers. The size of the shifts is of an order that can not be neglected but that would also not make the modelling impossible. Thus the errors from the residuals of this shift should have no effect on modelling.

Scale lengths for the host galaxy were set using the values determined from the multicolour modelling in chapter 2. We compiled the values together with the types used in Table 4.1. We list two types for HE 1201–2409, which was identified to be have very compact spheroidal host. As the first fit using this model was unsuccessful, we used a wider disk model. Usually disk models are better to converge to useful values in numerically difficult fits. They will not fit a QSO with a spheroidal host perfectly, but will still make use of the spatial information contained in the model.

## 4.2 Modelling results

Modelling without further modification of the resulting host galaxy spectra was only successful for a part of the sample. In the following we are going to comment on the individual objects, describe modifications applied and the resulting spectra. Wherever possible, rotation velocities are extracted.

The figures Fig. 4.1 through 4.8 show the modelling results for each object. In the top panel is always shown the original spectrum of the QSO (black), the model for the nucleus (red), the resulting host spectrum after subtraction of the nuclear model (green) and the residual after subtraction of nuclear and host model (blue). The bottom panel shows the host spectrum, for several objects with different modifications applied to the original fit. The kind of modification and its justification are described for each object.

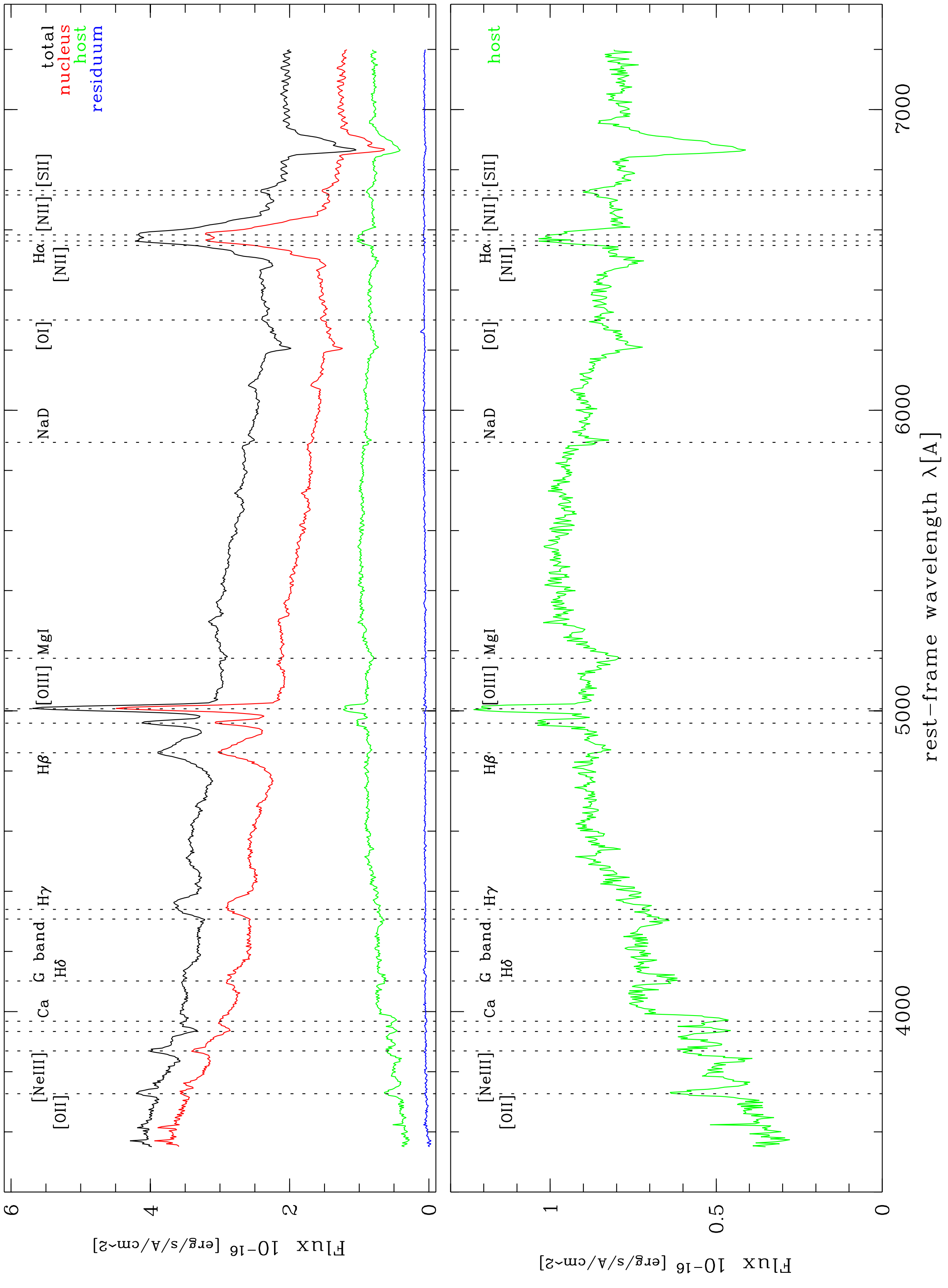

**Figure 4.1.** Modelling result EFOSC sample: HE 0952–1552, see text for description.

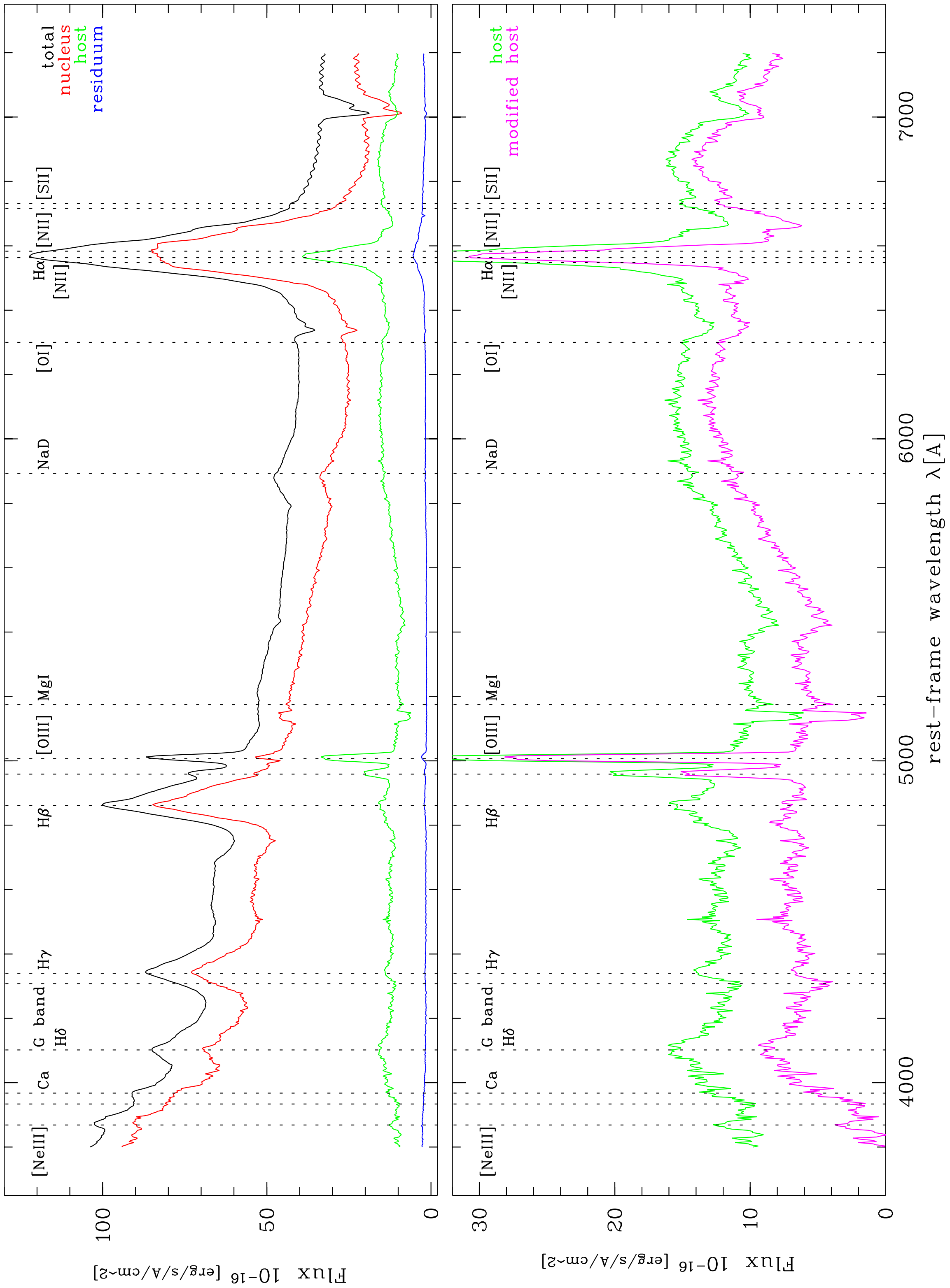

**Figure 4.2.** Modelling result EFOSC sample: HE 1029–1401, see text for description.

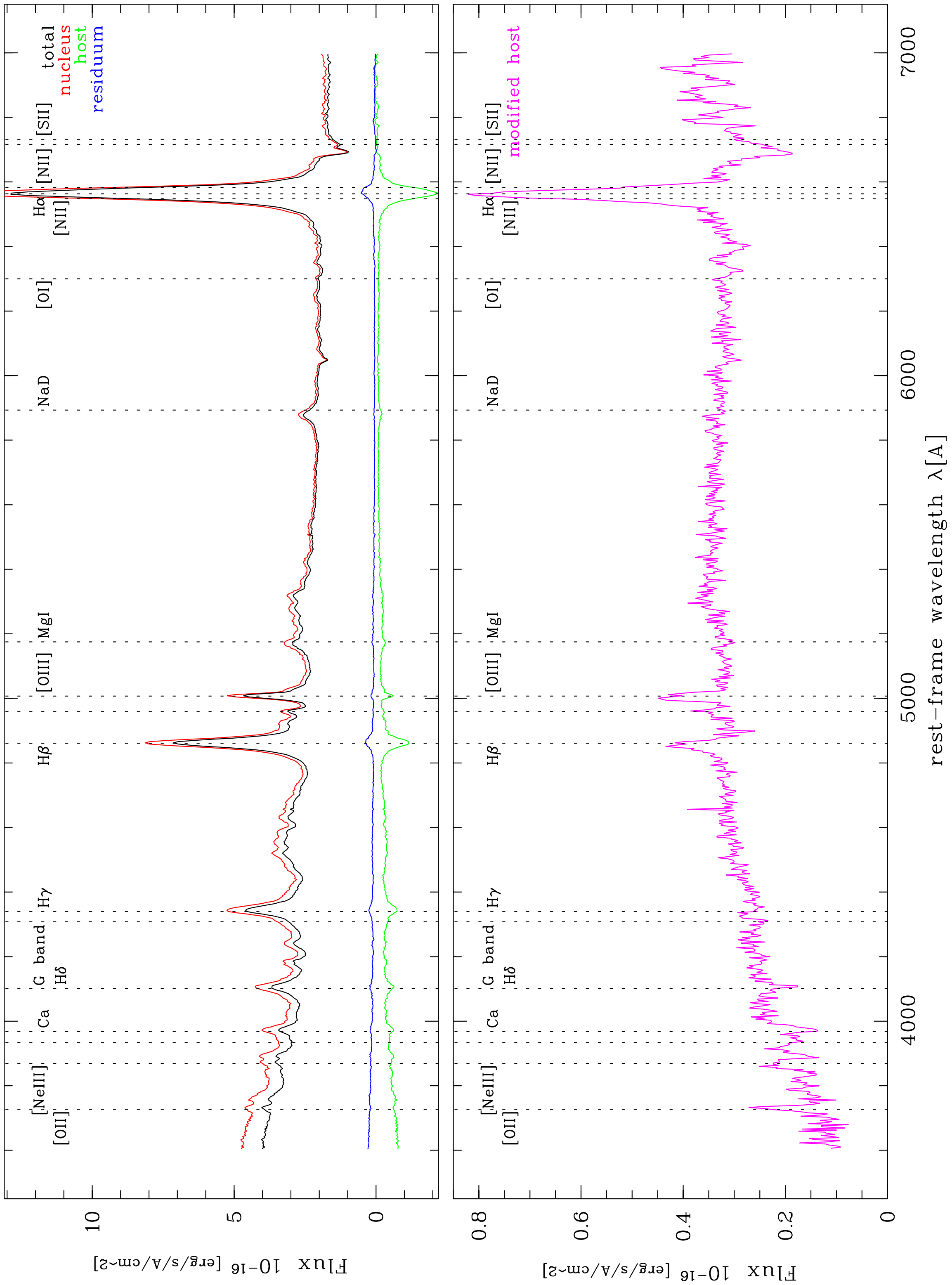

**Figure 4.3.** Modelling result EFOSC sample: HE 1201–2409, see text for description.

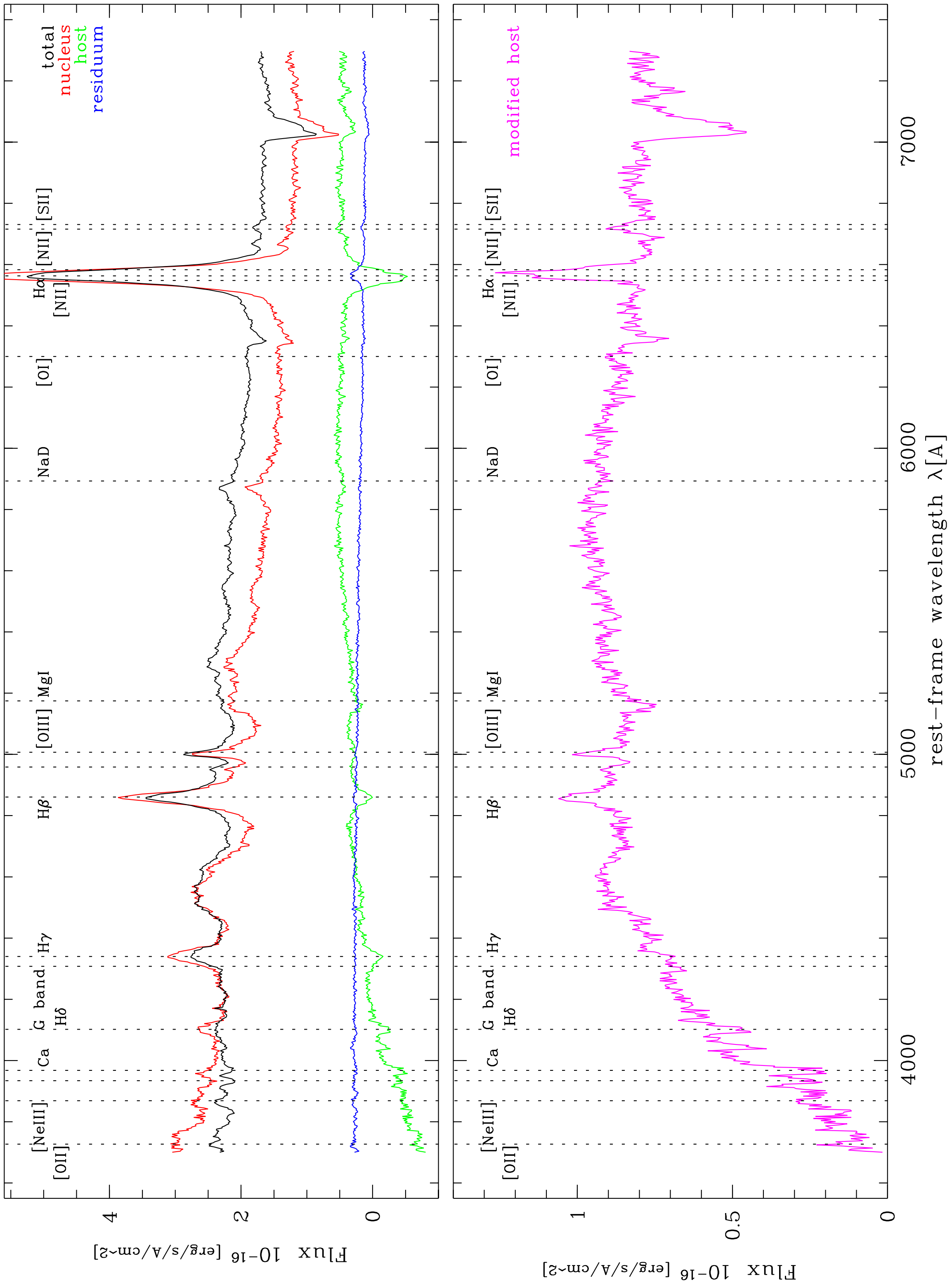

**Figure 4.4.** Modelling result EFOSC sample: HE 1239–2426, see text for description.

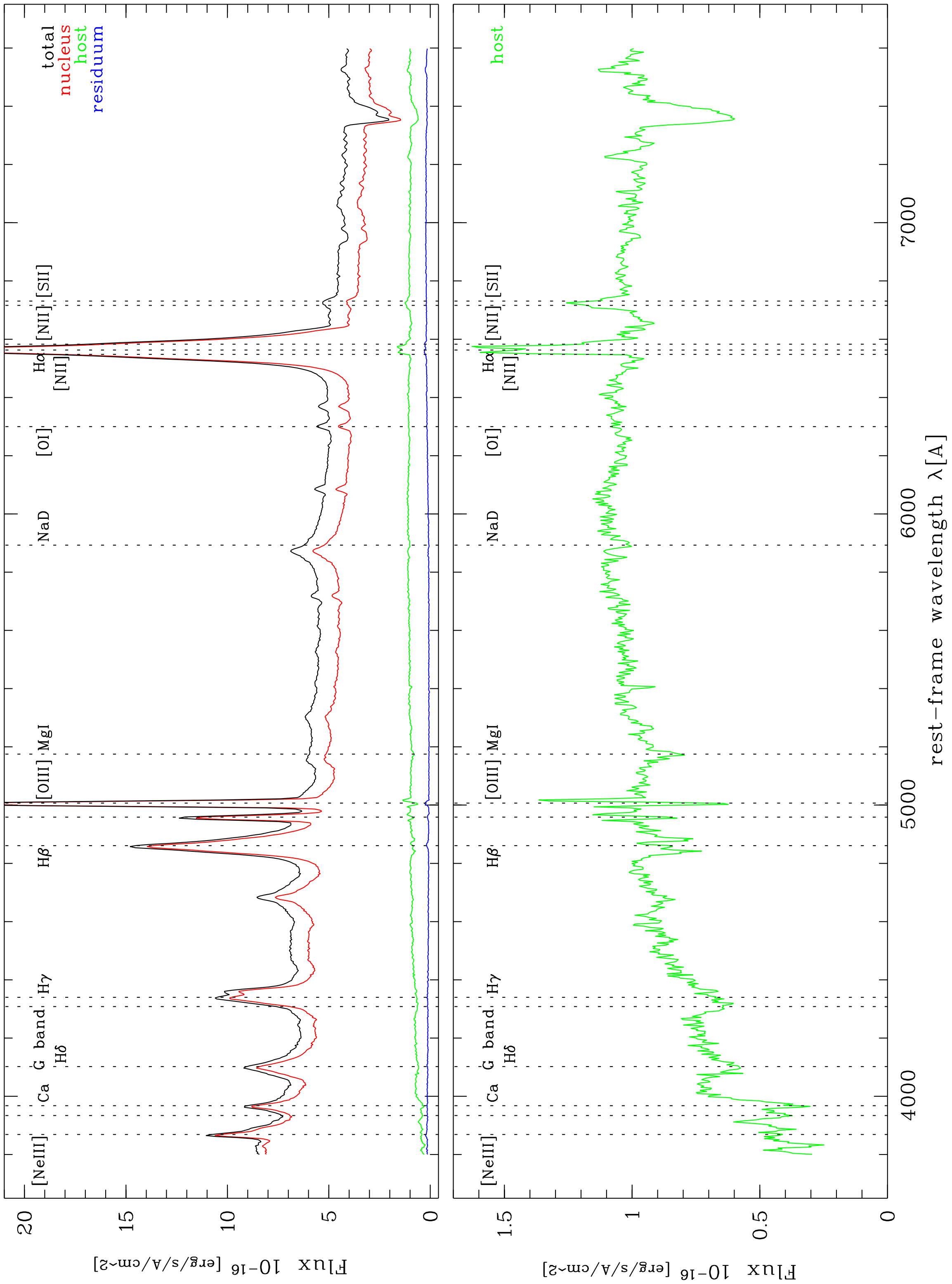

**Figure 4.5.** Modelling result EFOSC sample: HE 1310–1051, see text for description.

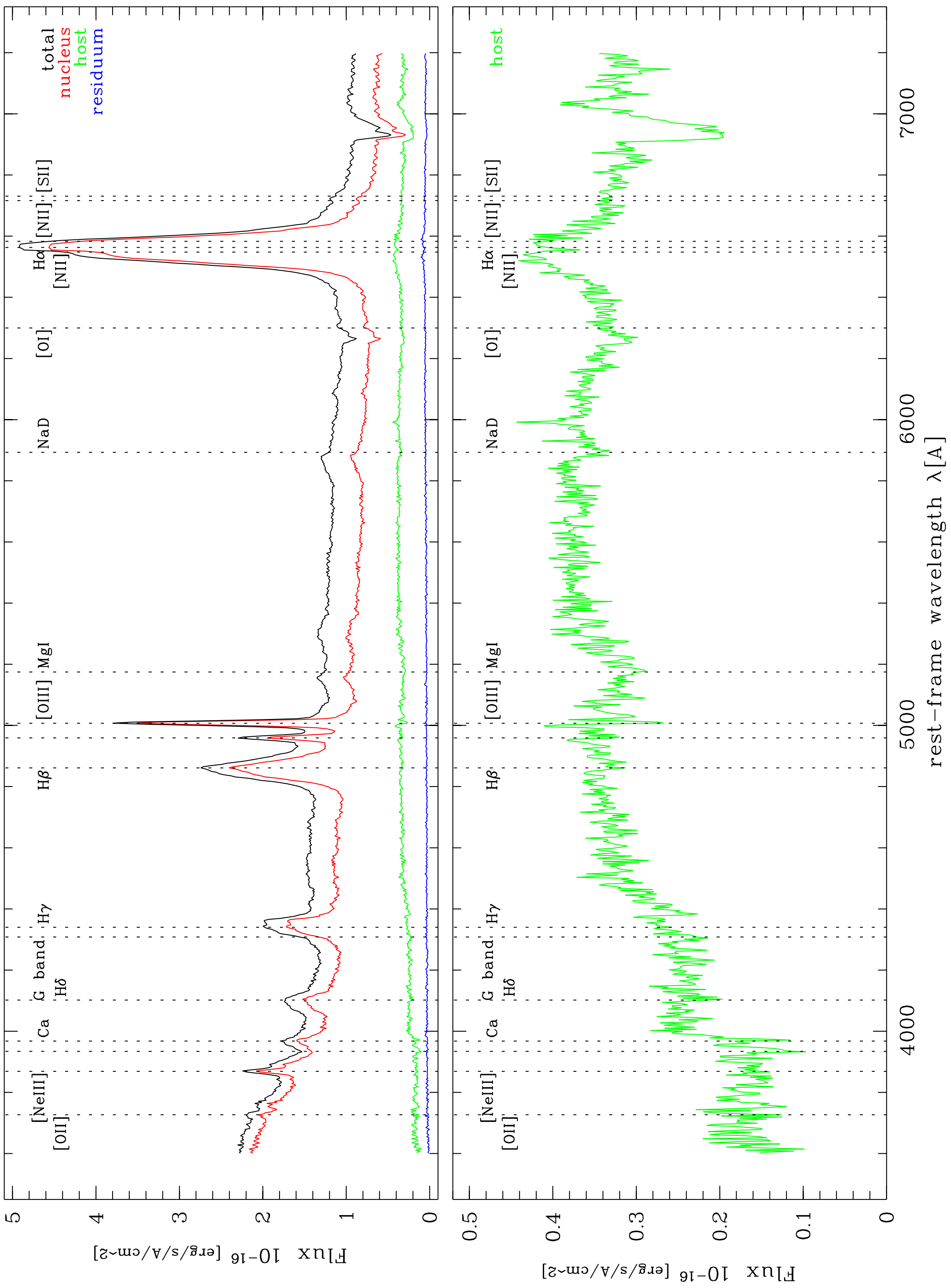

**Figure 4.6.** Modelling result EFOSC sample: HE 1315–1028, see text for description.

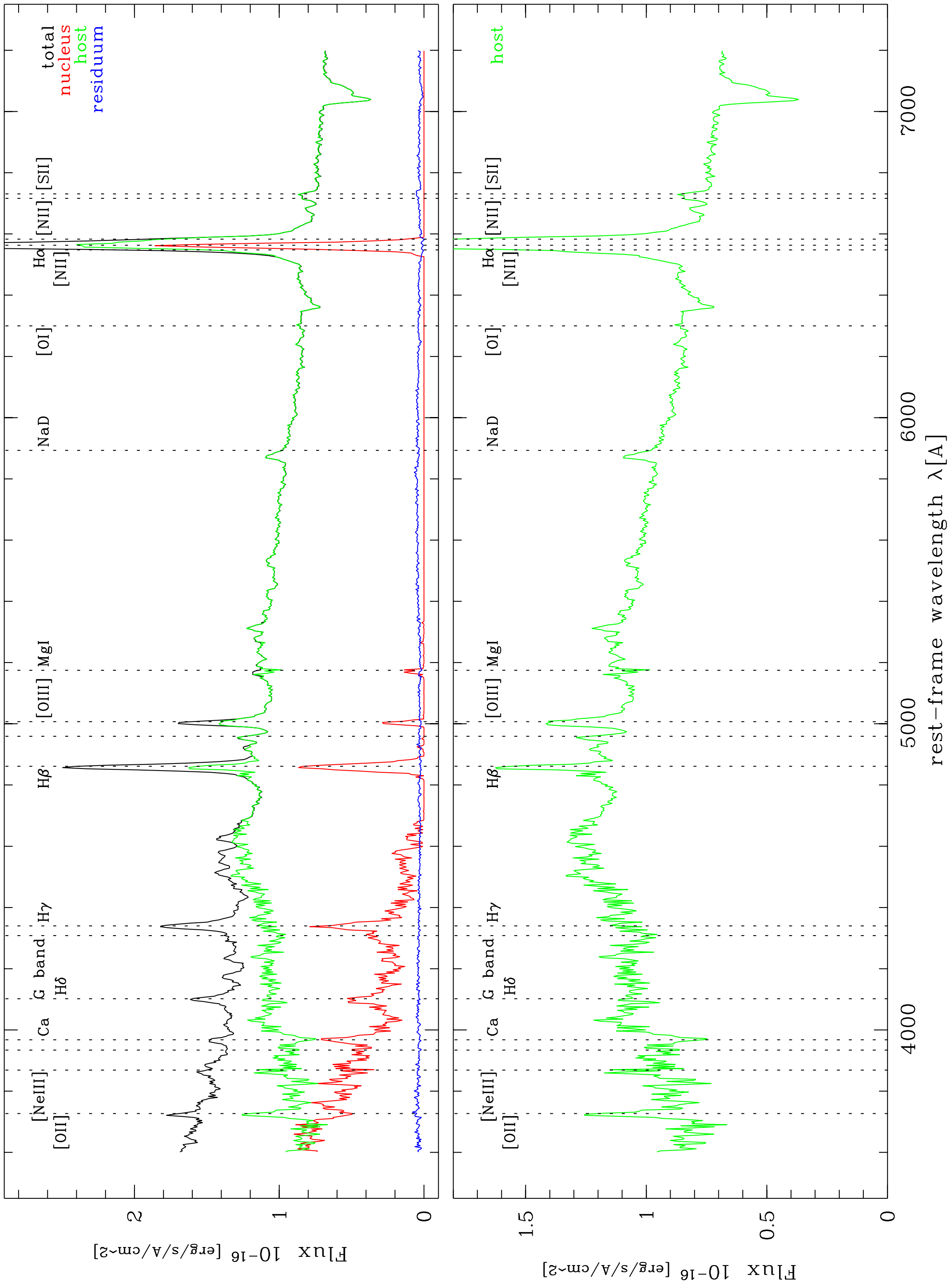

**Figure 4.7.** Modelling result EFOSC sample: HE 1335–0847, see text for description.

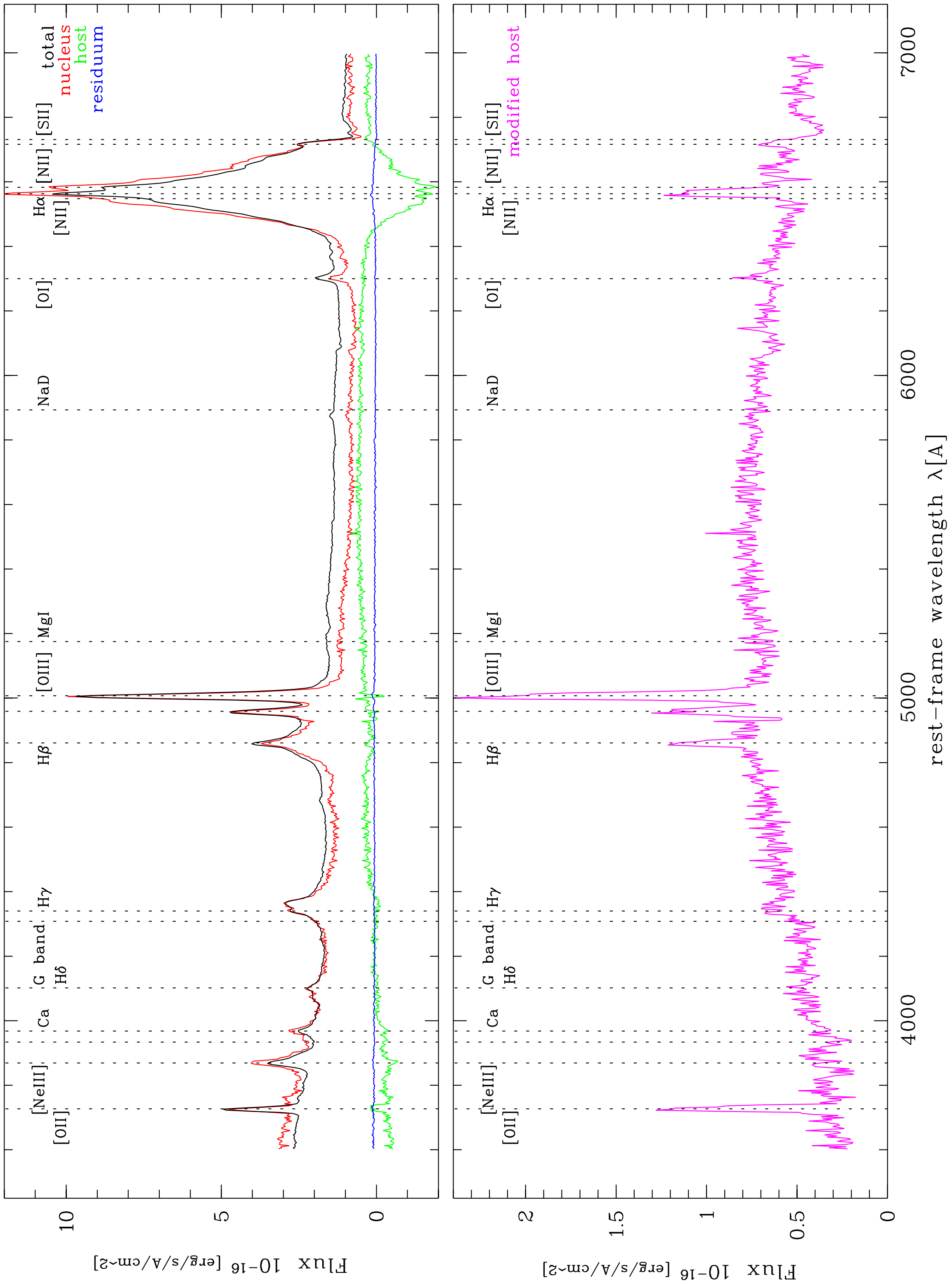

**Figure 4.8.** Modelling result EFOSC sample: HE 1416–1256, see text for description.

### 4.2.1 HE 0952–1552

Modelling for this prominent spiral was straightforward. No additional modifications were necessary to receive the spectra shown in Figure 4.1. Clearly visible are the stellar absorption lines, Ca H and K, G band, Mg I, Na D, plus Balmer absorption in H$\beta$ to H$\delta$. The 4000 Å break is prominent. Emission lines are also found, [O II], the [O III] doublet, [N II] and H$\alpha$ also in emission, although the three components are not resolved, and the [S II] doublet, also blended.

The 2d residuals show significant structure on a level of 10% of the host count rate, or $< 2\%$ of the count rate of the input QSO spectrum. In the [O III] 5007 Å component there is clearly rotational wavelength shift visible. Even though the line strength of the [O III] emission seems to be spatially asymmetric, numbers can be estimated, yielding values for the average rotation velocity of 350 km/s between $1.5''$ and $3.5''$ radius, 248 km/s from the 4959 Å component and 457 km/s from the 5007 Å component. This clearly identifies the emission lines as gas emission.

Judging if the strength of the emission lines determined is real, or if numerical flux transfer has happened from the nucleus to the host, is difficult. It is not possible to apply a single sided modelling to the lines, due to the low resolution. The model for the [O II] line shows a somewhat disturbed spectral geometry, with a small dip in the center, while the (much stronger) [O III] lines appear completely undisturbed. Close to the nominal position of the latter appears absorption, compatible with the Balmer absorption in H$\gamma$ and H$\delta$. But it is shifted by 12 Å, which is not due to errors in calibration. H$\alpha$ and the [N II] doublet are blended. In the host spectrum a dip is visible at the nominal H$\alpha$ position. This is also compatible with a superposed gas emission and stellar absorption. In total there are no signs of flux transfer. This would also be expected if gas disk and stellar disk have a similar geometry.

Rotation in the absorption lines is also visible. Ca K shows a shift of 8.5 Å between $1.5''$ and $3.5''$ radius of the left and right side, corresponding to an observed rotation velocity of 325 km/s, very similar to the gas rotation.

In section 4.3 the extracted host spectrum is compared to theoretical evolution synthesis models.

### 4.2.2 HE 1029–1401

This object is the only common object to all three samples. It has a spheroidal host and spatial modelling is thus more difficult than for the disk of HE 0952–1552.

The resulting spectrum given in Figure 4.2 shows strong signs of residual broad H$\alpha$ to H$\delta$ emission with added narrow cores. Narrow gas emission is prominent and, as the 2d spectra show, rotationally shifted. It seems that also in the narrow emission lines strong flux transfer has happened from nucleus to host. The flux transfer manifests its cause in the strong residuals visible in the 2d spectrum. In the centre the size of the residual structures is of 3% of the total flux or of more than 15% of the host flux. The shape difference between PSF star and the PSF at the position of the QSO is apparently large, due to only a rather weak PSF star being available close to the QSO.

In order to remove the broad emission bases, approximately 10% of the nuclear flux have to be subtracted from the host spectrum. In the bottom diagram of Fig. 4.2 the original (upper green) and resulting (lower magenta) spectrum are shown. The broad components are gone. Remaining are overestimated narrow lines and several absorption line features, Ca K, G band, Mg I, and Na D, however relatively weak. The dip next to Mg I is an artifact due to residuals in the sky subtraction. The bump at 4100 Å and between 5500 Å and 6400 Å are peculiar and likely due to modelling artefacts. Thus the general shape of the should not be taken at face value. This is a pity because of the available VLT spectra and broad band data, but the artefacts induced from only a weak PSF star available do not allow a comparison.

Measuring the rotational shift in [O III] 4959 Å and 5007 Å yields identical values of 6.8 Å shift between the two sides, corresponding to a rotation velocity of 204 km/s, between $2.5''$ and $8''$ radius.

### 4.2.3 HE 1201–2409

This object is a very compact elliptical, at $z = 0.137$. In broad-band imaging it proved difficult to model this object and it is similar for spectroscopy. Initially a spheroidal model with a scale length as determined in the broad-band modelling was used. Numerically this showed convergence problems and the resulting host spectrum showed not only negative flux for all wavelengths, but could be described as a being the total flux mirrored at the zero line, and amplified by a magnitude. The reason for this numerical behaviour were again a mismatch between PSF star and QSO, resulting in strong residuals that required a negative contribution of the host, in combination with a scale length of the order of the pixel scale.

As mentioned above the spatial modelling is generally the more stable, the larger the differences in the spatial distribution of the two components. In a second attempt we therefore used an exponential model. The scale length was chosen from a model fitted to the radial profile of a broad-band frame, to match the outer parts of the profile.

The resulting host galaxy spectrum is still negative, but of much smaller amplitude than with a spheroidal model. In order to extract any information about the host from this spectrum, we add a fraction of 17% of the nuclear model, to make the resulting spectrum positive. In the bottom of Figure 4.3 the magenta curve is showing the modified spectrum. If the spectral shape is real, it is generally compatible with stellar population of age 1 Gyr. Some Balmer absorption like features are visible in Hδ , and also as a blend of Hε with Ca H, and possible absorption in Mg I and the G band, but stellar absorption is weak. The narrow emission lines superposed show a broad base, but less than in the total QSO spectrum and no rotation is visible. Without further knowledge it is difficult to judge in detail which features of the spectrum are real and which might be artefacts, but as will be shown in section 4.3.2 the broad band fluxes agree very well with the determined spectrum.

### 4.2.4 HE 1239–2426

In imaging the host of HE 1239–2426 shows two components, a central part surrounded with a ring of stars around it. The original modelling again determines negative fluxes for a part of the spectrum. Adding 27% of the nuclear model to the host spectrum yields the spectrum shown in the bottom of Figure 4.4. In the so modified 2d frame even the ring structure of the host becomes visible.

The resulting spectrum shows G band, Mg I and Na D absorption, with superposed gas emission lines. Spectral features as the constant rise between 4000 and 4600 Å could be artefactual, thus it is not clear whether a young star forming components is present.

In the emission lines rotation is not visible. With a resolution of 0.5 pixel, this corresponds to a lower limit of 55 km/s projected velocity. Either the projected rotation is slower than this value or the distortions are too strong and thus the S/N to low to detect it. The latter is in any case a problem.

### 4.2.5 HE 1310–1051

This is the least distant object in the sample, with $z = 0.034$, being a classical Sy 1. The modelling was successful without need for modifications, the results are shown in Figure 4.5. The spectral shape is compatible of an evolved stellar population with additional star formation (see section 4.3). Stellar absorption features and superposed gas emission are clearly visible, the [O III] and Hβ emission is clearly rotationally shifted but [O III] 5007 Å is disturbed in the centre by modelling. Both [O III] components as well as Hβ show a bright knot of emission at $4''$ distance from the center with no apparent rotational shift. The measured rotational shift of the gas disk lies around $470 \pm 60$ km/s.

### 4.2.6 HE 1315–1028

The modelling of this disk was also successful without further modifications (Fig. 4.6), even though at the position of Hα a broad base is visible. Gas emission is very weak, only traces of [O III] and [S II] are visible. A strong 4000 Å break is seen, Balmer absorption in Hβ and Hδ, and strong G band, Mg I and Na D. The absorption lines show rotation. Ca K yields 160 km/s, Na D 275 km/s, with the latter having the lower error bar.

The spectrum in total is compatible with an intermediatly old population (see section 4.3).

### 4.2.7 HE 1335–0847

For this spheroidal modelling failed. As visible in Figure 4.7 for $\lambda > 5000$ Å the host is substituting the nucleus, for smaller wavelengths host and nuclear model are merely complements. Obviously the PSF star shape differs that strongly from the nuclear shape of the QSO that the spheroidal host model matches the QSO nucleus better than the PSF star. For small values the PSF is used as a “correction” for the host model in order to fit the QSO. Because of the value zero as a set lower limit for the nuclear model, the nuclear model becomes zero at some point.

A PSF error of this kind will make any attempt to extract host information impossible.

### 4.2.8 HE 1416–1256

The spectrum resulting from modelling this spheroid shows negative parts and strong broad negative Hα (Fig. 4.8). Adding 24% of the nuclear model to the host compensates for the oversubtraction without leaving broad emission line bases in Hα or Hβ. Except for Ca K no stellar absorption lines and no break at 4000 Å are visible. Gas rotation is not detectable, neither in [O II] nor [O III].

## 4.3 Analysis results

In this section we want to give results on dynamics in the host and the stellar content as derived from model fitting.

### 4.3.1 Host dynamics from line diagnostics

To summarise the individual object descriptions: For most objects that modelling was successful for, strong narrow gas emission lines are visible. At least a part of the extracted emission line flux can be attributed to the host. For the hosts identified as disks this is likely to be all flux.

All disks except HE 1315–1028 show strong gas emission. Rotation can be found for all of them except HE 1239–2426. Here 2d PSF distortions might be the reason for a non-detection. Rotation of the stellar disk can be seen in HE 0952–1552 and HE 1315–1028.

Rotation is also found in the gas of the spheroid HE 1029–1401. Only one of the remaining spheroids, HE 1416–1256, does not show any sign of rotation and has reasonable S/N that would make rotation possible to detect, if present. For all objects the 2d spectra give the impression that the wavelength shift is systematic and not simply due to turbulences in the gas, induced by merger or smaller tidal events. This is particularly valid for HE 1029–1401. Here the rotation is traceable all across the host, out to radii of at least 22 kpc.

For the disks it is possible to deproject the observed rotation velocities to estimate the intrinsic rotation velocities. We make two assumptions: First that stellar and gas disk are lying in the same plane, second, the observed velocity is a projection due to the inclination $i$ of the galaxy to the plane of the sky and due to an angle between slit and major axis of the inclined galaxy. From geometrical consideration one can relate observed velocity $v_{\mathrm{obs}}(x)$ and intrinsic rotation velocity $v_{\mathrm{rot}}(r)$,

$$v_{\mathrm{rot}} = v_{\mathrm{obs}} \cdot \frac{\sqrt{1+\frac{\tan^2\phi}{\cos^2 i}}}{\sin i}$$

with inclination $i$, and angle $\phi$ between slit axis and major axis of the inclined galaxy. Also radii have to be deprojected. The position along the slit axis $x$ and the deprojected radius in the galaxy $r$ are related by

$$r = x \cdot \sqrt{\frac{\sin^2\phi}{\cos^2 i} + \cos^2\phi}.$$

We summarise the extracted and deprojected rotation velocities in Table 4.2. In the case of HE 1310–1051 the deprojection yields a very high value for the rotation velocity of $> 1000$ km/s. This seems unrealistically high. There are two possible solutions. As the visible spiral arms are asymmetric, the rotation could stem from induced turbulence and not from a stable gas disk. However the spectrum shows no signs of induced star formation beyond normal for a spiral (see next section 4.3.2). Thus possibly the gas disk is warped or tilted against the plane of the disk, showing higher inclinations and thus a smaller projection of the rotation. A second argument against turbulence is that signs of coordinated rotation are visible for a range of radii as for HE 1029–1401, though not as prominent, making turbulence not very probable. If shift measurement and deprojection factor are correct, then a very massive core would be needed to create such a velocity. The data are insufficient to resolve this issue.

**Table 4.2.** Rotation properties of the EFOSC sample. Rotation velocities are in units of km/s. A “?” is given, if this property is not known, “–” if this property is not accessible.

| Object | Type | $i$ [°] | $\phi$ [°] | Gas rot. | $v_{\mathrm{g,obs}}$ | $v_{\mathrm{g,rot}}$ | Stell. rot. | $v_{\mathrm{s,obs}}$ | $v_{\mathrm{s,rot}}$ |
|---|---|---|---|---|---|---|---|---|---|
| HE 0952–1552 | D | 48 | 25 | y | 350 | 575 | y | 325 | 530 |
| HE 1029–1401 | S | – | – | y | 204 | – | n | – | – |
| HE 1201–2409 | S | – | – | ? | – | – | ? | – | – |
| HE 1239–2426 | D | 38 | 40 | ? | $< 55$ | $< 140$ | ? | – | – |
| HE 1310–1051 | D | 27 | 10 | y | 470 | $> 1000$ | ? | – | – |
| HE 1315–1028 | D | – | – | ? | – | – | y | $\sim$215 | $\sim$650 |
| HE 1335–0847 | S | – | – | ? | – | – | ? | – | – |
| HE 1416–1256 | S | – | – | ? | – | – | ? | – | – |

Also for HE 1315–1028 the deprojected rotation velocities are high, $\sim$ 650 km/s. As this velocity is determined from stellar absorption lines, turbulence is unlikely to be the cause for high velocity. Apart from an asymmetry no potential tidal distortions are visible in the direct images.

In total, the host dynamics shows no strong peculiarities if the high rotation velocity of HE 1310–1051 is attributed to projection effects.

### 4.3.2 Stellar populations and broadband colours

For four objects the spectra extracted appear to be of sufficient quality to be compared to theoretical models and to the broadband colours derived in chapter 2. Again we make use of the model family by Bruzual & Charlot (1996), already used for modelling broad band colours in section 2.7. Used are models based on the Scalo IMF and of solar metallicity. We used single stellar population (SSP) models of different ages, from 0.01 to 14 Gyr, plus a continuous star formation (CSF) model with constant star formation rate for 14 Gyr, created from the SSP models.

Of the four objects, HE 0952–1552, HE 1201–2409, HE 1310–1051 and HE 1315–1028, three were identified as being disk dominated, only HE 1201–2409 is a spheroid (we noted the correction applied to the latter and possible resulting errors but the broad band colours agree remarkably well so that we included HE 1201–2409).

In Fig. 4.9 spectra are shown for the four objects. The black line represents the extracted host spectrum, the red lines are models. The green symbols correspond to fluxes derived from broadband imaging with the $B$, $V$, $R$ and $I$ filter, the fluxes scaled to fit the absolute calibration of the observed spectrum. We include the $I$ band point, even though the spectra don’t cover that wavelength region. We found it nevertheless very instructive to compare the models fitted to the spectra to the $I$ point. The $B$ band data point is missing for the last object. Plotted is rest frame wavelength, the broadband flux wavelength centres are shifted with $z$ accordingly.

The spectrum of HE 0952–1552 is best fitted with a single 2 Gyr SSP. This model reproduces the general shape of the object best, but predicts a somewhat too large 4000 Å break, suggesting a younger population. However, a combination of an old and an 0.1 Gyr component give a similar but not better fit. Pure CSF yields too blue colours, a pure evolved (10 Gyr) population

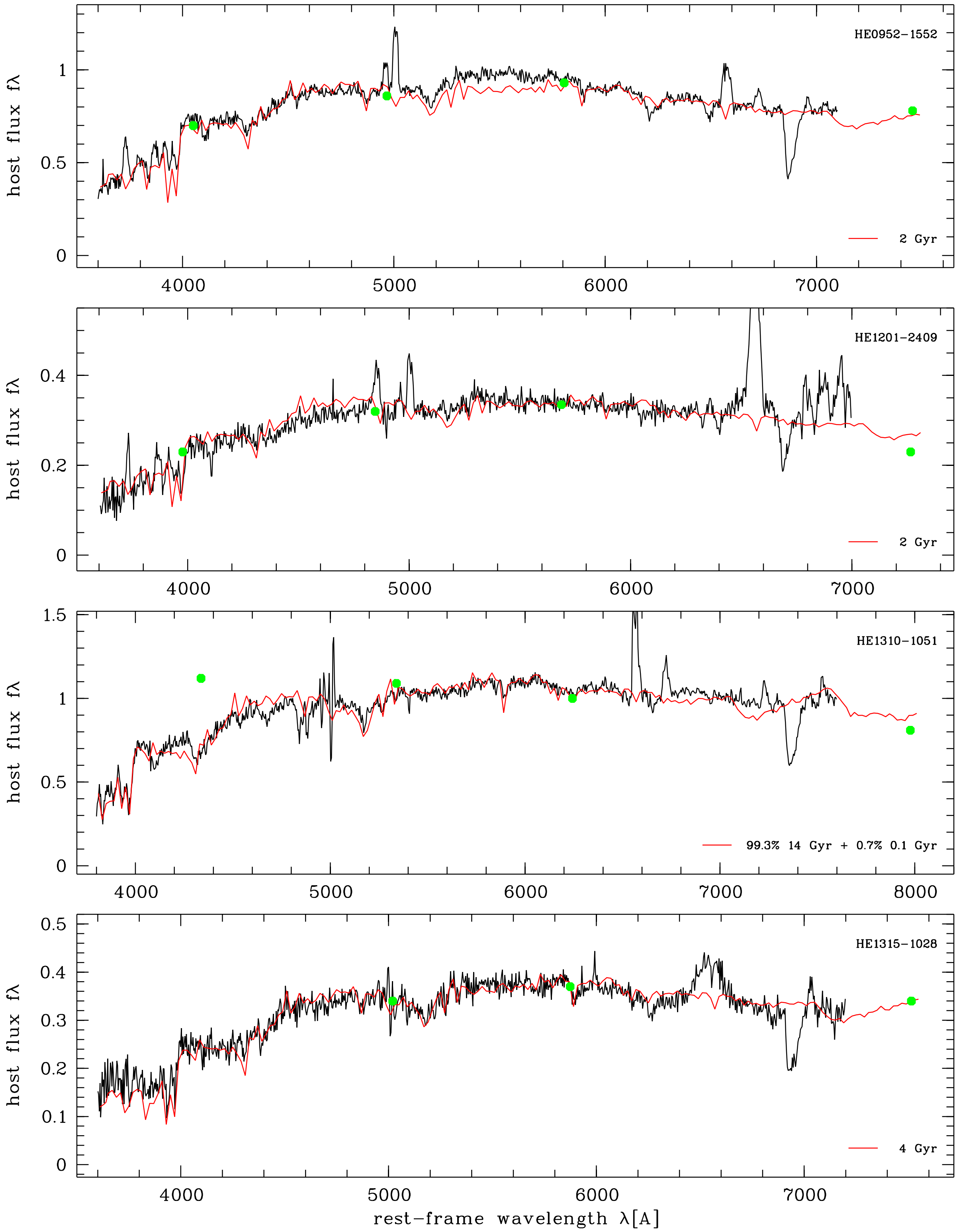

**Figure 4.9.** Model fits for four EFOSC objects with sufficient quality. See text for description.

is too red. The broad band fluxes found for this object agree very well with the spectrum and the model.

For HE 1201–2409 description also with a 2 Gyr model is very good and the spectrum and the broad band colors also agree. Again the absorption redward of 4000 Å is stronger in the model. This and the very small absorption visible in Mg I and Na D point to a relatively young dominating stellar population.

HE 1310–1051 is best described with a combination of an old and less than one percent in visible mass of a 0.1 Gyr component, a 2 Gyr or younger model is too blue. Here the *B* broad band flux is strongly off, by 0.5 mag. As the *B* band image is of very good quality, and so is the modelling for the image, this offset could be due to a calibration problem of unknown origin. A possible second explanation is the asymmetry and distortion of the host, probably due to tidal interaction. The slit position used could have sampled a trace in the host with an older than average population, which is unlikely, because the tidal features were masked in the broad band photometry. But the asymetries are not large enough to explain a 0.5 mag deviation from the average for the slit position used. The *B* band data point should be disregarded.

The spectrum of HE 1315–1028 is well matched by a 4 Gyr old population, with no signs for a significant additional young component. However it seems that the calibration for this object produces a spectrum slightly too red by about 10% more flux in the red than appropriate, as we found in a comparison with a second set of spectra. This would change the age of the best fitting population toward younger values, approximately again 2 Gyr. A significant fraction of a very young (0.1 Gyr) component is still ruled out.

For this object the *B* broad band point is missing, but the remaining three do perfectly coincide with the extracted spectrum.

# 5 Spectroscopic decomposition: The “VLT” sample

One of the design goals of the ESO Very Large Telescope and its instrumentation was the study of QSO host galaxies (ESO 1998). Our second spectroscopic sample for the first time makes use of the spectroscopy capabilities of the VLT for this task. We observed with FORS1 at the ESO VLT ANTU in the context of programmes 65.P-0361(A) and 66.B-0139(A). The study was proposed in collaboration with colleagues from Liége/Belgium, Chile and ESO, with F. Courbin (Liége) being the principle investigator. It is targeted at studying the spectral properties of the low redshift, $z < 0.33$ host galaxy population, its differences and similarities to inactive galaxies. The data was used as a first application of a spatial deconvolution algorithm recently developed by F. Courbin. First results of this complementary approach have been published Courbin et al. (2002a) with a more detailed analysis following in Courbin et al. (2002b).

In this section we want to describe the sample and data obtained, the modelling, the quality of the results, and the calibration. After that results from and methods used in an analysis of the resulting 1d- and 2d-spectra are presented.

## 5.1 Sample and data

The sample investigated in the following is the first half of a statistically complete sample, again drawn from the HES. The objects have $M_B < -24.0$, the redshift limit was set at $z < 0.33$. The objects were observed with the MOS unit of FORS1, allowing to observe one or two PSF star simultaneously with the QSO. It has to be noted that FORS is also a focal reducer type instrument, thus similar problems concerning PSF variation in the FOV arise as for EFOSC, the scale of these variations is smaller. The detector used has a 2k×2k chip, for 19 slitlets in the MOS unit this yields just above 100 pixels per slitlet.

The objects were observed using the three high resolution grisms, and the standard collimator, yielding an average spectral resolution of 700 and a pixel scale of $0.2''$/pixel. Slit size was $1''$, the integration time was typically 1200 s, for some objects this was increased. This corresponds to on average 3.5 times deeper spectra than for the EFOSC sample. All nights of observation were clear, seeing was below $1.5''$, sometimes as low as $0.6''$. For wavelength calibration standard lamp spectra were obtained, standard stars for flux calibration.

For all objects we have $H$ band images available, observed with SOFI at the ESO NTT, to seperately determine morphological type, scale length, and nucleus-to-host ratio. The imaging data is part of a different project, not part of this work, and will be described in a separate paper. Grey scale maps of the QSO images and radial profiles of QSO and PSF are shown in Figure 5.1. The objects in the sample, their properties and integration times are listed in Tab. 5.1.

### 5.1.1 Reduction

The spectra were debiased and flatfielded by G. Letawe in Liége using a standard reduction routine inside IRAF, after which the data were transfered to Hamburg. We then subtracted the night sky spectrum by fitting a constant sky for each wavelength row. Because of the small width of the individual MOS slitlet spectra (100 pixels or $20''$), only a narrow strip of object-free

**Table 5.1.** Objects in the VLT sample. Listed are redshift $z$, total apparent $B$ magnitude (extinction corrected), total apparent $H$ magnitude, approximate nucleus-to-host brightness ratio in the $H$ band, morphological type of the host ((E)lliptical or (D)isk; ED describes objects fit better with an spheroidal model, but a significant disk contribution can not be ruled out, DE vice versa), scale length $r_{1/2}$ used in modelling, and integration time of the spectra. Except for HE 1029–1401 and HE 1434–1600, which are part of the multicolour sample investigated in chapter 2, the morphological properties are preliminary results communicated by B. Kuhlbrodt and L. Wisotzki.

| Object | $z$ | $B$ | $H$ | N/H ($H$) | Type | $r_{1/2}$ [“] | Int. time |
|---|---|---|---|---|---|---|---|
| HE 0914–0031 | 0.322 | 16.02 | 15.04 | 3.5 | D | 2.0 | 1200 |
| HE 0956–0720 | 0.3259 | 16.27 | 14.26 | 3.0 | D | 3.0 | 1200 |
| HE 1009–0702 | 0.2710 | 16.39 | 14.29 | 1.8 | ED | 0.55 | 2400 |
| HE 1015–1618 | 0.2475 | 15.36 | 13.60 | 6.0 | D | 2.2 | 1200 |
| HE 1029–1401 | 0.0859 | 13.29 | 12.16 | 2.1 | E | 1.45 | 1200 |
| HE 1228+0131 | 0.117 | 14.68 | 12.89 | 5.4 | DE | 1.65 | 1200 |
| PKS 1302–1017 | 0.2784 | 14.58 | 13.63 | 1.7 | E | 0.6 | $B$: 2400<br>$R$+$I$: 1800 |
| HE 1434–1600 | 0.1445 | 15.08 | 13.64 | 1.2 | E | 2.2 | 1200 |
| HE 1442–1139 | 0.2569 | 16.76 | 14.60 | 0.45 | D | 1.95 | 1200 |
| HE 1503+0228 | 0.1350 | 16.27 | 13.61 | 1.5 | D | 2.2 | 1200 |

background was available, but higher degree polynomials were also not needed for the QSO images. In two cases the host was not completely covered by the length of the slitlet, resulting in a non-zero flux level at both ends of the slit. Here the sky background was estimated by extrapolating the radial profile of the host further out. The remaining host flux at these radii was small, of the order of $< 5e^-$.

We created cosmic ray maps for all PSF and QSO frames. The pixels with identified cosmics were assigned a very large variance and thus entered the modelling with weight zero. Also rows where sky subtraction was non-perfect were marked separately and excluded from modelling. This was particularly the case for PSF stars and appeared strongest for the strong lines in the $I$ grism: It seems that some slitlets in the MOS unit were improperly alligned with the CCD pixel grid. This was never the case for the QSO spectra, which were always taken with the central slitlet #9 (of 19), but for several of the other slitlets used for the PSF stars. This resulted in slightly rotated lines in the PSF star 2d spectrum and made the sky subtraction faulty at the edges of each line. Here many (up to 150 of 2048) rows had to be masked out. Due to the nature of the PSF modelling routine with the smoothing fit this only entered in the creation of the LUT.

### 5.1.2 Calibration

Wavelength calibration was done using standard lamp spectra, and was successful with a precision of better than 0.25 pixels ($< 0.3$ Å) in all cases.

For spectrophotometric calibration response curves were created using a spectrophotometric standard from Hamuy et al. (1992, 1994). We included an airmass correction and applied a correction for galaxtic extinction taken from Schlegel et al. (1998). The goal, however, was not absolute spectrophotometry, which would have required a much larger overhead.

Thus the resulting QSO spectra did not always show identical fluxes in the common wavelength overlap regions. The deviation were not systematic and were of the order of 0–15% of the flux. We therefore decided to modify the spectrum from the central 600R grism to make is connect to the two other grisms. For this task we multiplied the spectrum with a first order polynomial, with coefficients determined individually for each case.

### 5.1.3 Modelling

The modelling to separate nucleus and host component was done as described in section 3.1. We used 80 subpixels per input data pixel in the spatial coordinate. The LUTs were created averaging the normalised PSF residuals with a radius of 60 pixels in each direction, which guaranteed a minimum of 60 pixels entering into the averaging also for both ends of the spectrum. The rms spread of the centering was less than 0.1 pixel, both for PSF stars and QSOs.

Detailed diagrams of the modelled PSF parameters and the QSO center are collected for all objects in appendix D.

## 5.2 Modelling results and analysis

In this section we present the modelling results with comments on the modelling process and describe the resulting spectra. All descriptions are meant for the resulting host galaxy spectrum, unless stated otherwise.

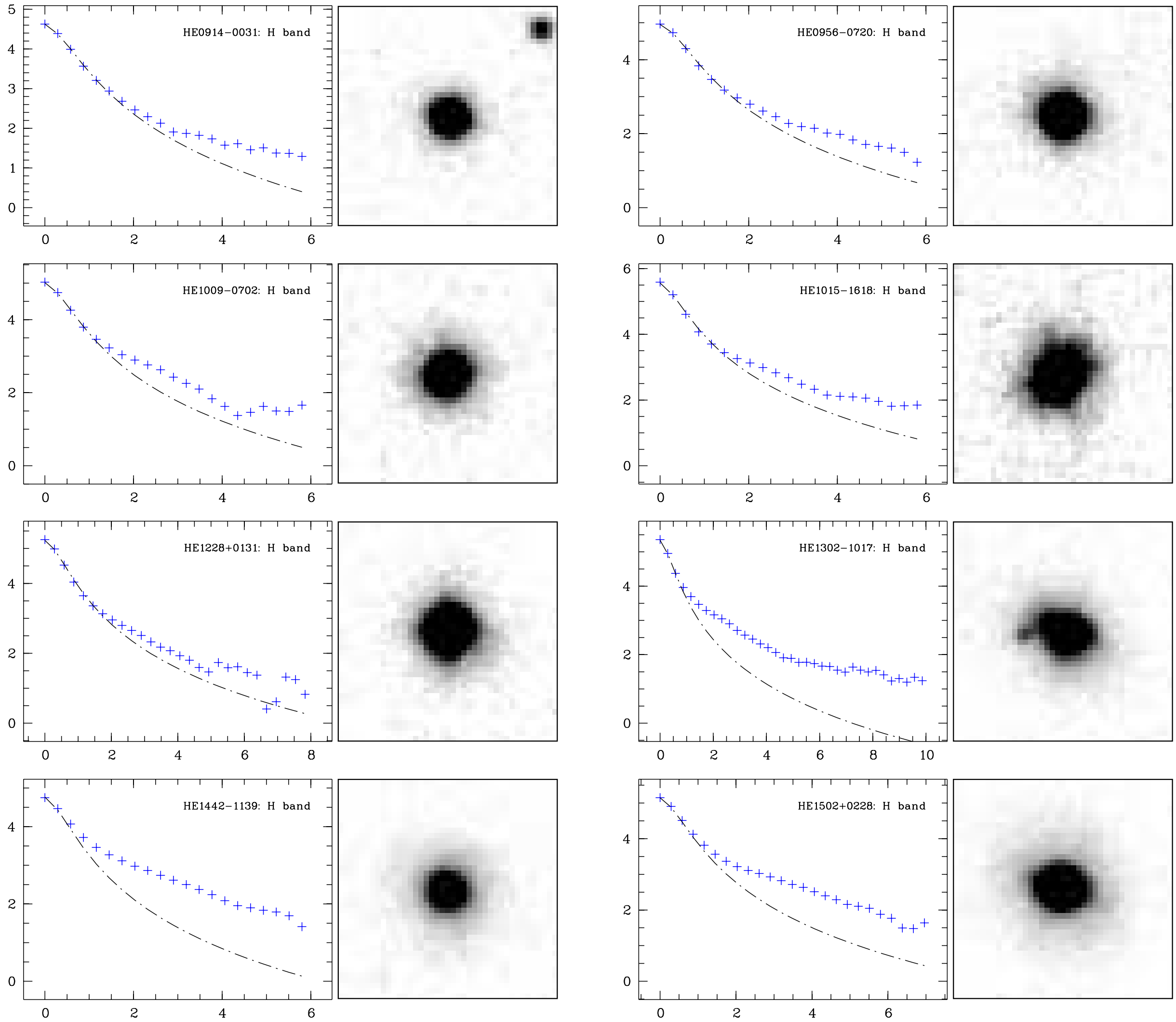

**Figure 5.1.** The objects in the VLT spectroscopy sample: The diagrams show radial profiles of the objects in the *H* band, flux is logarithmic in arbitrary units, radius is in arscseconds. The symbols mark the data points, the dot dashed line marks the PSF. Profiles and grey scale images of HE 1029–1401 and HE 1434–1600 can be found in Figure 2.9, as they are already part of the multicolour sample. The gray scale images show the QSO, including the nucleus in the *H* band. Images are centered on the nucleus. The side length of the images is 5.8$''$ for all objects.

### 5.2.1 HE 0914–0031

For this host classified as a disk ($z = 0.322$) modelling has been attempted with $r_{1/2} = 2.0''$ and $3.0''$. The results shown in Figure 5.2 are for $r_{1/2} = 2.0''$ but no significant changes appear for $r_{1/2} = 3.0''$. In all three grisms the host continuum is compatible with noise thus in the continuum the host is not resolved. The only clearly visible emission lines in the host are [O III] 4959 Å and 5007 Å in the $R$ grism, which are clearly rotationally shifted. In the $B$ grism a very noisy [O II] might be visible. Hα in the $I$ grism appears negative, of the order of 10% of the nuclear flux. If this amount is added, as done in Fig. 5.2, a trace of narrow Hα and [N II] doublet might be there, but too weak for analysis.

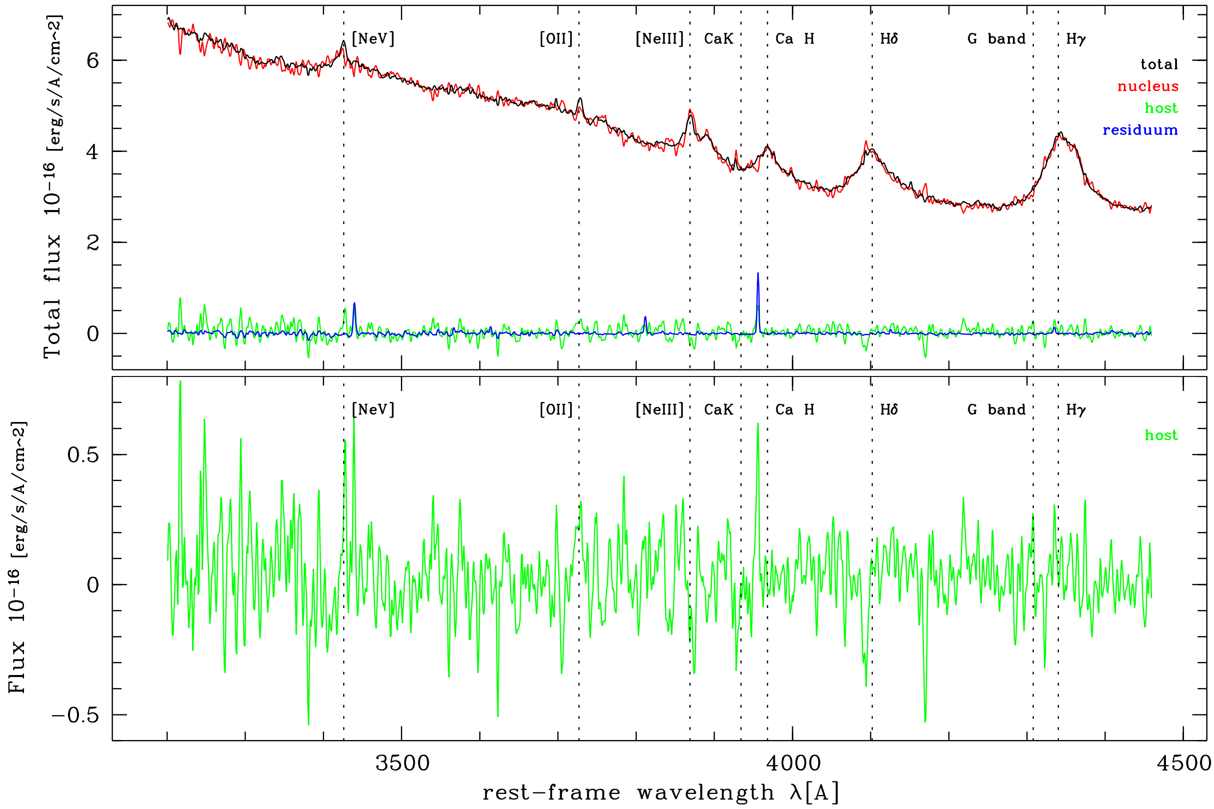

**Figure 5.2.** HE 0914–0031 modelling results for the three grisms (600B here, 600R and 600I on the next page). Shown are, in the top panel, extracted spectra of the total QSO (top black line), nucleus (red line), host after subtraction of the nuclear model (green line) and residuum after subtraction of nucleus and host model (blue). The bottom panel shows the host spectrum alone, some important lines are marked. Given is the rest-frame wavelength. For presentation the spectra have been slightly smoothed to enhance the visibility of spectral features.

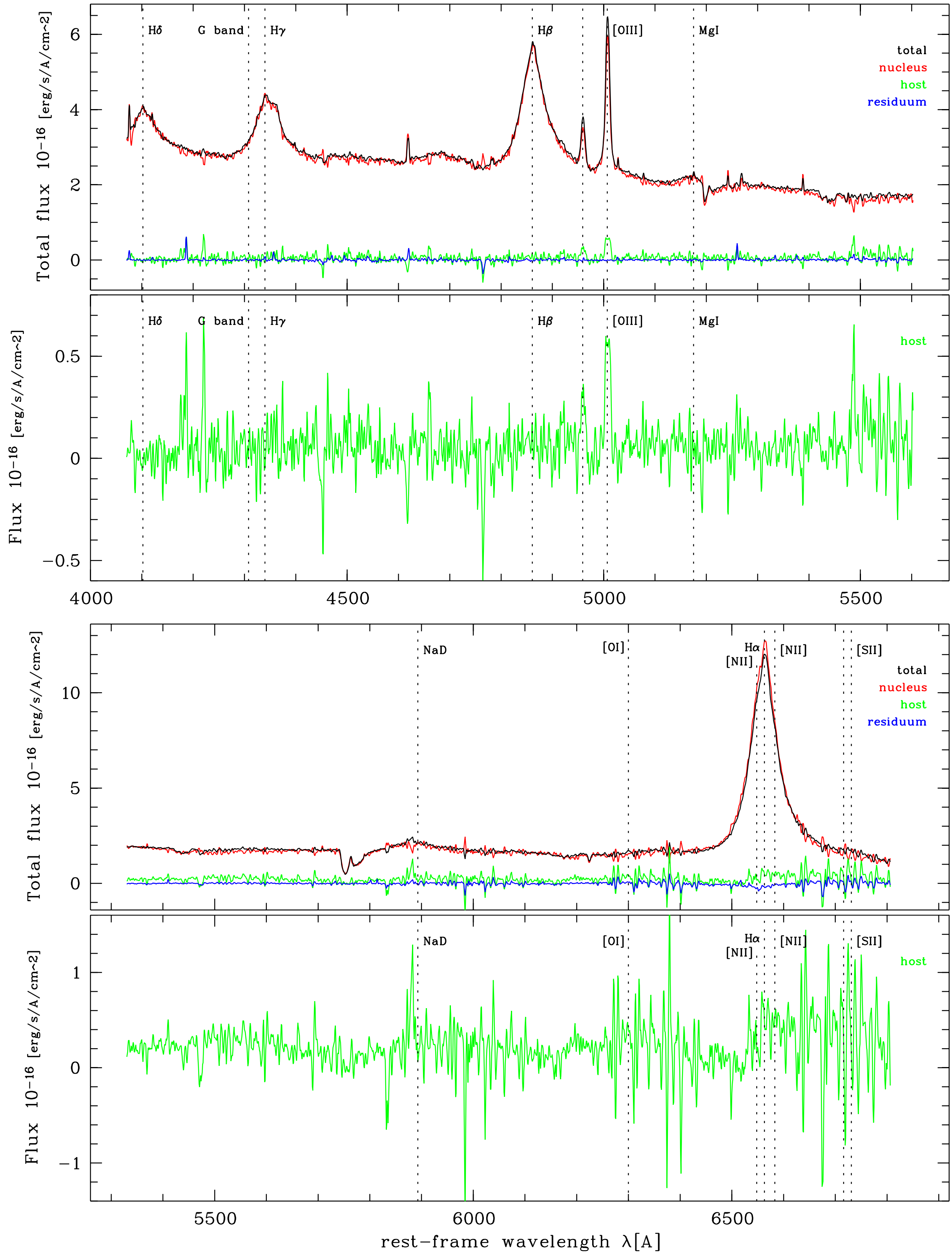

**Figure 5.2.** continued. HE 0914–0031 (top: 600R, bottom: 600I)

### 5.2.2 HE 0956–0720

With $z = 0.3259$ this object has the highest redshift in the sample. Even though the $H$ band nucleus-to-host ratio (N/H) is around 3:1, the host flux contained in the slit is low due to the large scale length of this disk, $r_{1/2} \sim 3''$,. Thus in the spectrum it appears as a very weak and noisy host. Even if the resulting flux is real, it contributes less than 1–2% of the total light in the slit. No apparent absorption or emission lines are visible in the $B$ and $R$ grism. In $I$ grism Hα appears negative, due to flux transfer from the nucleus. Adding a constant fraction on nuclear flux can not resolve this – the S/N is too low for separation and analysis.

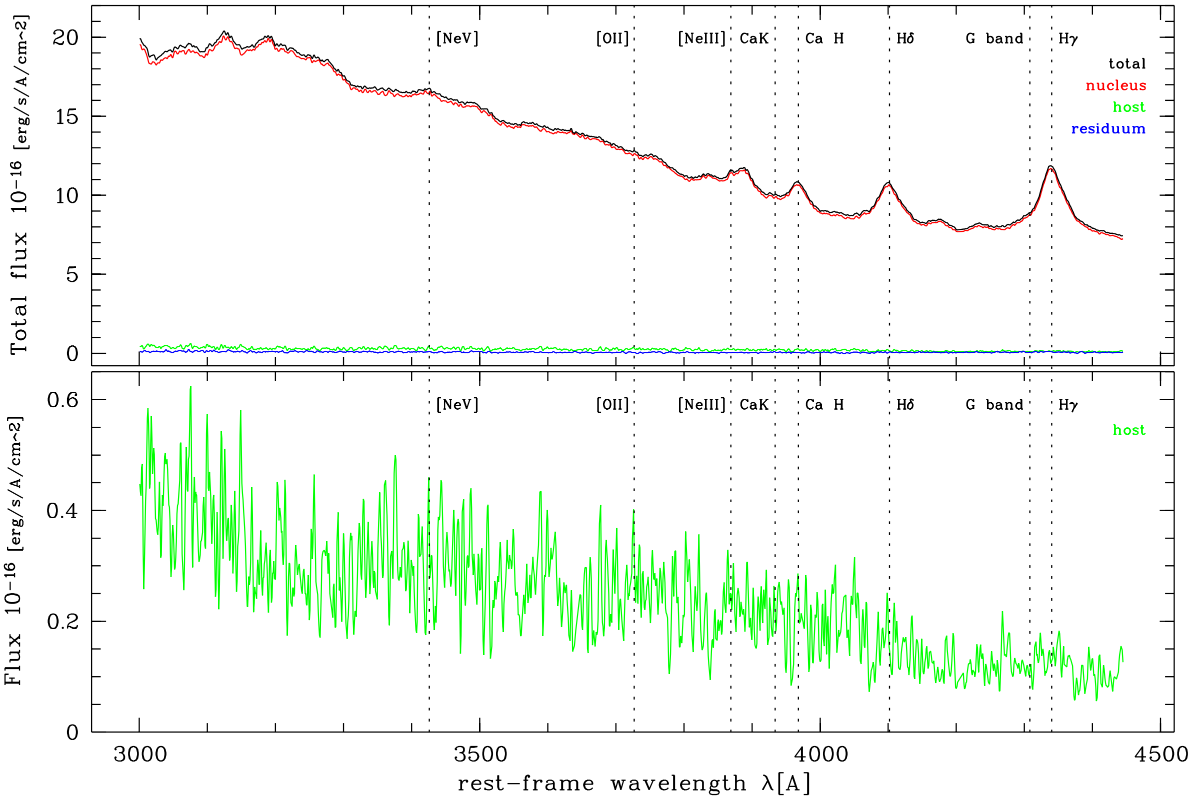

**Figure 5.3.** HE 0956–0720 modelling results for the three grisms (600B here, 600R and 600I on the next page). Lines as in Fig. 5.2.

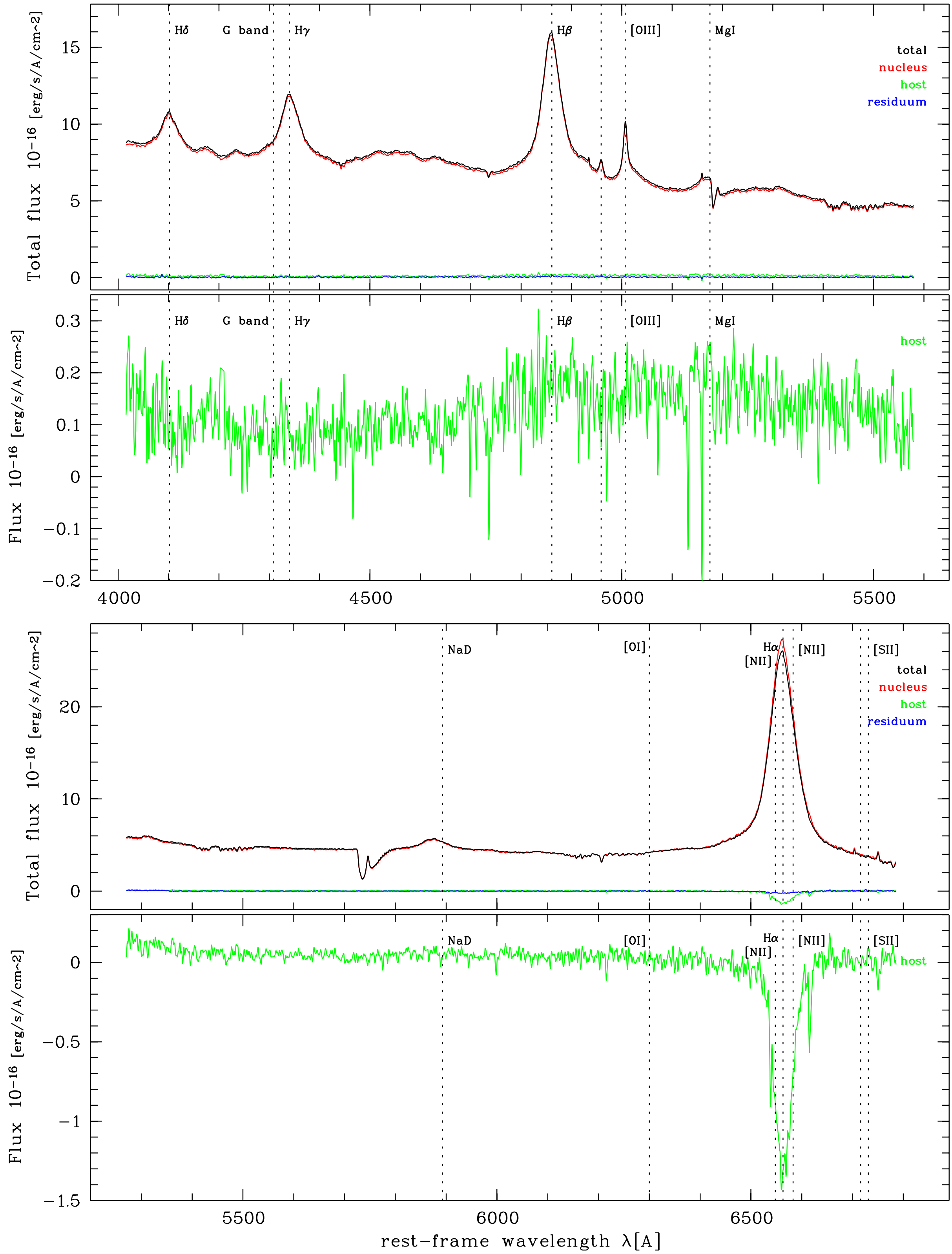

**Figure 5.3.** continued. HE 0956–0720 (top: 600R, bottom: 600I)

### 5.2.3 HE 1009–0702

The morphology of the host of this QSO ($z = 0.271$) is somewhat ambiguous, a spheroidal fit is clearly better fitting only for the inner regions (L. Wisotzki, priv. comm.). After modelling, the host flux becomes slightly negative in the *B* grism for $\lambda < 4000$ Å. We added 20% of the nuclear flux to resolve this (so plotted in Fig. 5.4). This modification makes the range $\lambda > 3500$ positive, avoids broad emission for Hγ, and removes the discrepancies in the common spectral range of the *B* and *R* grism. A 4000 Å break is visible, also individual Ca H and K absorption, but these two lines are very noisy. Also narrow [O II] emission at 3727 Å is visible with very slight rotational shift and substantial flux transfer from the nucleus.

In the *R* grism a line is visible at 5014 Å, shifted from the [O III] 5007 Å position. This is likely a combination of weak [O III] 5007 Å emission and the effect of sky line residuals at 5018 Å.

In the *I* grism narrow Hα and the [N II] doublet are visible, the slight rotational shift again appears for Hα and [N II] 6583 Å. Hα and [N II] were seperately treated with single sided modelling. Also [S II] 6716 Å and 6731 Å are clearly there. For this object modelling was successful apart from the sub-zero flux in *B* grism.

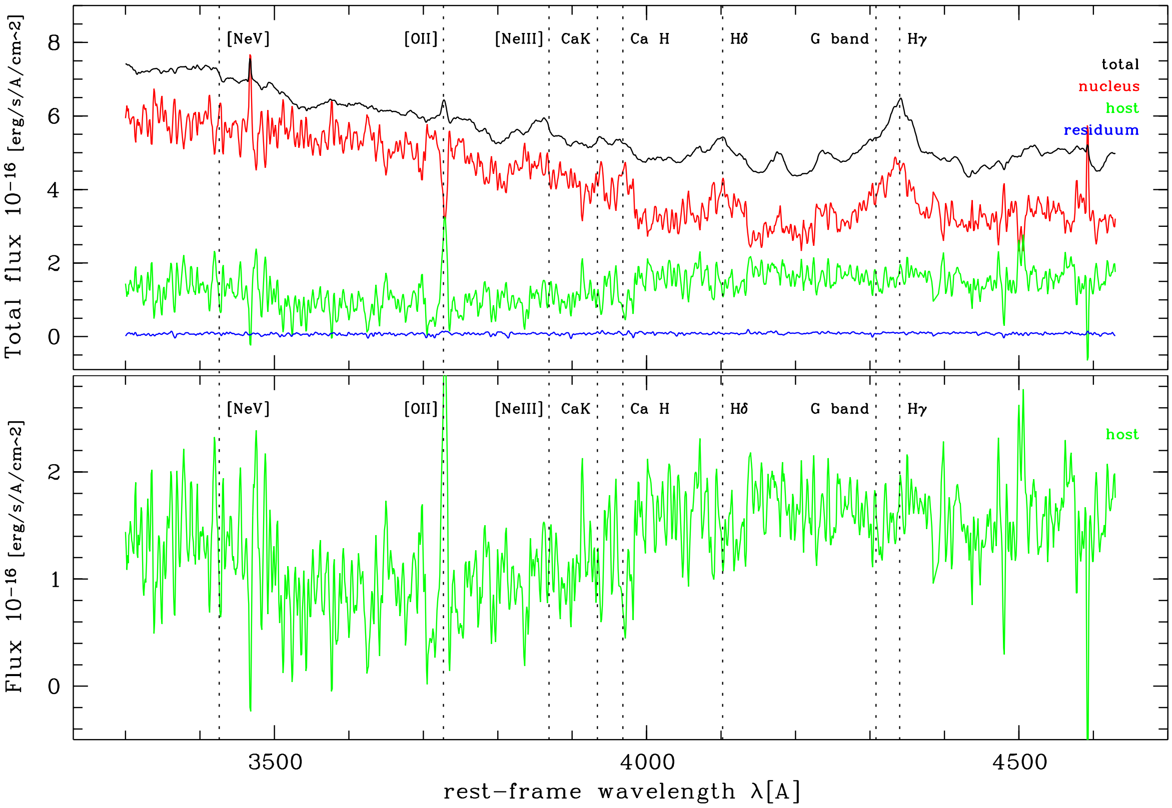

**Figure 5.4.** HE 1009–0702 modelling results for the three grisms (600B here, 600R and 600I on the next page). Lines as in Fig. 5.2.

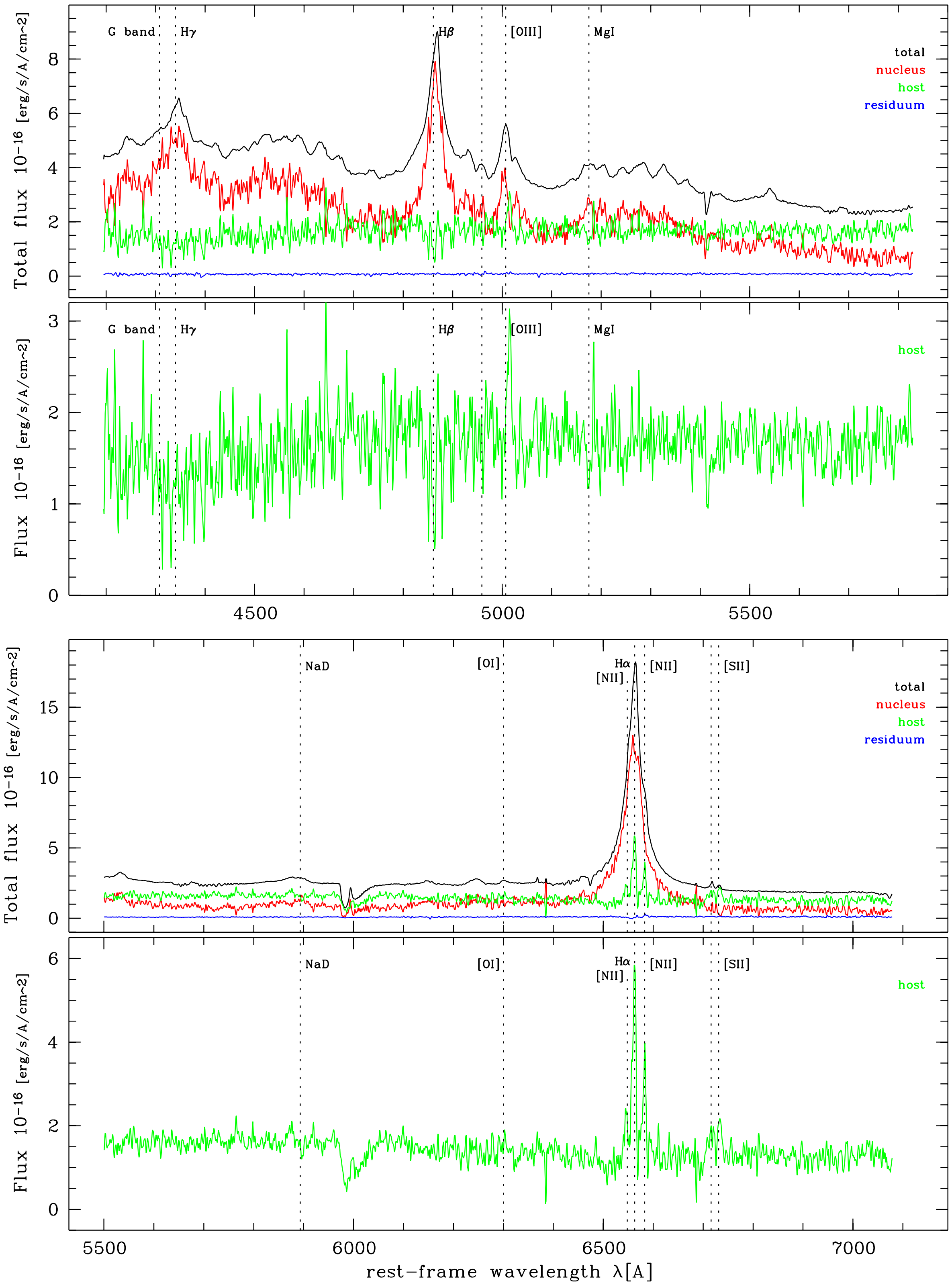

**Figure 5.4.** continued. HE 1009–0702 (top: 600R, bottom: 600I)

### 5.2.4 HE 1015–1618

The morphology of this very weak host ($z = 0.2475$) is not clear. The *H* band imaging shows a double sloped radial profile, indicative of a disk with spiral arms, and in total an exponential disk model does fit better than a spheroidal. The spectral modelling assigns 1–2% of the total flux to host. Even though no positivity criterium has been imposed on the host flux in modelling, it is close to zero for all λ except around Hα. Thus the modelling of the continuum is consistent with the detection of only a point source – the host is not resolved.

In the *B* grism no narrow emission lines are visible, there is no trace of [O II] 3727 Å. In the *R* grism possibly a trace of [O III] can be seen, but the spectrum is very noisy. An artefactually broad Hα appears in the *I* grism. For analysis the S/N is too low also for this object.

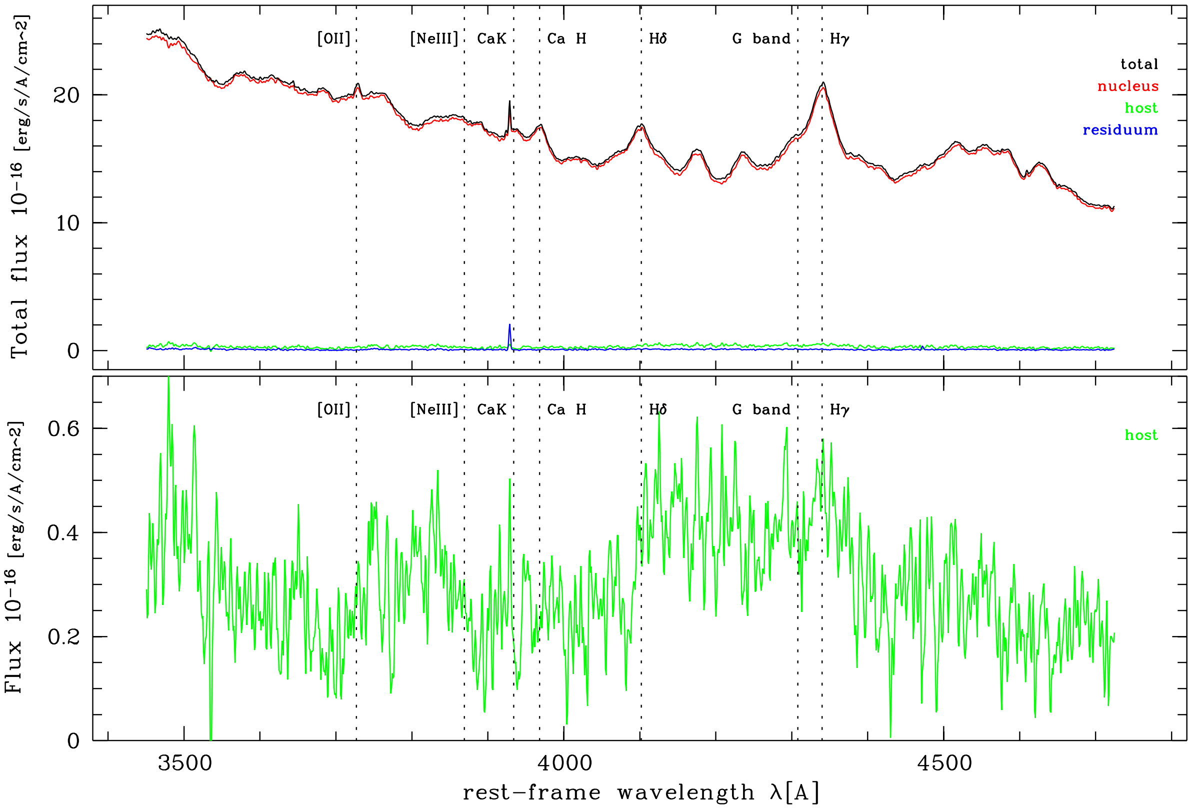

**Figure 5.5.** HE 1015–1618 modelling results for the three grisms (600B here, 600R and 600I on the next page). Lines as in Fig. 5.2.

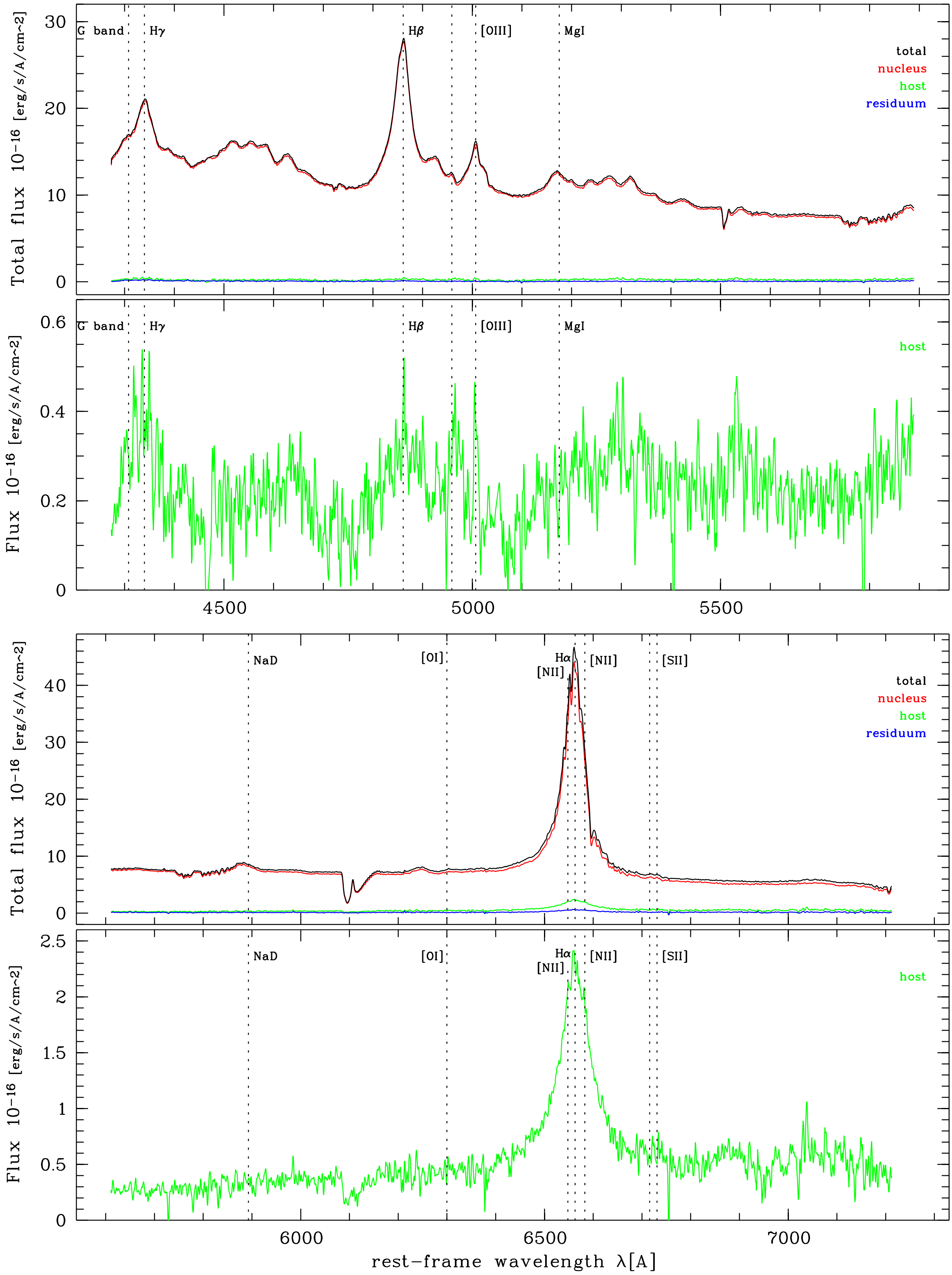

**Figure 5.5.** continued. HE 1015–1618 (top: 600R, bottom: 600I)

### 5.2.5 HE 1029–1401

This is the lowest redshift object and one of two objects common with the multicolour sample from chapter 2. The host is a luminous spheroidal that contains ∼20% of the total flux. All visible narrow emission lines show a rotational shift of similar size. In the *B* grism a very small 4000 Å break and Ca K are visible, Ca H is blended with an emission line and is not visible. [O II] is contaminated with nuclear contribution, [O III] 4959 Å and 5007 Å are very strong, the 4363 Å component is also visible. We separately modelled [O III] 4959 Å and 5007 Å in order to assess line ratios. Weak narrow Hβ is visible without any broadened base. The spectral region of Hβ and [O III] also appears in the *R* grism. Strong narrow Hα and [N II] are present, with a broad dip in Hα spectral range. A single sided modelling of the lines is not possible due to relatively strong residuals appearing in the 2d spectrum around Hα. Possibly present are also Mg I 5175 Å and Na D absorption. If the [S II] 6716 Å component is visible, the 6731 Å component is not.

In the *I* grism Hα and [N II] appear again, with the same residual problems and no possibility for single sided modelling. [S II] is completely blotted out by sky subtraction residuals. There is a discrepancy in resulting host flux in the overlapping spectral region of the *R* and *I* grism, the latter showing 30–50% more flux than the *I* grism. As seen for other objects, this is likely due to Hα which fills the overlap range. The Hα and [N II] emission lines in the host show similar intensity values in both cases.

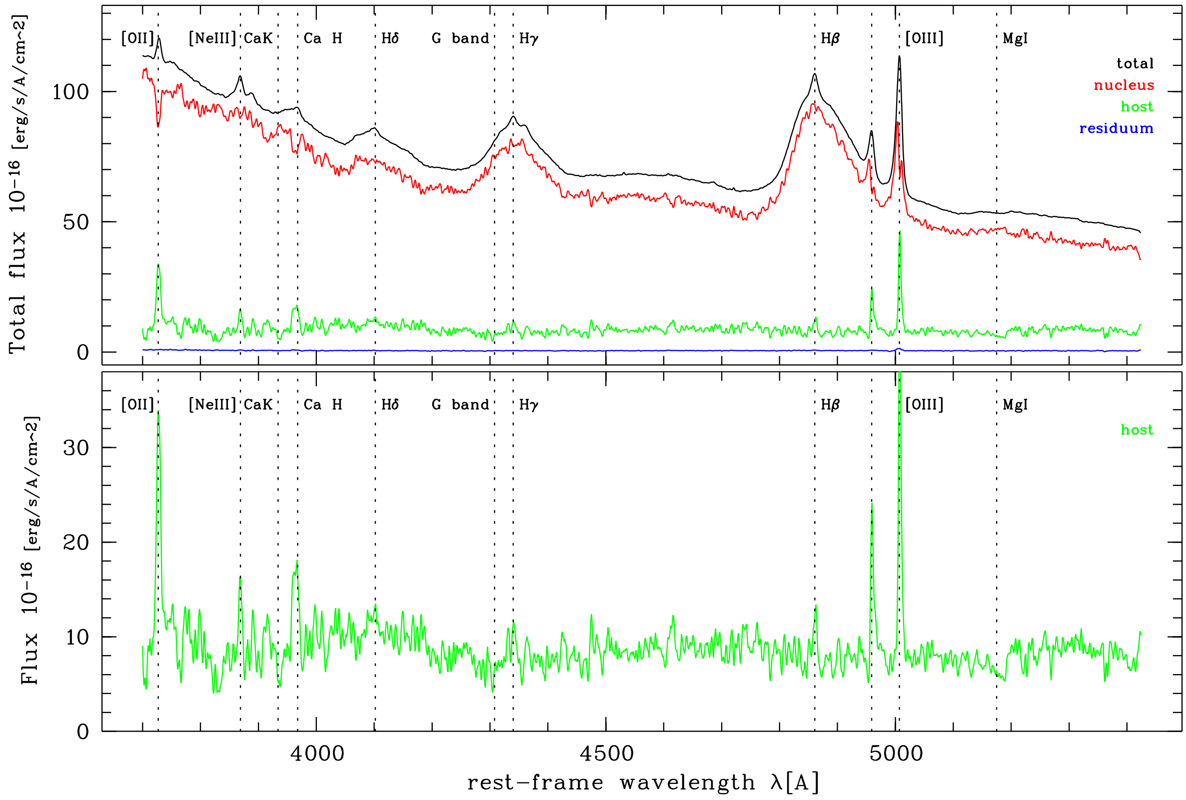

**Figure 5.6.** HE 1029–1401 modelling results. Lines as in Fig. 5.2.

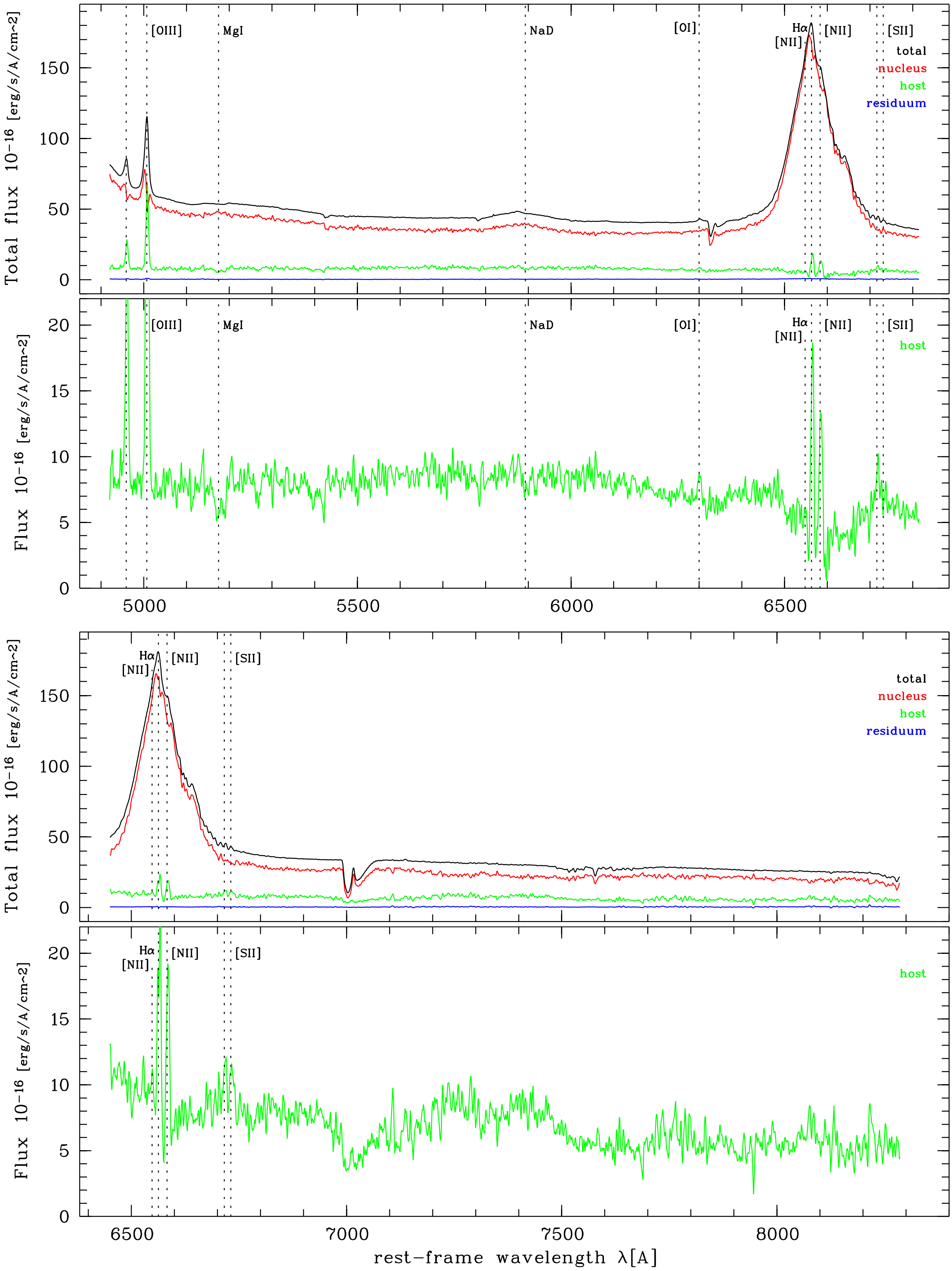

**Figure 5.6.** continued. HE 1029–1401 (top: 600R, bottom: 600I)

### 5.2.6 HE 1228+0131

Morphologically this host is probably a spheroid ($z = 0.117$). The resulting host flux is very weak, as suggested from the *H* band N/H flux ratio of ~5:1. In the *B* grism the host flux is about 2% of the total flux. There is no trace of narrow lines visible. A mismatch exists between the extracted host spectra in the common spectral regions of *B* and *R* grisms and *R* and *I* grisms. In the *R* grism Hα is oversubtracted in the host. Transfering 0.8% of the nuclear flux into the host brings Hα to zero, but then the disagreement to the *I* grism still remains. Also while in the *B* grism no trace of Hβ is found in the host, it appears strongly in the *R* grism, even in the unmodified host spectrum, which must be an artefact. Again here no narrow lines are visible.

In *I* grism the host spectrum contains 4% of the total flux. Narrow Hα and the [N II] doublet can be seen, but the 2d host frame is too distorted to extract reliable line ratios. The distortions are too large to possibly detect rotation for the gas. The S/N in total is too low for analysis.

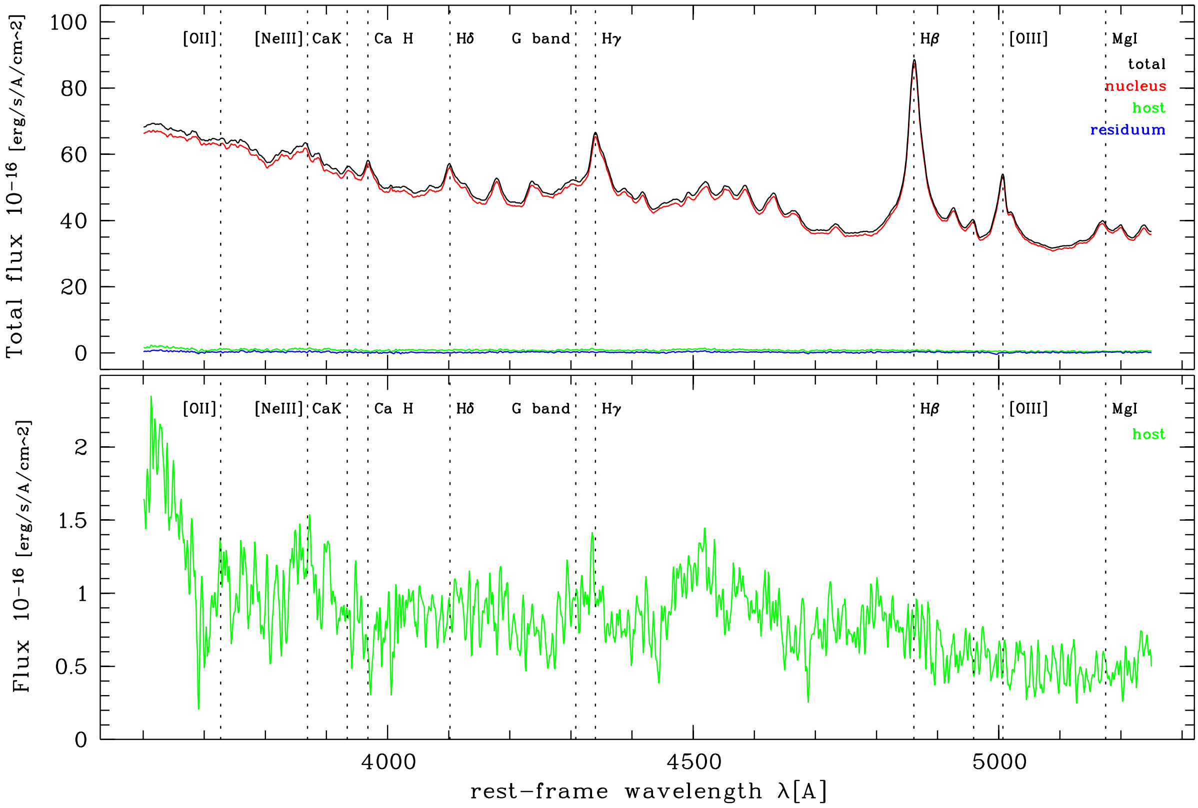

**Figure 5.7.** HE 1228+0131 modelling results for the three grisms (600B here, 600R and 600I on the next page). Lines as in Fig. 5.2.

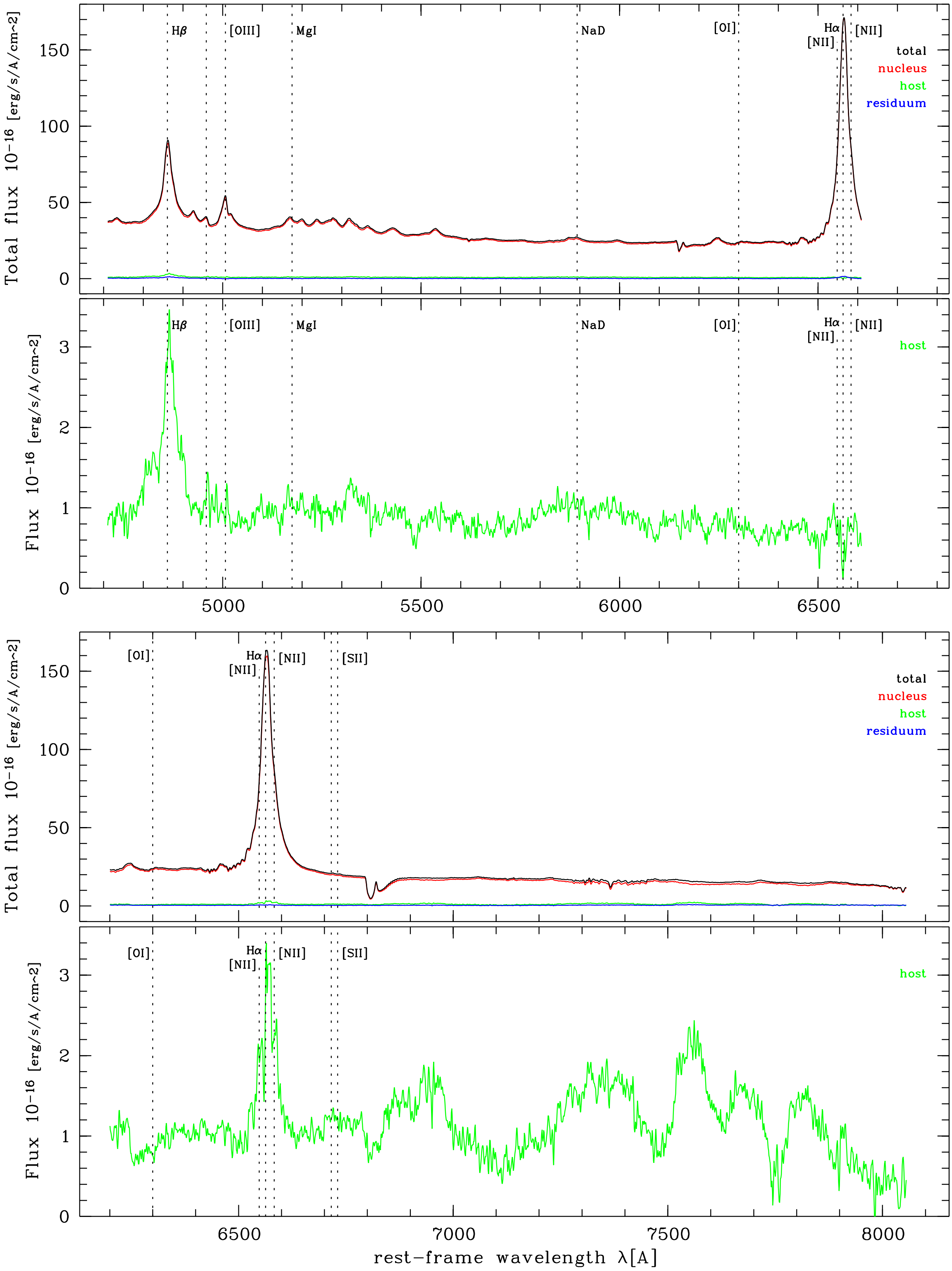

**Figure 5.7.** continued. HE 1228+0131 (top: 600R, bottom: 600I)

### 5.2.7 PKS 1302–1017

The host continuum of this clear spheroidal ($z = 0.2784$) contains a substantial fraction of the total QSO flux, between 10% and 25%, but there is a mismatch in the two overlap regions. Blueward of 4450 Å the host flux in the *R* grism decreases and deviates from the *B* grism flux, being more or less constant in this range. For 4450 Å $< \lambda <$ 4600 Å the two fluxes are identical. For the *R* and *I* overlap there is a similar effect, although smaller. Why this happens is not clear. The overlap regions are free of broad lines and the PSF star is also very bright there. It must be noted that the two-dimensional structure of the residuum is stronger in the *B* grism than in the *R* grisms, which can have an influence on the absolute scaling of the resulting host flux. In general the extracted host continuum is extremely blue.

All gas emission lines have only a slight rotational shift. [O II] and [O III] are visible, both showing flux transfer from the nucleus. In Hγ a trace of narrow emission is visible. Also small and noisy Ca K can be seen, but no Ca H, which might be contaminated by Hε emission. In the *R* grism [O III] was separately modelled with single side modelling, for Hβ this was not possible. The peak at 5258 Å is due to an unmasked central cosmic. Single side modelling in the *I* grism for Hα and [N II] is not possible due to the small rotation, they remain contaminated.

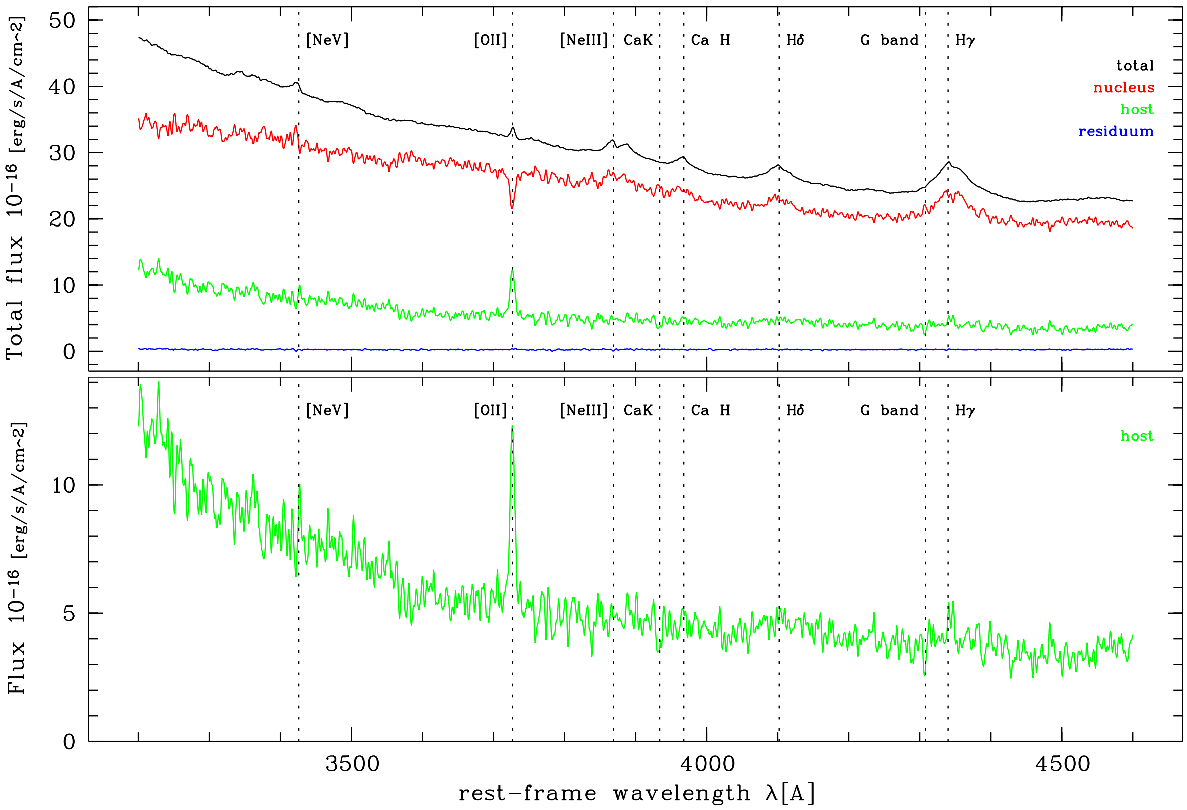

**Figure 5.8.** PKS 1302–1017 modelling results. Lines as in Fig. 5.2.

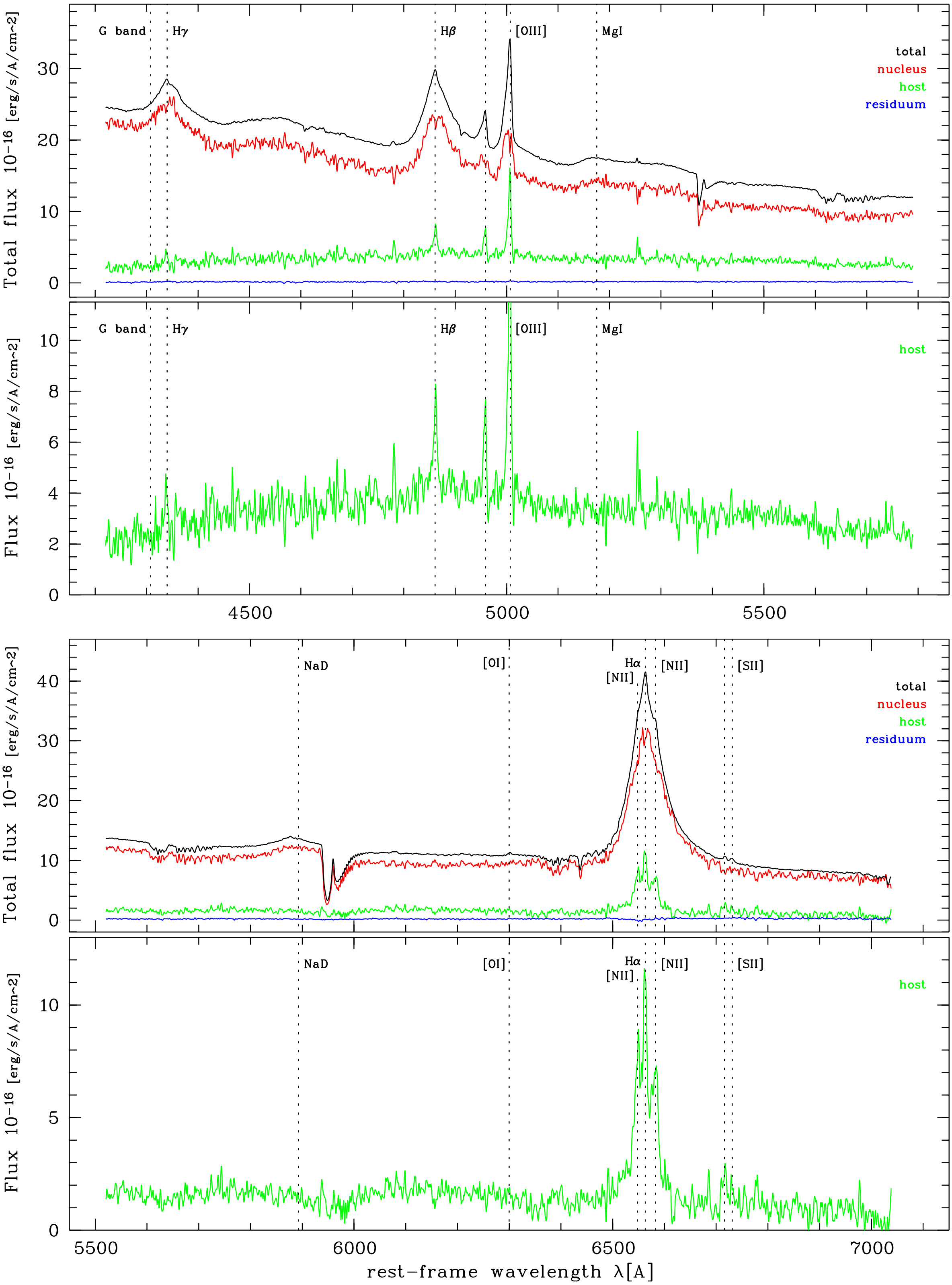

**Figure 5.8.** continued. PKS 1302–1017 (top: 600R, bottom: 600I)

### 5.2.8 HE 1434–1600

This is the second object in common with the multicolour sample from chapter 2, and showing a clearly spheroidal host. Even though this object has a relatively large host flux, compared to some of the other objects in the sample, in the *B* grism its determined flux dips below zero for $\lambda < 4400$ Å. Only adding a substantial fraction of the nuclear model (13%) brings the flux to positive values. Possibly Ca H and the G band absorption are visible. All emission lines are prominent and appear rotationally shifted. The [O II] line shows flux transfer from the nucleus. Emission in Hγ is visible, in Hβ, very prominent [O III] 4959 Å and 5007 Å and also [O III] 4363 Å. Hβ and [O III] are corrected with single side modelling.

Hβ in *R* and Hα in *I* grism are also oversubtracted and adding 10% and 22% respectively of the nuclear model brings host to positive fluxes. In the overlap regions of the grisms the fluxes do not coincide completely, but only for some of the range. In *R* grism also [O III] reappears. The nuclear Hα emission is very broad. The host shows clear narrow Hα, [N II] and [S II] emission.

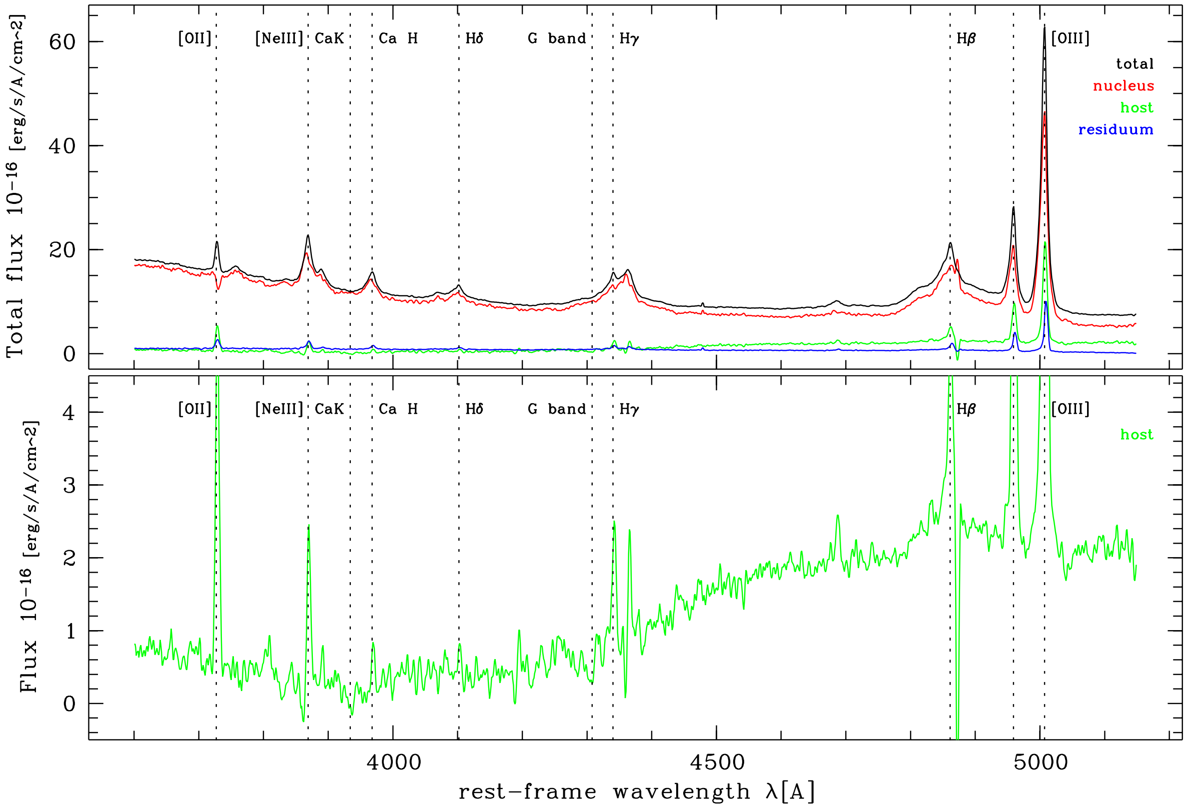

**Figure 5.9.** HE 1434–1600 modelling results for the three grisms (600B here, 600R and 600I on the next page). Lines as in Fig. 5.2.

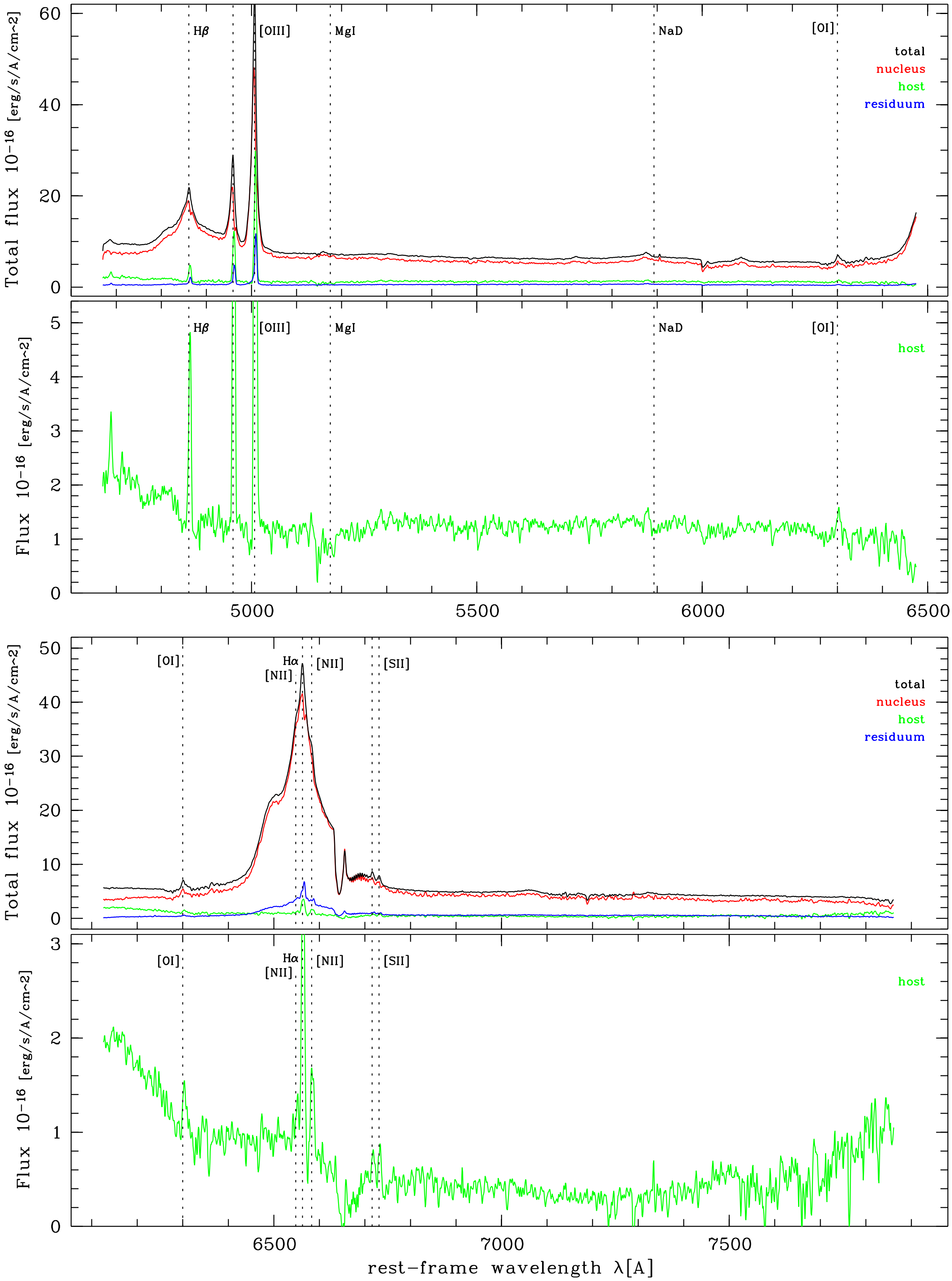

**Figure 5.9.** continued. HE 1434–1600 (top: 600R, bottom: 600I)

### 5.2.9 HE 1442–1139

The host of this object ($z = 0.2596$) clearly is a disk, relatively bright compared to the nucleus in $H$ band imaging (N/H $> 1:1$). In the slit in appears weak in absolute terms but contains 5–20% of the total flux. Only very weak gas emission lines can be seen, [O II] and [O III] 5007 Å present with rotational shift, and traces of [N II] emission. Several prominent stellar absorption lines are present, Ca K, Ca H with a weak 4000 Å break, also G band visible. There seems to be Balmer absorption in Hβ to Hε while Hα is contaminated with a central cosmic. The flux in the overlap regions coincides perfectly.

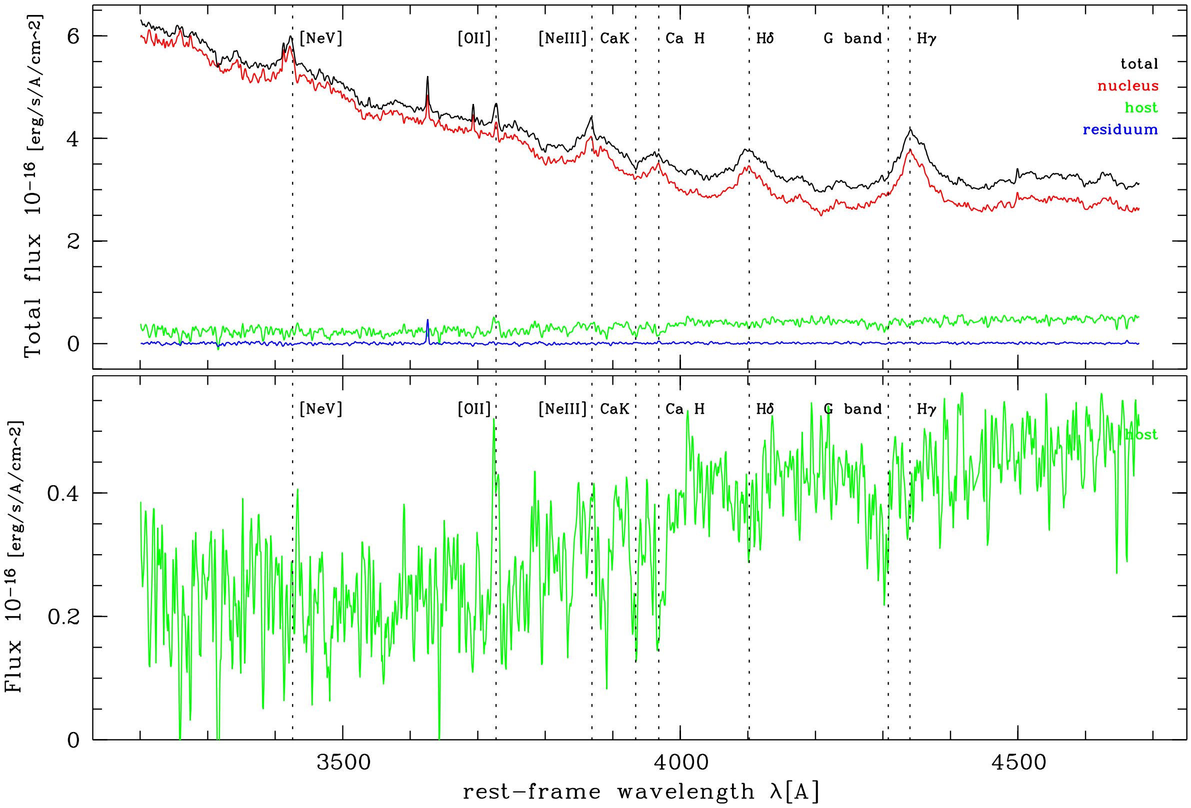

**Figure 5.10.** HE 1442–1139 modelling results for the three grisms (600B here, 600R and 600I on the next page). Lines as in Fig. 5.2.

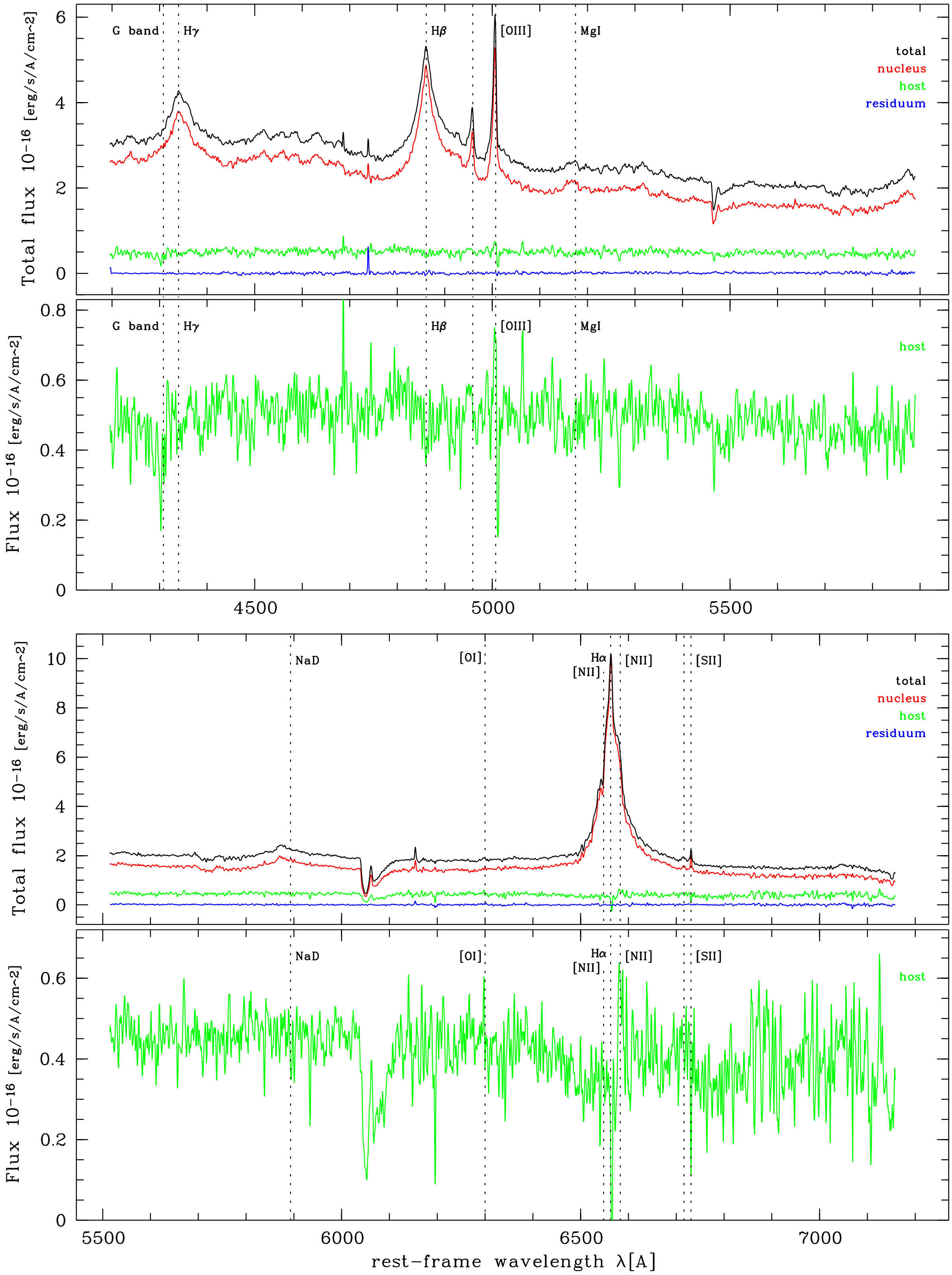

**Figure 5.10.** continued. HE 1442–1139 (top: 600R, bottom: 600I)

### 5.2.10 HE 1503+0228

This is the object with the second lowest redshift ($z = 0.1350$) and best studyable spiral in the sample with similar continuum N/H ratio as HE 1442–1139. Several prominent gas lines are visible. In the $B$ grism [O II], [O III], Hβ, Ca H and K and Fe I 5270 are separately modelled with single sided fit, in the $R$ grism Hβ, [O III] and Hα/[N II], in the $I$ grism Hα/[N II] and [S II]. The latter is disturbed by the atmospheric A band. A slight offset in the overlap regions of $B$ and $R$ grism exists, of the order of 10% at 5100 Å.

The detected gas emission is clearly rotated, so are the stellar absorption features. The Ca H and K, G band, Mg I and Na D absorption lines are prominent.

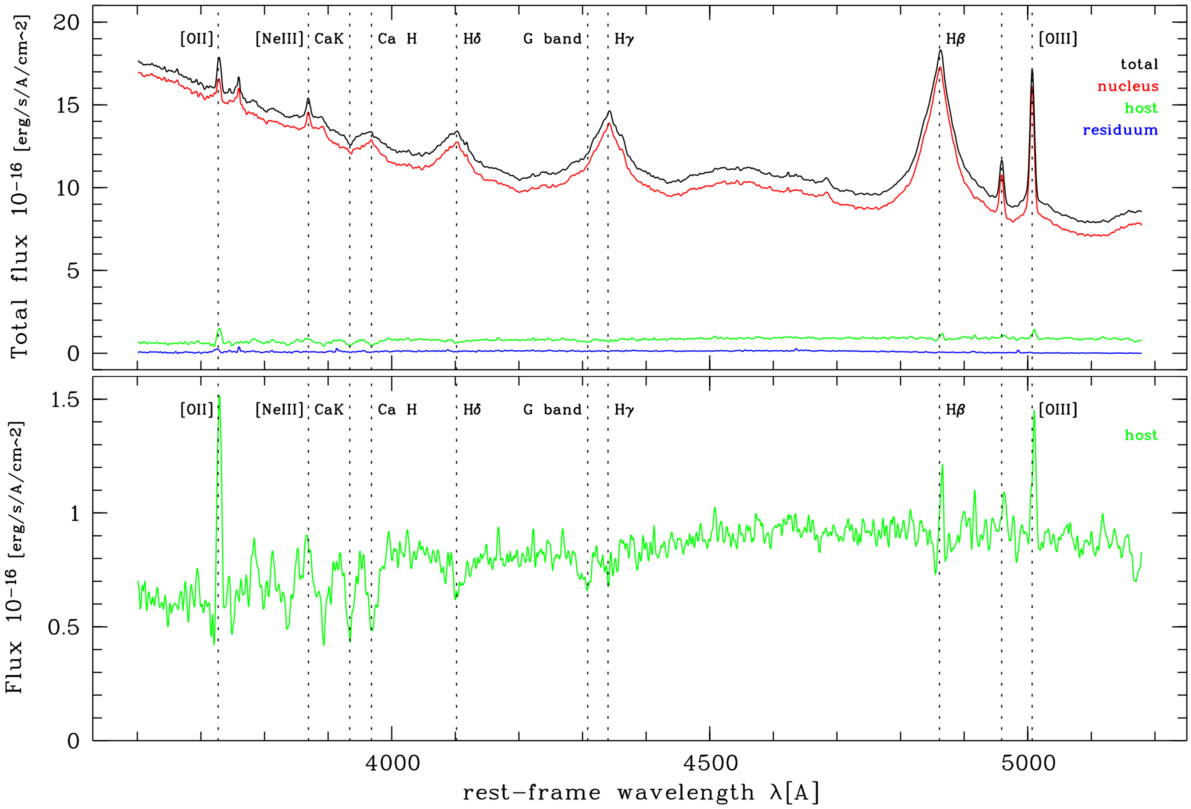

**Figure 5.11.** HE 1503+0228 modelling results for the three grisms (600B here, 600R and 600I on the next page). Lines as in Fig. 5.2.

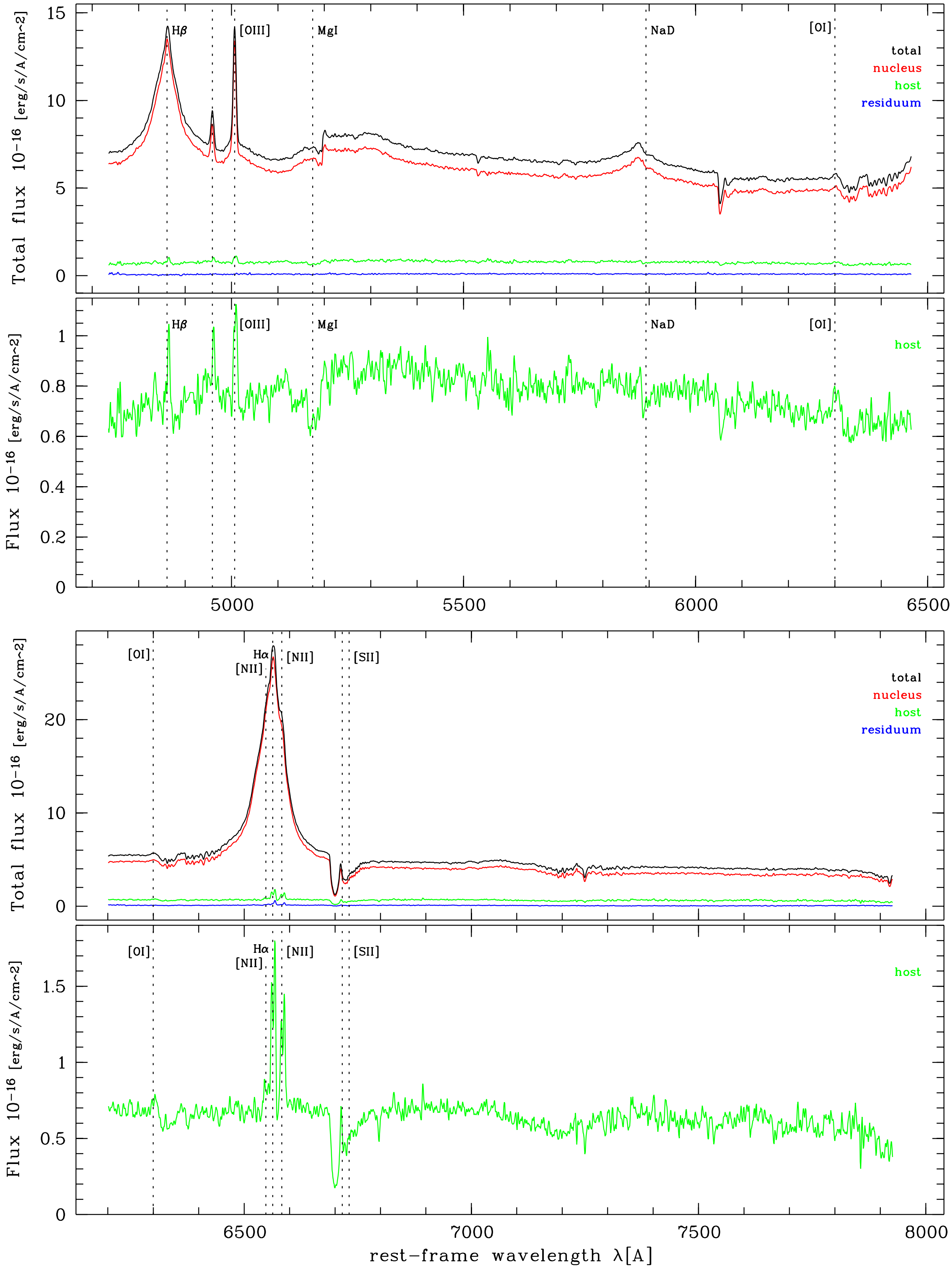

**Figure 5.11.** continued. HE 1503+0228 (top: 600R, bottom: 600I)

## 5.3 Results

The modelling yielded usable results for seven of the ten objects. For HE 0956-0720, HE 1015-1618 and HE 1228+0131 we conclude that the S/N of the host is too low to reliably model the system and analyse the host. These three objects are thus excluded in the following.

### 5.3.1 Host dynamics from line shifts

Coordinated rotation of stars and/or gas inside a galaxy can yield information about the dynamics of the host and, if the data quality permits, also about the mass distribution. Depending on the S/N of the data it is possible to extract detailed rotation curves, giving spatially resolved information about rotation, or average rotation velocities.

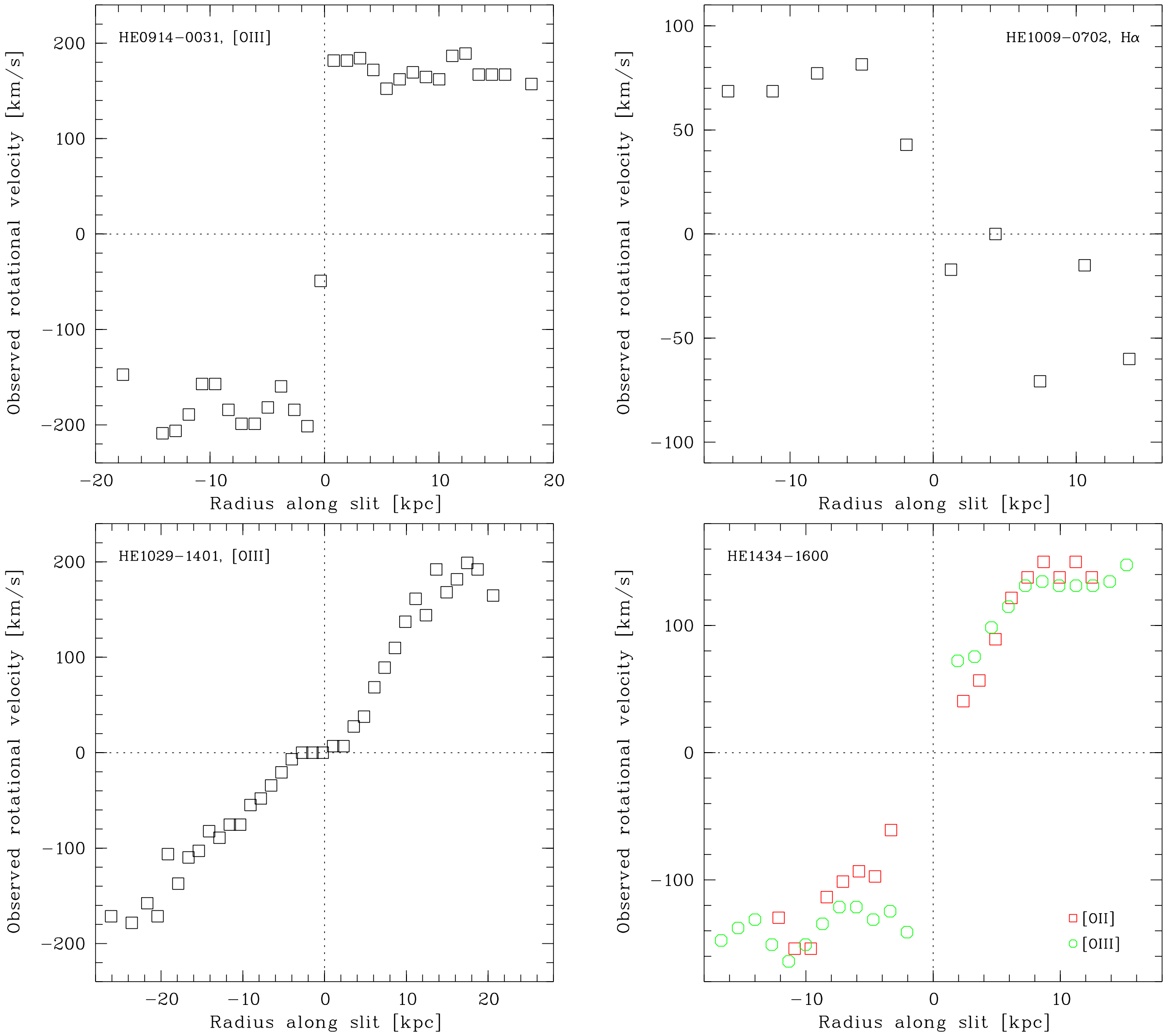

**Figure 5.12.** Observed rotation curves of four objects as measured from the [O III] 5007 Å line, and for HE 1434–1600 also from [O II] 3727 Å: Plotted are the observed velocities against the radius coordinate along the slit, centered on the QSO center.

The achievable spatial resolution for investigation of the rotation velocities depends on the angular resolution of the detector pixel grid, the seeing, the S/N and the magnitude of modelling residuals contained in the 2d host spectrum.

We extract rotation curves by fitting a Gaussian to the variance-weighed average of, in most cases two, adjacent columns. At large radii more than two columns are used to increase S/N. For HE 1503+0228 we coadded several columns to increase S/N (see below). Fitting of the gaussian was done after smoothing the spectrum by convolution with a gaussian of usually $\sigma = 2$ pixel corresponding to a FWHM of $\sim 4\ldots5$ Å. The smoothing was necessary to avoid local minima in the fitting process.

In addition to spatially resolved rotation curves we tried to obtain average values of rotation velocities for the two sides of the object. This increased the S/N of the measurement for low S/N lines for which rotation curves would not be extractable.

We find clear signs of a rotating gas disk in six of the seven objects remaining. For five of those we could obtain rotation curves, in addition for HE 1442–1139 an averaged rotation velocity is available. Figures 5.12 and 5.16 show the observed emission line rotation curves for these objects. This means that beside the three disks left in the sample also most of the spheroids contain visible rotating gas disks. For three objects the strength of the Ca H and K absorption was sufficient to measure systematic offsets. For HE 1029–1401 clearly non-rotation is found, as expected for a spheroidal. For the two other objects, HE 1442–1139 and HE 1503+0228, both disks, rotation is detected.

Since we only have tentative results on the morphology of the host galaxies available, we do not know the exact inclination and orientation of the objects. Only for HE 1503+0228 we know the inclination of the disk and the orientation of the slit axis with respect to the major axis of the host from Courbin et al. (2002b). In order to estimate the mass distribution creating the rotation curve for HE 1503+0228, we compute models assuming three different components present in the QSO, following the approach described in Courbin et al. (2002b): A central mass excerting the force

$$F_{\mathrm{cent}}(r) = -\frac{GM_{\mathrm{cent}}}{r},$$

with $M_{\mathrm{cent}}$ being a central mass containing the nucleus and all unresolved central mass of the host, a thin disk

$$F_{\mathrm{disk}}(r,z) = -\frac{r^2 GM_{\mathrm{disk}}}{(r^2+(R_{\mathrm{disk}}+|z|)^2)^{\frac{3}{2}}},$$

with $M_{\mathrm{disk}}$, and $R_{\mathrm{disk}}$ being the mass and scale length of the disk respectively, and assuming a negligible scale height $z = 0$ for simplicity. The third component is a spherically symmetric dark matter halo with decreasing density, parametrised as

$$F_{\mathrm{dark}}(r) = -\frac{4\pi G\rho_{0,\mathrm{dark}}R^3_{\mathrm{dark}}}{r}\left(\frac{r}{R_{\mathrm{dark}}} - \arctan\frac{r}{R_{\mathrm{dark}}}\right),$$

(Binney & Tremaine 1987) with $R_{\mathrm{dark}}$ and $\rho_{0,\mathrm{dark}}$ being the scale length and central density. The model rotation velocity is then given by

$$V_{\mathrm{mod}}(r) = \sqrt{-r(F_{\mathrm{cent}}(r)+F_{\mathrm{disk}}(r)+F_{\mathrm{dark}}(r))}.$$

We compute this model velocity curve on a very fine grid and convolve it with a one-dimensional gaussian with a width according to the seeing of the spectrum in question. The velocities and radii involved are the intrinsic values, the measured values are projections as described in section 4.3.1. The computed models are compared to the deprojected data points. In this approach we disregard the mixing of velocity components due to the influence of the seeing, the width of the slit, and the averaging of columns, but this method can deliver ballpark numbers on $M_{\mathrm{cent}}$, $M_{\mathrm{disk}}$, $R_{\mathrm{disk}}$, $R_{\mathrm{dark}}$ and $\rho_{0,\mathrm{dark}}$ for HE 1503+0228.

Investigating all seven objects in detail:

- **HE 0914–0031**: The only clear lines are in the [O III] doublet, being the only detectable emission at all. Both are rotated, but the 4959 Å component is rather weak. The 5007 Å component was used to construct the rotation curve in Fig. 5.12 (top left). As the residual was very good, the central pixels could be included, even though we do not resolve the central kiloparsec. The velocity is rather constant with radius for $r > 1$ kpc and can be traced to 20 kpc radius. This points to a massive extended halo. The steep rise in the center is unresolved, but suggests a relatively large mass contained within the smallest resolved radius for the object, counting the core of the galaxy and central black hole combined. Working with the projected parameters, this mass is of the order of $2.0\ldots3.0 \cdot 10^9\ M_\odot$.

- **HE 1009–0702**: H$\alpha$ was used to create the rotation curve shown in the top right of Fig. 5.12. The line is disturbed on the right side, which can be attributed to the low S/N. We had to average three columns to even receive this curve. Nevertheless, the left side shows the typical shape of a rotation curve, thus clearly a gas disk is present also in this likely spheroidal host. As the inclination on the disk is unknown, it is not possible to compute $v_{\mathrm{rot}}$.

- **HE 1029–1401**: For the extraction of this rotation curve of HE 1029–1401, [O III] was modelled with single side modelling and rescaling of the central two rows. The central part of the rotation curve (bottom left in Fig. 5.12) looks very peculiar. It is almost flat, with a slow increase of the rotation velocity with radius. This zero rotation could be caused by residual nuclear contribution, being symmetric and thus decreasing any existing shift in the host. At radii $r > 15$ kpc, corresponding to $5''$, the influence of the seeing and thus potential nuclear flux would drop to very small values and the true rotation becomes visible. Even though we do not see any unusual oversubtraction in the resulting nuclear model or apparent extra flux in the host, the central part of the rotation curve suggests a contamination with residual nuclear flux. It is clear, however, that in this massive spheroidal a gas disk exists, extending throughout the host, with normal rotation velocities. If the nuclear contribution in fact is small, and assuming spherical symmetry, the rotation curve traces an increase $M(r) \propto r^2$ up to $r = 15$ kpc.

  HE 1029–1401 is the only spheroidal in the sample where the rotation of an absorption line could be investigated. For this task the left and right part of Ca K at 3934 Å were averaged separately. As shown in Fig. 5.13 the line has the same shape and centre in wavelength on both sides. The apparent shift from its nominal position is due to modelling noise and determining the redshift from the emission lines. As expected for a spheroidal, no systematic rotation is visible.

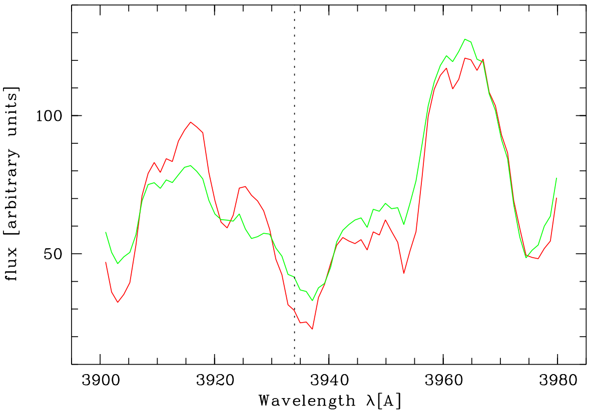

**Figure 5.13.** Ca K line of HE 1029–1401: separately extracted left (red) and left (green) sides of the Ca K 3934 Å stellar absorption line show no rotation, as expected from morphology. The apparent line shift from the nominal position (vetical line) is not real and due to modelling noise, which appears symmetrically for both sides.

- **PKS 1302–1017**: For this radio-loud spheroid we modelled the [O III] 5007 Å line to investigate rotation. We only find a trace of rotation, shown in Fig. 5.14: Shown is a contour plot of the 5007 Å line, with contours equally spaced in log. The line shown is connecting the loci of the largest extentions of the individual isophotes, thus tracing the local maxima at each radius. Visible are variations corresponding to a variation of 80 km/s or a rotation velocity of half of that. Interestingly the line is suggestive of point symmetry to the centre of the line, compatible with rotation. So if this is real, either there exists only a very small coordinated rotation component, or a very strong projection effect of a disk with very small inclination reduces the velocity.

- **HE 1434–1600**: For this spheroidal we extracted rotation curves for [O II] 3727 Å and [O III] 5007 Å, which were individually modelled. The rotation curve in Fig. 5.12 (bottom right) might contain slight residuals of nuclear contamination in [O II] as for HE 1029–1401, but rotation is clearly detected, thus a gas disk exists. The long linear increase in

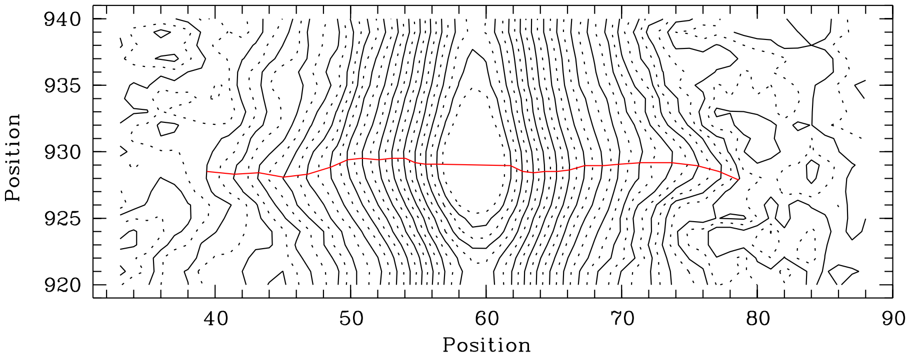

**Figure 5.14.** Contour plot of the [O III] 5007 Å emission line of the host of PKS 1302–1017. Spatial direction is horizontal, dispersion vertical, contours are spaced evenly in logarithm, the scale is in pixels. The red curve is tracing the loci of the largest radial extention of each isophote. A point symmetry of this line to the centre of the emission line is visible. If this is due to rotation, the variation of velocity is $< 40$ km/s. The length of the line corresponds to 40 kpc.

rotation velocity to $r \sim 8$ kpc shows a mass increase with $r^2$ until this radius, which demands a density decline much shallower than the de Vaucouleurs law for surface brightness. Again a strong evidence for a massive halo.

- **HE 1442–1139**: No emission line had sufficiently high S/N and was undisturbed to generate a rotation curve. In the left part of Fig. 5.15 a contour plot of [O III] 5007 Å is shown, as for PKS 1302–1017. Again overplotted is a line connecting the loci of the largest extention of each isophote, tracing the line. The line is disturbed by a range of rows with residuals from sky subtraction, marked with the horizontal lines. The lower half of the emission line of the left side seems to lie in this area thus the rotational shift will be somewhat larger than seen in the plot. We estimate the shift to be at least 4.5 pixels, corresponding to an average rotation velocity of 115 km/s.

  For HE 1442–1139 rotating absorption lines are visible. We coadded the 2d frames for the two components of the Ca line and extracted the left and right sides separately. The right part of Fig. 5.15 shows the results: Both sides are shifted from the nominal position (vertical dashed line), but only by about half a pixel. There is a large uncertainty in the velocity, but the rotation seen is clearly slower than the gas rotation, an upper limit lies around 40 km/s. This seems incompatible with corotation with the gas. Thus either gas disk and stellar disk are not aligned, or we see the signature of a bulge in this object, which is also seen in the modelling of the *H* band images. A bulge would contribute more flux in a long slit spectrum than a stellar disk of equal total luminosity, due to its compactness. Thus what we see could be a mix of bulge and disk light, with the bulge producing non-shifted absorption, and only a smaller contribution by the stellar disk, reducing the total observed rotation shift as could be expected from the disk alone.

- **HE 1503+0228**: The highest S/N host spectrum comes from HE 1503+0228. Here it was

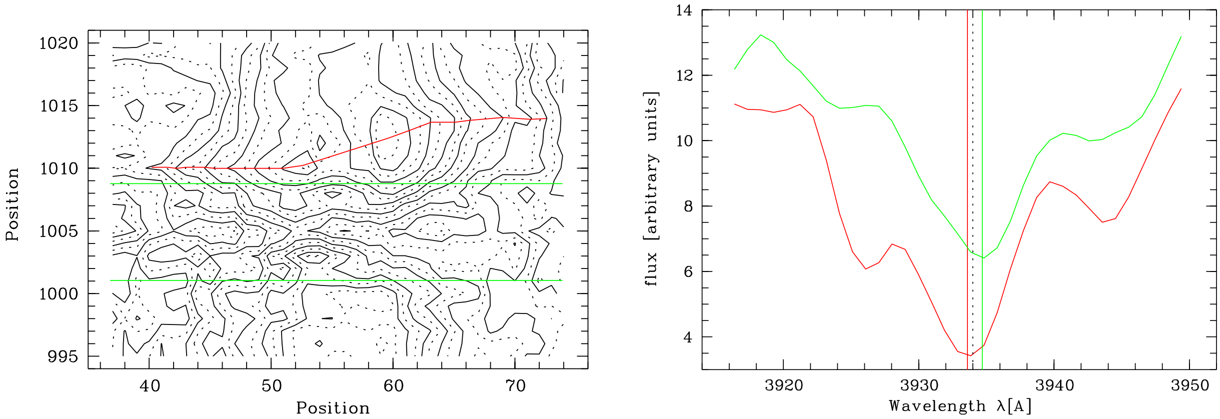

**Figure 5.15.** Rotation of HE 1442–1139. Left: Contour plot of the [O III] 5007 Å emission line similar to Fig. 5.14. The green horizontal lines delimit an area of residuals from sky subtraction that blot out half of the left side of the line. The length of the red line corresponds to 33.5 kpc, rotation velocity is about 115 km/s. Right: Combined Ca H and K absorption line. The two sides (red left, green right) are shifted against the nominal position marked by the dashed line. Rotation is in the same direction as the gas rotation, but velocity is only $< 40$ km/s.

possible to model all parts of all emission lines detected with single sided modelling, thus giving very reliable estimates of the host's emission lines free of nuclear contamination.

In the *B* grism we modelled [O II], Hβ, the [O III] doublet, Fe I 5270 Å and the Ca H and K absorption lines, in the *R* grism again Hβ, and [O III] as well as Hα and the [N II] doublet. In the *I* grism Hα and [N II] and the [S II] doublet. For the construction of the rotation curve shown of the left side of Fig. 5.16, we coadded all available emission lines in the *B* and *R* grism separately, weighing according to variance, to again increase the S/N. In this process the images were rebinned to correct for the different centre coordinates and rotation velocity per pixel with the "drizzle" algorithm by Fruchter & Hook (2002).

The coadded lines and thus the rotation curves are dominated by the brightest line, being [O II] in the *B* grism and [O III] 5007 Å in the *R* grism. On both sides of the object the rotation curves are similar, the right side being symmetric to the left side, except for a dip in the *B* curve around $r = 6$ kpc. We show the rotation curves using deprojected values, intrinsic velocity and radius along major axis. They were computed using inclination $i = 46°$ and angle between slit and major axis $\phi = 23$, taken from Courbin et al. (2002b), corresponding to conversion factors of 1.08 from radius along slit to radius along major axis, and 1.63 between observed and intrinsic velocity.

Interestingly we find a variation for the average rotation velocities measured for each line shown in the right panel of Fig. 5.16. The strongest line, [O II], shows also the highest rotation velocity of all emission lines, if the weak Fe I emission at 5270 Å is left out, but there is no obvious trend with line intensity.

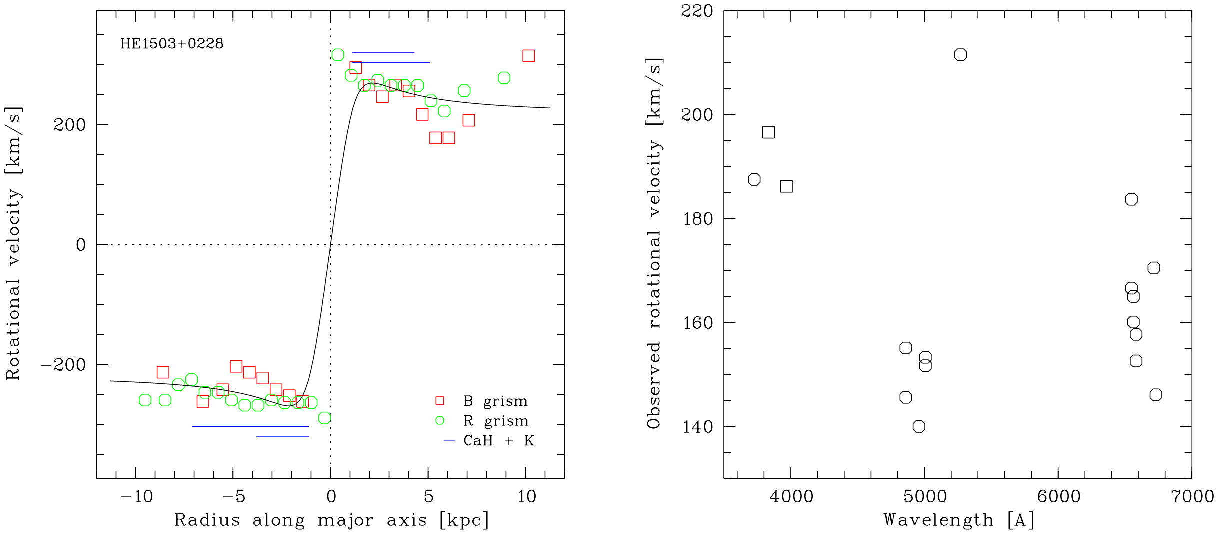

**Figure 5.16.** Rotation of HE 1503+0228. Left: Rotation curve from coadded emission line images in two grisms. The horizontal lines mark the average stellar rotation velocities from Ca H and K with their respective range of averaging. The velocities and radii are deprojected and correspond to radius along major axis of the galaxy and intrinsic velocity, assuming inclination $i = 46°$ and angle between slit and major axis $\phi = 23$. The solid line is a model (see text). Right: Observed rotation velocities for all measurable lines. Circles mark emission lines, the two squares Ca H and K stellar absorption lines.

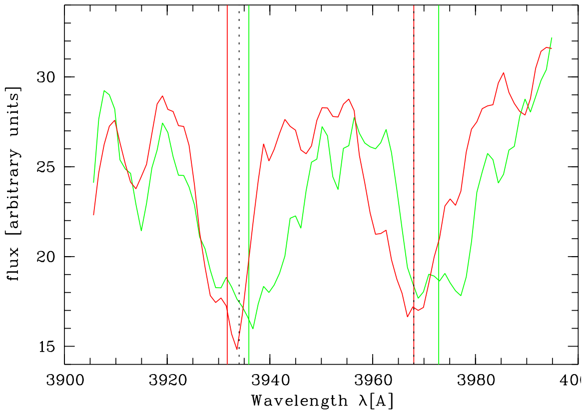

**Figure 5.17.** The Ca absorption doublet of HE 1503+0228: Separately extracted left (red) and left (green) sides of both lines show clear rotation of the order of 150 km/s. Both sides of Ca H are shifted against the nominal position (dashed line) determined from Ca K and the narrow gas lines, probably due to a blend with another line.

Using the model described above, we estimate the best fitting model parameters for the observed rotation curve. We find that we do not resolve the innermost rise of the velocity, thus the mass of the central component $M_{\mathrm{nuc}}$ can not be estimated. We can give, however, a value of $M_{\mathrm{nuc}} \sim 5 \cdot 10^9 M_\odot$ that is necessary to fit the innermost points. The mass of the disk component is of the order of $M_{\mathrm{disk}} \sim 4 \cdot 10^{10} M_\odot$, with a scale length of $R_{\mathrm{disk}} \sim 1$ kpc. The dark matter halo central density and scale are strongly correlated, a valid combination is $\rho_{0,\mathrm{dark}} = 0.33 M_\odot/\mathrm{pc}^3$ and $R_{\mathrm{dark}} = 1.6$ kpc.

Comparing this with the results of Courbin et al., the determined rotation curves are very similar. The main difference lies in resolution and thus the inner few parsecs. Here Courbin et al. trace a decrease of the rotation velocity down to zero in the center. We find modelling residuals in the in the two centre pixels in our 2d spectrum. It is however not clear if the decrease found by Courbin et al. is real, or if it is an artefact created by their deconvolution routine. We find that for the innermost points our velocities are lying systematically higher than found by Courbin et al.. We can't model these with the parameters given by Courbin et al., unless a substantial central mass of several $10^9 M_\odot$ is added. It is unclear if this might in part be due to our simplified approach using one-dimensional convolution in the rotation curve modelling. If this were the case, our parameters are consistent with Courbin et al..

The high S/N of the spectrum allows to detect stellar rotation also in absorption lines. Extracted spectra of the left and right side of the spectrum of the Ca doublet are shown in Fig. 5.17. Both components show rotation with observed velocities of 140 and 160 km/s. These are similar velocities as measured for the gas rotation – both in value and in sign. Thus gas and stars corotate.

We summarise the rotation properties of the sample in Table 5.2. Gas rotation is visible for all except PKS 1302–1017 which only shows a trace. Stellar rotation derived from Ca absorption lines could be investigated in three objects. The one spheroid shows no coordinated stellar rotation, the two disks do, as expected. For one disk a corotation of gas and stars is likely detected, the other one might show a substantial bulge component.

**Table 5.2.** Rotation properties of the sample. Rotation velocities are in units of km/s. A "?" is given, if this property is not known, "–" if this property is not accessible.

| Object | Type | $i$ [°] | $\phi$ [°] | Gas rot. | $v_{\rm g,obs}$ | $v_{\rm g,rot}$ | Stell. rot. | $v_{\rm s,obs}$ | $v_{\rm s,rot}$ |
|---|---|---|---|---|---|---|---|---|---|
| HE 0914–0031 | D | – | – | y | 180 | – | ? | – | – |
| HE 1009–0702 | ED | – | – | y | 75 | – | ? | – | – |
| HE 1029–1401 | E | – | – | y | 180 | – | n | 0 | – |
| PKS 1302–1017 | E | – | – | ? | $<40$ | – | ? | – | – |
| HE 1434–1600 | E | – | – | y | 140 | – | ? | – | – |
| HE 1442–1139 | D | – | – | y | 115 | – | y | $\sim 40$ | – |
| HE 1503+0228 | D | 43 | 23 | y | 160 | 260 | y | 150 | 245 |

### 5.3.2 Spatial gas distribution

Velocity estimates of the interstellar gas in the host can be complemented by an analysis of the spatial shape of emission lines. In case that the ionising radiation reaches the outer limits of the host, and the ionising spectrum doesn't change, the radial profile of an emission line simply map the distribution of the gas. Thus if an emission line can be continuously traced to fainter surface brightness down to the noise level, and if this coincides with the traceability of the continuum, then this is suggestive of ionisation throughout the galaxy. If, however, at some radius the profile ends, one of two causes are possible. Either a limited extention of the gas, or, if the nucleus or a circumnuclear starburst were the source for ionised gas, and the number of high energy photons were limited so that only inside a given radius the gas was ionised.

To study the radial shape, we created variance weighed averages of the spatial profile of emission lines, subtracting the underlying continuum and compare it to the shape of the continuum itself. Usually the [O III] lines were used, being the strongest lines, if possible the two components coadded. The continuum used for comparison was taken from adjacent wavelength ranges, to guarantee similar width and centering of PSF and QSO as for the line. For HE 1503+0228 we coadded all available lines in the *B* grism. For HE 1009-0702 no extraction was possible, as the [O III] 5007 Å line is disturbed and the others are too noisy. For HE 0914-0031 no continuum can be extracted, because, as noted in 5.2.1, this is not resolved.

The results for the the six objects are shown in Figure 5.18. Plotted is the logarithm of the flux against a radial coordinate, given in seconds of arc. The solid curve is the emission line, the dashed red curve the continuum, scaled to match the emission in flux. We ordered the objects so that the three disks are shown on the left side, the spheroidal hosts on the right side. The disks are more or less conform with the exponential disk profile, which would appear as a straight line in the log diagram, modified by the seeing.

- HE 0914–0031 shows no cutoff or deviation from a pure exponential disk profile.
- For HE 1442–1139 continuum and line seem to have different centers, but this is due to a quarter of the line missing as was described in the previous section and shown in Fig. 5.15. With this in mind the two profiles are compatible with identical surface brightness distributions. The profiles do not suggest any reason for the different rotation velocities found for stellar and gas component.

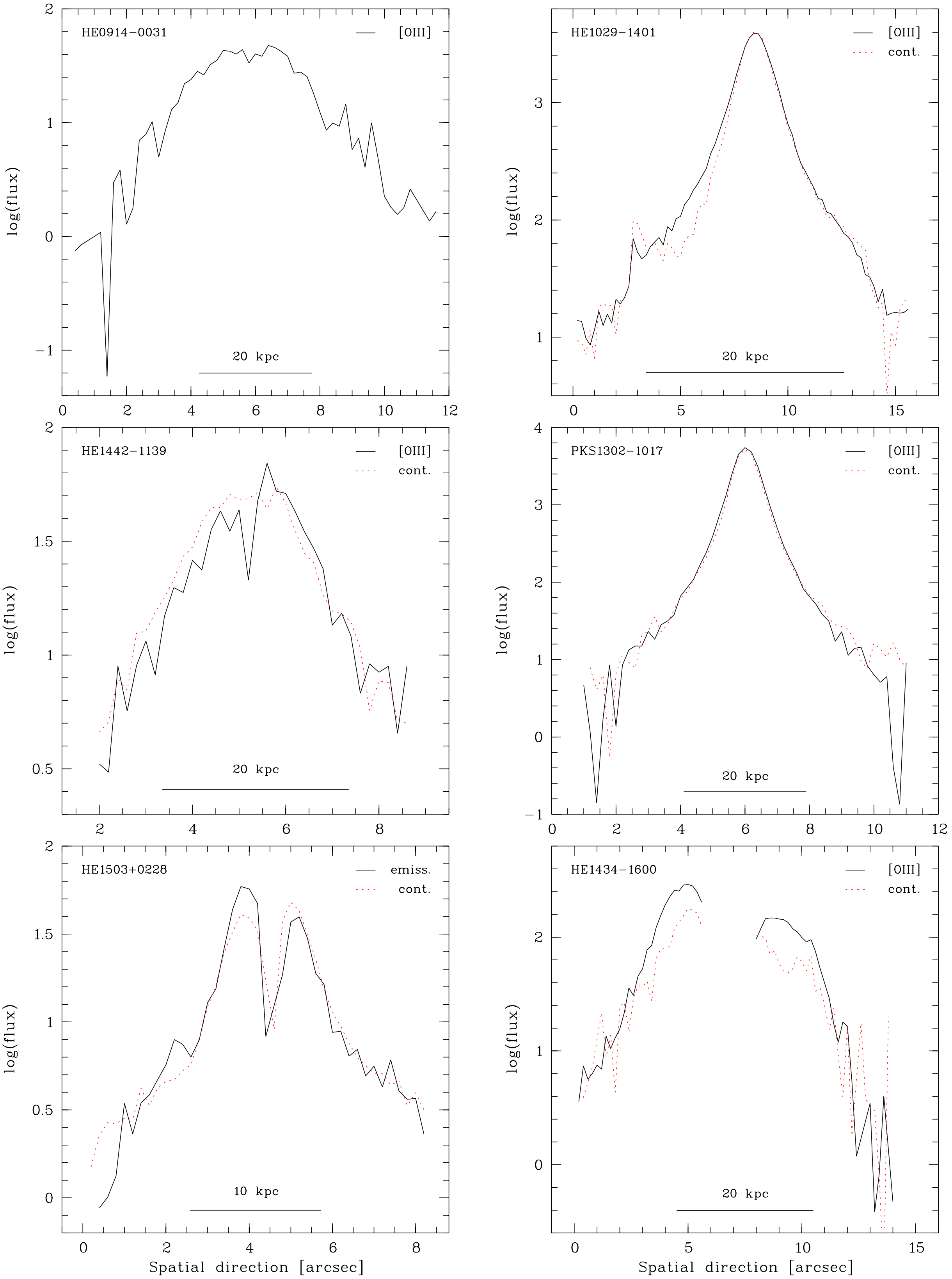

**Figure 5.18.** Radial profiles of the [O III] 5007 Å emission line and adjacent continuum.

- The profiles of HE 1503+0228 are disturbed in the centre as a result of modelling. While for the very centre the profiles are oversubtracted, they show an excess at around $1.5''$ distance from the center, creating an inflection further out. This is a signature of the residuals of the nuclear model, not a sign for a spheroidal host. Line and continuum are compatible.

- For HE 1029–1402 the profile of the line on the right side coincides with the profile of the continuum. As noted in the previous chapter, the rotation curve created from the same [O III] line seems to be contaminated with residual nuclear contribution. This explains why the emission line profile has inflections points and a clearly non-exponential core, and becomes more exponential like in the outer parts ($r > 5''$). No apparent cutoff is visible, the secondary peak and drop at $3.5''$ is due to structure in the CCD and flatfielding and visible for all of the spectrum.

- PKS 1302–1017 shows two very similar profiles, supporting the case of no rotating gas disk present in the spheroidal host. Even if the disk were seen almost face-on and thus the observed rotation velocity close to zero, the radial surface brightness profile would appear as an exponential disk.

- HE 1434–1600 is a very interesting case. The central pixels are disturbed by modelling residuals. When scaling the continuum so that the outer parts of the two profiles coincide, an excess of line emission can be seen further in.

  Looking at a contour plot of the total 2d spectrum, i.e. without the nuclear component removed (Fig. 5.19), one can clearly see the two rotated parts of the emission line, that *decrease* again toward the center. In the profile this decrease is blotted out by the bad centre pixels. As the nucleus is clearly the source of ionising radiation (see next section), this means that the gas does not extend all through the galaxy but is depleted in the centre.

### 5.3.3 Emission line ratios

The spectra have a quality that allows to estimate several diagnostic line ratios. To study the main ionisation mechanisms and their sources, it is particularly interesting to determine the [O III] 5007/H$\beta$, [N II] 6583/H$\alpha$, [S II] (6716+6731)/H$\alpha$, and [O I] 6300/H$\alpha$ line ratios, because

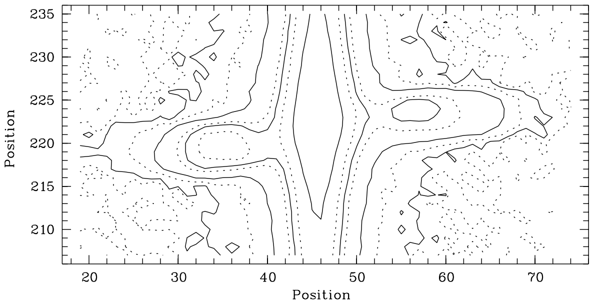

**Figure 5.19.** [O III] 5007 Å emission line of HE 1434-1600. This is the composite line, i.e. with host and nucleus combined. Clearly visible are rotated emission line components that *decrease* again towards the center. Position is given in pixels, with a scale of $0.2''$ and 1.1 Å per pixel, respectively.

they are relatively insensitive to internal extinction (Veilleux & Osterbrock 1987). For determination of temperatures we investigate the [O III] (4959+5007)/4363 line ratio and for electron densities the ratio of the [S II] 6716+6731 doublet (Osterbrock 1989).

A difficult task is error estimation for line strengths, as three errors sources have to be considered:

- photon shot noise
- modelling errors
- continuum estimate errors

The only formally describable error source is the photon shot noise. Modelling errors are difficult to quantify, but due to the similar treatment of all lines, with single sided modelling, it can be expected that the modelling error contribution for line ratios is much smaller than for line intensities. A particular problem is stellar continuum Balmer absorption with a superposed gas emission. Wherever possible we fit a model spectrum of a single stellar population of intermediate age (Bruzual & Charlot 1993, 1996) to the local continuum and adopt the model continuum as the local continuum for the line.

The final error is given by a combination of remaining uncertainties for the continuum, increased by a contribution for modelling uncertainties. Due to the common background fit for [O III] 5007 Å and Hβ as well as [N II] and Hα the errors are not independent. The errors given are not meant as formal errors but as good estimates to for the uncertainty.

In Table 5.3 we compiled for the sample the available diagnostic emission line ratios for determining the source of ionisation. Veilleux & Osterbrock (1987) give three pairs of diagnostic line ratios that clearly distinguish AGN and stellar ionisation objects. Thus the underlying dominant ionisation mechanism can be determined if these ratios are known. Figure 5.20 shows our values with the division lines determined by Veilleux & Osterbrock. According to Veilleux & Osterbrock the line ratios used are very insensitive to internal extinction. The corrections to be applied in their samples is of similar size, or even smaller, than our error bars. It has to be kept in mind, however, that lines, for which individual modelling was not possible, might still be overestimated from nuclear contamination. This is particularly the case for [O I] 6300 Å. Because this line appears rather weak, modelling errors would not be obvious. A 30% overestimation would change the $\log([\mathrm{O\,I}]/\mathrm{H}\alpha)$ ratio by $-0.12$ dex. Such a change has not been incorporated

**Table 5.3.** Available diagnostic emission line ratios for determining the ionisation source.

| Object | $\log\frac{[\mathrm{O\,III}]}{\mathrm{H}\beta}$ | $\log\frac{[\mathrm{N\,II}]}{\mathrm{H}\alpha}$ | $\log\frac{[\mathrm{S\,II}]}{\mathrm{H}\alpha}$ | $\log\frac{[\mathrm{O\,I}]}{\mathrm{H}\alpha}$ |
|---|---|---|---|---|
| HE 0914–0031 | $> 0.75$ | – | – | – |
| HE 1009–0702 | – | $-0.27 \pm 0.07$ | – | – |
| HE 1029–1401 | $0.44 \pm 0.06$ | $-0.09 \pm 0.05$ | – | $-0.77 \pm 0.1$ |
| PKS 1302–1017 | $0.80 \pm 0.15$ | $-0.12 \pm 0.15$ | – | – |
| HE 1434–1600 | $0.92 \pm 0.1$ | $-0.39 \pm 0.1$ | $-0.45 \pm 0.08$ | $-0.76 \pm 0.1$ |
| HE 1442–1139 | – | – | – | – |
| HE 1503+0228 | $0.15 \pm 0.05$ | $-0.20 \pm 0.05$ | – | $-0.93 \pm 0.15$ |

in the values in Table 5.3. For the stronger lines modelling errors would be apparent in the 2d residuals of the modelling if the lines are rotationally shifted. Contaminations with nuclear flux by factors $> 3$ that would be needed to shift several of the objects into the stellar ionisation area in Figure 5.20 can definitely by ruled out.

The point for HE 1009–0702 in the bottom diagram of Fig. 5.20 is a $\log([\mathrm{N\,II}]/\mathrm{H}\alpha)$ value only, $\log([\mathrm{O\,III}]/\mathrm{H}\beta)$ could not be determined. In addition, an upper limit for HE 0914–0031, $\log([\mathrm{O\,III}]\,5007/\mathrm{H}\beta) > 0.75$, is not shown.

All of our objects lie in the AGN region for all diagrams. The object closest to the dividing line is HE 1503+0220, the only disk for which line ratios are available. Courbin et al. did not measure these line ratios but measured equivalent widths (EW) of [O II] 3727 Å, the [O III] doublet and Hα and [N II]. They find a larger EW for [O III] 5007 Å than for a sample of inactive spirals investigated by Kennicut (1992), pointing to an excitation process related to the AGN. Apart from that no signs are found for power-law ionisation. The object falls directly onto the relation for normal spiral galaxies found by Kennicut. The two line ratio pairs for HE 1503+0228 shown in Fig. 5.20 suggests that at least some excitation comes from the AGN.

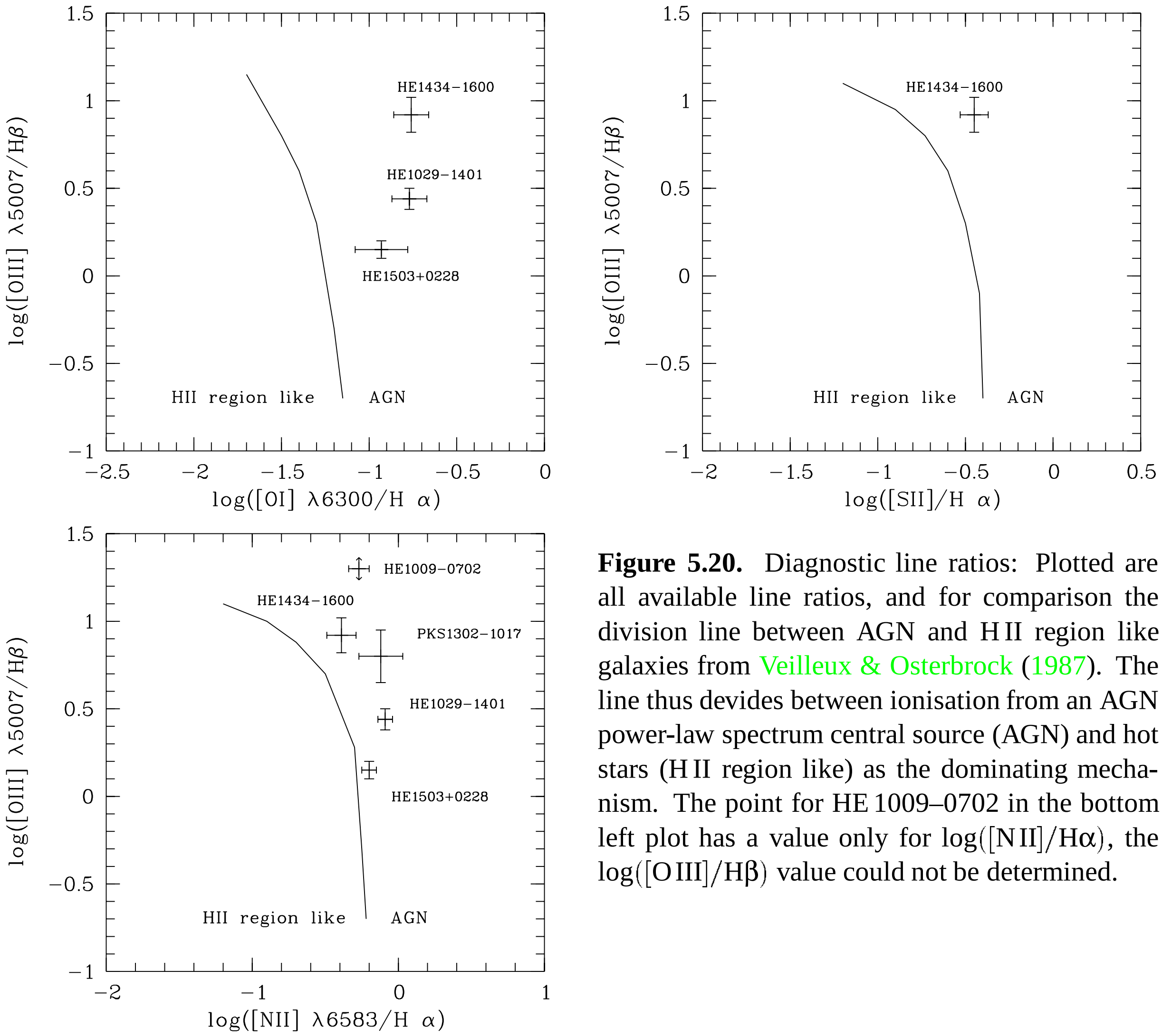

**Figure 5.20.** Diagnostic line ratios: Plotted are all available line ratios, and for comparison the division line between AGN and H II region like galaxies from Veilleux & Osterbrock (1987). The line thus devides between ionisation from an AGN power-law spectrum central source (AGN) and hot stars (H II region like) as the dominating mechanism. The point for HE 1009–0702 in the bottom left plot has a value only for $\log([\mathrm{N\,II}]/\mathrm{H}\alpha)$, the $\log([\mathrm{O\,III}]/\mathrm{H}\beta)$ value could not be determined.

The other objects with measured line ratios are spheroids. They all lie systematically further inside the AGN areas of Fig. 5.20 than HE 1503+0228. The best measurements were possible for HE 1434-1600. There is no doubt that the ISM of this object is ionised mainly by the central AGN and not by hot stars. It was possible to extract spatially resolved line ratios for $\log([\mathrm{O\,III}]/\mathrm{H}\beta)$ and $\log([\mathrm{N\,II}]/\mathrm{H}\alpha)$. From a distance of $2''$ from the centre to $4.5''$ the $\log([\mathrm{O\,III}]/\mathrm{H}\beta)$ decreases from $\sim 1.15$ to $\sim 0.9$. At the same time $\log([\mathrm{N\,II}]/\mathrm{H}\alpha)$ increases from $\sim -0.75$ to $\sim -0.5$, thus the object moves rather parallel to the division line. This indicates no tendency for a stronger contribution from hot stars with increasing distance to the nucleus, thus the AGN is the ionising source throughout this range.

In summary, all the spheroidal hosts show strong signs of excitation due to the central AGN. For the disk HE 1503+0228 the nucleus contributes at least a part.

### 5.3.4 Electron densities and temperatures

It was possible to measure [S II] 6716 Å and 6731 Å lines for HE 1434–1600. Following Osterbrock (1989) this can generally be used to derive electron densities due to the different collisional de-excitation rates of the two levels involved. For HE 1434–1600 we find the ratio [S II] $\frac{\lambda 6716}{6731} = 0.94$, corresponding to an electron density $N_e = 10^3\left(10^4/T\right)^{\frac{1}{2}}\,\mathrm{cm}^{-3}$, well above the low density limit of this diagnostic.

However it is not possible to measure these lines spatially resolved, only this global value is available. It is an average over all radii of the host with a strong gradient in densities and the stronger emissions in the centre are contributing differently than the weaker emission further out due to variance weighting. Thus electron densities from this ratio represent a mix of different radii, and will be dominated by the densest clumps. Numbers have only limited meaning for local electron densities at any radius.

The temperature $T$ can be determined by measurement of the ratio of line intensities $[\mathrm{O\,III}]4959+5007/[\mathrm{O\,III}]4363$ (Osterbrock 1989). It was possible to determine this ratio for HE 1434–1600 and HE 1029–1401. For both objects we receive very low values (9±3 and 13±5 respectively), due to a (relatively) strong [O III] 4363 Å component, even though the determination is strongly affected by noise. $T$ is related to the ratio by

$$\frac{[\mathrm{O\,III}]4959+5007}{[\mathrm{O\,III}]4363} = \frac{8.32\exp\left(\frac{3.29\cdot 10^4}{T}\right)}{1+4.5\cdot 10^{-4}\frac{N_e}{T^{\frac{1}{2}}}}.$$

Calculating $T$ from this equation shows that a ratio of 9.0 is not realistic, because for $N_e = 1000\,\mathrm{cm}^{-3}$, the relation converges to about 10. Using a value of 15 (twice the error given) would give a lower limit of $T > 55000$ K, a value of 18 $T > 42000$ K. Thus $T$ is not very well constrained, but it shows that very high temperatures have to be expected. This does not change, if the electron density is recomputed according to $T > 50000$ K, yielding $N_e = 450\,\mathrm{cm}^{-3}$. To yield values below $T = 20000$ K, the ratio would need to be above 40, for $T < 10000$ K above 190. From this is clear that temperatures are high, again indicative of non-stellar excitation.

### 5.3.5 Stellar populations

We identify four objects for which it is possible to combine the three grisms to spectra of good quality. These can be compared to spectral models as for the EFOSC sample (sec. 4.3.2). The remaining three in sample are HE 0914–0031, showing no continuum flux, and HE 1434–1600, that suffers from differences in the overlap region of *B* and *R* grism, and HE 1029–1401 with problems between *R* and *I* band.

Spectra and models for the four objects are shown in Fig. 5.21. Any spectral model fails for PKS 1302–1017. The stellar continuum shows remarkably few spectral features – no significant stellar absorption, no 4000 Å break. Up to 4500 Å the shape of the spectrum is similar to that of the AGN, but without the broad Balmer emission visible for the nucleus. In the other spectral range also no broad emission is visible. It resembles the “blue featureless continuum” hosts, observed in off-nucleus spectroscopy by J. Miller with the Keck telescope (presented only at conferences, not published). The slope of the spectrum is roughly that of a very young population, a 0.1 Gyr SSP spectrum as comparison is overplotted in Fig. 5.21 (red line). However in PKS 1302–1017 there are no signs of the Balmer limit present in the model. The nature of this continuum shape remains unknown.

For HE 1009–0702 it is interesting that while a mix of two intermediately young components (in mass 53% of 0.7 Gyr plus 47% of 1 Gyr) fits the spectrum best, it was classified morphologically as probably being a spheroidal. Thus the spectrum points to on-going star formation or the presence of a relatively young component. In any case an old, evolved population as the only constituent can be ruled out.

HE 1442–1139 is consistent with pure continuous star formation (CSF, red line), only slightly improved by addition of a 1 Gyr component (25% in mass, yellow line).

HE 1503+0228 is classified as a disk. Its spectrum is pointing to a young population beyond CSF. In Fig. 5.21 the CSF model is plotted in red. The yellow line, fitting the data much better, adds 2.5% in mass of a very young 0.1 Gyr old population. This can be seen as an indicator for enhanced star formation activity.

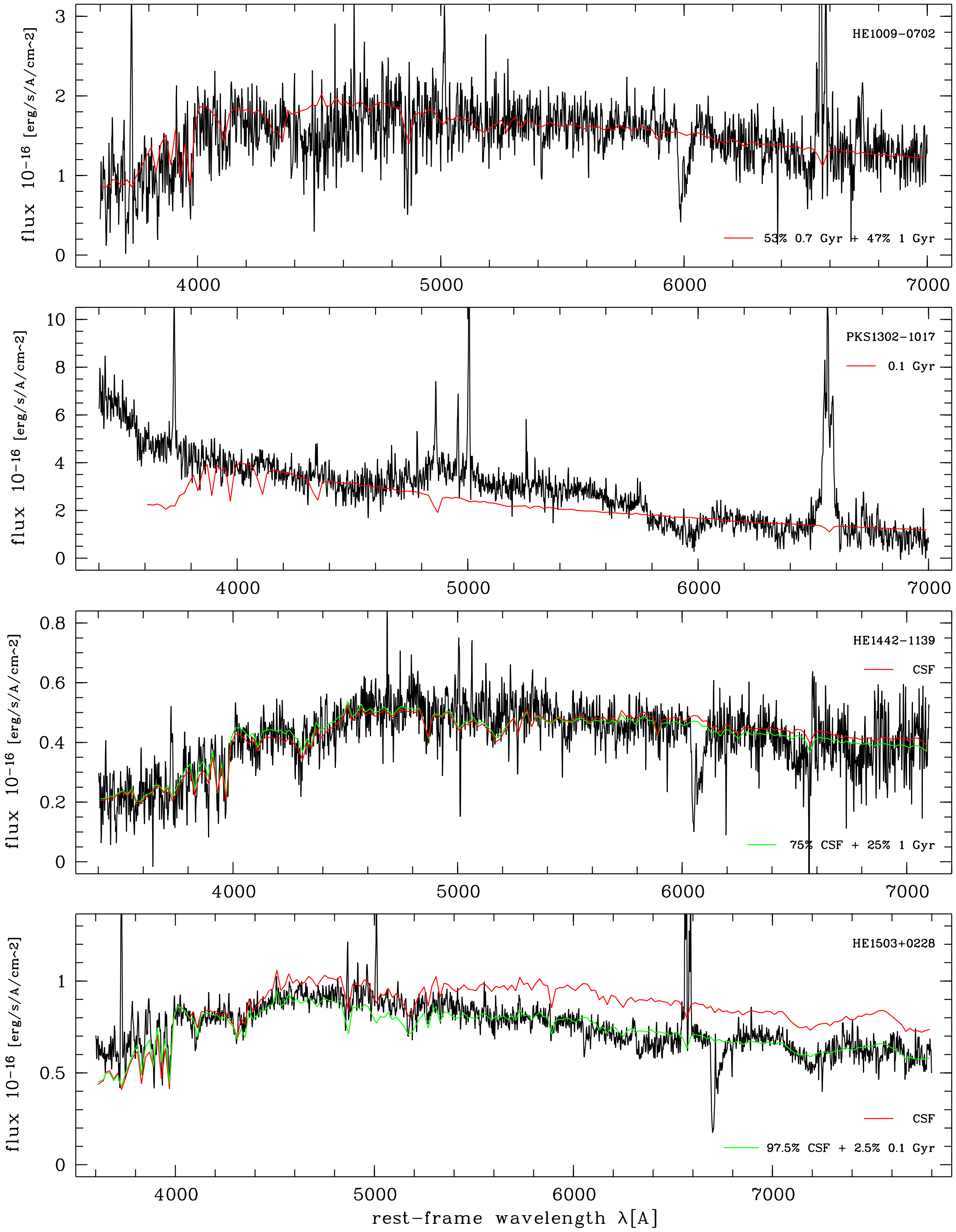

**Figure 5.21.** Spectral models for four VLT objects with good quality. See text for description.

# 6 Discussion

## 6.1 Astrophysical discussion

Before we start with the discussion, a few word should be repeated on the statistical value of the results. The samples under investigation are statistically well defined. Taken from the Hamburg/ESO survey for bright QSOs, the multicolour sample is complete within the flux limits of the survey, for a certain area in the sky, and redshift $z < 0.2$. The spectroscopic VLT sample extends to higher redshifts, $z < 0.33$, and is a subsample of a larger representative sample of objects to study the duty-cycle of QSO activity. The subsample of the multicolour sample for which on-nuclear spectra were observed with EFOSC is similarly not complete. The remaining objects had off-nuclear spectra taken and were not analysed in this study thus missing in the interpretation. Thus both spectroscopic samples are not strictly complete, but they are subsamples of complete samples.

The central results of the previous chapters are the very blue colours and young populations found particularly for the elliptical QSO host galaxies found in all samples. The colours and ages found are unexpected when compared to inactive ellipticals. In this chapter we want to summarise the results and discuss colours, ages and all other evidence found. We propose a scenario that is able to explain all observed facts within a framework of combined QSO formation and hierarchical galaxy formation.

### 6.1.1 Host luminosities and morphology

In the broad band (BB) sample about half of the objects are ellipticals, the other half is disk dominated. In $V$ band luminosities the sample is distributed around the classical dividing line of Sy 1 and luminous QSOs. For this range of QSO luminosities, the morphological classification found for the sample agrees well with previous findings (e.g. Smith et al. 1986; McLeod & Rieke 1995a; Taylor et al. 1996; Schade et al. 2000). The lower the luminosities of the nucleus, the larger the probability to find a disk as the host galaxy, the higher the QSO luminosities the more probable to find an elliptical. In absolute luminosities of the host, given in Table 2.5, the ellipticals in our BB sample are brighter than the disks, on average by 0.4 mag in $V$, 0.2 mag in $K$, in spite of having a flux-limited sample.

We do not sample the the highest luminosity regime for both components, when comparing with data on low and intermediate redshift QSOs in McLeod et al. (1999) compiled from a number of studies (McLeod & Rieke 1994b, 1995a; Bahcall et al. 1997; Rönnback et al. 1996; McLure et al. 1999). Even though our sample is complete, thus representative for the local QSO and host galaxy population, we have fainter flux limits compared to the PG survey (Schmidt & Green 1983) or hand-selected samples as used by Dunlop et al. (2001).

In the $H$ band about half of our objects are brighter than $L^*$ for inactive galaxies (McLeod et al. 1999), thus are generally bright (Figure 6.1). Connected via the Magorrian relation between mass of the central black hole and the bulge mass of the galaxy we also expect to find on average brighter hosts for brighter nuclei (Taylor et al. 1996; McLeod et al. 1999). In Figure 6.1 we find this relation confirmed by our BB sample, showing a correlation of host and nuclear luminosities. All of our hosts accrete with less or equal to 10% of their Eddington luminosity, independent of

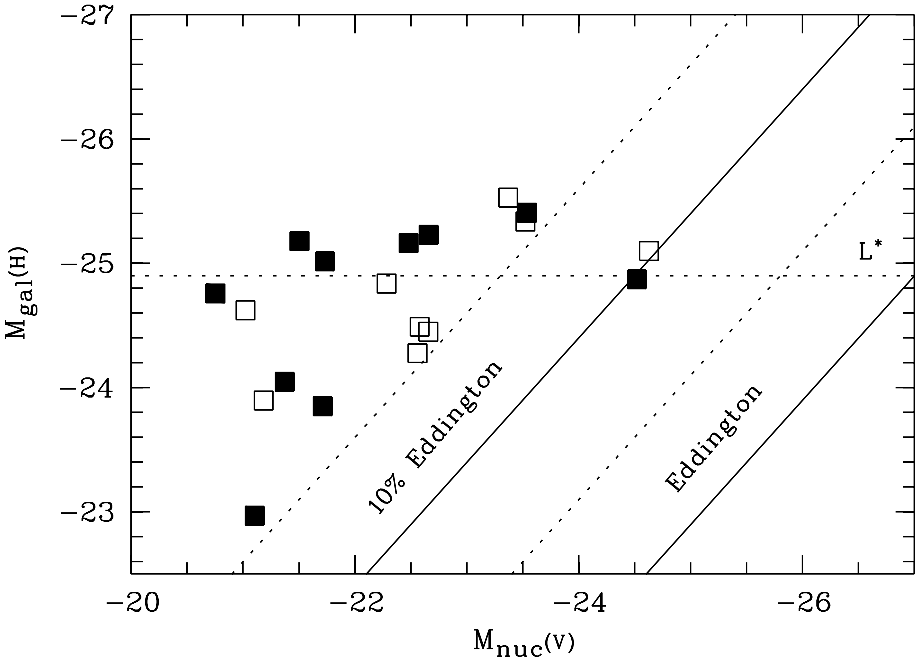

**Figure 6.1.** Host *H* band magnitude vs. nuclear *V* band magnitude for the multicolour sample. The dotted line shows the magnitude of an L* galaxy in the *H* band, the solid diagonal lines mark the loci of Eddington (right) and 10% Eddington (left) luminosities for galaxies following the Magorrian et al. (1998) relation $M_{\rm bh} = 0.006 \cdot M_{\rm sph}$ (McLeod et al. 1999). If more recent values are used for the relation between black hole and bulge luminosity, $M_{\rm bh} = 0.002 \cdot M_{\rm sph}$ (see Dunlop et al. 2001, and referenced therein), then the dashed diagonal lines apply.

morphology and host luminosity.

As already mentioned in section 2.5.2, the axial ratios of the disks are not uniformly distributed, but lack high inclination objects. This is compatible with a detailed study on Sy 1 morphology by McLeod & Rieke (1995b) and is to be expected from unified models of AGN (Antonucci 1993) if stellar disks and obscuring tori are aligned. Since no information on this is available, we can not draw final conclusions.

More interesting is the distribution of axial ratios ($q = b/a = 1 - e$) for the spheroids in the sample. We find an average of $q = 0.82 \pm 0.04$. Tremblay & Merritt (1996) investigate the general population of inactive ellipticals and confirm previous ideas about two distinct populations of ellipticals, with different morphologies and luminosities. Both from axial ratio as well as luminosity our ellipticals agree well with their bright elliptical population ($q = 0.85$ for $M_B \sim -20.0$). They conclude that this bright population is created by major merger events of spiral galaxies and that the ellipticals are slowly rotating and probably triaxial in morphology. That creation of ellipticals in merger events of spirals is possible is confirmed by numerical simulations e.g. by Heyl et al. (1994), who model merger events of spirals of similar size. They find triaxial ellipticals as results, even though their axial ratios are slightly lower than found by Tremblay & Merritt and us.

From morphology alone there are no signs that our elliptical hosts are deviating from the inactive galaxy population. Concerning luminosities, our sample size is too small to construct the type dependent luminosity function of QSO host galaxies, to test if they are randomly drawn from the inactive elliptical galaxy population.

### 6.1.2 Blue host colours, gas emission and young stellar ages

As we have stressed in section 2.6, the host galaxies show blue colours, both for short and long wavelength baselines. In $V-K$ we see the disks being bluer by 0.15 mag than inactive Sb galaxies, and the elliptical hosts being bluer by 0.5 mag than their inactive counterparts. The ellipticals are even bluer than the disks by 0.25 mag.

As we noted earlier in section 2.6.3, there exists one point for a potential bias in these colours. The spectra for the two samples show gas lines for the hosts of all except a few objects. As we noted, they are particularly strong for the objects identified as being ellipticals. This yields two sources for a bias towards bluer optical to NIR colours: a) the optical gas line emission and b) errors in modelling due to gas line emission.

In section 3.5.3 we discussed the influence of emission lines from gas in spheroids when separating nuclear and host spectrum. The gas in the spheroids is mainly present in rotating gas disks, as we deducted from line shifts. This means that the gas has a different morphology than the model assumed for the host, resulting in a boost for the host flux in the line, thus overestimating the line emission for the gas, and underestimating the nucleus. This is an effective numerical flux transfer from nucleus to host, as is illustrated e.g. in the [O II] line of PKS 1302–1017 (Fig. 5.8), which was not corrected for this flux transfer.

For $z < 0.2$ the $V$ broad band filter contains Hβ and the [O III] doublet around 5000 Å, which are three of the strongest gas emission lines in the extracted host galaxy spectra. From our host spectra we estimate the line flux to correspond to an equivalent of 0.5–0.15 mag of the elliptical hosts $V$ band continuum emission, the exact value depending on object. For the disks this is less, due to the much smaller gas emission. Including the errors of flux transfer from the nucleus, the line is boosted by up to a factor of two, thus in total adding 0.2 mag to the $V$ band for at least some of the ellipticals.

When looking at the multi-component modelling in the imaging case. Here the gas disk will also create a deviation from the assumed de Vaucouleurs profile for the ellipticals, inducing errors in the separation modelling. We estimate that the error will not be higher than estimated from the errors in spectroscopy modelling. It will probably be lower. The exact size of the error has not been simulated, but judging from the radial profiles (Figures A.1 to A.19) systematic larger deviation in the $V$ band can be excluded.

Thus the flux in the $V$ band, containing Hβ and [O III], is boosted by the emission lines, compared to inactive ellipticals showing no emission lines. When assuming for our ellipticals on average 0.15 mag for this effect, the ellipticals have $V-K = 2.63$, the difference to inactive ellipticals decreases from 0.5 mag to 0.35 mag, and the difference to the disks in the sample decreases to 0.1 mag. We test several hypotheses: While with the original $V-K$ value for the ellipticals we could reject that disks and ellipticals have the same mean colour (with a significance level of 97%), this is not possible with the modified value. We can still reject identical colours for active and inactive ellipticals (significance level $> 99.9\%$), but only marginally that our ellipticals have the same colour as inactive Sb galaxies (significance level 95%). The disks in our sample are slightly bluer than inactive Sb spirals, but not with a high significance.

Thus from BB colours alone we find bluer optical to NIR colours than previously found and predicted for inactive galaxies of similar type. Interestingly this is the case even though asymmetries, in part marking tidal tails with potentially increased star formation have been masked out in the modelling and photometry process. Particularly the ellipticals are bluer than expected, showing colours of intermediate to late type spirals.

Comparisons of the optical BB colours to the spectra for four objects in section 4.3.2 shows a very good match between the broad band colours and their spectral counterparts, even for the most compact object in the sample. This is unlike to be a coincidence: The modelling procedures for spectra and BB images would both need to create undetected artefacts in the results, that produce an exactly identical spectral bias. This seems impossible, because the two modelling procedures with the additional spectral domain for spectroscopic modelling differ substantially. Furthermore the very similar results for the modelling of HE 1503+0228 by Courbin et al. speak against a systematic fault in the spectral modelling.

Incorporating the biases estimated in the previous paragraph into BB population model fitting, assuming $V$ and also $I$ to show boosted flux, $I$ because of the emission in H$\alpha$ and the [N II] doublet, the BB fitting results do not change fundamentally. E.g. instead of being compatible with a pure 2 Gyr population, 10% of an older population have to be added.

The presence of intermediatly or young stellar population is supported when comparing the extracted host galaxy spectra with available BB colours. Both, fits of theoretical evolution synthesis models to BB fluxes as well as fits to the extracted spectra find model ages for the host galaxies of an order of 2 Gyr. For several of the disks as well as some of the ellipticals a continuous star formation model is also adequate. The VLT sample shows slightly younger ages than the EFOSC sample. But for the BB sample as well as both spectroscopic samples *none of the ellipticals* is modelled best by an old, evolved population. On the other hand there are no general trends for massive on-going starburst, manifested in a significant young population ($\ll 1$ Gyr). This is only seen for two objects – being both disks. The overall shape of the spectra, the size of absorption features, the 4000 Å break, all signal that a part of the mass is contained in fairly evolved stars, but the average age is rather young, $\leq 2$ Gyr. The average spectra of the ellipticals and disks in the samples are, with some dispersion, very similar. Thus we conclude that the unexpected blue colours and young ages for the ellipticals are real.

All objects show gas emission. The ionisation mechanism for several ellipticals in the VLT sample could be determined from line ratios. Here the AGN is clearly the dominating source of ionisation. For these objects we see continuous narrow emission from the NLR, via an extended NLR, until the material would be called ISM further out in the host. The ionising spectrum might change in detail, but the main difference between these zones is likely only density.

For only one disk line ratios were available, HE 1503+0228, and we find a probable mix of ionisation mechanisms. Judging from $\log([\mathrm{O\,III}]/\mathrm{H}\beta) - \log([\mathrm{O\,I}]/\mathrm{H}\alpha)$ (Fig. 5.20) the object is close to the dividing line between the two mechanisms. The division is computed from photoionisation models and Veilleux & Osterbrock (1987) note that an uncertainty of ±0.15 dex applies, thus HE 1503+0228 might come to lie in either region. We find on-going star formation, as do Courbin et al. (2002b), slightly more than from continuous star formation. The least gas emission is found in HE 1315-1028. For this object also one of the reddest continuum spectra is found, and fits show one of the oldest population found in both samples, 4 Gyrs.

### 6.1.3 Two comparison studies: Boroson et al. (1985), Nolan et al. (2001)

There are basically no more than two studies that allow a detailed comparison. The first is by Boroson, Persson, & Oke (1985), still the most thorough study to date. Most of their results are still valid and have never been disputed, because their study is up to the present the most systematic approach. The second study is part of a comparison of radio-quiet (RQQ) and radio-lout QSOs (RLQ), and radio galaxies, started ten years ago (Dunlop et al. 1993; Taylor et al. 1996; McLure et al. 1999; Dunlop et al. 2001). For nine RQQs and ten RLQs on-nuclear spectra were observed (Hughes et al. 2000) and theoretical models fitted (Nolan et al. 2001).

Boroson, Persson, & Oke (1985) presented off-nuclear spectra for 24 low and high luminosity QSOs, removing the nuclear contributions with a scaled on-nuclear spectrum. They place their slits at approximately 10-15 kpc distance from the centre of the QSOs. Apart from the uncertainties introduced by this approach, and the fact that they did not have morphological data available, they find interesting results.

They classify their objects into two distinct classes. About half of the hosts show relatively faint gas line emission, some of them with rather red spectra. The other half of the hosts shows strong gas lines and generally bluer spectra. Further they group into a "high" and "low" luminosity class, according to [O III] equivalent width, with no colour information available for the low luminosity bin. They correlate this classification with the shape and width of the broad Balmer lines: The "line objects" show larger FWHM (though not equivalent width) and more uneven lines, exibiting shoulders and bumps. The "continuum objects" have comparably smaller FWHM and more symmetric and even broad lines. Boroson et al. further relate the classification to radio properties and Fe I emission.

If we classify the objects in our spectroscopic samples according to the criteria used by Boroson, Persson, & Oke, we receive Table 6.1. It is remarkable how well the morphological type determined from imaging agrees with the spectral classification. Only one disk is part of the first group, only two spheroids part of the second. One of them, HE 1335–0847, we classified as a spheroid but mentioned in section 2.5.2 that its morphology somewhat deviates from the ideal case.

Concerning continuum colour, we can not follow Boroson et al., as we do not find really red, evolved spectra. However their classification for line dominated objects largely conforms with our spheroids. Our ellipticals indeed are blue, as shown. That their objects with low line emission and show red continua are similar to our (normally blue) disks is unlikely. If we samples our disks at 15 kpc from the center they will not appear redder. Colour gradients in spirals, as expected for inactive galaxies, will make them rather bluer in the optical, as the stellar populations in spirals become younger with increasing radius (de Jong 1996).

Using the host galaxy line intensities measured by Boroson et al., we can compute the line ratio $\log([\mathrm{O\,III}]/\mathrm{H}\beta)$, available for a total of seven of their objects. Five show ratios of 0.75 to 1.0, a strong sign for ionisation by a power-law spectrum. Only very few of the objects in Veilleux & Osterbrock (1987) ionised by very hot stars reach these values. The remaining two objects have values of 0.26 and an upper limit of –1.4, respectively. The power-law ionised objects are all part of the line-object class, the other two of the continuum object class. Even though the amount of evidence is sparse, it seems as if the continuum objects in question have a tendency for ionisation from a stellar continuum. For the line objects clearly the AGN is the dominating source.

**Table 6.1.** The objects in our study with available spectra, classified according to Boroson, Persson, & Oke (1985). The columns classify the shape of the broad lines ("BL shape"), and their FWHM ("BL width"), the amount of gas emission compared to the continuum ("Gas") and an estimate of their stellar age. The last column gives the morphological type as determined from imaging. The upper half corresponds to the "line objects", the lower to the "continuum objects". The two objects in between are undecided.

| Object | BL shape | BL width | Gas | Age | Type |
|---|---|---|---|---|---|
| HE 0952–1552 | bumpy | broad | strong | intermediate | D |
| HE 1029–1401 | bumpy | broad | strong | young | E |
| HE 1416–1256 | bumpy | broad | strong | $<2$ Gyr | E |
| PKS 1302–1017 | bumpy | broad | strong | peculiar | E |
| HE 1434–1600 | bumpy | broad | strong | young | E |
| HE 1009–0702 | bumpy | intermediate | intermediate | 0.7–1 Gyr | E? |
| HE 1228+0131 | ? | intermediate | ? | - | E? |
| HE 0914–0031 | even | narrow | ? | - | D |
| HE 0956–0720 | even | narrow | ? | - | D |
| HE 1015–1618 | even | narrow | ? | - | D? |
| HE 1201–2409 | even | narrow | weak | 2 Gyr | E |
| HE 1239–2426 | even | narrow | weak | - | D |
| HE 1310–1051 | even | narrow | weak | CSF? | D |
| HE 1315–1028 | ? | narrow | weak | 4 Gyr | D |
| HE 1335–0847 | even | narrow | ? | - | E? |
| HE 1442–1139 | even | narrow | weak | CSF–1 Gyr | D |
| HE 1503+0228 | even | narrow | weak | CSF+burst | D |

For the different amounts of line emission in the host Boroson & Oke find a geometrical explanation most probable: the ionising radiation from the accretion disk would be blocked from reaching the gas in the host by an obscuring torus. This could work if the gas is contained in a disk, which we can confirm for most of our objects, and if the torus and disk are aligned. If the torus is either non-existing, or incompletely covering the accretion disk, then the radiation would escape and could ionise the gas. A sign for the incomplete covering could be the bumpiness and asymetry of the broad line emission of the nucleus. A low number of BLR clouds with a chaotic velocity field could both explain the broad line shape as well as the escaping radiation in the line objects.

We find significant amounts of ionised gas in the ellipticals in the samples. Even though the forbidden lines are stronger due to the type of the ionising radiation field in our ellipticals than in the disks, the Balmer lines show that the ellipticals also have substantial amounts of gas, comparable to the disks. For all cases tested, the gas is ionised throughout the whole galaxy: The spatial profiles of [O III] lines and continuum in Figure 5.18 show no cutoff radius at which the ionisation ends. The changing line ratios observed for HE 1434–1600 (sec. 5.3.3) might be a sign for a change in the ionising spectrum, loosing part of the high energy UV photons due to absorption. This however is just a qualitative scenario, and would need detailed modelling of the processes involved to be quantified. From the ionised gas seen all through the hosts of our ellipticals, we see evidence that most of the ionising radiation in QSOs in fact escapes the host into the intergalactic medium. This could also be the case for the disks, if all gas was contained in a disk and would be shielded from the radiation by a non-spherical instance. Then radiation could escape perpendicular to the plane of the disk.

Before we draw conclusions from all this evidence, we want to summarise the results of the second study, by Nolan et al. (2001). As mentioned they observed off-nuclear spectra of 19 QSO with different radio properties (data published in Hughes et al. 2000). Their hosts are all ellipticals, on average the QSOs in their sample are about 1.5 mag brighter than our BB objects. Their host galaxies are brighter in the NIR by about 1.2 mag, corresponding to a factor of 3 in luminosity (Taylor et al. 1996; Dunlop et al. 2001), and their scale lengths are larger by a factor of 2 (Dunlop et al. 2001). They attempted to sample the host galaxies at very large radii, of up to $5''$ or 20 kpc distance from the nucleus, to avoid as much nuclear contribution as possible while still receiving satisfying S/N. Whereever they detected traces of nuclear contamination they subtracted a scaled nuclear spectrum for correction.

They fit a two component model spectrum to their data, using evolution synthesis models by R. Jimenez (unpublished). As we did, they used single age stellar population models of solar metallicity. Keeping the age of a young component fixed at 0.1 Gyr, they searched for the best age and mass ratio of an older population. In all cases they found evolved stars as the dominating population, with ages of 6–14 Gyr, with little or no contribution of the young component required. For the discussion we want to dub their objects “red ellipticals” as a difference to our “blue ellipticals”. At first sight this seems to contradict our results, but can be explained.

### 6.1.4 Two classes of ellipticals: first time merger and old ellipticals?

We find all of our presented evidence suggestive of a hierarchichal merger scenario as the trigger for QSO activity and for the evolution of galaxies in accordance with Kauffmann & Haehnelt (2000). We want to propose that the ellipticals in our sample are created in the merger of two similar sized inactive disks, as described in simulations (e.g. Heyl et al. 1994). The ellipticals created, our “blue ellipticals”, would be part of the bright population of elliptical as found by Tremblay & Merritt (1996). In the merging event the stellar components of the two disk galaxies mix. As the dynamical timescales of such a merger are relatively short, strong morphological signs will only be left in a part of the objects investigated. After a few 100 Gyr the tidal features vanish and what remains is morphologically a normal elliptical of the bright type.

In the merging event some of the gas contained in the galaxies is channeled into the center, creating an accretion disk around the black hole in the center – the black hole is inherited from the precursor galaxies. The nuclear activity begins. One obstacle has to be overcome: Most numerical simulations of merging galaxies of similar size find that most of the gas falls rather quickly to the central 10 kpc, creating a strong starburst. This we do not observe. What we observe is an extended rotating disk of gas and only small traces of extra star formation. However, the physical processes involved in the creation, or survival, of a massive gas disk in merger events are not finally investigated. There exist several observations of inactive ellipticals exhibiting massive gas disks (Oosterloo et al. 2002). These are relatively massive – H I masses up $4.5\times10^9 M_\odot$ are observed – but do not have a high enough surface brightness to engage in strong star formation. There are suggestions about the formation of these disks, involving infall of gas ejected in the merging process (see discussion and references in Oosterloo et al. 2002), but the timescales estimated for individual objects seem to be a bit high to explain both gas disk and observed spectrum of our ellipticals. If the gas disk formed in this way, it would not create strong star formation, except in the center, in accordance with our observations.

After the merger the galaxy has an elliptical morphology, but the spectrum of its progenitor disks. In the following several 100 Myrs the continuous star formation spectrum is passively evolving, the star formation rate will be small. The CSF spectrum and added local starburst at merging time will rapidly become redder. We calculated the $V-K$ colour evolution of a CSF spectrum when the star formation is stopped. During the first 100 Myrs the spectrum will become reder by 0.05 to 0.07 mag in $V-K$, after 300 Myrs by 0.11 to 0.14 mag and after 1 Gyr between 0.22 and 0.27 mag. The ranges come from different assumed CSF spectra, with prior CSF durations of 6, 10 and 14 Gyr. We find for our BB ellipticals $V-K = 2.63$ including the correction for emission line contribution and overestimation. For inactive ellipticals we derived $V-K = 2.99$ in section 2.6.1 at the luminosity of our sample. Thus within 1 Gyr colours of such a merging host will evolve to within 0.1 mag of this value! The intrinsic scatter $\delta$ of the colour-magnitude diagram for inactive ellipticals was derived by Fioc & Rocca-Volmerange (1999) to be $\delta = 0.12$ mag. Thus 1 Gyr after a merger, our elliptical would not appear peculiarly blue, but as a normal elliptical. Even the colour-magnitude-relation for our hosts, as shown in Figure 2.15, being 0.3 mag off the relation for inactive galaxies by Fioc & Rocca-Volmerange (1999) at the time of observation, will evolve with time and be indistinguishable from the inactive relation for the ellipticals after 0.5–1 Gyr.

If all lower luminosity elliptical host galaxies were created in this way, they all would be part of the bright, triaxial, slowly rotating population of Tremblay & Merritt. Thus their luminosity would lie above the dividing line between the high and low luminosity types. The authors draw the line at $M_B = -20$. If we compare this to our BB sample, being representative for the low redshift QSO host population, and convert the division line to $H$ band colour to avoid influence of induced star formation, we receive a limit of $M_H = -23.75$, with $B-H$ taken from Tab. 2.8. Our ellipticals have on average $M_H = -24.7$ and the lowest luminosity object has $M_H = -23.9$, just above this limit.

On the other side, elliptical galaxies created in such a merger event could not have luminosities more than two times the luminosity of the brightest Sa to Sc spirals. To allow a rule of thumb estimate, we look at the luminosity function of field galaxies. Most of the galaxies have luminosities below L$^*$. A merger of two very bright spirals each 0.5 mag brighter than L$^*$ would create a blue elliptical two times or 0.75 mag brighter than each spiral, or 1.25 mag brighter than L$^*$. The luminosity function of freshly created elliptical hosts still showing the SED of the spirals, should rapidly descrease for luminosites above this value. For $M_H^* = -24.9$ this limit is $M_H = -26.15$ – our brightest host has $M_H = -25.55$ being well inside this limit. Using the $M_R$ and $R-K$ values from Dunlop et al. (2001), and $H-K = 0.2$, we recomputed the $K$ band luminosities for 17 objects observed by Taylor et al. (1996) that were part of the Nolan et al. (2001) spectroscopic sample. Their original morphological measurements were biased (see discussion in Dunlop et al. 2001). With these new colours, we receive an average luminosity of $M_H = -26.2$ for their objects. The faintest hosts has $M_H = -24.9$, and shows a dominating population of 5 Gyr age. Their faintest host with a really old dominating population has $M_H = -25.4$.

We see that an overlap exists in luminosity, their red ellipticals are not exclusively brighter than our blue ellipticals. This is plausible: If tidal events are involved in activating the AGN, an event with a small gas rich companion galaxy might be sufficient to ignite the AGN in a large, evolved normal elliptical. After the event one would observe a red elliptical host, with almost the same mass as the blue elliptical the galaxy was a longer time ago. Thus the lower luminosity limit for red ellipticals is not expected to be the same as the upper limit for blue ellipticals.

We do not find larger numbers of their red ellipticals in our sample, simply because of sample selection effects. In our flux limited sample, we do not expect more than one red elliptical host, when simply scaling the luminosity function of QSOs or host galaxies. Hughes et al. on the other hand selected not complete samples, but samples of RLQ and RQQ matched in luminosity, thus sampling much brighter QSOs on average.

Incidently one of their faintest and our brightest elliptical host are the same object, HE 1020–1022, showing a difference of 0.1 mag in derived $K$ band magnitude. For precisely this object Nolan et al. find the youngest population in their sample. Their best fits suggest either a 5 Gyr component plus 0.6% of 0.1 Gyr, or 4 Gyr when using only a single component. With multi-colour fitting we found 6 Gyr plus 1% of 0.1 Gyr and compatibility with a pure 2 Gyr component. The 6 Gyr fit would make this object the one with the oldest population in our sample. Nolan et al. take their spectra further outside of the host and would miss any local central star-formation making our spectra slightly bluer. The results are very similar, and in total this object gets to lie somewhere between the two classes of ellipticals proposed, thus shows a continuity of properties between the two classes.

The general influence of slit position in the host should be small. Hughes et al. (2000) sample the host galaxies at about 15 kpc from the nucleus. If their hosts were indeed normal ellipticals, the colour gradients are small from this radius to the center. But what about a strong circumnuclear starburst? As we discussed we do not find evidence for strong starburst in our spectra. Both the SSP fits to the BB fluxes as well as the model fits to the host spectra strongly suggest CSF or 2 Gyr spectra and not combinations of old and very young populations. Thus the different slit positions are unlikely to be the reason for the spectral differences.

We conclude that on average the hosts investigated by Nolan et al. do not have the same formation history as our blue ellipticals. The red ellipticals' stellar populations and elliptical morphology would be older, they would be rather normal inactive giant ellipticals. The current nuclear activity could be created in a merger event in which the major component was already a relatively massive elliptical with an evolved stellar population dominating its spectrum. This progenitor elliptical would already have been created in an earlier merger event, with possible nuclear activity, and show corresponding older stellar populations.

If this scenario is true, their results for ellipticals are similar to ours, if we removed the fact that we are observing two populations of elliptical hosts: Both times the nuclear activity is not related to extremely strong starbursts.

One of our ellipticals, HE 1300–1325, could be in the act of a secondary merger event, showing tidal distortions induced from a nearby galaxy, probably a spiral, 1.5 mag fainter than the host. The spiral is thus half as bright as two theoretical progenitor galaxies that formed the elliptical in a primary merger. The result of the current merger will be an elliptical of $L^*$ luminosity. Around this object several other galaxies can be seen. Being part of a group of galaxies, possibly the primary merger event was not too long ago?

This illustrates a dispersion contained in the luminosities of the blue and red elliptical hosts.

From morphological appearance alone they will not be distinguishable. This can be done only with colour and spectral information.

The extensive discussion by Dunlop et al. (2001) include estimates on the relation between the general population of ellipticals and luminous (red) elliptical QSO host galaxies. Supportive of our posted scenario they find no differences in a) axial ratio, b) $R-K$ colour, c) clustering properties, and d) companion statistics and asymmetry. This is expected if hierarchical merging is in fact happening. Particularly the companion statistic is interesting. It fuels the idea that not only elliptical host galaxies are otherwise normal galaxies, but potentially also that every inactive elliptical is a potential QSO host, waiting for the next merger to happen.

Dunlop et al. make some remarks on their red ellipticals not being the result of a major merger of two disks, but the retriggering of an existing black hole in an evolved massive elliptical. The also discuss the creation of ULIRGs in violent merger events, and conclude that this is unlikely. While ULIRGs are likely to be ellipticals, they are more compact than the luminous elliptical host galaxies investigated. Does the argument against major merger extend to our ellipticals as well? Our ellipticals do not span the complete range of scale lengths observed for giant ellipticals and their red elliptical hosts. But this we also do not expect, as we assume merger events of intermediate to luminous spirals, not creating a giant elliptical. Judging from scale lengths, our ellipticals are nevertheless compatible with being part of the bright elliptical population as found by Faber et al. (1997), defined similarly to the definition of Tremblay & Merritt (1996). ULIRGs, however, have on average $\sim$3 times smaller scale lengths than our sample, being clearly part of the lower luminosity type elliptical, showing central cusps, different from our blue ellipticals' morphology. We conclude that if ULIRGs are also created in major merger of disks, then a) the disks are different from the progenitors of our ellipticals, and/or b) the dynamical processes involved are different, leading to more compact, dusty and starbursting galaxies. If ULIRGs are starbursting, dust enshrouded AGN and develope to normal RQQs in timescales of 1 Gyr as suggested (Sanders & Mirabel 1996), then this would be an alternative route to create elliptical QSO hosts, although of different morphology than our blue ellipticals.

A few remarks on the disks in our sample. We see starburst activity of a maximum of 1% in mass, more for only two objects, making the disks only slightly bluer than their inactive counterparts. For Sa–Sc host galaxies the trigger for the nuclear activity can not be major mergers – they would destroy the disk morphology – but minor mergers or other tidal events. Evidence for companions involved in tidal interactions are plenty. We find companions and supposed tidal asymetries for at least half of our disks imaged in the BB sample: HE 1019–1414, HE 1237–2252, HE 1254–0934, HE 1315–1028, HE 1405–1545, but for none of our ellipticals.

### 6.1.5 Boroson et al. classification revised

It is time to discuss the classification of Boroson et al. in more detail. As a difference to our classification in Table 6.1 they have observed higher luminosity objects. Following the discussion above, their high-luminosity continuum objects can be identified with the red elliptical QSO hosts investigated by Nolan et al., being active from later merger events. This is strengthened by one object in common in both studies, showing $R-K = 2.69$ (Dunlop et al. 2001) and an evolved population (Nolan et al. 2001). The majority of their low luminosity line objects is clearly like the blue ellipticals in our sample, being the result of a major merger of two disks.

**Table 6.2.** Classification scheme according to host morphology ((E)lliptical or (D)isk) and stellar age. The other columns give the observed properties broad line shape, luminosity, the amount of gas in the host, the star formation rate, and amount of nuclear ionising radiation reaching the ISM and a prototype object or group of objects.

| Morph. | Age | BL shape | *L* | Gas | SFR | Rad. | Examples |
|---|---|---|---|---|---|---|---|
| E | old | ? | higher | low | low | high? | Nolan et al., Boroson high *L* continuum objects |
| E | young | bumpy | lower | high | stopped | high | HE 1434–1600, Boroson line objects |
| D | young | even | lower | high | high | low | HE 1503+0228, Boroson low *L* continuum objects |

For their low-luminosity continuum objects no colour estimates exist, except for one object in common with Dunlop et al. It is found to be a disk with a prominent bulge, being quite red in $R-K$.

We assume that the majority of the Boroson et al. low luminosity continuum objects does not have a red continuum and can be identified to be similar to our disks, showing little gas lines emission and being blue from a CSF spectrum with an optionally added small starburst. Boroson et al. find some stellar Mg I absorption, indicative of the presence of some older component, though no absorption line strengths indicative of an old population. This is compatible to a CSF spectrum present in our spirals, showing several stellar absorption lines.

We are left with the hosts of Boroson et al. from the high-luminosity line object class. We conclude that they also are like our blue ellipticals. For them the authors estimated luminosities between $M_V = -22.7$ and $-23.5$, when being ellipticals. Assuming they have the same $V-H = 2.2$ colours as the ellipticals in our sample, they would show $M_H = -24.9$ to $-25.7$. Even though these estimates involves a good portion of rule of thumb, these numbers, being only slightly more luminous than our ellipticals, leave some space to the Nolan et al. objects. They are on average 0.8 mag more luminous, but all lie below the mark of $M_H = -26.15$ that we set above, as a characteristic upper limit for blue ellipticals.

If we now regroup these classes and classify according to host morphology and population age, we receive the scheme displayed in Table 6.2. This classification explains the strong emission lines in some objects with gas contained in blue ellipticals, ionised by the central power-law spectrum. The absence of lines for higher luminosities is due to missing gas in evolved ellipticals, for lower luminosities due to potential blockage of the power-law radiation close to the nucleus in gas rich disk hosts. For the latter objects the remaining line emission is primarily created by ionising radiation from hot stars.

We do not want to rule out that a distinct class of really luminous objects with strong line emission exists, with properties different to our blue ellipticals. There exists a group of QSOs displaying peculiar host galaxies, one of them PKS 1302–1017 (Figs. 5.8 and 5.21). The host continuum is almost featureless and very blue. It is difficult to determine if very young stellar populations are the reason for the blue colour, because no sign of Balmer absorption particularly at the Balmer limit is visible, but absorption lines are very weak or missing. From its host spectrum PKS 1302–1017 seems to be similar to a number of objects observed by J. Miller with the Keck telescope in off-nuclear spectroscopy, analysed in part by A. Sheinis. Being unpublished, complete spectra of the hosts were so far only shown at conferences. As shown, PKS 1302–1017 is the only spheroid that shows gas emission but no detectable gas disk. It is completely unclear if any connection between the shape of the spectrum and the gas distribution or other physical properties of the QSO exist, but we want to take this as a potential candidate for a high luminosity line object class.

### 6.1.6 Radio properties

A few words on radio properties. We lack information on the radio emission of most of our objects. A detailed study is in progress but no results are available at the moment. For two objects found in other surveys we know that they are radio-loud, HE 1020-1022 and PKS 1302–1017, but of the remaining the large majority is expected to be radio-quiet, judging from the distribution of QSO radio emission at the luminosity range in question.

It is unclear which physical processes are involved in the radio emission of QSOs. Judging from the results of Dunlop et al. (2001) it seems that the while the strength of radio emission is somehow related to black hole mass, mass or fuelling rate alone can not explain the differences in radio emission of QSOs.

We can also not solve the problem with our data but want to note one peculiar correlation. Boroson et al. point out that their two part classification into line and continuum objects could be done by either the host spectrum, but also the shape and width of the Balmer lines in the nuclear spectrum. They discuss the classification by Miley & Miller (1979) on radio morphology and their Balmer line shape. Broad, asymetric and “bumpy” Balmer lines are found for extended, double lobed, steep-spectrum radio sources, while the smoother, narrower Balmer lines are found for compact, flat spectrum radio sources.

Dunlop et al. (2001) point out that they do not find a correlation between the strength of radio emission and host morphology, because for increasing QSO luminosity, RQQs show an increasing fraction of elliptical hosts. Without suggesting a direct causal relation we find it remarkable that the nuclear Balmer line shape for our objects is on one side related to the strength of gas lines and thus amount of ionising radiation escaping from the nucleus into the ISM of the host, and on the other side related to the radio spectrum of RLQs. This relation could not as easily be detected for higher luminosity QSOs. If higher luminosity QSOs are primarily found in ellipticals, with less gas content than our ellipticals, then it is difficult to detect the amount of ionising radiation escaping beyond the NLR.

This connection between ionising radiation not escaping beyond the NLR, the shape of the optical emission from the BLR and the radio spectrum is a very interesting one. It does not need to be that one of these properties is the cause for the other, but they could both be caused by the same physical process. Trying to speculate, this could be the density or shape of material in or around the NLR absorbing some of the radiation. To make an orientation effect the basis for the separation in to steep- and flat-spectrum radio sources, as proposed in the unified schemes, compatible with this, any material would need to be oriented in the plane of the gas disk.

## 6.2 Diagnostic capabilities and limits of multicolour imaging

We conclude from the results of this study that multicolour imaging is a very powerful tool to study the morphological and spectral properties of QSO host galaxies. Particularly the comparison with extracted host galaxy spectra (Fig. 4.9) shows that it is possible to extract spectral information from broad band imaging with high accuracy. Here as well as in the separation of 2d spectra, the use of external or global information in individual modelling steps strongly improves the resulting quality. For imaging this is the global determination of a morphological model by assessing similarities and differences in the individual bands. Effectively we performed a simultaneous fit of our model to all bands thus using the joint S/N.

In the astrophysical discussion we noted the potential double influence from emission lines in the image modelling when using a one component model for the host. For comparison to inactive ellipticals the emission lines themselves are cause of a bias, because inactive ellipticals are usually free of strong gas emission. Secondly the different geometry of a disk of gas emission compared to the spheroid model used for an elliptical can introduce an error in the modelling, but the size of the bias is limited.

In images of sufficiently high S/N and resolution relative to the size of the seeing, it is theoretically possible to circumvent the introduced error by using a two component model for the host, with a disk model for the gas emission and a potential stellar disk, and a spheroid. However in the present of a pure stellar elliptical with only gas emission in a disk geometry, the errors in the determined PSF model, however small, will make it very difficult to determine precisely how much of the disk component is due to line emission and how much is due to the imperfect model.

In total this is not a significant problem. An erroneous overestimate of the host flux of more than 0.1 mag will only be introduced in the strongest line emitting spheroids, and only for the bands containing Hβ/[O III] and Hα/[N II]. The remaining bands are free of this error and if enough broad band information exists to determine a rough SED, it might be possible to detect erroneously high fluxes from comparison with neighboring bands. Furthermore we have seen that this problem only occurs for the type of ellipticals appearing in our broad band study, showing significantly blue spectra and optical to NIR colours. The red "normal" ellipticals seen e.g. by Hughes et al. (2000) will not suffer from this problem. Thus if an elliptical shows blue optical–NIR colours, determined from bands free of line emission, this problem can be detected and caution taken in interpreting the results.

The S/N required to model broad band images and successfully extract reliable host information is depending on the general S/N of the image, the nuclear-to-host ratio and the seeing. Our EFOSC1/2 *B* band images are clearly at or below the limit for such a task, for several objects fluxes could only be extracted with external information about the morphology. For a standalone modelling their S/N would in many cases have been too low.

We conclude that the assessment of stellar populations from multicolour imaging is possible, judging from the similar results of fitting models to the optical EFOSC spectra and to broad band colours. It is possible to discriminate between old, intermediate, and young dominating populations and to find additional starburst activity. An important role to distinguish between different composite models like CSF vs. an evolved plus a very young population is the *B* band, giving information about the 4000 Å break. If the *B* band is missing it is only possible to determine an approximate average age.

## 6.3 Capabilities and limits of the 2d decomposition of spectra

The results of the spectral modelling decomposition make us very confident about the capabilities and potential of the 2d decomposition to extract host galaxy spectra from a composite QSO spectrum with a strong nuclear component.

As we stressed before, there is a good aggreement between extracted host broadband fluxes and spectra. The algorithmic methods involved are sufficiently different to guarantee that this is not due to an identical bias in both programs, thus the results can be trusted. The second comparison, directly to the results of Courbin et al. (2002a), also shows that the extracted spectra are similar, thus can be assumed to represent the host.

The limit on nuclear-to-host flux ratio for which the host spectrum can reliably be extracted, primarily depends on three points: The S/N, the compactness of the host compared to the nucleus, and the accuracy with which the shape of the PSF can be determined. More compact sources need a better S/N to increase the S/N for the host at smaller distances from the center, thus increase the range of radii at which host and nucleus can be distinguished in shape. Secondarily the quality of the fit depends on the precision of the external contraints and the amount of variation of the scalelength of the host with wavelength.

We have shown that e.g. for HE 1503+0228 the nuclear-to-host limit in the area covered by the slit can lie above 15 and still deliver reliable results with a spectral resulution of 700-1000. The EFOSC spectra are at the lower limit for this task, in combination with the rather strong PSF distortion. In order to assess the dynamic situation in a QSO host galaxy, it is necessary to clearly resolve the narrow lines spectroscopically, which is hardly done in the EFOSC spectra. Particularly the separate modelling of the gas lines requires spectral resolution.

For compact ellipticals it is possible to replace the spheroidal model for the host with an exponential disk model. This increases the difference between host and nucleus on the model side and allows a more solid estimate of the spectrum than the “real” model. In this case the *2d spectrum* extracted for the host might not be very instructive, thus we loose the spatial domain of the result, but the *1d spectrum* might still yield information. The amount of error in the host spectrum introduced by this procedure, and its dependence on the local nucleus-to-host ratio and size of PSF error, has not been finally investigated.

Comparing again to the method developed by Courbin et al., we see a potentially effective lower resolution in the centre of our host spectra, due to the imperfect model, although it is not clear if the innermost shape of their rotation curves is free of modelling artefacts. In any case, for the quality of the total extracted spectrum our results are potentially more robust, because of the additional external knowledge on host galaxy morphology that was not used by Courbin et al. Being algorithmically different, we see these two methods as being complementary and very well suited to produce reliable results by cross-checking.

In the future our programm will be extended to use a three-component model for emission line extraction. This should increase the precision of line ratio estimates and rotation curves.

The second part of the VLT sample will be observed with integration times doubled to 2400 s per band and object. At the resolution of the FORS spectra (700-1000) and $1''$ seeing, we conclude that a sucessful extraction of optical QSO host spectra is possible to a nucleus-to-host ratio of the total QSO (not only inside the slit) of $\sim$3 at $z = 0.2$ and $\sim$2 at $z = 0.35$. Doubling the integration time should extend this to about 5 at $z = 0.25$ which reaches the majority of QSOs at the given luminosity and redshift.

With 8m-class telescopes the limit for host spectra in long-slit spectroscopy should be reached at around $z = 0.5$. If the PSF is well defined, then with IFS instruments, sampling a much larger fraction of the host flux, the redshift limit should be significantly increased beyond that.

## 6.4 Summary

We have developed two methods to extract spectral information on QSO host galaxies. For both the use of external information about the morphology of host and PSF is strongly increasing the quality of the results.

Using broad band imaging, coarse spectral information can be extracted over a large wavelength baseline, for a relatively small investment in observation time. With this method it is possible to determine the morphology of the host, the presence of asymmetries and its optical and NIR colours. By fitting model spectra it is possible to determine its dominating stellar populations.

Using a similar approach for spectroscopy, we developed a technique to extract the host galaxy part of on-nuclear spectra. This is done by modelling the different spatial distributions of nucleus and host galaxy. Using external information about the morphology of the host (from imaging) and the shape of the PSF (from a PSF star) allows a separation in nuclear and host spectrum. Comparison with broad band flux information shows that the extraction is reliable, as soon as a minimum S/N and PSF quality are reached.

Using this method it is possible to extract information about gas and stellar dynamics of the host, its stellar composition with ages and potentially metallicities, ionisation mechanisms of the ISM, and potentially velocity dispersions. All of these parameters can be investigated with spatially resolution, if the S/N permits.

We applied the mulicolour imaging approach to a complete sample of 19 intermediately luminous QSOs with $z < 0.2$, taken from the Hamburg/ESO survey. The sample was images in the optical *BRVI* and near-infrared *JHK* bands. We found disk dominated host galaxies for half of the objects, spheroid dominated hosts for the rest. The objects show relatively blue colours, particularly the ellipticals in the sample. Including a correction for gas emission lines they are on average 0.35 mag bluer in $V - K$ than their inactive counterparts, correspondingly in the other colours. They are statistically not compatible with the colours of inactive ellipticals, but rather with those of Sb spirals, thus disagreeing with the colours expected from optical and NIR morphology.

Fitting stellar population models finds relatively young populations for both disks and spirals, in many cases pointing to continuous star formation or ages of 2 Gyr. In no case we find signs for a pure evolved population, but also in only one case signs for significant starburst activity is seen.

We further investigated two samples of QSOs, for which on-nucleus spectra were obtained. This is the first study to assess host galaxy properties directly in the centre of the QSO, and, from the number of objects, the third largest spectroscopic study on QSO host galaxies in general.

The first sample is an eight object subsample of the broad band imaging sample. Spectra were obtained with ESO 3.6m telescope and EFOSC, with a spectral resolution of about 250. The second sample consisted of 10 slightly higher luminosity objects and was observed with the FORS spectrograph at the ESO VLT and a spectral resolution of 700-1000. We were able to extract reliable spectra for about half of the first sample and found signs of the host in all but three cases for the second. The spectra extracted showed a very good agreement with broad band fluxes, where available.

Fitting models of stellar populations to the data confirmed generally young ages for the host galaxies. In addition we found significant gas disks in several of the spheroids, unusual for massive ellipticals, and generally stronger forbidden line emission in ellipticals than disks. From emission line ratios the ionising radiation in the ellipticals was found to come from the power-law emission of the nucleus, while for one disk it was more likely the radiation of hot stars.

In comparison to the results from Boroson et al. (1985) and Nolan et al. (2001) we propose the following explanation:

- Our blue ellipticals were recently created as the results of a major merger event of two disks. They still show the young stellar composition of their progenitor galaxies, but their change in morphology through the merger is complete.

- In these merger events no strong starburst is induced in the hosts. Gas from the progenitors is assembled in a low surface density gas disk with a low star formation rate. In the course of the merger the nuclear activity is ignited.

- In the disks in our samples the nuclear activity was started also by a tidal event. These events were smaller in scale, in a sense that one of the galaxies involved was significantly smaller than the other, insufficient to dynamically destroy both disks and form a spheroidal. Tidal features are visible in a large number of objects.

- The space density of our type of blue elliptical host galaxy should decrease with luminosity, because of the rapid decrease of the disk galaxy luminosity function beyond $L^*$.

- More luminous and redder elliptical hosts as found by Nolan et al. are not of this type. Their nuclear activity is created not in a merger of two disks, but in an encounter or merger of one luminous elliptical with a smaller galaxy. This explains their spectrum being mainly that of an old evolved population.

- An evolution from our blue ellipticals to a red elliptical can happen within 1 Gyr, when the high level star formation previously present in the progenitor disks is stopped at the merger event. Within 0.5–1 Gyr the spectrum will change to resemble an evolved stellar population.

- The amount of gas emission in the host induced by the nucleus is different for disks and ellipticals in our sample. We translate the classification by Boroson et al. of “line dominated” and “continuum dominated” objects. Their high and low luminosity line objects are identical to our blue ellipticals, their low luminosity continuum objects mainly to our disks and their high luminosity continuum objects to older red ellipticals.

- The connection between nuclear Balmer line shape and QSO radio morphology on one side and Balmer line shape and optical host morphology on the other side might give more insights into the radio emission processes in the future.

- The scenario proposed is a support for hierarchical galaxy formation scenarios. QSOs would mark the – or at least a part of the – events of hierarchical galaxy evolution. Their host galaxies are a snapshot of a particular phase in each galaxies' life. Snapshots of other merging variants might be seen in ULIRGs and starburst galaxies, as well as the other members of the AGN zoo, representing other initial conditions (gas content, merger geometry, line of sight, etc.).

- The different classes like blue and red ellipticals, disk shaped hosts will have a dispersion in their host and nuclear luminosities, and colours, with individual parameter ranges overlapping. Distiguishing between these classes will in many cases only be possible using spectral information.

## 6.5 Outlook into the future

The results of this study show the diagnostic capabilities made possible by spectral information. So far we analysed samples from a fairly narrow range of QSO luminosities. According to our scenario, extending this to higher luminosities should follow the evolutionary merger sequence, moving away from disks towards blue ellipticals, and then to more and more red ellipticals. We will have to support this with data from homogenously selected, representative samples.

We have already available a second low-*z* multicolour sample, drawn from the PG survey (Schmidt & Green 1983), being brighter by about a magnitude than our current broad band sample. For this sample of almost 40 objects we obtained images in the optical *BVR* and for some objects also *I* band, and just recently also in the NIR *H* and for some also *K* band, all with the Nordic Optical Telescope. Even though the number of NIR filters is reduced compared to the multicolour sample presented here, we will not loose much information if the NIR calibration is reliable. Having available the *B* band for all objects will give us more information about the young populations present.

For two further samples we have images in at least one optical to NIR colour available, one of them being significantly brighter than the current sample. These samples will supplement the colour investigation for more luminous objects and particularly elliptical hosts. They are also to be used to determine the duty-cycle of QSOs.

Further it is interesting to follow the line of thought concerning the Balmer line shape. Our data is insufficient to relate radio properties, Balmer line shape, host galaxy morphology and state of the ISM. Selecting a sample on basis of Balmer line shape and width could prove very interesting in this respect, searching for correlations and physical processes in a potential sequence of narrow line Sy 1 like I Zw 1 at one end, via normal Sy 1, objects like HE 0952–1552 (Fig. 4.1) being a morphological disk but showing a somewhat broader and asymmetric H$\beta$ line, and bumpy red ellipticals on the other end. Again imaging to assess morphologies as well as on-nuclear spectroscopy will complement each other. This could be combined with deep radio data to assess the radio properties also for the radio quiet, though not radio silent objects.

As we mentioned before, the VLT sample investigated in this study was only the first half of the approved program. The data of the second half will soon be available, being much deeper than the present data. We will be able to model the resulting spectra in more detail, attempting also the determination of velocity dispersions for the centre of the object, thus receiving a direct independent estimate for the mass of the central black hole. An extraction of diagnostic absorption line indices in combination with model fitting will make possible to determine metallicities and detailed ages of the galaxies. This is a very important test for the merger hypothesis put forward in this study.

Furthermore it is useful to extend spectroscopy further to the UV. The ground based efficiency is dropping rapidly in this regime, but information about the spectral range at 4000 Å and shorter wavelengths is necessary for higher redshifts and the study of objects like PKS 1302–1017 with its blue featureless continuum.

For further developement of analysis techniques we already mentioned the implementation of a third component for the gas emission, when modelling the emission lines. A more fundamental extension would be the application to off-nuclear modelling. In general the spectral 2d modelling as implemented is not restricted to on-nuclear spectra. Application to off-nuclear spectra requires a precise measurement of the slit position relative to the centre of the QSO. If the spectrum of the PSF star would be observed at an identical distance of the slit from the center, the PSF would again be well defined. A second possibility would the re-computation of the PSF from an on-nuclear spectrum, incorporating the geometry of the slit. This however has not yet been incorporated, but would be very interesting with respect to already existing data, also from other groups.

The second extention and planned application is the use of PMAS (Potsdam Multi-Apertur Spectrometer), the integral field spectroscopy unit from the AIP. PMAS is to be used at the Calar Alto 3.5m and later possibly at the Large Binocular Telescope. It is currently equipped with 16×16 lenslets (Roth et al. 2000) that sample the whole spatial domain in the focal plane. The lenslets are connected to optical fibres that remap the image to the long slit of the spectrograph, producing one spectrum per lenslet. A future upgrade to 1024 fibres is planned, the current spatial resolution is $0.5''$.

PMAS will be used to obtain spatially resolved spectra of an area of $8'' \times 8''$ around the centre of low-*z* QSOs. When integrating along $2\pi$, PMAS at the Calar Alto 3.5m telescope has the same photon collection ability as long slit spectroscopy with the VLT, because of it sampling the full plane and not only along a line. Used with the full spatially resolution, PMAS and future instruments like VIRMOS at the VLT enables us to spectroscopically study the the inner parts, if not complete host galaxy, not only a slice through it. This can be used to search for an ionisation torus found in Seyfert galaxies also in luminous QSOs. Is the complete ISM of a host galaxy ionised by the nucleus, or just a part? Do we see a geometry of absorbing material? Is there a systematic difference to low luminosity AGN? One of the candidates for resolved studies with PMAS is HE 1434–1600, with its changing line ratios and inner cutoff for gas emission, to study the possible depletion of hard radiation and the escape fraction of UV photons.

The last years have brought much new understanding of QSOs, their morphology and physics behind it. Now the new possibilities on QSO host galaxy spectroscopy will be a large and thrilling field to be explored in the future.

# A Multicolour sample modelling results: all radial profiles

Modelling results for the broad band sample. Shown are radial surface brightness profiles for all objects and bands. The symbols mark the data points, the different lines are: nuclear model (dot-dashed black), host model (long dashed, green spheroidal, red disk), combined nuclear plus host model (solid black), remaining host after subtraction of the nuclear model (dotted light blue). The vertical line marks the radius of the area inside which was fitted.

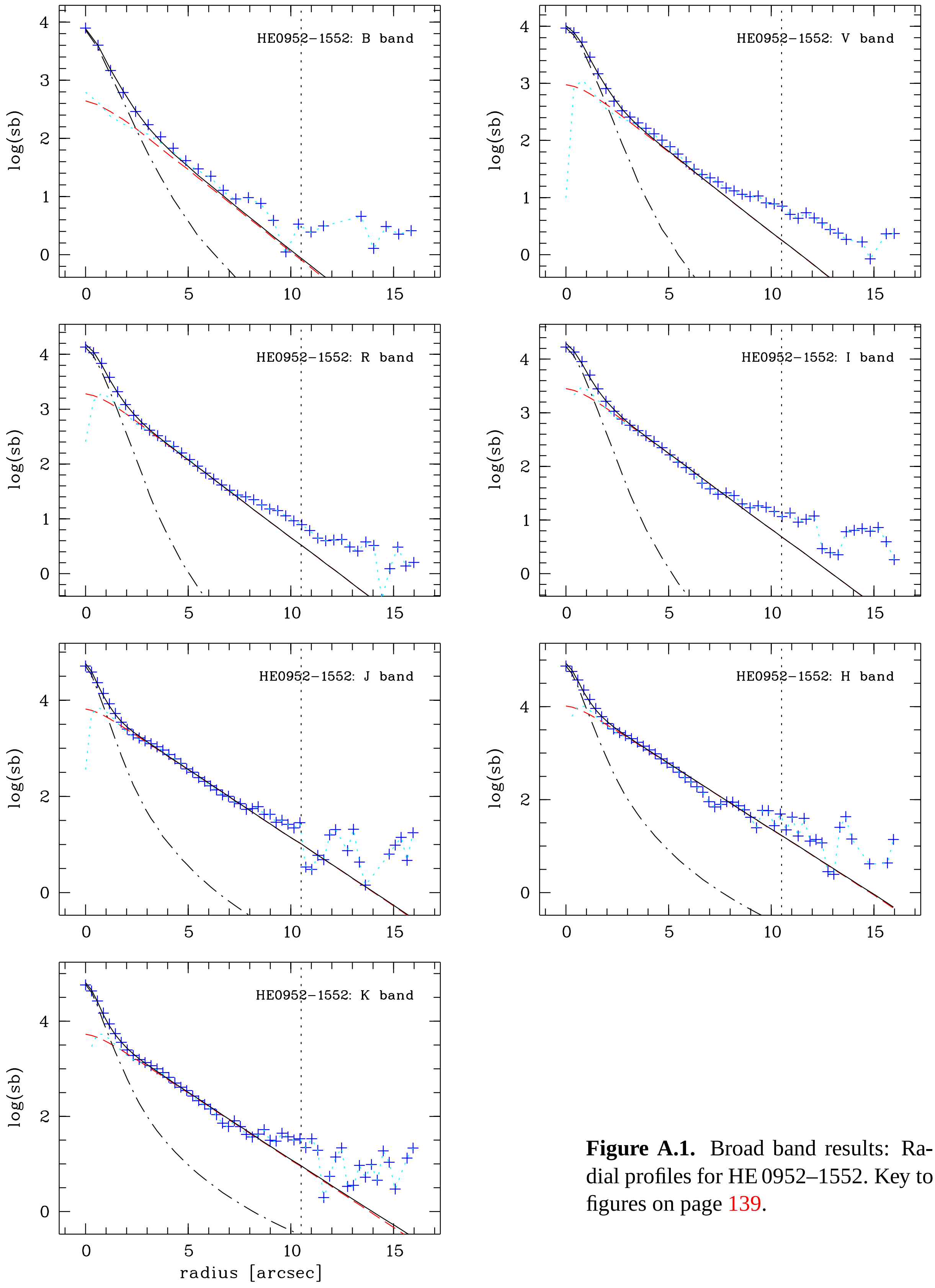

**Figure A.1.** Broad band results: Radial profiles for HE 0952–1552. Key to figures on page 139.

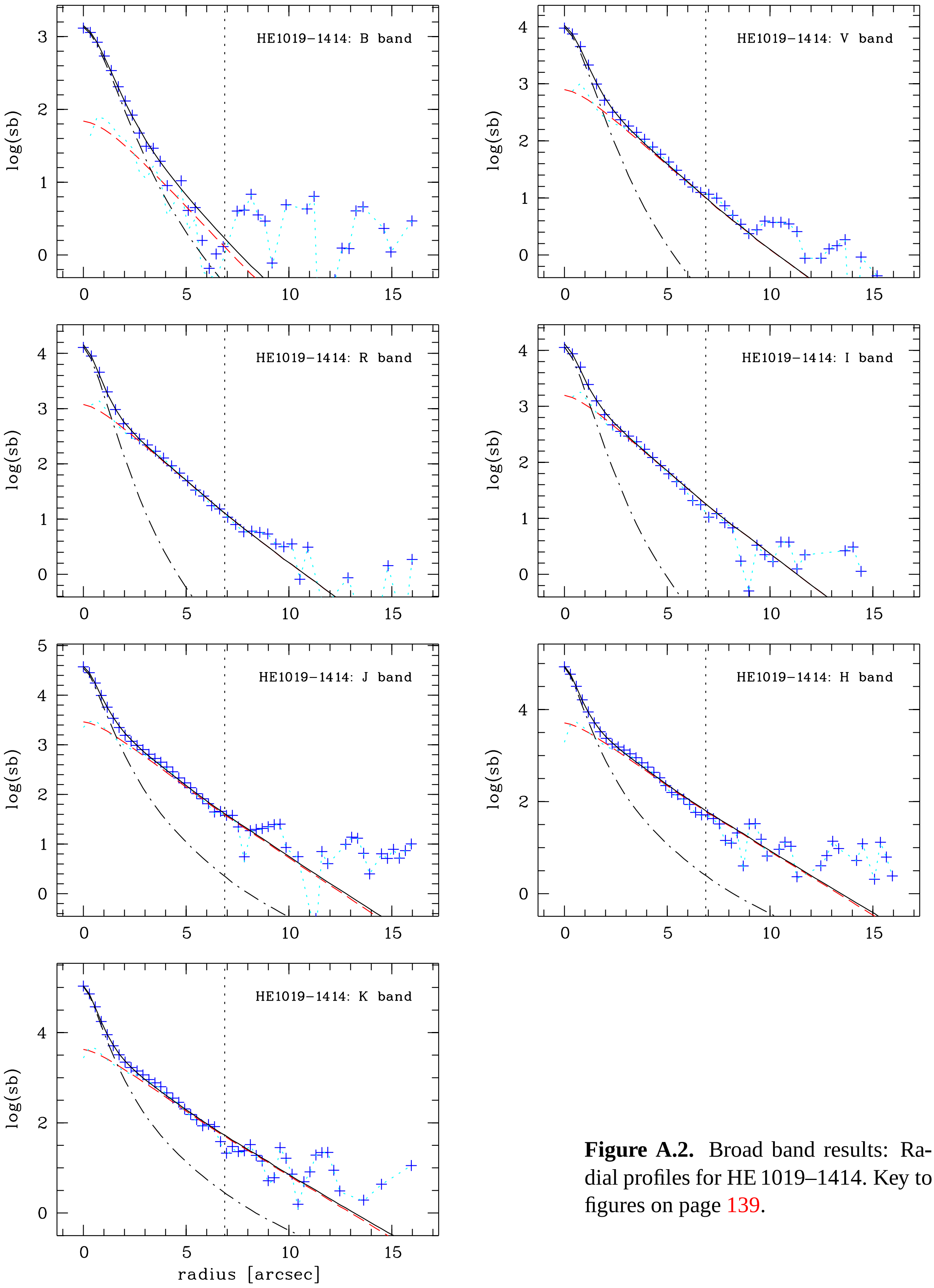

**Figure A.2.** Broad band results: Radial profiles for HE 1019–1414. Key to figures on page 139.

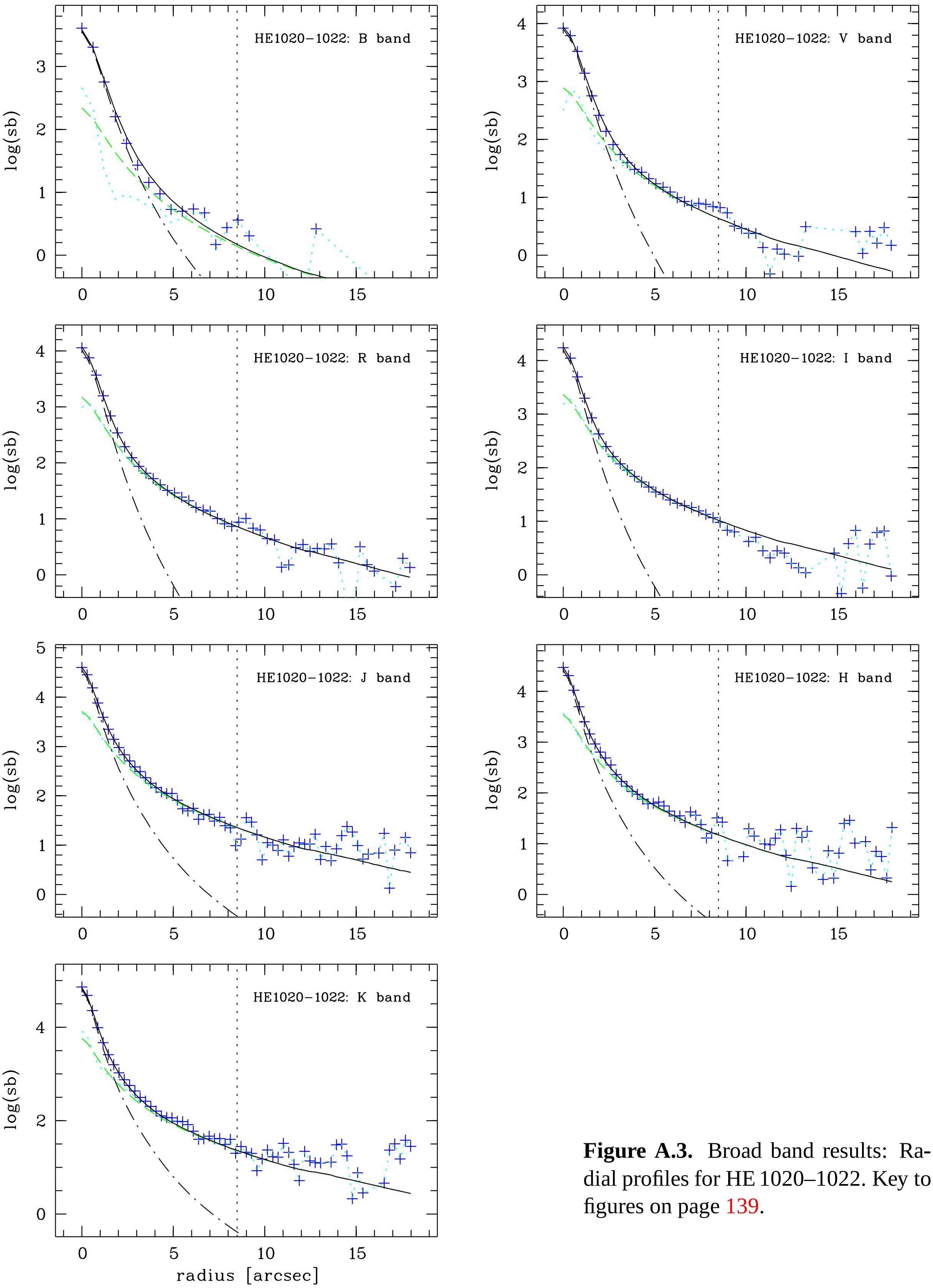

**Figure A.3.** Broad band results: Radial profiles for HE 1020–1022. Key to figures on page 139.

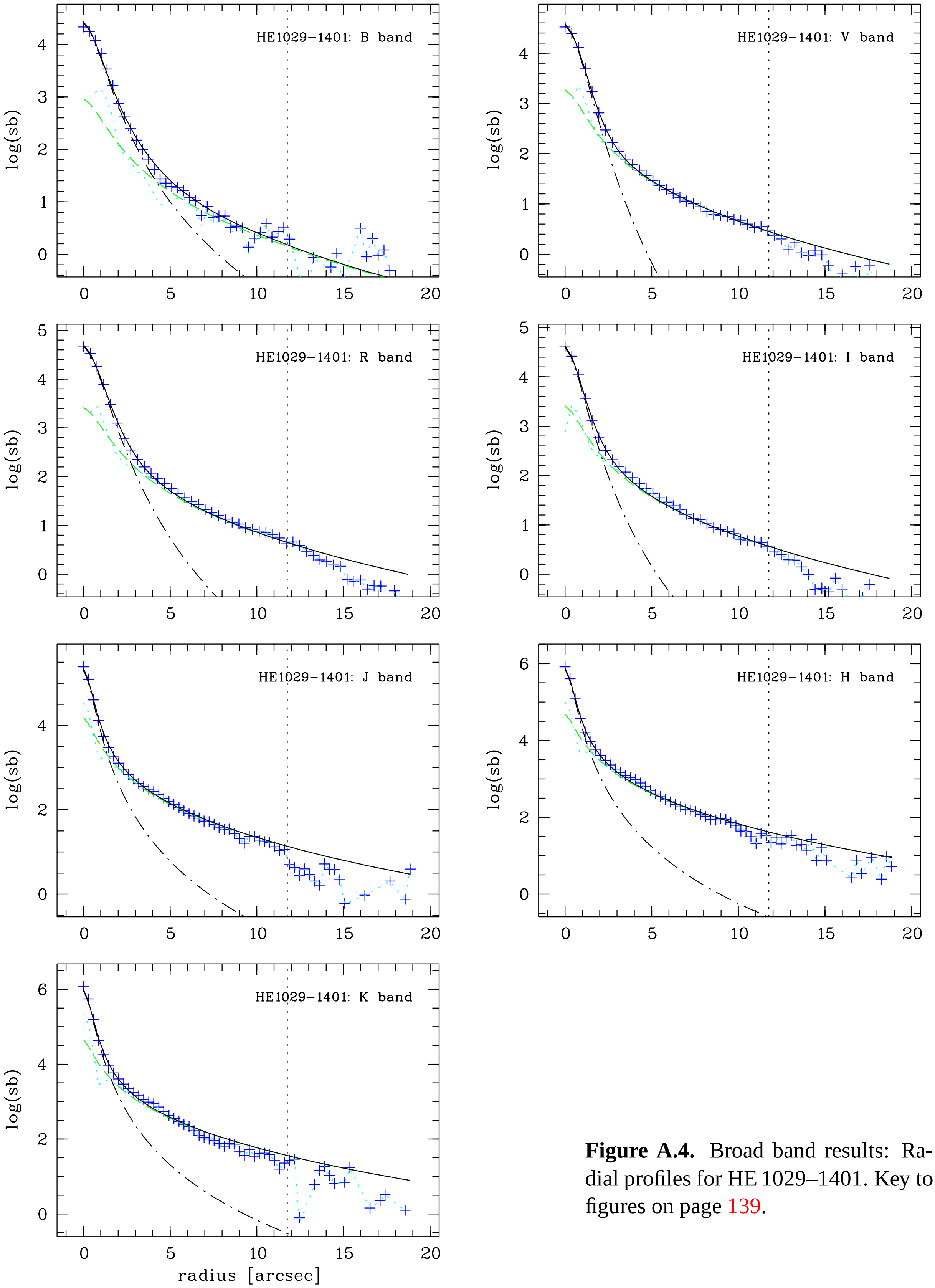

**Figure A.4.** Broad band results: Radial profiles for HE 1029–1401. Key to figures on page 139.

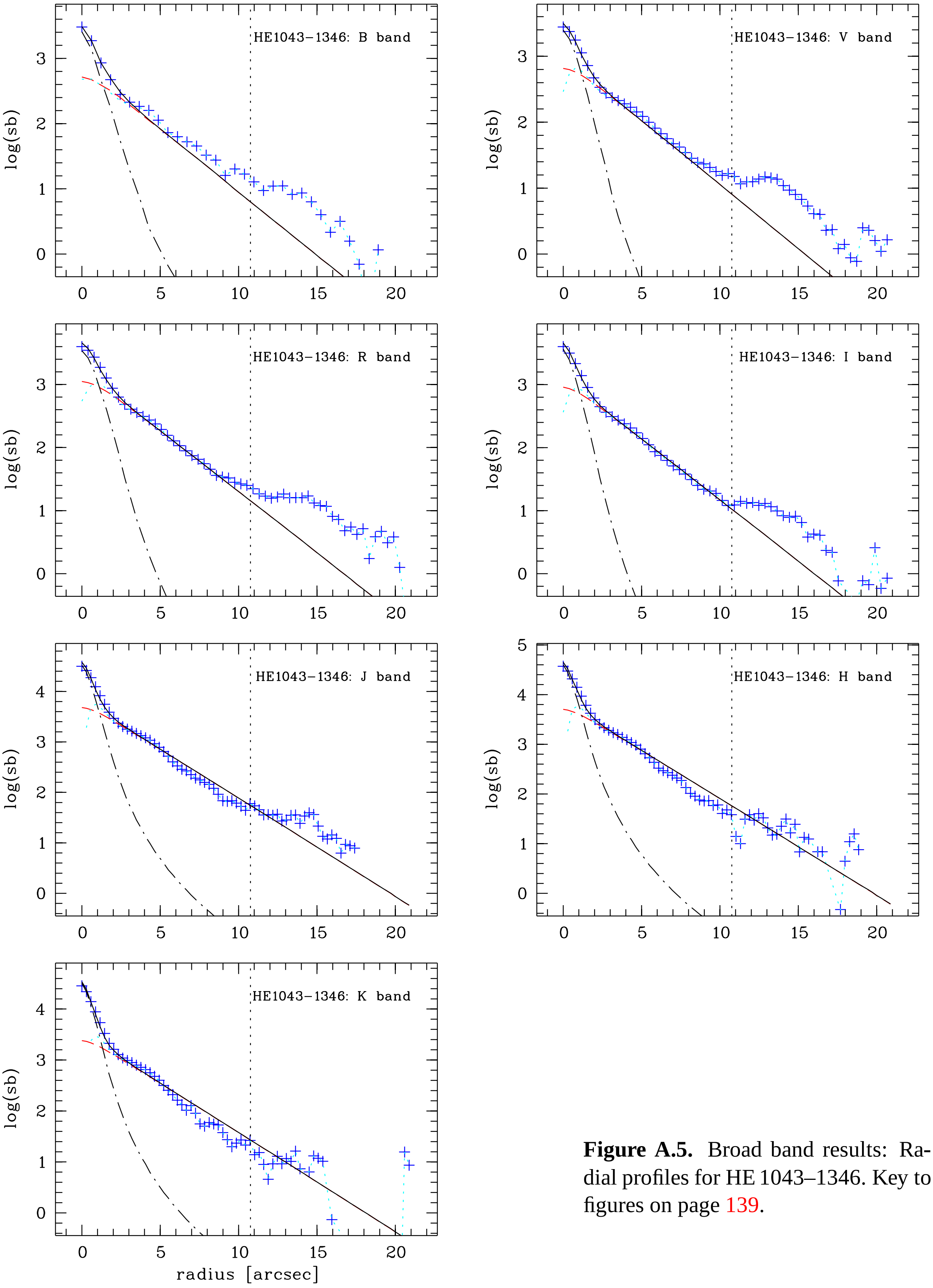

**Figure A.5.** Broad band results: Radial profiles for HE 1043–1346. Key to figures on page 139.

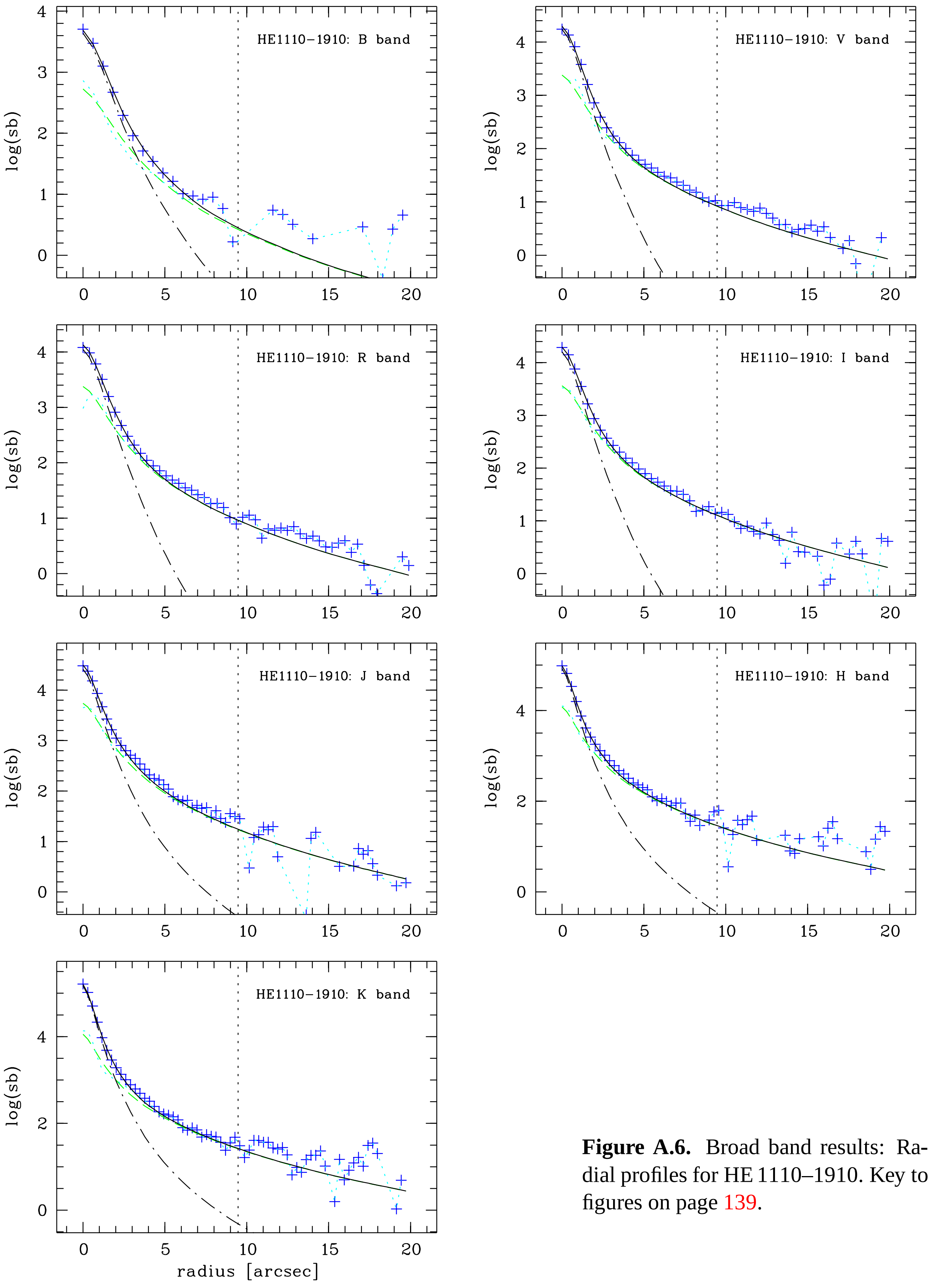

**Figure A.6.** Broad band results: Radial profiles for HE 1110–1910. Key to figures on page 139.

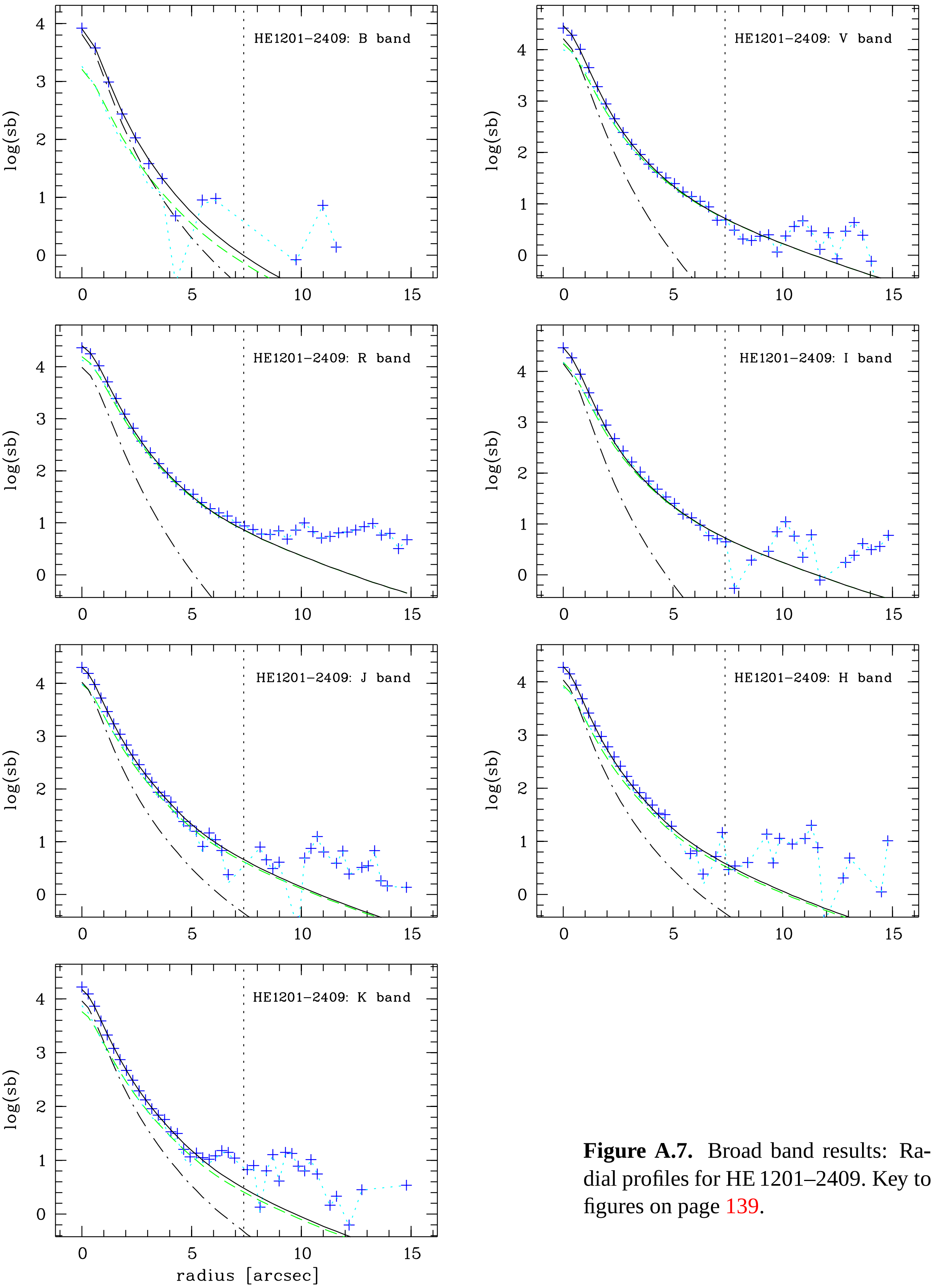

**Figure A.7.** Broad band results: Radial profiles for HE 1201–2409. Key to figures on page 139.

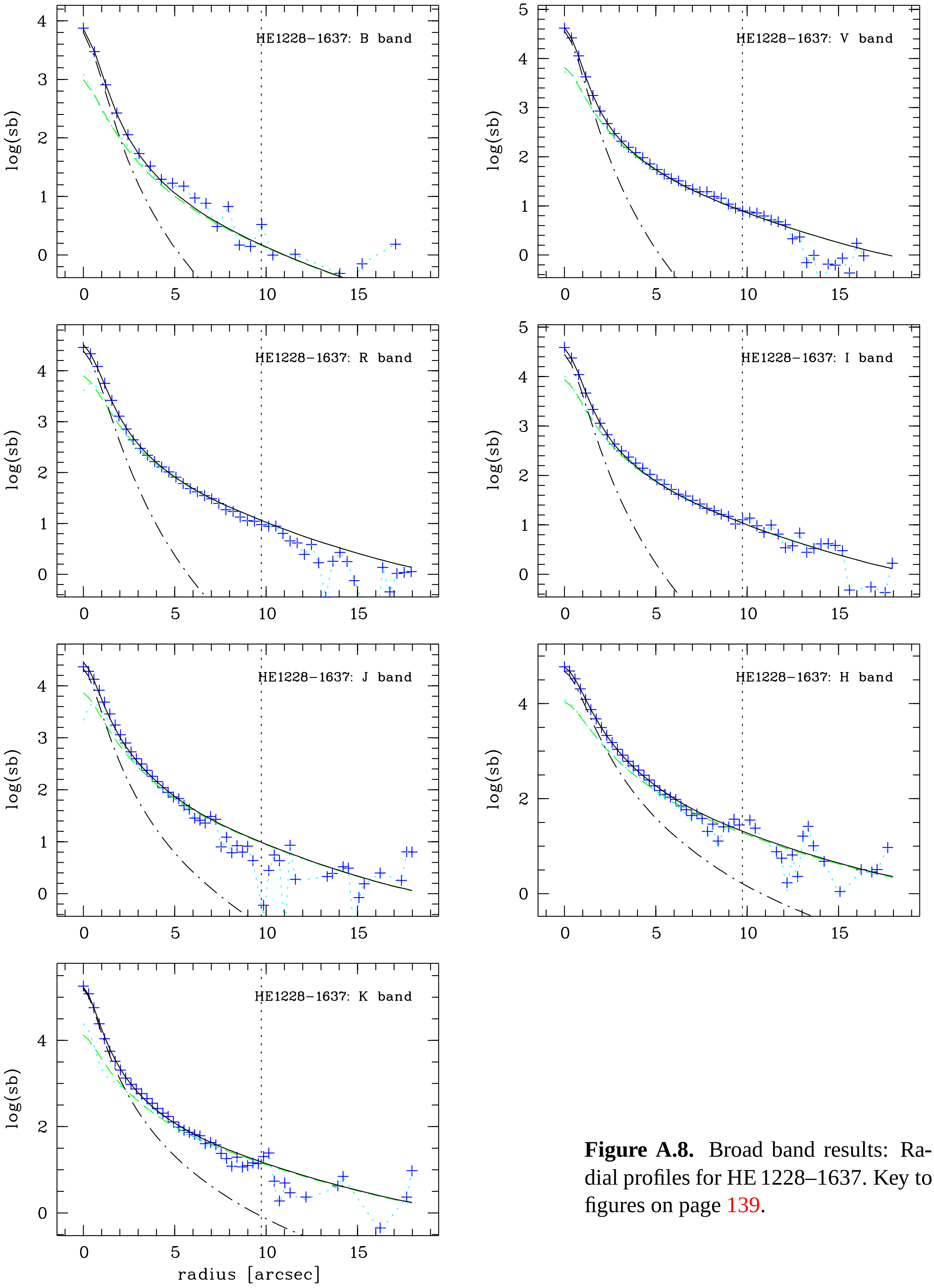

**Figure A.8.** Broad band results: Radial profiles for HE 1228–1637. Key to figures on page 139.

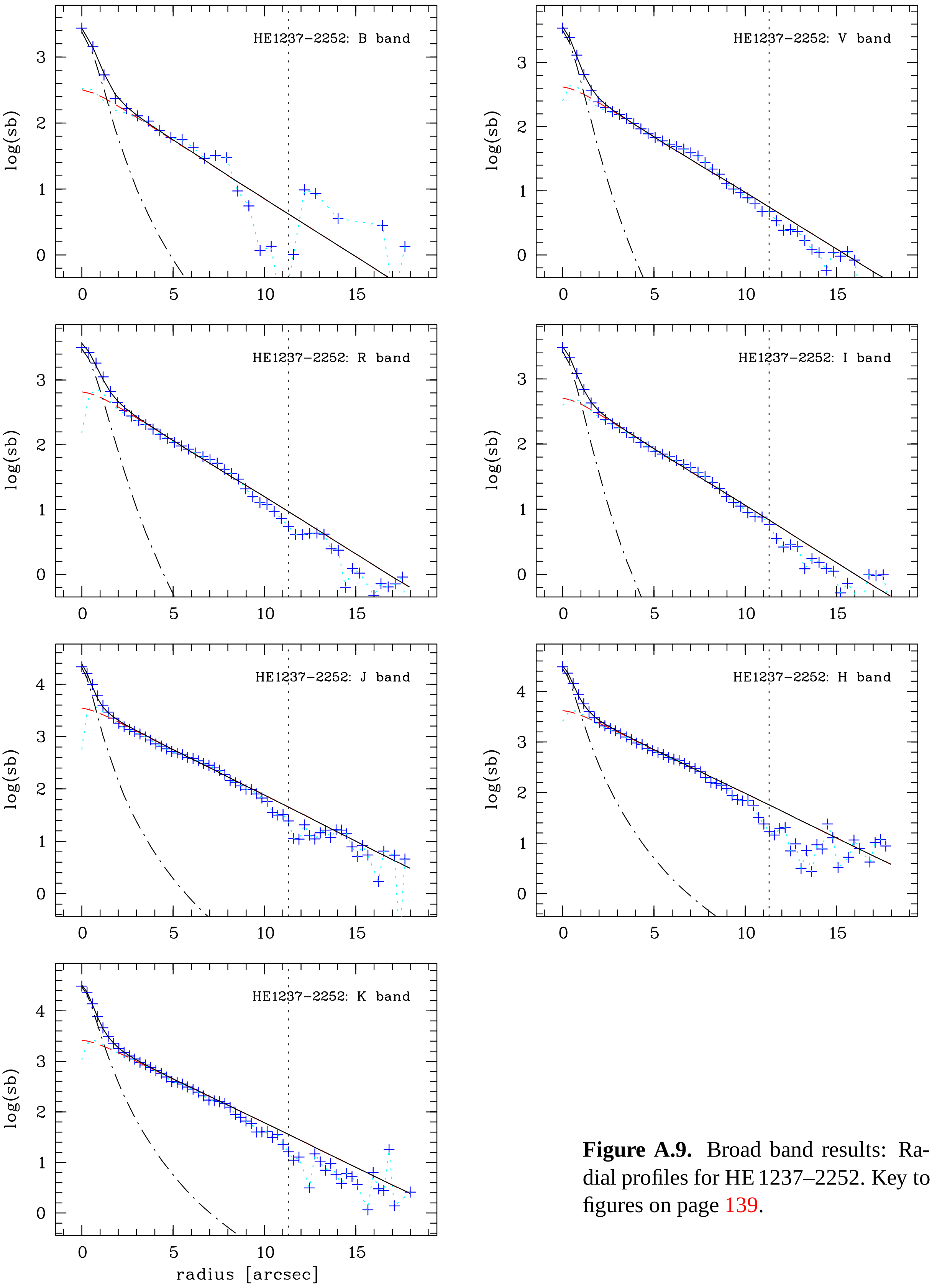

**Figure A.9.** Broad band results: Radial profiles for HE 1237–2252. Key to figures on page 139.

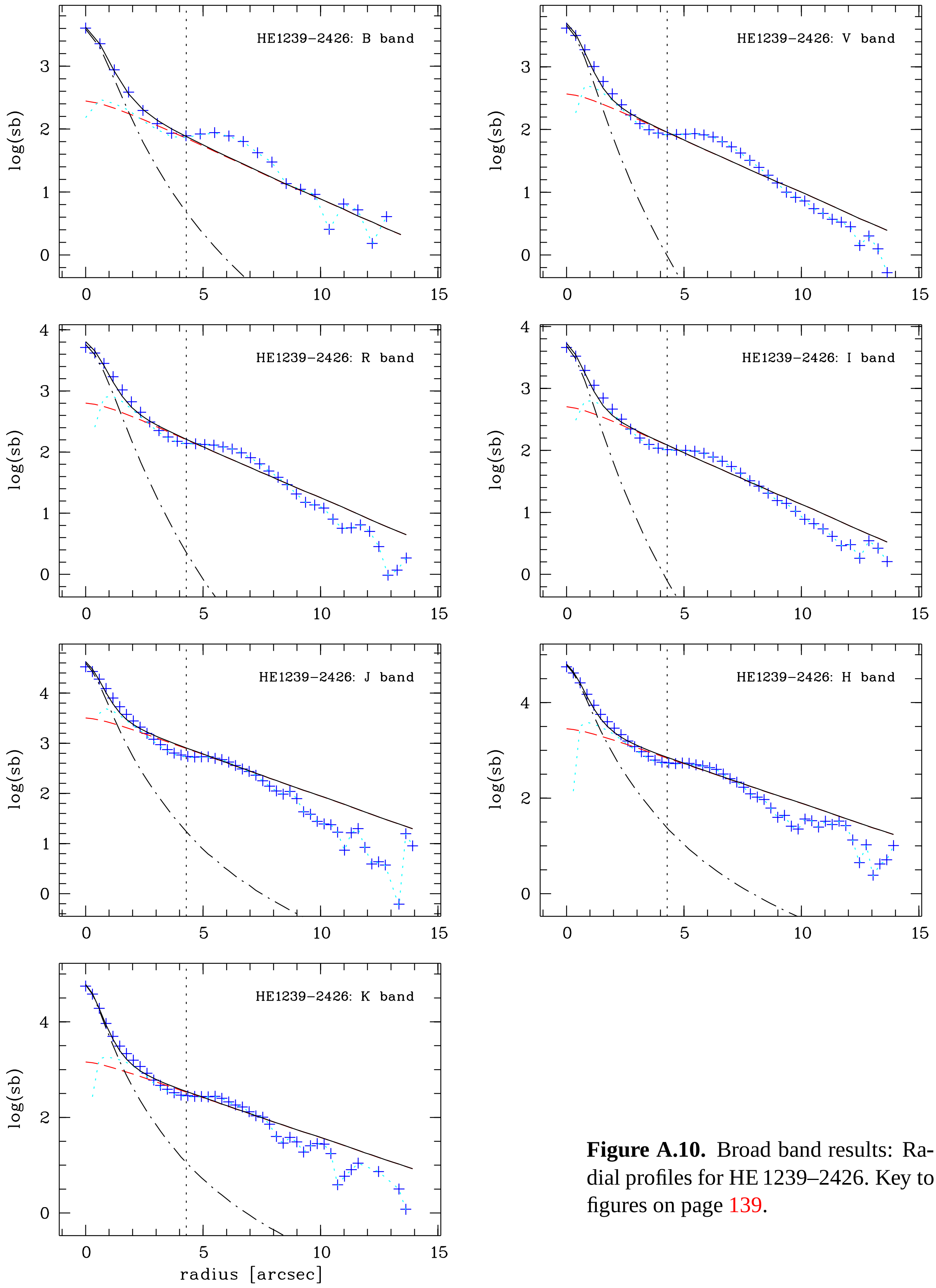

**Figure A.10.** Broad band results: Radial profiles for HE 1239–2426. Key to figures on page 139.

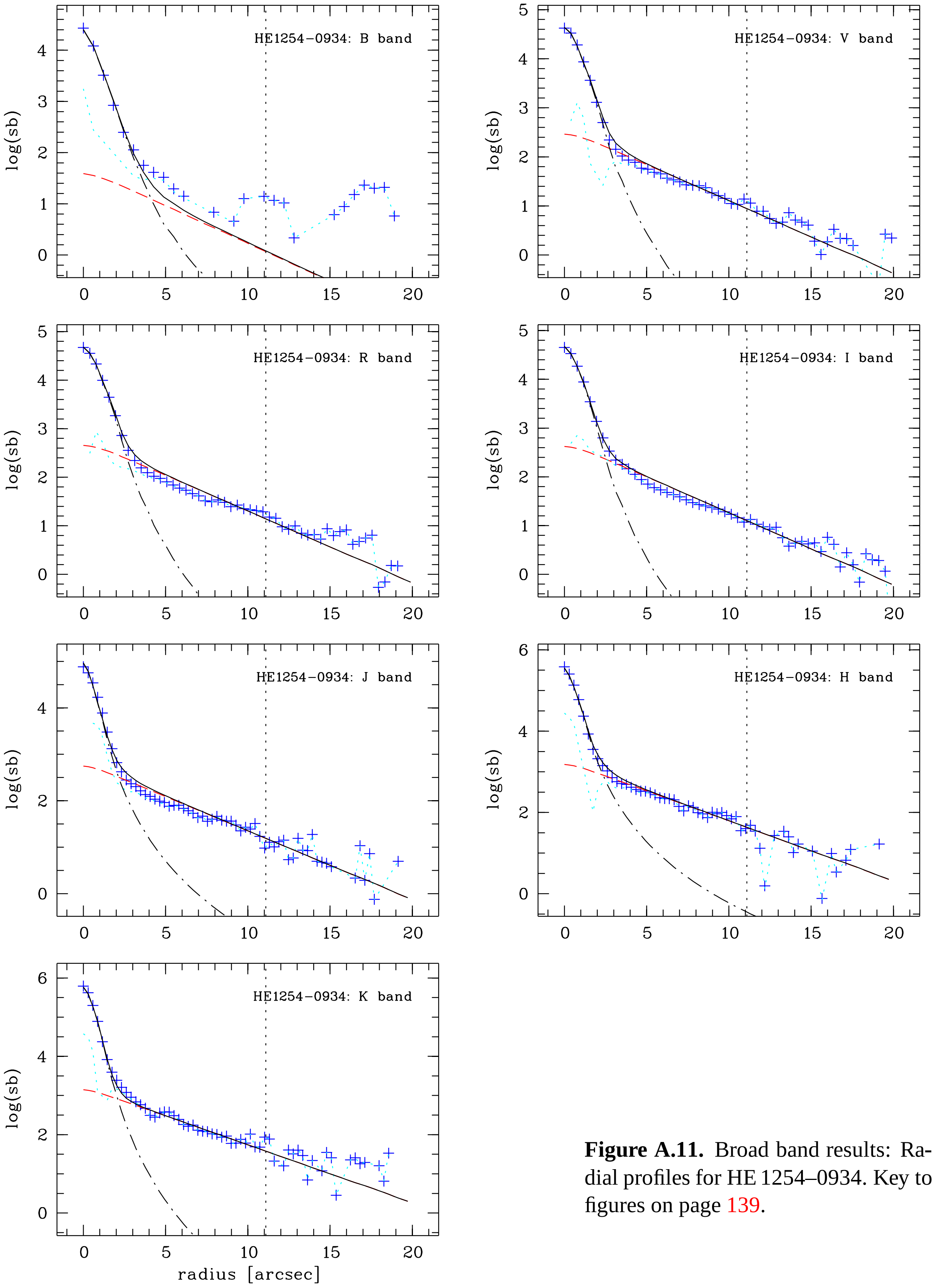

**Figure A.11.** Broad band results: Radial profiles for HE 1254–0934. Key to figures on page 139.

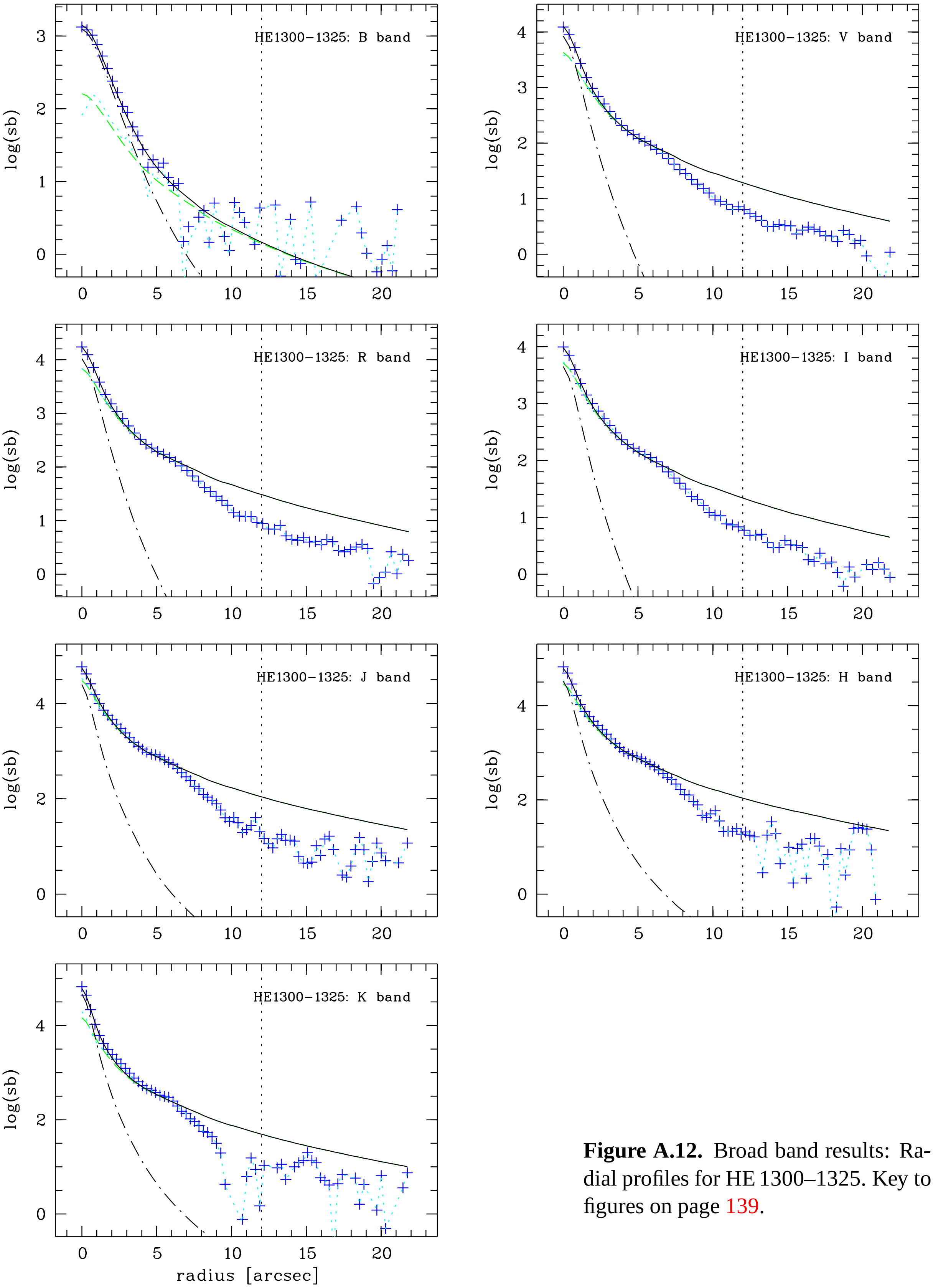

**Figure A.12.** Broad band results: Radial profiles for HE 1300–1325. Key to figures on page 139.

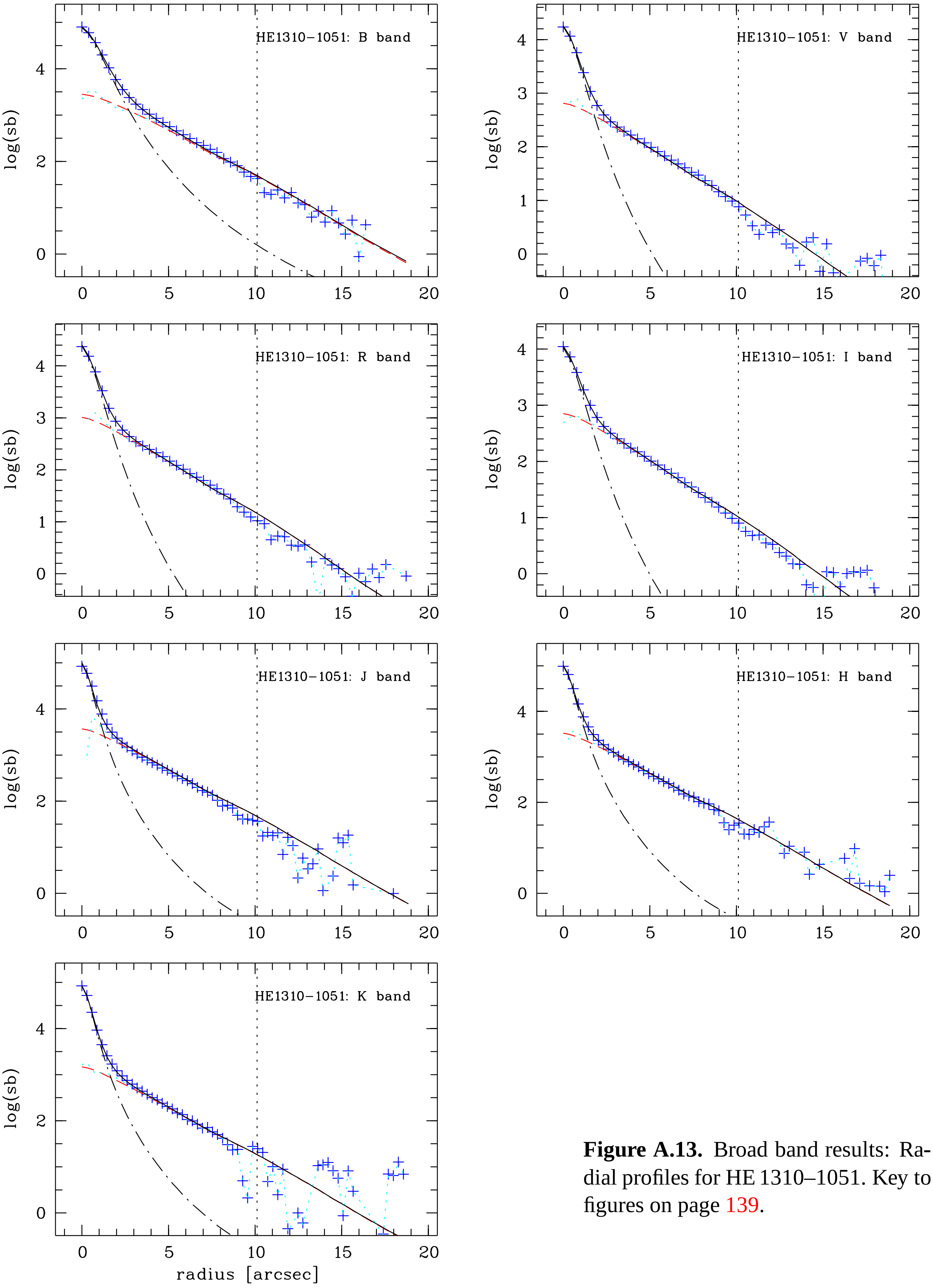

**Figure A.13.** Broad band results: Radial profiles for HE 1310–1051. Key to figures on page 139.

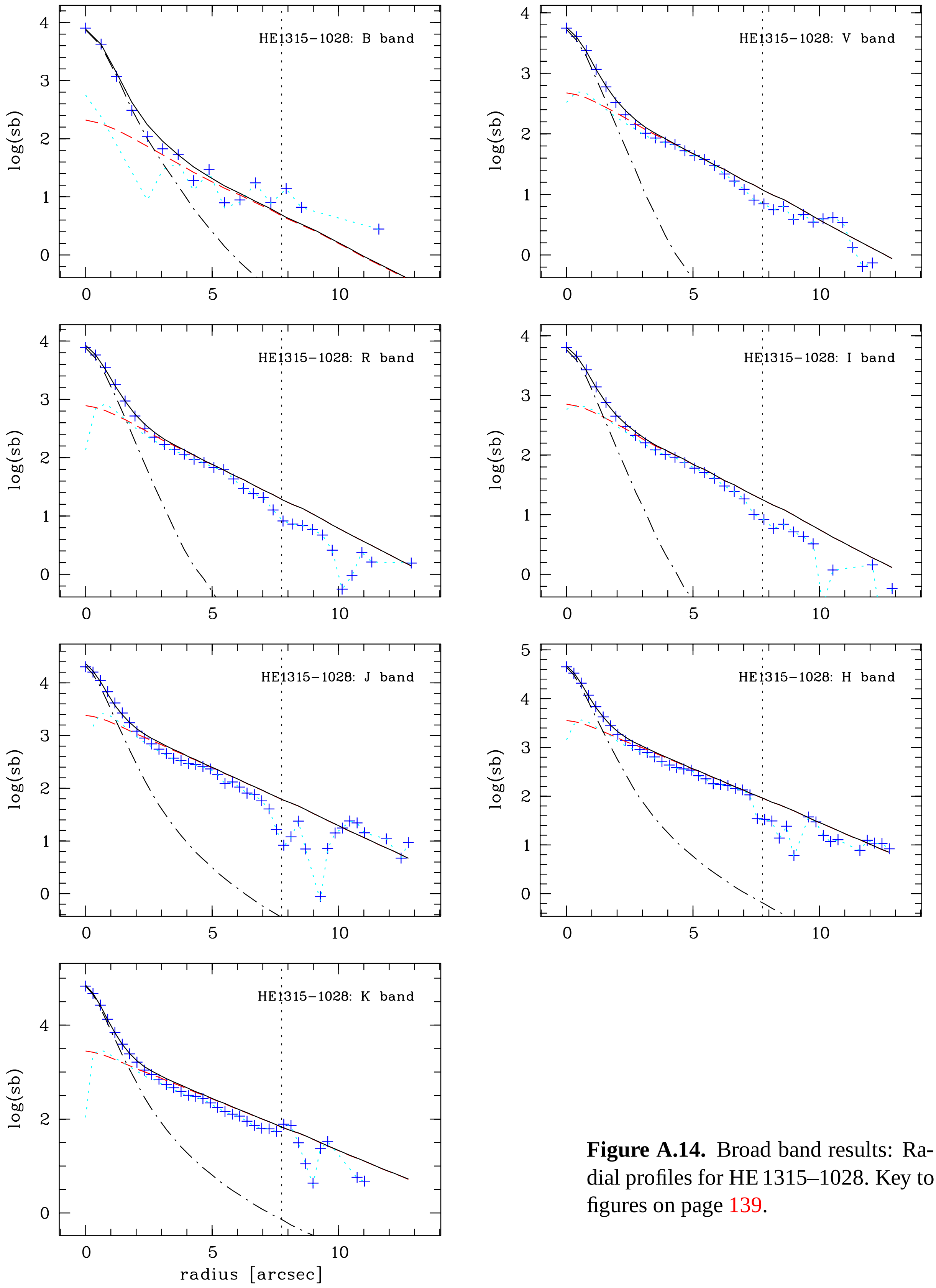

**Figure A.14.** Broad band results: Radial profiles for HE 1315–1028. Key to figures on page 139.

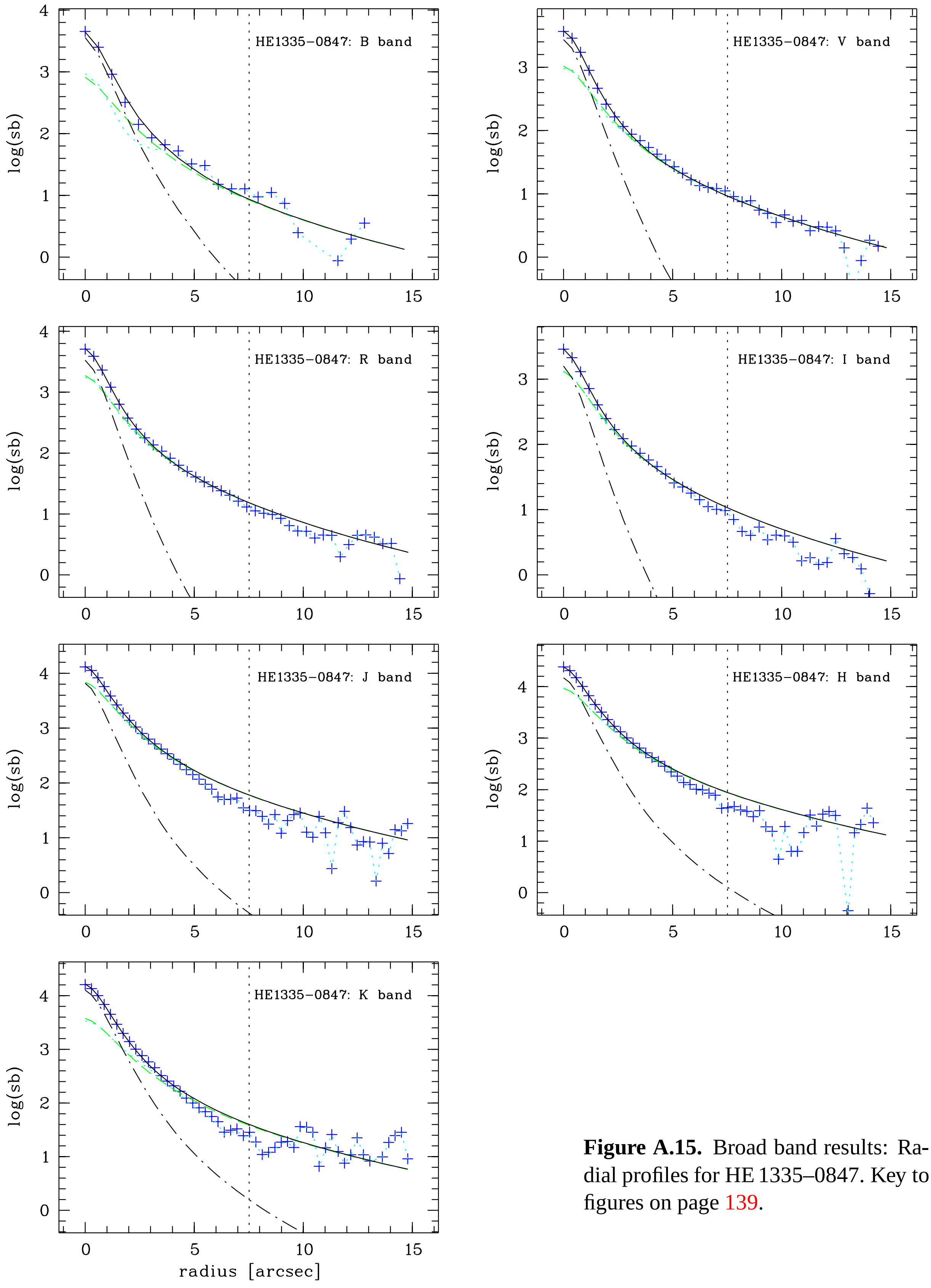

**Figure A.15.** Broad band results: Radial profiles for HE 1335–0847. Key to figures on page 139.

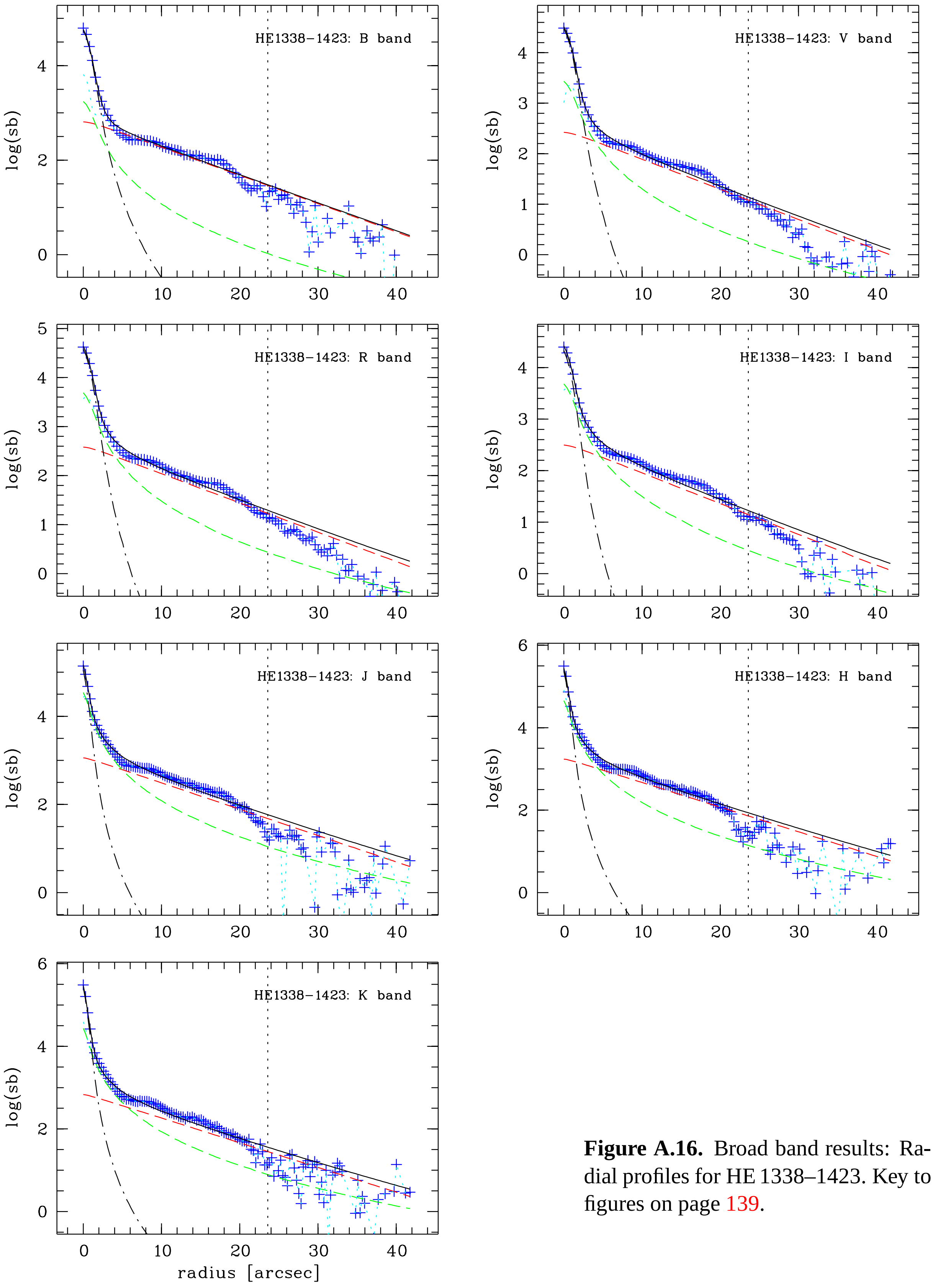

**Figure A.16.** Broad band results: Radial profiles for HE 1338–1423. Key to figures on page 139.

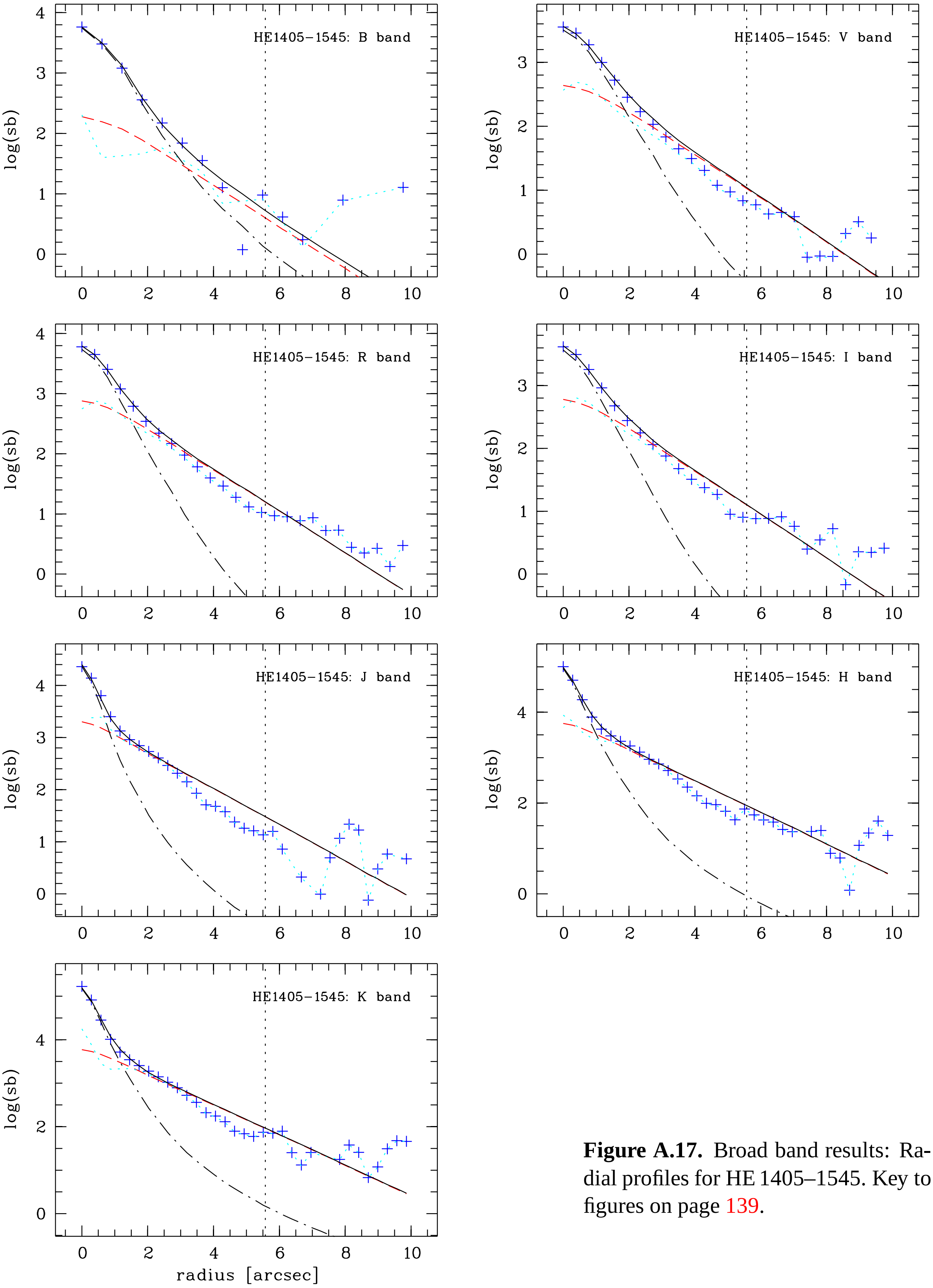

**Figure A.17.** Broad band results: Radial profiles for HE 1405–1545. Key to figures on page 139.

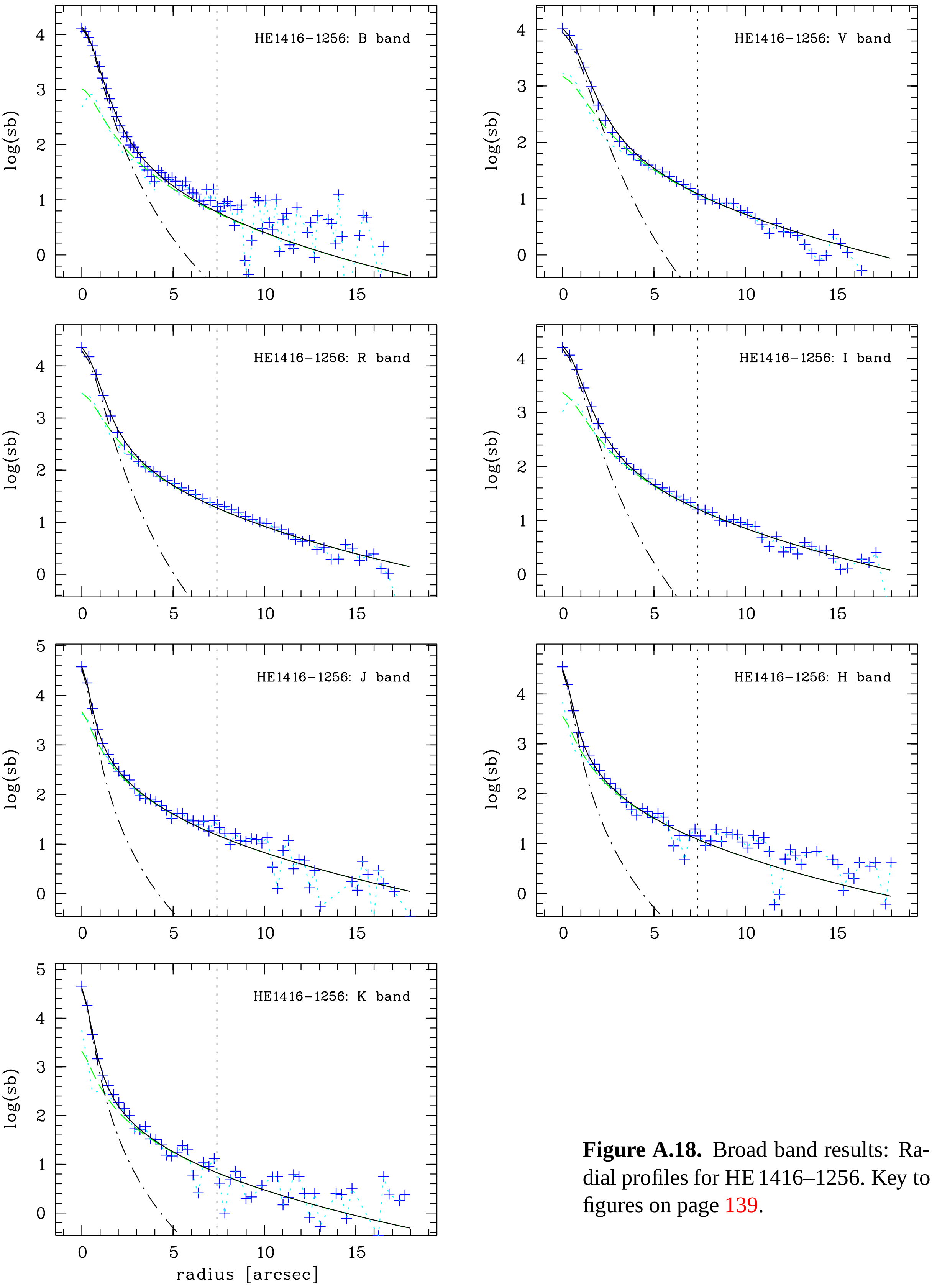

**Figure A.18.** Broad band results: Radial profiles for HE 1416–1256. Key to figures on page 139.

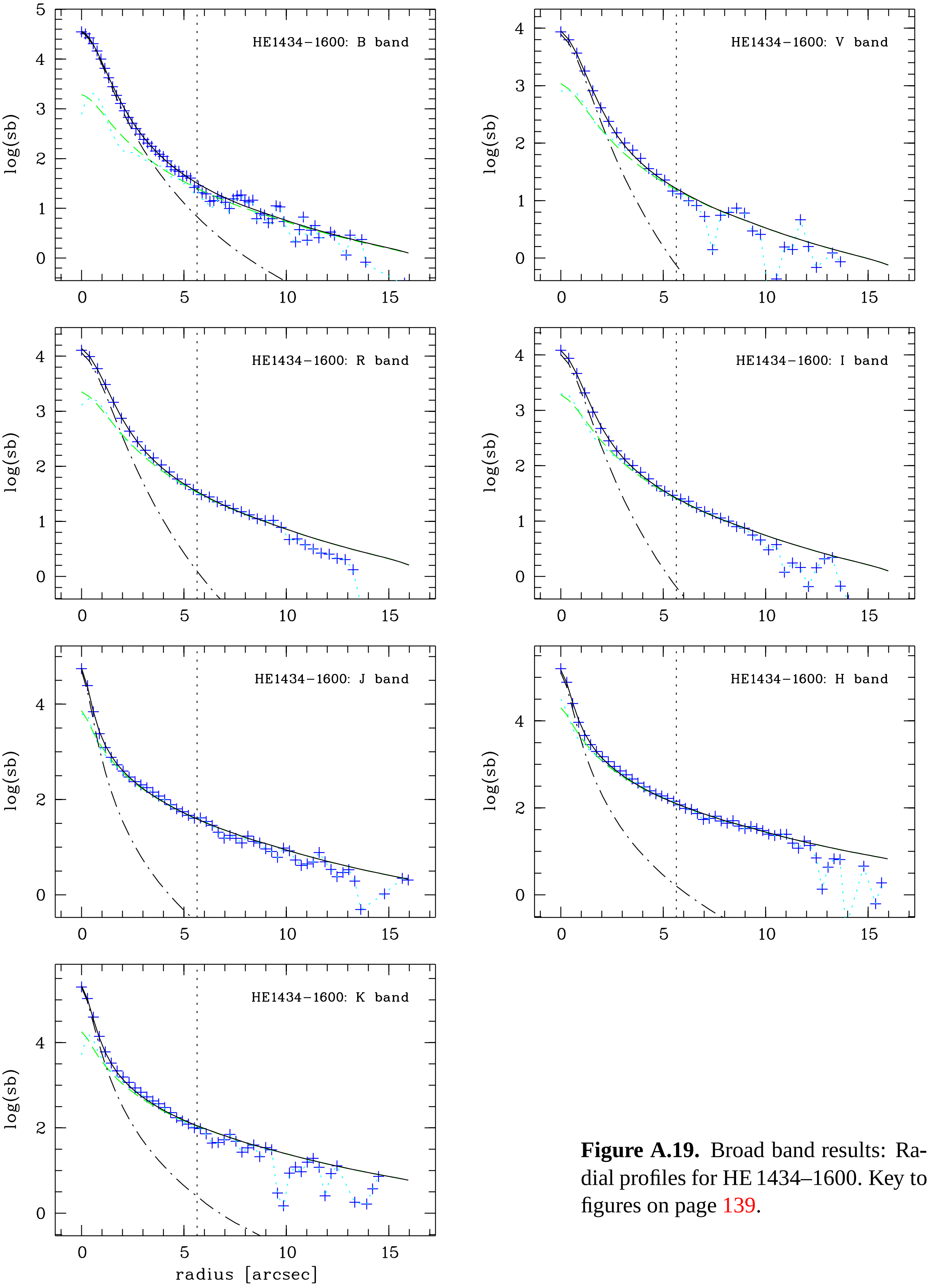

**Figure A.19.** Broad band results: Radial profiles for HE 1434–1600. Key to figures on page 139.

# B Multicolour population fits: data points and model spectra

**Figure B.1.** Results from fitting evolution synthesis stellar population models to multicolour host galaxy fluxes in section 2.7. The plots are described in Table 2.16. For HE 1043–1346 and HE 1300–1325 two diagrams are shown. One version where the continuous star formation (CSF) model which was selected best model in the two-component fit, is used, and a second version with the best non-CSF SSP.


data ×
model single □
0.7 Gyr
model double △
89.27% * 2 Gyr
10.73% * 0.1 Gyr
HE 1029−1401, z=0.085
data ×
model single □
CSF
model double △
94.9% * 6 Gyr
5.1% * 0.1 Gyr
HE 1043−1346, z=0.068
data ×
model single □
CSF
model double △
98.33% * CSF
1.67% * 0.1 Gyr
HE 1043−1346, z=0.068
data ×
model single □
2 Gyr
model double △
97.32% * 2 Gyr
2.68% * 0.1 Gyr
HE 1110−1910, z=0.111
5000
10000
15000
20000
lambda [A]


data ×
model single □
0.7 Gyr
model double △
100.0% * 0.7 Gyr
0.0% * 0.1 Gyr
HE 1201−2409, z=0.137
data ×
model single □
0.7 Gyr
model double △
94.44% * 2 Gyr
5.56% * 0.1 Gyr
HE 1228−1637, z=0.102
data ×
model single □
CSF
model double △
95.23% * 6 Gyr
4.77% * 0.1 Gyr
HE 1237−2252, z=0.096
data ×
model single □
CSF
model double △
95.91% * 14 Gyr
4.09% * 0.1 Gyr
HE 1239−2426, z=0.082
5000
10000
15000
20000
lambda [A]


data
model single
2 Gyr
model double
99.3% * 2 Gyr
0.7% * 0.1 Gyr
HE 1254−0934, z=0.139
data
model single
2 Gyr
model double
96.17% * 6 Gyr
3.83% * 0.1 Gyr
HE 1300−1325, z=0.047
data
model single
2 Gyr
model double
98.86% * CSF
1.14% * 0.1 Gyr
HE 1300−1325, z=0.047
data
model single
0.7 Gyr
model double
93.1% * 6 Gyr
6.9% * 0.1 Gyr
HE 1310−1051, z=0.034
5000
10000
15000
20000
lambda [A]


data ×
model single □
6 Gyr
model double △
98.86% * 6 Gyr
1.14% * 0.1 Gyr
HE 1315−1028, z=0.099
data ×
model single □
2 Gyr
model double △
93.1% * 2 Gyr
6.9% * 0.1 Gyr
HE 1335−0847, z=0.08
data ×
model single □
CSF
model double △
95.53% * 6 Gyr
4.47% * 0.1 Gyr
HE 1338−1423, z=0.041
data ×
model single □
0.7 Gyr
model double △
90.72% * 2 Gyr
9.28% * 0.1 Gyr
HE 1405−1545, z=0.194
5000
10000
15000
20000
lambda [A]

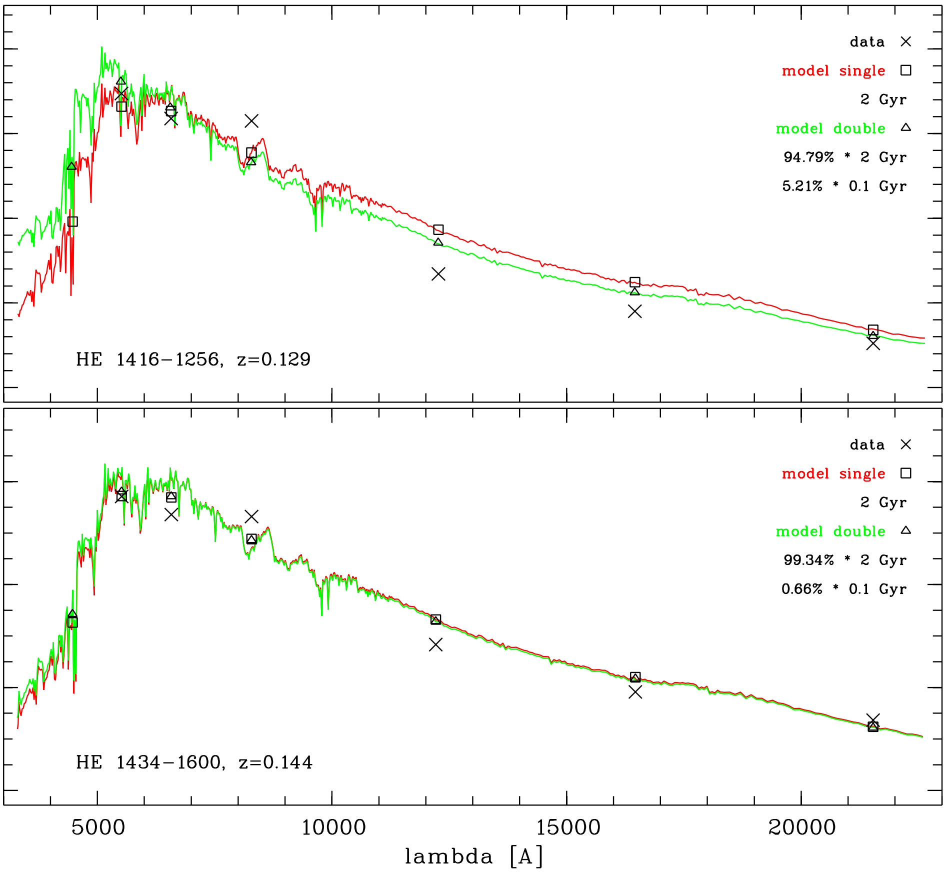
data ×
model single □
2 Gyr
model double △
94.79% * 2 Gyr
5.21% * 0.1 Gyr
HE 1416−1256, z=0.129
data ×
model single □
2 Gyr
model double △
99.34% * 2 Gyr
0.66% * 0.1 Gyr
HE 1434−1600, z=0.144
5000
10000
15000
20000
lambda [A]

# C EFOSC spectroscopy sample: modelling diagnostics

The following plots show diagnostics for the spatial modelling of PSF stars and QSOs from the ESO 3.6m EFOSC sample from section 4. The diagrams shown are (from top): PSF star center $x_0$, PSF star width $\alpha$, PSF star central flux $I_0$ and residual flux, QSO center $x_0$. All values are plotted against image row, which runs inversely to the direction of dispersion (smallest wavelength at highest pixel coordinate). For $x_0$ and $\alpha$ the individually determined values are plotted (points) and the polynomial smoothing fit (solid line). The PSF star residual is not plotted to scale to enhance structures.

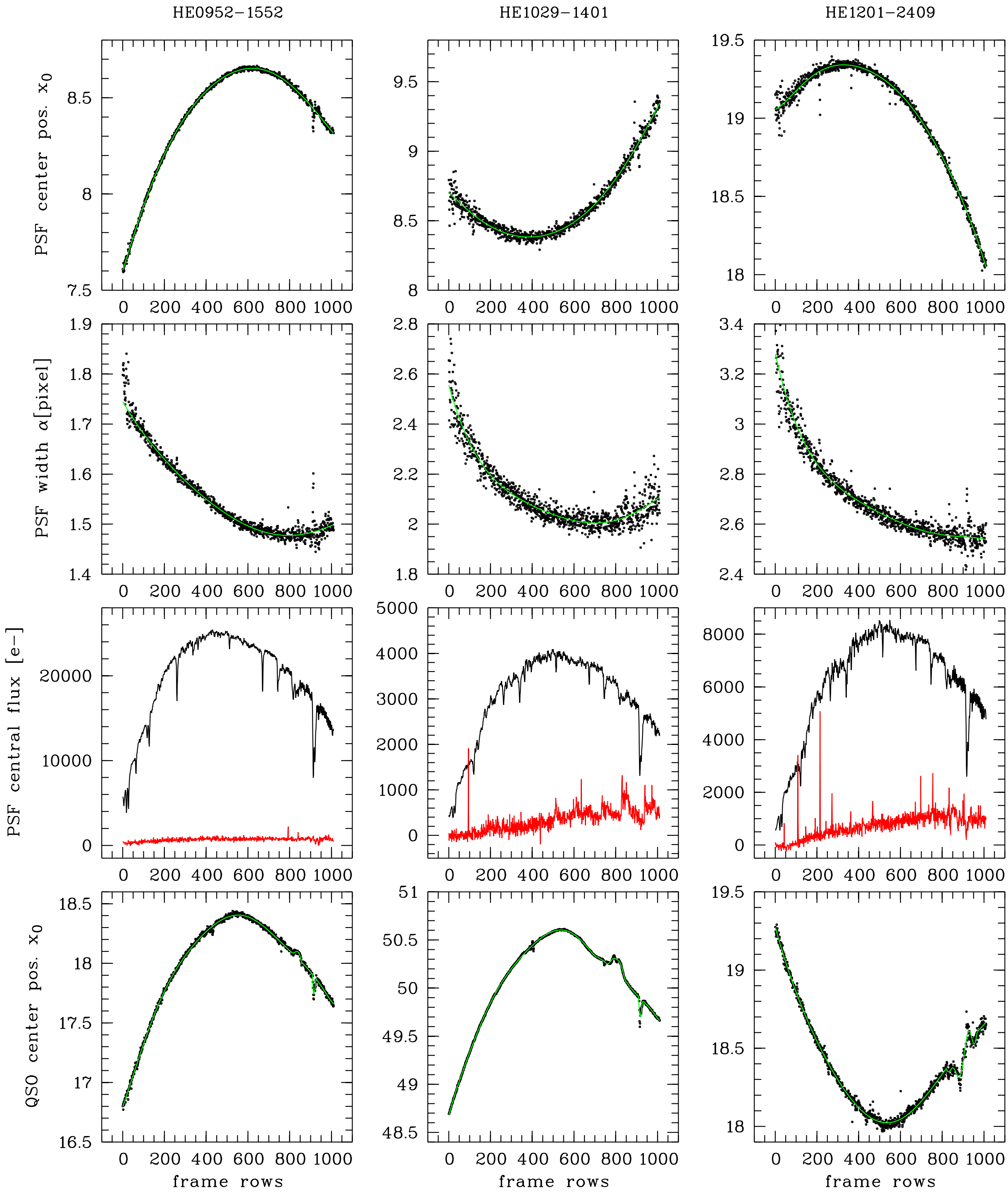

**Figure C.1.** Diagnostics for PSF star and QSO modelling of HE 0952–1552, HE 1029–1401 and HE 1201–2409.

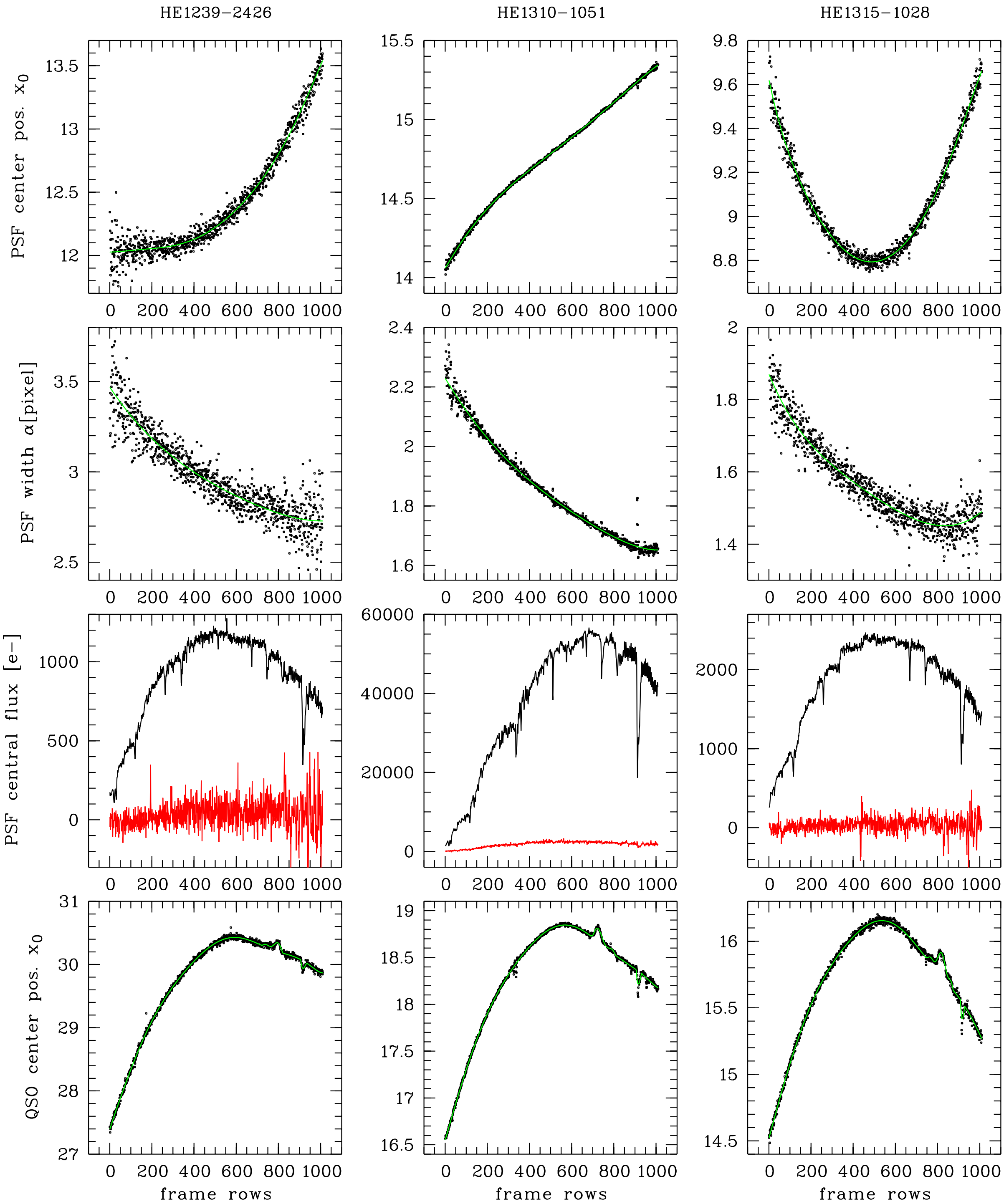

**Figure C.2.** Diagnostics for PSF star and QSO modelling of HE 1239–2426, HE 1310–1051 and HE 1315–1028.

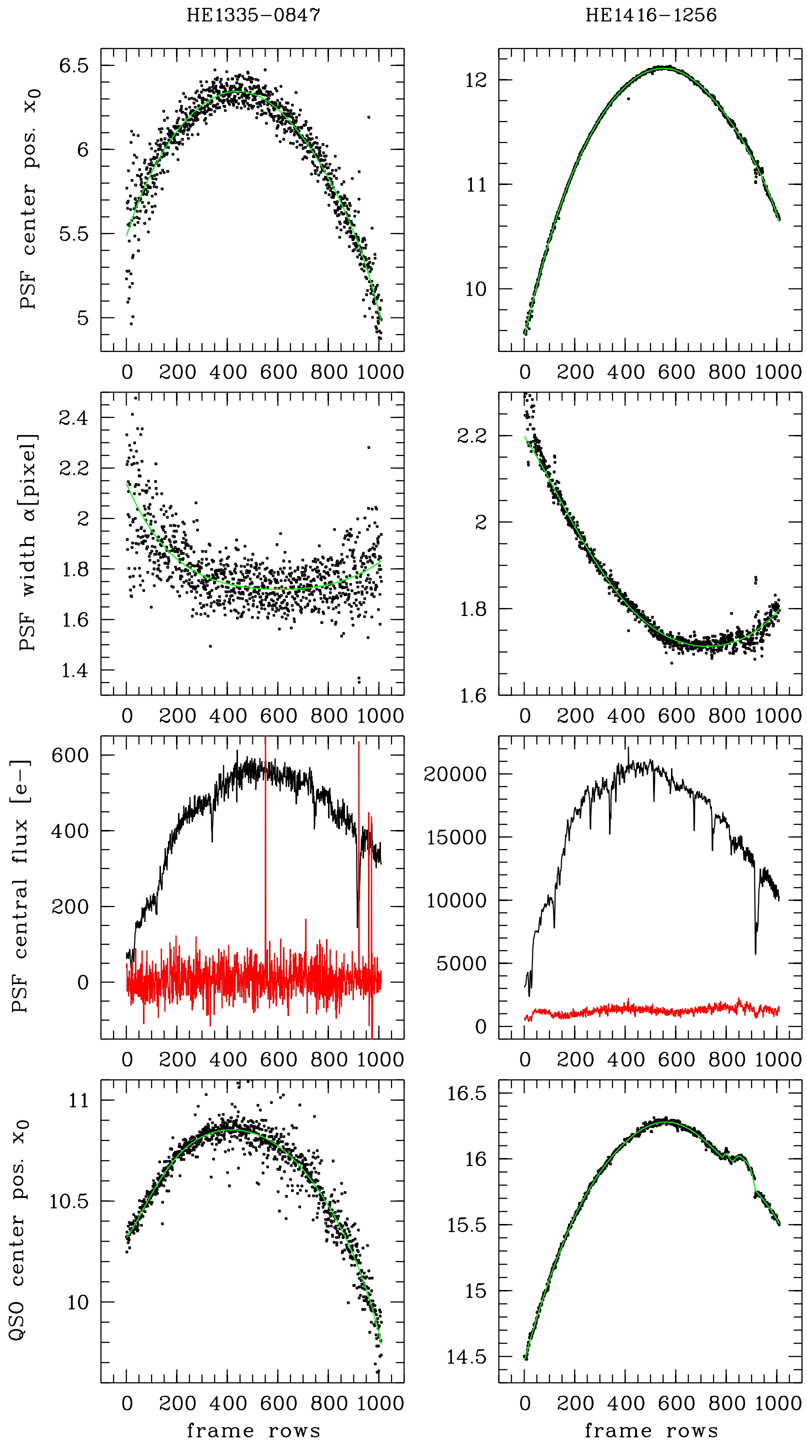

**Figure C.3.** Diagnostics for PSF star and QSO modelling of HE 1335–0847 and HE 1416–1256.

# D VLT spectroscopy sample: modelling diagnostics

Diagnostic plots as for the EFOSC sample (previous appendix), now for the FORS1 VLT sample from section 5. The diagrams shown are (from top): PSF star center $x_0$, PSF star width $\alpha$, PSF star central flux $I_0$ and residual flux, QSO center $x_0$. All values are plotted against image row, which runs inversely to the direction of dispersion (smallest wavelength at highest pixel coordinate). For $x_0$ and $\alpha$ the individually determined values are plotted (points) and the polynomial smoothing fit (solid line). The PSF star residual is not plotted to scale to enhance structures. All three grisms are shown, 600I to the left, 600R in the center, 600B to the right.

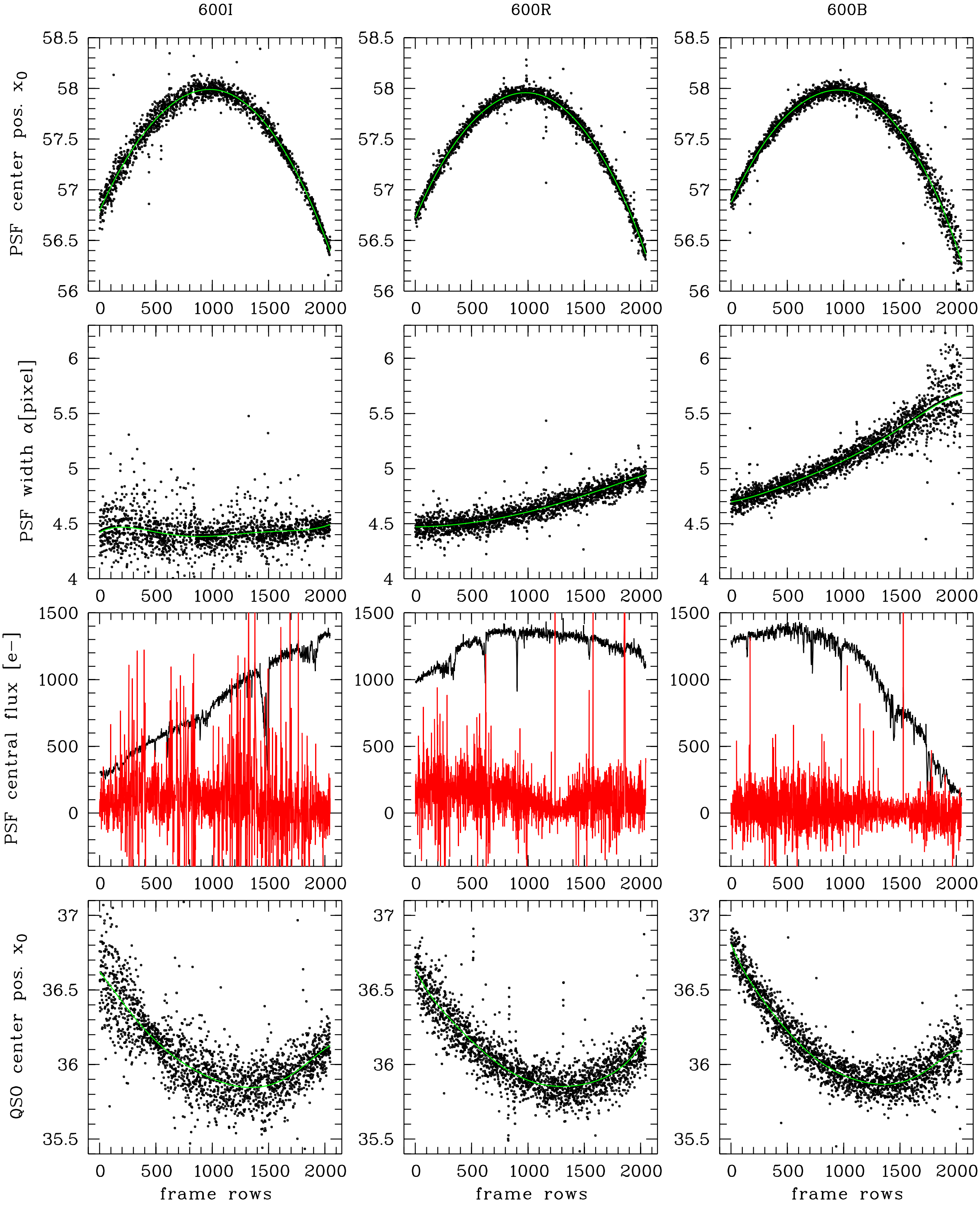

**Figure D.1.** Diagnostics for PSF star and QSO modelling of HE 0914–0031.

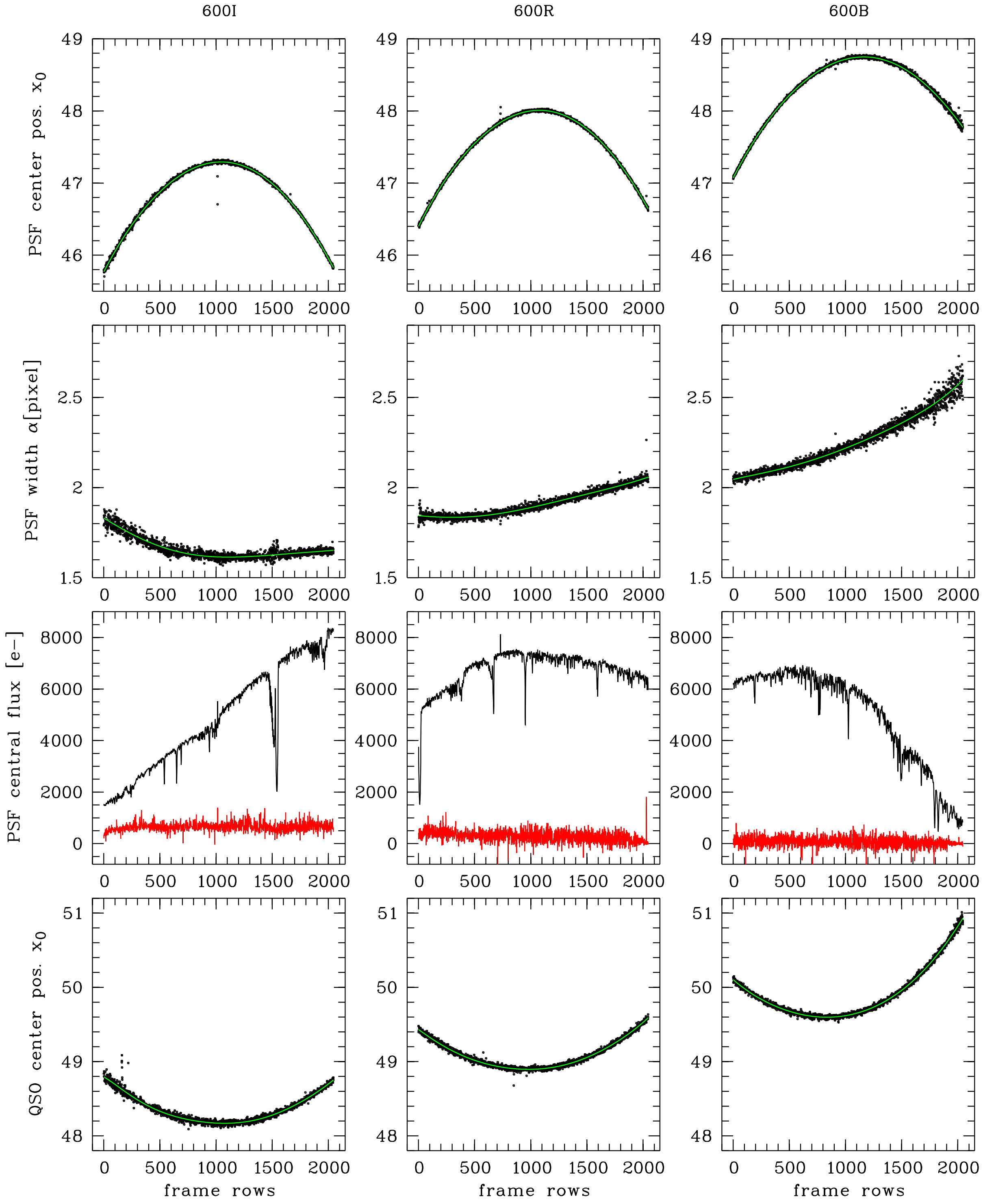

**Figure D.2.** Diagnostics for PSF star and QSO modelling of HE 0956–0720.

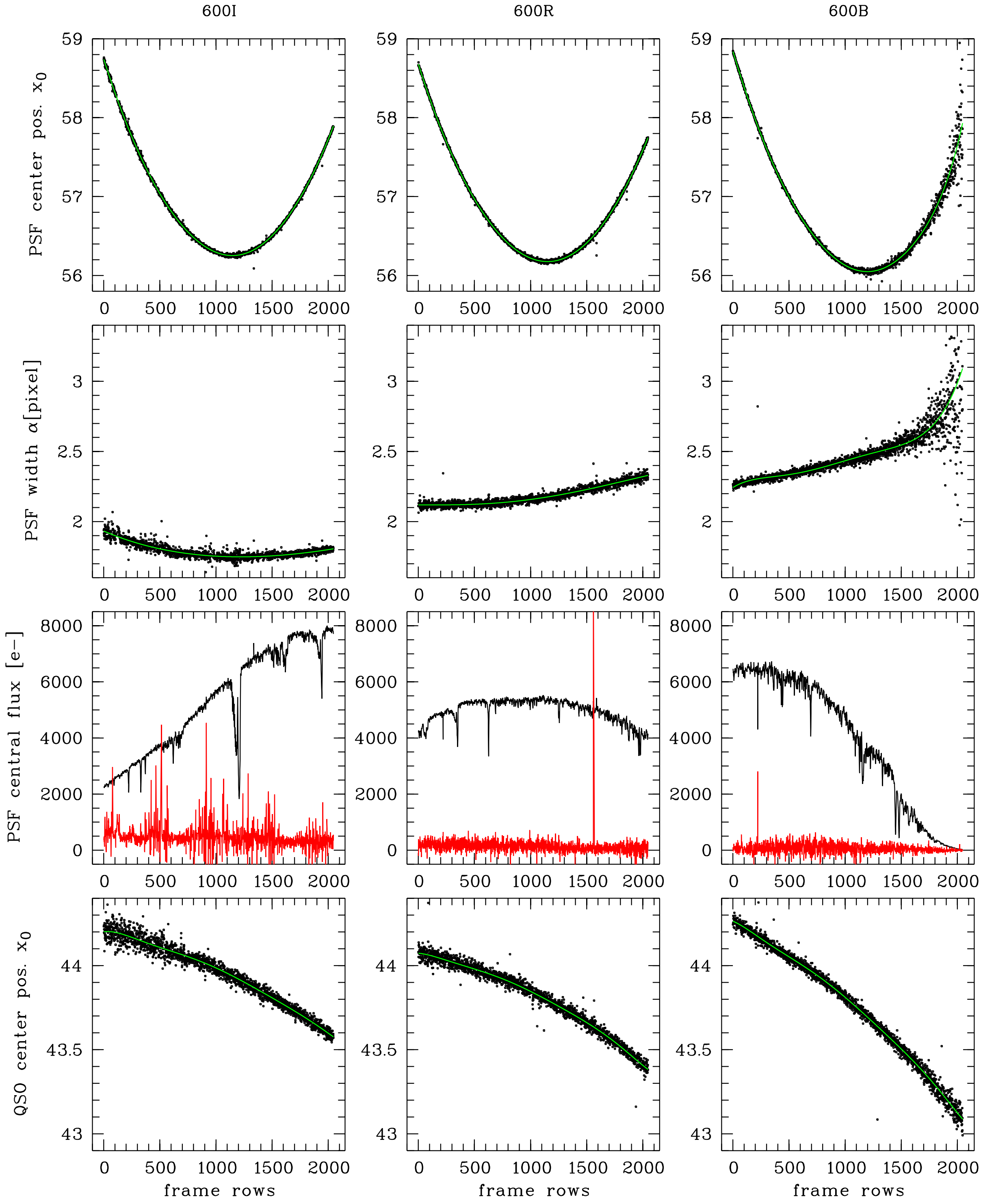

**Figure D.3.** Diagnostics for PSF star and QSO modelling of HE 1009-0702.

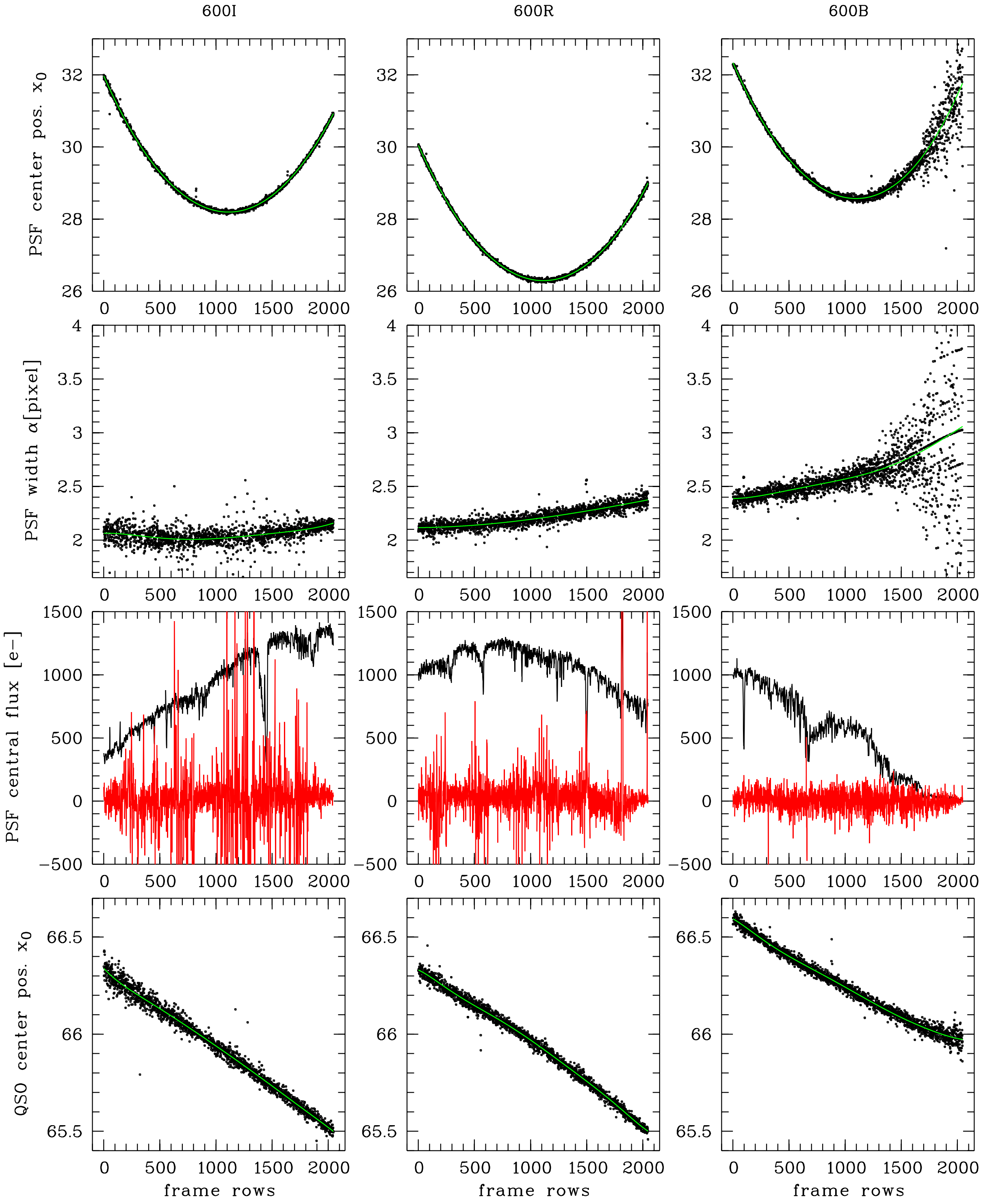

**Figure D.4.** Diagnostics for PSF star and QSO modelling of HE 1015–1618.

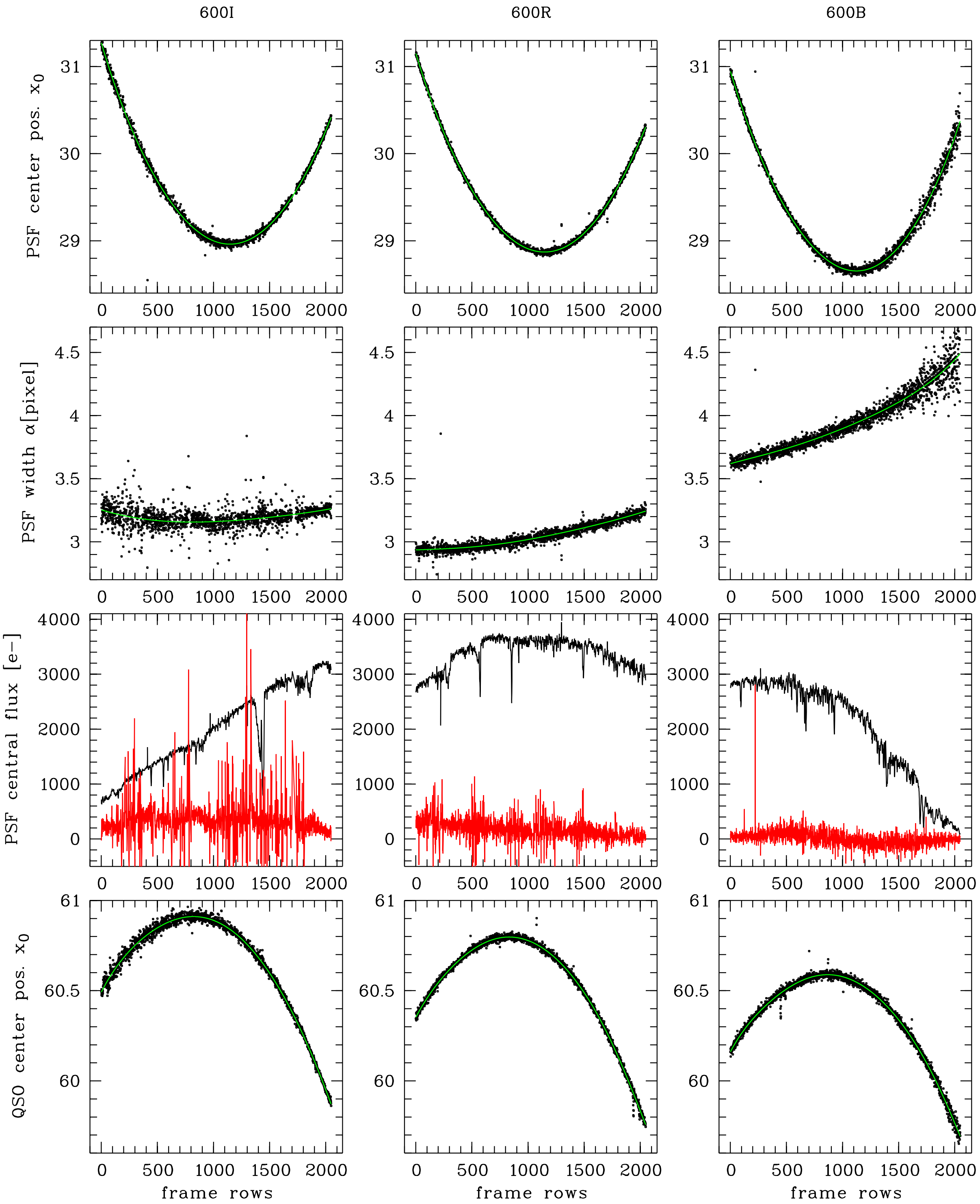

**Figure D.5.** Diagnostics for PSF star and QSO modelling of HE 1029–1401.

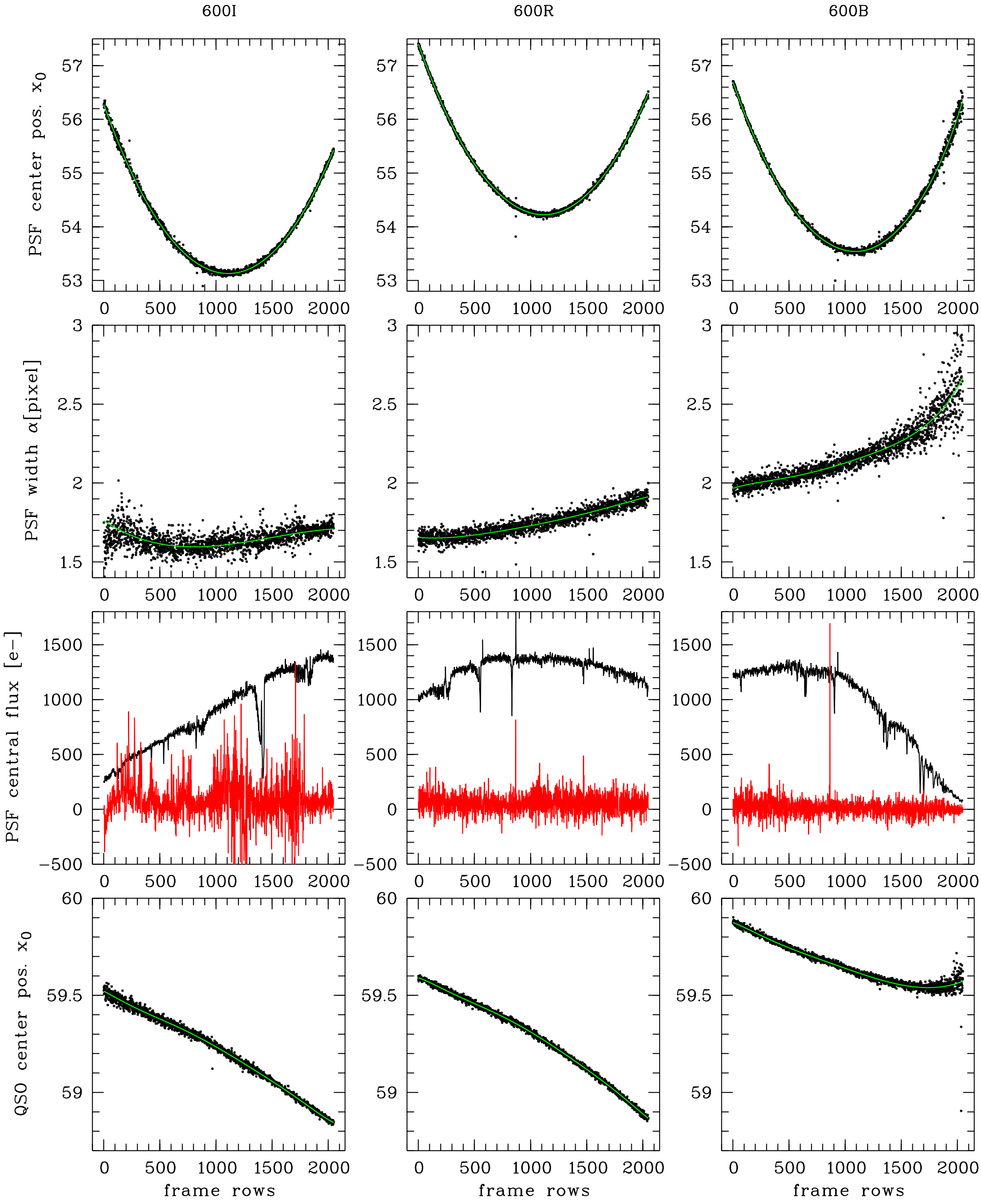

**Figure D.6.** Diagnostics for PSF star and QSO modelling of HE 1228+0131.

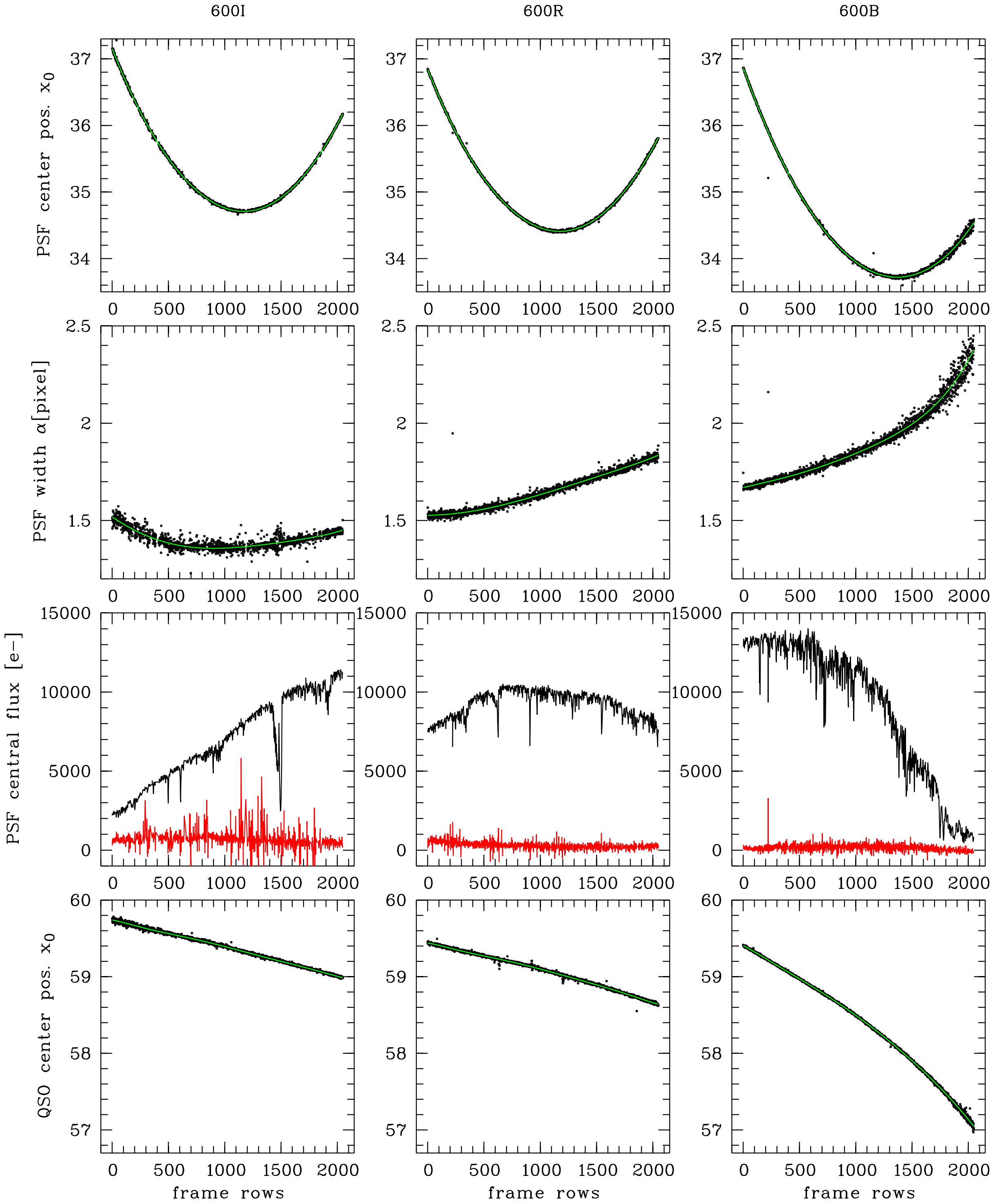

**Figure D.7.** Diagnostics for PSF star and QSO modelling of HE 1302–1017.

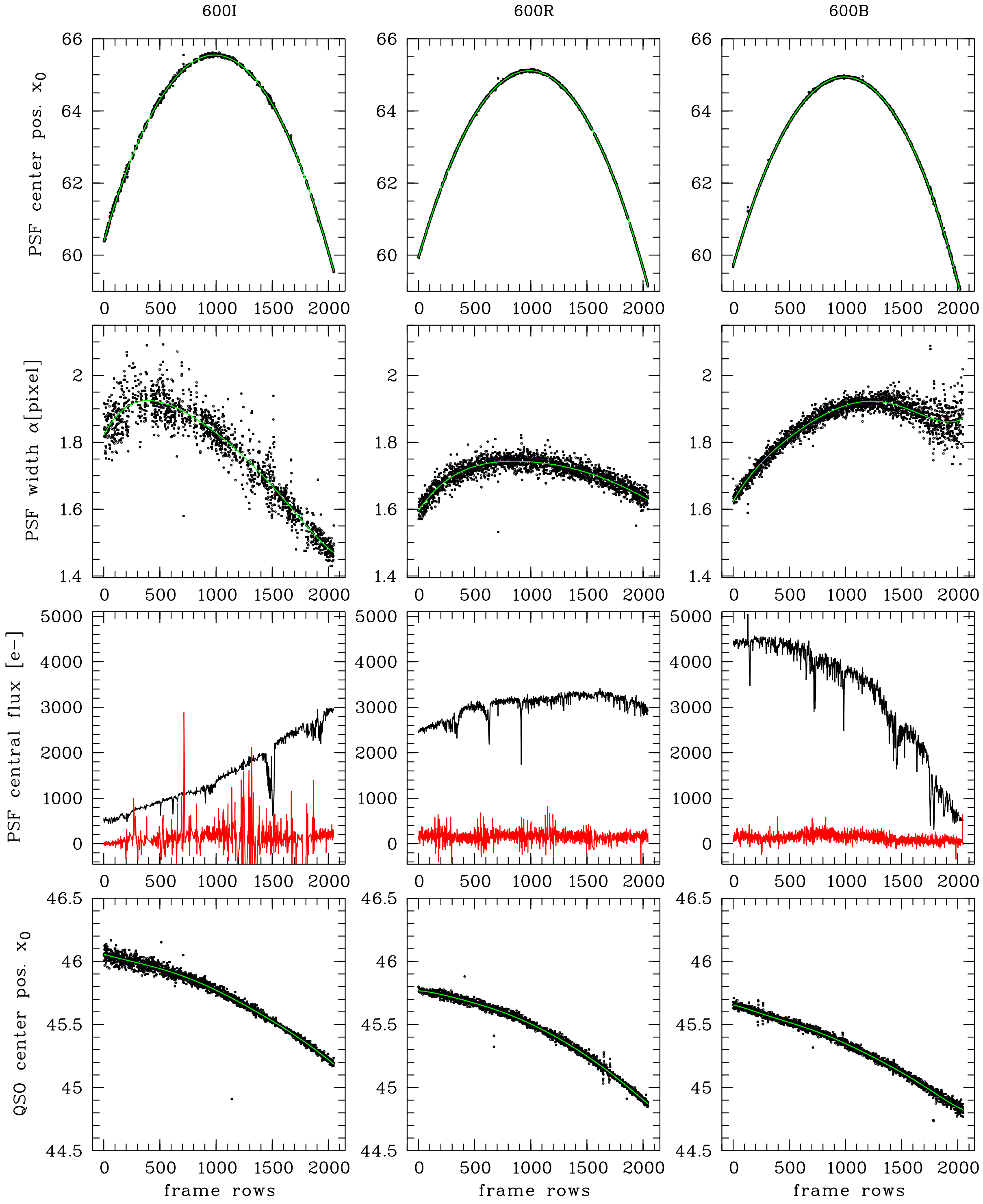

**Figure D.8.** Diagnostics for PSF star and QSO modelling of HE 1434–1600.

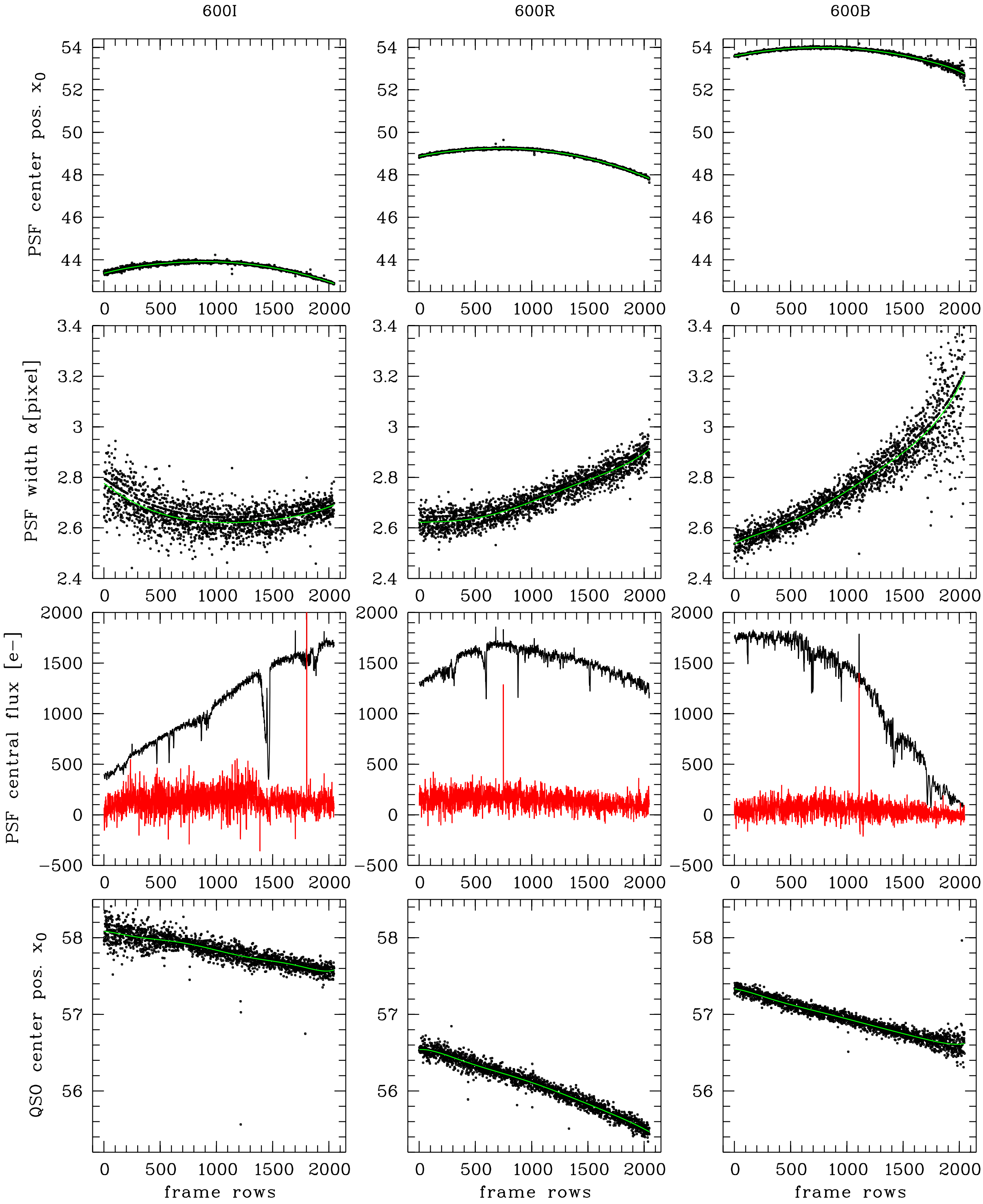

**Figure D.9.** Diagnostics for PSF star and QSO modelling of HE 1442–1139.

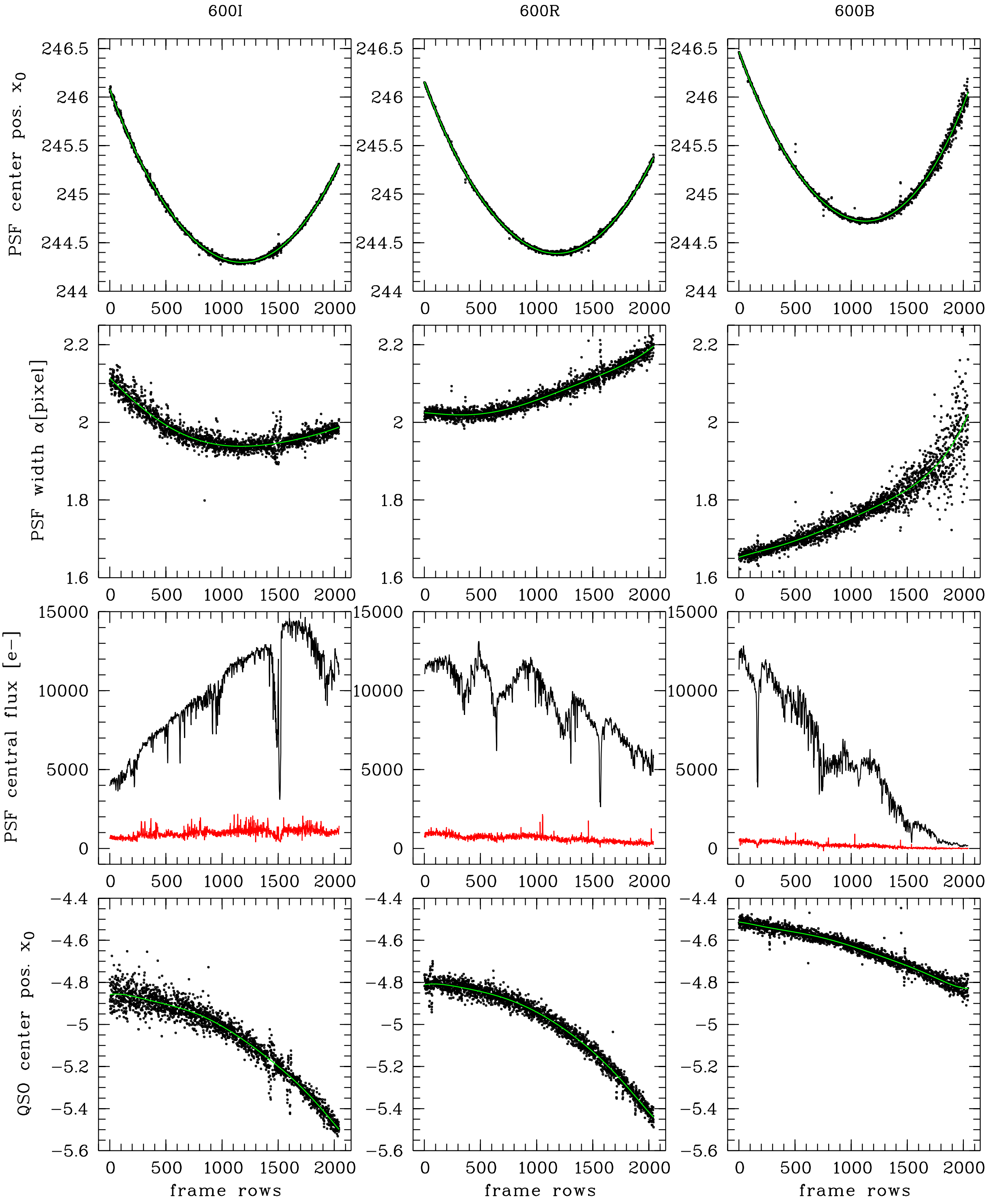

**Figure D.10.** Diagnostics for PSF star and QSO modelling of HE 1503+0228.

# Abbreviations and Acronyms

| | |
|---|---|
| 1C | one component |
| 1d | one-dimensional |
| 2C | two component |
| 2d | two-dimensional |
| AGB | asymptotic giant branch |
| AGN | active galactic nucleus/nuclei |
| ALFOSC | *Andalucia Faint Object Spectrograph and Camera*, NOT instrument |
| BLR | broad line region |
| CMR | colour-magnitude relation |
| CSF | constant star formation |
| DFOSC | *Danish Faint Object Spectrograph and Camera*, ESO/Danish 1.54m instrument |
| EFOSC | *ESO Faint Object Spectrograph and Camera*, ESO/3.6m instrument |
| ENLR | extended narrow line region |
| ESM | evolution synthesis models |
| ESO | *European Southern Observatory* |
| FORS | *Focal Reducer/low dispersion Spectrograph*, ESO/VLT instrument |
| FOV | field of view |
| HES | *Hamburg/ESO Survey* |
| IFS | integral field spectroscopy |
| IR | infrared |
| ISM | interstellar matter |
| LUT | look-up-table |
| MOS | multi object spectrograph |
| NIR | near infrared |
| NOT | *Nordic Optical Telescope*, La Palma |
| NTT | *New Technology Telescope*, ESO/La Silla |
| NLR | narrow line region |
| PMAS | *Potsdam Multi-Apertur Spectrometer* |
| PSF | point spread function |
| QSO | quasi stellar object |
| S/N | signal-to-noise ratio |
| SED | spectral energy distribution |
| SOFI | *Son Of Isaac*, ESO/NTT instrument |
| SSP | single stellar population |
| ULIRG, ULIG | ultra luminous infrared galaxy |
| UV | ultraviolet |
| VLT | *Very Large Telescope*, ESO/Cerro Paranal |

# Bibliography

Abraham, R. G., Crawford, C. S., & McHardy, I. M. 1992, ApJ, 401, 474

Antonucci, R. 1993, Ann. Rev. A&A, 31, 473

Aretxaga, I., Cid Fernandes Jr., R., & Terlevich, R. J. 1997, MNRAS, 287, 271

Aretxaga, I., Le Mignant, D., Melnick, J., Terlevich, R. J., & Boyle, B. J. 1998a, MNRAS, 298, L13

Aretxaga, I., Terlevich, R. J., & Boyle, B. J. 1998b, MNRAS, 296, 643

Bahcall, J. N., Kirhakos, S., Saxe, D. H., & Schneider, D. P. 1997, ApJ, 479, 642

Bahcall, J. N., Kirhakos, S., & Schneider, D. P. 1995, ApJ, 450, 486

Binney, J. & Tremaine, S. 1987, Galactic Dynamics, Princeton Series in Astrophysics (Princeton)

Boroson, T. A. & Oke, J. B. 1982, Nature, 296, 397

—. 1984, ApJ, 281, 535

Boroson, T. A., Oke, J. B., & Green, R. F. 1982, ApJ, 263, 32

Boroson, T. A., Persson, S. E., & Oke, J. B. 1985, ApJ, 293, 120

Bronstein, I. N. & Semedjajew, K. A. 1991, Taschenbuch der Mathematik, 21st edn. (Stuttgart/Leipzig: B. G. Teubner)

Bruzual, G. A. & Charlot, S. 1993, ApJ, 405, 538

—. 1996, `ftp://gemini.tuc.noao.edu/pub/charlot/bc96`

Canalizo, G. & Stockton, A. 2000, ApJ, 528, 201

Courbin, F., Letawe, G., Magain, P., et al. 2002a, The Messenger, 107, 28

—. 2002b, A&A, submitted

Courbin, F., Magain, P., Kirkove, M., & Sohy, S. 2000, ApJ, 529, 1136

de Grijs, R. 1998, MNRAS, 299, 595

de Jong, R. S. 1996, A&A, 313, 377

de Vaucouleurs, G. 1948, Ann. Astrophys., 11, 247

de Vaucouleurs, G. & Capaccioli, M. 1979, ApJS, 40, 699

Dunlop, J. S., McLure, R. J., Kukula, M. J., et al. 2001, MNRAS, astro-ph/0108397

Dunlop, J. S., Taylor, G. L., Hughes, D. H., & Robson, E. I. 1993, MNRAS, 264, 455

Elvis, M., Wilkes, B. J., McDowell, J. C., et al. 1994, ApJS, 95, 1

ESO. 1998, The VLT White Book, `http://www.eso.org/outreach/info-events/ut1fl/whitebook/`

Faber, S. M., Tremaine, S., Ajhar, E. A., et al. 1997, AJ, 114, 1771

Fioc, M. & Rocca-Volmerange, B. 1999, A&A, 351, 869

Freeman, K. C. 1970, ApJ, 160, 812

Fruchter, A. S. & Hook, R. N. 2002, PASP, 114, 144

Fukugita, M., Shimasaku, K., & Ichikawa, T. 1995, PASP, 107, 945

Green, R. F., Williams, T. B., & Morton, D. C. 1978, ApJ, 226, 729

Haehnelt, M. & Rees, M. 1993, MNRAS, 263, 168

Hamilton, T. S., Casertano, S., & Turnshek, D. A. 2000, astro-ph/0011255

Hamuy, M., Suntzeff, N. B., Heathcote, S. R., et al. 1994, PASP, 106, 566

Hamuy, M., Walker, A. R., Suntzeff, N. B., et al. 1992, PASP, 104, 533

Heyl, J. S., Hernquist, L., & Spergel, D. N. 1994, ApJ, 427, 165

Hickson, P. & Hutchings, J. B. 1987, ApJ, 312, 518

Horne, K. 1986, PASP, 98, 609

Hubble, E. 1926, ApJ, 64, 321

Hughes, D. H., Kukula, M. J., Dunlop, J. S., & Boroson, T. 2000, MNRAS, 316, 204

Hutchings, J. B. 1987, ApJ, 320, 122

Hutchings, J. B. 1995, AJ, 110, 994

Hutchings, J. B. & Crampton, D. 1990, AJ, 99, 37

Hutchings, J. B., Crampton, D., & Campbell, B. 1984, ApJ, 280, 41

Hutchings, J. B. & Hickson, P. 1988, AJ, 95, 1363

Hutchings, J. B., Janson, T., & Neff, S. G. 1989, ApJ, 342, 660

Hutchings, J. B. & Neff, S. G. 1992, AJ, 104, 1

Jahnke, K. 1998, Master’s thesis, Universität Hamburg

Jamiroquai. 1996, Travelling Without Moving, Sony Records

Kauffmann, G. & Haehnelt, M. 2000, MNRAS, 311, 576

Kennicut, R. C. 1992, ApJS, 79, 255

Kinney, A. L., Calzetti, D., Bohlin, R. C., et al. 1996, ApJ, 467, 38

Köhler, T., Groote, D., Reimers, D., & Wisotzki, L. 1997, A&A, 325, 502

Kormendy, J. & Richstone, D. 1995, ARA&A, 33

Kotilainen, J. K. & Ward, M. J. 1994, MNRAS, 266, 953

Kristian, J. 1973, ApJ, 179, L61

Kuhlbrodt, B., Wisotzki, L., & Jahnke, K. 2001, in QSO Hosts and their Environments,, ed. I. Marqués, J. Masegosa, A. del Olmo, L. Lara, E. García, & J. Molina (Kluver Academic/Plenum Publishers), 347

Kukula, M. J., Dunlop, J. S., McLure, R. J., et al. 2001, MNRAS, 326, 1533

Lake, G., Katz, N., & Moore, B. 1998, ApJ, 495, 152

Leitherer, C. et al. 1996, PASP, 108, 996

Lowenthal, J. D., Heckman, T. M., Lehnert, M. D., & Elias, J. H. 1995, ApJ, 439, 588

MacKenty, J. W. & Stockton, A. 1984, ApJ, 283, 64

Magain, P., Courbin, F., & Sohy, S. 1998, ApJ, 494, 472

Magorrian, J., Tremaine, S., Richstone, D., et al. 1998, AJ, 115, 2285

Malkan, M. A. 1984, ApJ, 287, 555

Mannucci, F., Basile, F., Poggianti, B. M., et al. 2001, MNRAS, 326, 745

Maraston, C. 1998, MNRAS, 300, 872

McLeod, K. K. & Rieke, G. H. 1994a, ApJ, 420, 58, mR1

—. 1994b, ApJ, 431, 137, mR2

—. 1995a, ApJ, 454, L77

—. 1995b, ApJ, 441, 96, mR3

McLeod, K. K., Rieke, G. H., & Storri-Lombardi, L. J. 1999, ApJ, 511, L67

McLure, R. J. & Dunlop, J. S. 2001, MNRAS, 327, 199

—. 2002, MNRAS, 331, 795

McLure, R. J., Dunlop, J. S., & Kukula, M. J. 2000, MNRAS, 318, 693

McLure, R. J., Kukula, M. J., Dunlop, J. S., et al. 1999, MNRAS, 308, 377

Merrit, D. & Ferrarese, L. 2001, MNRAS, 320, L30

Miley, G. K. & Miller, J. S. 1979, ApJ, 228, L55

Moffat, A. F. J. 1969, A&A, 3, 455

Möllenhoff, C. & Heidt, J. 2001, A&A, 368, 16

Morton, D. C., Williams, T. B., & Green, R. F. 1978, ApJ, 219, 381

Nolan, L. A., Dunlop, J. S., Kukula, M. J., et al. 2001, MNRAS, 323, 308

Oosterloo, T. A., Morganti, R., Sadler, E. M., Vergani, D., & Caldwell, N. 2002, AJ, 123, 729

Örndahl, E. & Rönnback, J. 2001, in QSO Hosts and their Environments,, ed. I. Marqués, J. Masegosa, A. del Olmo, L. Lara, E. García, & J. Molina (Kluver Academic/Plenum Publishers), 61

Osterbrock, D. E. 1989, Astrophysics of gaseous nebulae and Active Galactic Nuclei (University Science Books)

Percival, W. J., Miller, L., McLure, R. J., & Dunlop, J. S. 2001, MNRAS, accepted, astro-ph/0002199

Press, W. H., Teukolsky, S. A., Vetterling, W. T., & Flannery, B. P. 1995, Numerical recipes in C, 2nd edn. (Cambridge University Press)

Reimers, D., Köhler, T., & Wisotzki, L. 1996, A&AS, 115, 235

Richstone, D. O. & Oke, J. B. 1977, ApJ, 213, 8

Rönnback, J., Van Groningen, E., Wanders, I., & Örndahl, E. 1996, MNRAS, 283, 282

Roth, M. M., Bauer, S. M., Dionies, F., et al. 2000, SPIE, 4008, 277

Saglia, R. P., Bertschinger, E., Baggley, G., et al. 1993, MNRAS, 264, 961

Sanders, D. B. & Mirabel, I. F. 1996, ARA&A, 34, 749

Scalo, J. M. 1986, Fund Cosmic Phys, 11, 1

Schade, D., Boyle, B. J., & Letawsky, M. 2000, MNRAS, 315, 498

Schlegel, D. J., Finkbeiner, D. P., & Davis, M. 1998, ApJ, 500, 525

Schmidt, M. & Green, R. F. 1983, ApJ, 269, 352

Sheinis, A. I. 2001, in QSO Hosts and their Environments,, ed. I. Marqués, J. Masegosa, A. del Olmo, L. Lara, E. García, & J. Molina (Kluver Academic/Plenum Publishers), 141

Smith, E. P., Heckman, T. M., Bothun, G. D., Romanishin, W., & Balick, B. 1986, ApJ, 306, 64

Sparke, L. S. & Gallagher, J. S. 2000, Galaxies in the Universe (Cambridge University Press)

Stetson, P. B. 1987, PASP, 99, 191

Stockton, A. 1976, ApJ, 205, L113

Surace, J. A., Sanders, D. B., & Evans, A. S. 2001, AJ, 122, 2791

Taylor, G. L., Dunlop, J. S., Hughes, D. H., & Robson, E. I. 1996, MNRAS, 283, 930

Terlevich, R., Tenorio-Tagle, G., Franco, J., & Melnick, J. 1992, MNRAS, 255, 713

Terlevich, R., Tenorio-Tagle, G., Rozyczka, M., Franco, J., & Melnick, J. 1995, MNRAS, 272, 198

Tremblay, B. & Merritt, D. 1996, AJ, 111, 2243

Trujillo, I., Aguerri, J. A., Cepa, J., & Gutiérrez, C. M. 2001, MNRAS, 328, 977

Veilleux, S. & Osterbrock, D. E. 1987, ApJS, 63, 295

Wampler, E. J., Burbidge, E. M., Baldwin, J. A., & Robinson, L. B. 1975, ApJ, 198, L49

Wisotzki, L., Christlieb, N., Bade, N., et al. 2000, A&A, 358, 77

Wisotzki, L., Köhler, T., Groote, D., & Reimers, D. 1996, A&AS, 115, 227

Wisotzki, L., Kuhlbrodt, B., & Jahnke, K. 2001, in QSO Hosts and their Environments,, ed. I. Marqués, J. Masegosa, A. del Olmo, L. Lara, E. García, & J. Molina (Kluver Academic/Plenum Publishers), 83

Wyckoff, S., Gehren, T., Morton, D. C., et al. 1980a, ApJ, 242, L59

Wyckoff, S., Wehinger, P. A., Spinrad, H., & Boksenberg, A. 1980b, ApJ, 240, 25

# Acknowledgements

The first thanks go to Prof. Dieter Reimers for his help to make it possible for me to do research in his group, leading to this thesis. It was also him that opened the doors towards the grant that guaranteed my subsistence and simultaneously gave me the freedom I enjoyed during this time.

Much of this thesis I also owe to my supervisor and remote-coach Lutz Wisotzki. Even though being usually somewhere else, a different city, different country, different continent, he always asked the right questions, honest but fair, and managed to give the right dose of kick-in-the-but at times. His office, mailbox and phone were and are always open, whenever needed. I'm looking forward to a continued co-operation (and maybe some more cycling trips).

The next on the list is coworker and office-mate Björn Kuhlbrodt: Thank you for working in the same field, I do not know if I would have made it alone! I always enjoyed sharing lunch, computer frustration, serious cooking, travels and stories. And PAMDAI rulez!

A big thanks I also owe to the Villa people, especially Hans Hagen, Dieter Engels, Olaf Wucknitz and Volker Beckmann, but also all the others. It was great to have you next door or upstairs, with a lot of fun during those years.

I don't want to forget Eva Örndahl. Observing at La Palma, the conferences, our working sessions and everything around that were always very enjoyable. Maybe we'll manage to get a joint paper published before 2010?

I also thank Prof. H. P. Bull and Dr. Max Brocker for their energy and support with grants, travels, and applications. The Studienstiftung gave me a lot of insights into subjects I would otherwise not have had access to. I really enjoyed the language course, summer school, the Jerusalem Doktorandenmeeting and all those Stifti group evening.

Zum Schluß, aber nicht als letzte danke ich meinen Eltern für ihre Unterstützung und Ermutigungen. Und natürlich Friederike K: Danke für Deine Geduld, Deinen Rundumsorglosservice während der letzten Wochen und daß es dich gibt!